UNIVERSITÉ DE SHERBROOKE
Faculté de génie
Département de génie mécanique

Analyse des sources du bruit de jeu dans les ventilateurs axiaux

Analysis of Tip Leakage Flow Noise Inception in Axial Fans

Thèse de doctorat
Specialité : génie mécanique

Dominic LALLIER-DANIELS

Jury: Stéphane MOREAU (directeur)
Philippe LAVOIE
Martin BROUILLETTE
Adrien MANN
Marlène SANJOSÉ

Sherbrooke (Québec) Canada Mai 2018

RÉSUMÉ

L'écoulement de jeu est un phénomène hautement complexe et inévitable dant les turbomachines étant donné la nécessité de prévenir l'interférence des éléments statiques avec le rotor. Il mène cependant à des pertes potentiellement importantes au niveau de la performance aérodynamique ainsi qu'à une augmentation de la signature acoustique de ces machines. Les mécanismes associés à ce type d'écoulement secondaire ont été largement étudiés dans les dernières décennies, mais étant donné les phénomènes complexes en présence, l'espace limité ainsi que l'interaction de pièces en mouvement rapide, une investigation expérimentale *in-situ* de l'écoulement de jeu est souvent ardue et requiert l'emploi de techniques avancées. En conséquence, la caractérisation de ce mécanisme est encore incomplète et demeure un sujet d'actualité dans le monde de la recherche ; des analyses conjointes des aspects aérodynamique et aéroacoustique sont particulièrement rares.

La présente thèse propose de tirer parti du potentiel des méthodes de simulation numérique d'écoulements fluide pour réaliser une étude aéroacoustique de l'écoulement de jeu dans les ventilateurs axiaux basse-vitesse. La méthode Lattice-Boltzmann a été choisie pour réaliser l'étude à cause de la capacité qu'elle a de réaliser simultanément une étude aérodynamique et aéroacoustique en propagation directe sur une série de ventilateurs basse-vitesse avec et sans virole tournante. Ceux-ci furent choisis en grande partie à cause de l'existence d'une banque de données expérimentale permettant de valider les résultats de simulation et dans l'optique de fournir une vue large sur les différents aspects géométriques et opérationnels pouvant avoir une influence sur la formation de l'écoulement de jeu.

Les résultats numériques ont été employés pour réaliser une analyse détaillée du champ associé à l'écoulement de jeu et permettre l'identification des sources de bruits rattachées à l'aide de techniques de visualisations basées sur l'emploi d'isosurfaces de critère λ_2 et l'emploi combiné de l'analogie acoustique de Ffowcs Williams et Hawkings et de visualisations de fluctuations de pression filtrés à la surface des rotors. La différence fondamentale dans le mécanisme de formation de l'écoulement de jeu entre les machines axiales avec et sans virole a été mis en évidence, mais l'apparition de composantes tonales dans le spectre acoustique associées à l'interaction des structures cohérentes provenant du jeu avec les pales des rotors a été observée dans tous les cas.

Dans le but de fournir une évaluation quantitative du champ de distorsion responsable de l'apparition de ce bruit tonal, une technique de corrélation spectrale précédemment employée pour la caractérisation d'instabilités dans les machines centrifuges a été adaptée à l'étude du champ inhomogène induit par l'écoulement de jeu dans la région de bout de pale et permettre l'évaluation de son effet sur la signature acoustique des machines axiales étudiées.

Mots-clés : Ventilateurs axiaux, Écoulement de jeu, Aéroacoustique, Simulation numérique d'écoulements fluides

ABSTRACT

Tip leakage flow is a highly complex phenomena that is unavoidable in turbomachinery applications due to the fact that a tip clearance is required to prevent the interference of the static elements of a turbomachine system with the moving rotor. It can lead to potentially large performance losses by modifying the aerodynamic conditions surrounding the blade as well as increases in the sound radiation of the fan. Tip leakage flow mechanics have been extensively studied in the last few decades, but given the complex flowfields encountered in turbomachine applications and the small geometric space coupled the moving parts of typical rotor geometries, *in-situ* experimental investigation of tip leakage flow is arduous at best, requiring advanced experimental setups, and at worst nigh impossible in normal turbomachine operation. As a result, the characterization of this highly complex phenomena is still incomplete and remains a very active research field. Furthermore, joint aerodynamic and aeroacoustic investigations are rare for that particular phenomena.

The current study was designed to leverage the potential of CFD methods for the evaluation of tip leakage flow mechanics and its impact on the acoustic radiation of low-speed axial fans, which arguably represent the most common and *simple* archetype of fans. A relatively recent class of CFD method called the Lattice-Boltzmann Method (LBM) was used to jointly evaluate the aerodynamic and aeroacoustic performance of selected fan systems, both free-tipped and ring-shrouded configurations, with an available experimental database to which the simulation data was compared. The fans were selected on to allow for an extensive foray into the mechanics of tip leakage flow for a wide variety of configurations and operating conditions.

The CFD results were leveraged to perform a detailed investigation of the tip clearance flowfield for each case and identify the noises sources associated with tip clearance flow using flow visualizations based on the λ_2 criteria for the identification of vortical structures and the combined use of the Ffowcs Williams and Hawkings' acoustic analogy with filtered wall-pressure fluctuation maps of the blade surfaces. The stark contrast in the tip flow mechanics associated with free-tipped and ring-shrouded fans was made evident from this analysis, but tonal components in the acoustic spectra of each of the configurations related to tip clearance mechanisms were also identified as a result of the interaction of the coherent turbulent structures generated by the rotor blades.

In order to characterize the flow distortions reponsible for the identified narrowband noise, a spectral correlation technique previously used for the experimental characterization of flow instabilities in centrifugal fans that was adapted to quantify the distortions in the flow induced by the tip leakage flow and their impact of the acoustic radiation of the fan. The analysis is carried out on each of the fan configurations studied and the structure of the distortion fields responsible for the tonal noise radiated as a result of the interaction of the tip leakage flow with the rotor blades is investigated.

Keywords: Axial Fans, Tip Leakage Flow, Aeroacoustics, Computational Fluid Dynamics

TABLE OF CONTENTS

LIST OF FIGURES

LIST OF TABLES

CHAPTER 1

Introduction

1.1 Context of the Study

Turbomachine systems are an integral part of everyday life in the modern world. Everyday applications encountered include Heating, Ventilation and Air Conditioning (HVAC) systems, cooling systems in the transportation industry (e.g. automotive engine cooling fans), cooling fans for consumer electronics, compressor units in food refrigeration appliances; one could extend the list to include high-speed rotors used in aircraft propulsion, as the air transportation market is slated to keep growing at a fast rate through 2037 [1]. However, the vast majority of the machines routinely encountered in a typical day can be classified in the low-speed fan category. They are often invisible to the naked eye, for security as well as aesthetic reasons, but also to mask their presence which can be felt through other means, not the least of which is through the noise they radiate. This acoustic contribution can be an annoyance in some cases or devolve into a health issue after prolonged exposure.

As a result, perpetually evolving performance standards for turbomachine operation, both aerodynamic and acoustic, are put in place to protect the public from any adverse effects, leading rotating machine designers to scramble and improve their design methodologies to meet these requirements. Turbomachine design is however a complex process in and of itself given the intricate flowfields encountered in such rotating machines and the sometimes very variable flow conditions they are exposed to. Furthermore, unwanted flow phenomena incurring losses and/or increased noise are inevitable even with careful design procedures as they are still ill-understood and not taken into account properly.

One of these unwanted phenomena occurs because of the tip clearance that is required to prevent the interference of the static elements of a turbomachine system with the moving rotor that is imparting (compressor, fan, pump) or retrieving (turbine) energy from the fluid flow, depending on the vocation of the system. That particular flow phenomena is called tip leakage flow (TLF) and is characterized by a passage of a certain portion of the fluid from the pressure side (high pressure) of a turbomachine blade towards its suction side

1. FAA Aerospace Forecast 2017-2037; `https://www.faa.gov/data_research/aviation/aerospace_forecasts/media/FY2017-37_FAA_Aerospace_Forecast.pdf`

(low pressure) across the tip clearance gap, forming a strong cross-flow perpendicular to the blade chord that is the turbomachine equivalent of the tip flow formed at the tip of finite aircraft wings. This flow in and of itself as well as its interaction with the throughflow in the machine leads to the creation of potentially large losses by modifying the aerodynamic conditions surrounding the blade as well as creating large turbulent structures that are convected in the passage flow. In addition to aerodynamic losses, tip leakage flow and the fluid phenomena that are created as a result of it can contribute to a large degree to the acoustic footprint of the affected turbomachine systems.

Tip leakage flow mechanics have been studied in the last few decades, with some studies dating as far back as the 1940s, with most of the investigative work being carried out through experiments. However, given the complex flowfields encountered in turbomachine applications and the small geometric space coupled the moving parts of typical rotor geometries, *in-situ* experimental investigation of tip leakage flow is arduous at best, requiring advanced experimental setups, and at worst nigh impossible in normal turbomachine operation. As a result, the characterization of this highly complex phenomena is still incomplete and it is still a very active research field. Furthermore, joint aerodynamic and aeroacoustic investigations are rare for that particular phenomena.

In parallel, the last decades have seen the emergence of computational fluid dynamics (CFD) as a way to simulate and more easily investigate such complex flowfields, with the advent of exponentially more powerful computers showcasing parallel processing capabilities and the continuous improvements in the numerical methods employed for simulating fluid flows. These numerical methods, should they prove reliable in reproducing the actual flow physics of complex turbomachine systems as well as the associated acoustic radiation, would prove an invaluable tool for joint aerodynamic/aeroacoustic investigations of tip leakage flow mechanics and the associated noise as well as for several other phenomena.

1.2 Framework of the Current Thesis

The current study was designed to leverage the potential of CFD methods for the evaluation of tip leakage flow mechanics and its impact on the acoustic radiation of low-speed axial fans, which arguably represent the most common and *simple* archetype of fans. The chosen method is thus required accurately represent the highly unsteady and turbulent flow features associated with the TLF phenomena. Concurrently, it must also be able to predict the acoustic radiation resulting from the interaction with the rotor blades numerically (Computation Aeroacoustics, CAA).

While this is theoretically achievable using so-called *traditional* unsteady CFD codes based on the Navier-Stokes equations (i.e. Large-Eddy Simulations, LES and Direct Numerical Simulations, DNS), it would require impractical amounts of computational resources for the direct propagation of the aeroacoustic properties in a realistic environment using these methods.

A relatively recent class of CFD method called the Lattice-Boltzmann Method (LBM), however, shows promise in that regard and has seen its usage grow in recent years, especially in the field of turbomachinery modeling for low-speed machines. Thus, one of the objectives of the current work was to evaluate the potential of the LBM for such a specialized study, which would allow for a joint aerodynamic/aeroacoustic investigation of TLF for complex configurations. To carry out the performance evaluation of the method, a series of low-speed fan geometries for which extensive experimental databases were available were evaluated in the course of the current work; they are described in Chap. 3 and include both free-tipped as well as ring-shrouded fan geometries. This allowed for the comparison of the numerical results with those from the experiments, as shown in Chap. 5.

The selected configurations allowed to evaluate the topology and acoustic impact of tip leakage flow for varied tip geometries. However, the investigated fan systems were operated in fairly different environments (test rigs), and the LBM simulations were setup to accurately represent and capture the differences between them, so the impact of the test environment on the formation of TLF and the associated acoustic impact could be investigated.

1.3 Outline of the Thesis

As a first step in this investigation of TLF, a review of the literature on the subject is first presented in Chap. 2. An overview of the noise mechanisms in low-speed fans is first presented, and their relative importance is qualitatively graded. A literature review on the subject of TLF specifically is then carried out, covering both the aerodynamic and aeroacoustic aspects.

The various fan configurations selected for the study of tip leakage flow in the course of this work are then described in Chap. 3. A total of 5 fan geometries were selected for investigation, with three from the free-tipped archetype of fans and two ring-shrouded rotors. The test rigs employed for the experimental characterization of each of these fans as well as the available data are detailed.

Chap. 4 introduces the numerical methods available for the purpose of carrying out a CAA investigation of tip leakage flow on the proposed geometries. The expected performance of *classical* unsteady CFD methods (LES, DNS) is measured against the emerging LBM for the purpose of carrying out direct aeroacoustic simulations. An informative section of so-called *hybrid* CAA methods is also presented, with a certain emphasis placed on a very powerful tool in the field of turbomachinery called the Ffowcs Williams and Hawkings (FWH) analogy.

In Chap. 5, the predictive performance of the LBM for the five studied geometries is evaluated by comparing the simulations with the available experimental data, from both the aerodynamic and the direct acoustic point of view.

A specific investigation of the tip leakage flow topology and associated acoustics is presented out in Chap. 6. The coherent structures generated by the TLF around the studied configurations are visualized using the λ_2 criterion proposed by Jeong and Hussain [Jeong and Hussain, 1995] using the unsteady volumetric data recorded in the simulations. The difference in the tip leakage flow mechanics between free-tipped and ring-shrouded fans is highlighted. The identification of the acoustic signature of the TLF is carried out using an approach based on the FWH analogy and the use of band-pass filtering techniques on the wall-pressure fluctuations from the rotor surface. The use of the FWH analogy is necessary to delineate the specific acoustic contribution of the fan from the installation effects which dominate the spectra for some of the configurations. The occurrence of quasi-tonal noise is linked to the presence of flow distortions generated by the tip leakage flow in the tip region of the blades.

Chap. 7 presents a spectral correlation technique previously used for the experimental characterization of flow instabilities in centrifugal fans [Bent, 1993; Bent *et al.*, 1993; Mongeau *et al.*, 1993] that was adapted to quantify the distortions in the flow induced by the tip leakage flow and their impact of the acoustic radiation of the fan. The analysis is carried out on each of the fan configurations studied and the structure of the distortion fields responsible for the tonal noise radiated as a result of the interaction of the tip leakage flow with the rotor blades is investigated.

Finally, Chap. 8 contains a summary of the work carried out and results obtained in the course of this thesis and highlights the main observations that can be drawn from this work.

CHAPTER 2

Literature Review

2.1 Context

In even the most carefully designed turbomachines, unwarranted flow phenomena having negative impacts on turbomachine operation are bound to occur. However, as there is a large variety in the shape and size of the various rotating machines, each individual case is slightly (or in some cases very) different from the next. The intended application of the machine may also emphasize the importance of controlling these flow phenomena. Turbomachinery design is thus a very complex process in and of itself, and is subjected to increasingly strict standards, be they self-imposed by manufacturers to improve market shares or meet required specifications, legislative in nature, or as a result of novel design methods becoming the norm, such as those based upon computational fluid dynamics (CFD).

Historically, a large emphasis on aerodynamic performance has driven development methods forward, especially improvements in efficiency of designed machines. However, undesirable flow phenomena incurring losses are inevitable even with careful design. In the last decades, the added complexity of more stringent regulations on the allowable noise levels for given applications has become critical in many engineering applications such as transportation (e.g. aeroengines, cooling systems) or ventilation systems for example. As manufacturers are quickly discovering, controlling the noise levels of novel machines at the design stage is a daunting task and requires knowledge of the mechanisms in play, therefore driving research and development in the field of turbomachinery aeroacoustics. This chapter proposes a brief review on the subject of fan acoustics, with an emphasis on low-speed axial fans, which are arguably the most common type encountered in everyday life and are typically used when high flow rates are required.

2.2 Noise Sources in Low-Speed Fans

The possible noise sources in a turbomachinery environment are multiple and possibly very dependant on the installation in their occurrence and importance. Fan noise mechanisms can be classified into two categories: rotational and non-rotational noise ([Longhouse,

1976], [Roger, 2009], [Moreau, 2011]). The rotational noise sources are dependant on the periodic interactions of the rotor with the flow causing a fluctuation of the blade loading, which normally produces strong tones around the BPF and its harmonics. Non-rotational noise is however considered to occur due to random turbulence and is mostly considered to radiate as broadband noise, with some tonal noise normally uncorrelated with the BPF also occuring due to some mechanisms.

Here, the concern regarding the noise mechanisms of low-speed fans in a ducted environment is considered, with possible interactions from the installation in a realistic environment also taken into account.

2.2.1 Rotational Noise Mechanisms

As explained before, rotational noise mechanisms are highly linked to the tonal noise near the BPF and its harmonics. These deterministic and periodic phenomena, when observed from the rotating frame of reference of the blades, cause periodic fluctuations in the blade loading and thus produce mainly tonal noise peaks.

Thickness Noise

The first rotational noise component which could be considered is the so-called thickness noise, which refers to the effect of the displacement of the fluid by the volume of the rotor blades themselves. This mechanism is however highly related to the compressibility of the fluid and is therefore more important at high rotor speeds and negligible in inhomogeneous low-speed applications where thickness noise will be drowned out by general turbulence in the passage flow [Caro and Moreau, 2000; Moreau, 2011; Roger, 2009].

Steady Blade Loading/Unsteady Blade Loading noise

The second source of noise takes root in the blade forces present on the blades themselves (loading noise). The blade load can be decomposed into two separate components: the steady blade load, which is the average blade force as seen from the perspective of the rotating blades, and an unsteady component which varies in a periodic manner during the course of one rotation of the blade due to natural turbulence in the boundary layer of the rotor blades or inhomogeneities in the inflow [Roger, 2009]. The rotation of these forces with the blades causes the appearance of a tonal noise component around the BPF and its hamonics. However, it should be noted that for low-speed applications, steady blade loading noise is negligible [Roger, 2009] and is dominated by unsteady blade loading effects.

Flow Distortion Noise

To the inherent blade thickness and loading noise can be added the inference of installation effects on the blade loading. A first source would be inflow distortions [Moreau, 2011]. These distortions can have different origins. For example, inflow distortions for an automotive cooling fan may be produced by struts present in the inlet portion of the fan assembly, forming a wake seen as a localized distortion of the flowfield periodically encountered by the rotating blades and causing a fluctuation of the blade loading, thus producing tonal noise. A second inflow distortion source which could be considered are the boundary layers developping on the hub and shroud surfaces of the fan assembly, distorting the flow locally on the blade near the hub and at the tip and causing fluctuating loading on the rotor blades. Thus the contouring of the duct surface to control boundary layer development is seen to have a rather important effect on both broadband and tonal noise levels of an axial fan as reported by [Maaloum *et al.*, 2003].

To the inflow distortion effects can be added to the potential effects of downstream structures on the blade loading ([Moreau, 2011; Roger, 2009]). Whereas structures situated upstream of the fan mainly cause inflow distortions, nearby structures situated downstream may interact with the fan blades via their potential field, which diverts the flow due to their volume, causing more or less localized distortions of the flowfield and causing fluctuating loads on the blades at frequencies near the BPF and its harmonics. This potential effect can also affect the inflow condition when strong blockage effects occur. In practice theses fluctuations may be caused by struts included in the fan assembly or any solid surface located in close proximity of the fan in the downstream section.

2.2.2 Non-Rotational Noise Mechanisms

The second class of noise mechanisms in turbomachinery applications is called non-rotational noise. They are caused by random turbulence and occur mainly as broadband noise with some tonal peaks.

Leading Edge Turbulence Ingestion

The first noise mechanism that can be identified is called leading edge or turbulence interaction noise. This mechanism stems from the interaction of the leading edge of the rotor blades with incoming random turbulence present in the flow or as a result of the ingestion of turbulent boundary layers; the turbulent eddies are scattered by the edge of the blades, thus producing wall-pressure fluctuations which propagate in the farfield as broadband noise [Carolus *et al.*, 2007; Moreau and Roger, 2007]. It is to be noted that this

particular phenomena can be amplified by the interaction with inflow distortions, which produce additional localized turbulence in the flow.

Trailing Edge Broadband Noise (or Self-Noise)

A second mechanism that is considered the minimum noise imprint that would be produced by a fan with the absence of any outside influence is trailing edge noise [Moreau and Roger, 2007]. It can be seen as a scattering of the turbulent eddies in the boundary layer by the trailing edge of the profile as broadband noise. The influence of trailing edge noise is seen to increase with the Reynolds number (flow velocity); as well, the increase of the angle of attack appears to increase the levels of the radiated noise in the lower frequencies whilst leaving the higher frequencies relatively untouched for a given Reynolds number [Moreau and Roger, 2005; Rozenberg, 2007].

Vortex Shedding

In the presence of a laminar boundary layer and trailing edge bluntness on the rotor blades, a different mechanism can also be seen to appear at the trailing edge. Thus, vortex shedding and the appearance of a Von Karman street was seen to appear on an engine cooling fan at higher flowrates for certain fan geometries and a relatively limited range of operation [Longhouse, 1977]. The appearance of vortex shedding on the blades, which occurs at different frequencies along the blade given the different relative flow velocities, led to a general increase in broadband noise for the fans and to the appearance of several tonal peaks at high frequency attributable to the vortex shedding mechanism proper.

Tip Leakage Noise

Finally, another mechanism considered as an important source of noise in low-speed axial fans is tip leakage noise. Tip leakage flow occurs across the tip from the pressure side to the suction side of any finite unshrouded aerodynamic body and is mainly driven by the pressure differential across the tip between the two surfaces and thus increases with blade loading. In turbomachinery applications, vortical structures are then formed in the adjoining passage flow in the tip area by the interaction with the relative free-flow. Tip leakage flow thus produces a highly turbulent flowfield in the tip area of the rotor blades. Several causes of increased noise as a result of tip clearance flow are identifiable. First, the diffraction of the tip leakage jet on the suction side of the tip of the blades [Grilliat, 2009; Mann *et al.*, 2016] causes increased broadband noise levels. The turbulent structures generated by the tip leakage flow impinging on the shroud and following blades increases the wall-pressure fluctuations on the affected surface and results in increased broadband noise levels, with tonal noise also generated in some cases.

2.2.3 Dominant Mechanisms during Nominal Operation

Even in nominal operating conditions, which is different for every fan design, experimental investigation of the dominant noise mechanisms is an arduous task at best given the complex flows and multiple interactions found in a turbomachine environment. However, some noise mechanisms identified in the previous section are found to have an important impact on the noise spectra of low-speed turbomachines.

First and foremost, tonal or quasi-tonal noise mechanisms related to rotational noise (frequencies around the BPF and harmonics) can most often be seen in the noise spectra or low-speed axial fans, sometimes dominating the broadband noise by several dB even without the presence of inflow disturbances other than the boundary layers on the hub and shroud surfaces, be they shrouded or unshrouded rotors [Carolus *et al.*, 2007; Fukano and Jang, 2004; Longhouse, 1978; Moreau and Roger, 2007]. These quasi-tonal occurrences can be related to a strong influence of unsteady blade loading.

Trailing edge noise is also an important mechanism found to have an important influence on broadband noise levels. Apposing fabric to the trailing edge of a low-speed free tip axial fan was shows to result in several dB of reduction in broadband noise levels at high frequencies, especially in the 2-4 kHz band [Quinlan and Bent, 1998]. This is in phase with the results of trailing edge modeling where the trailing edge noise seems to correlate well with very high frequency components of the noise spectra of a shrouded fan [Moreau and Roger, 2007]. However, the leading edge turbulence ingestion noise is a concurrent noise mechanism and can easily dominate the blade trailing edge noise at lower frequencies depending on the turbulence levels of the flow [Carolus *et al.*, 2007; Moreau and Roger, 2007]. Therefore, leading edge noise ingestion might also be an important noise mechanism.

Finally, it was shown by several authors that the tip clearance flow in axial turbomachines had a rather significant impact on fan noise. Some authors showed a large influence, for example, of the tip gap size on the noise spectra of tested axial fans [Fukano and Jang, 2004; Fukano *et al.*, 1986; Longhouse, 1978; Quinlan and Bent, 1998]. In practice, a larger tip gap increases broadband noise of the fan, which is linked to the concurrent increase in strength and size of the tip leakage flow.

Detailed spanwise investigations also show the tip region of a tested axial fan as being an important contributor to the overall noise spectra using cross-correlation analysis [Bianchi *et al.*, 2009]. The addition of tip flanges to control the formation of the tip leakage flow also achieves broadband noise reduction of several dB especially at high frequencies [Corsini

et al., 2007; Quinlan and Bent, 1998]. The addition of complete ringshrouds also shows a decrease of global noise levels in normal operation as a result of the modification of the tip leakage flow topology [Longhouse, 1978; Shimada *et al.*, 2003]. Tip clearance noise is thus an important characteristic of the noise spectra in the operation of low-speed axial fans.

Significant research efforts were made over the last several decades to try and understand the physical mechanisms associated with tip leakage flow and to gain a better grasp of their impact of the aeroacoustic performance on turbomachinery systems. However, its inner-workings are still ill-understood to this day. The next section proposes a brief overview of relevant research conducted on the topic of tip leakage flow.

2.3 Impact of Tip Gap Flow on Fan Characteristics

Tip leakage flow is an unavoidable consequence of the finite span of real-life lifting aerodynamic surfaces, from aircraft wings and propellers to turbomachine rotor blades. It can be responsible for introducing possibly drastic changes from the ideal flow conditions surrounding a given aerodynamic body and can degrade its performance characteristics. Tip leakage flow is essentially driven by the flow from the high pressure surface of an aerodynamic body spilling over to the low pressure side. This cross-stream flow thus interferes with the chordwise throughflow along the aerodynamic body and is swept downstream. This results in velocity deficits in the main flow, modifying the local angle of attack and generating detached flow structures/vortices which are then free to interact with the involved geometry and impact the efficiency of the system further.

In the case of turbomachine applications appears the added complexity of the relative motion of the blades as well as, in several cases, the proximity of a shroud surface influencing the shape and size of the tip clearance and the formation of the tip leakage flow features.

In this section, an overview of the literature regarding tip leakage flow physics and their impact on the acoustic performance of turbomachine systems is proposed.

2.3.1 Physics of Tip Leakage Flow

Research on the physics of tip leakage flow is not a recent development, but it has proven to be a phenomenon difficult to investigate experimentally, requiring extensive and often costly mockups to be manufactured. Tip leakage and the flow features associated with it are also very complex in nature, appear highly dependant on the geometry and loading of

the blade. They are also impacted by other flow phenomena such as upstream disturbances (e.g. turbulence coming from developping boundary layers or inlet guide vanes). Published work going back decades can be seen to be concerned with the influence of tip clearance flow on fan performance. Most of the work, though, was focused on the aerodynamic effect with little to no emphasis on the potential acoustic impacts. Based on literature from the 1940s and 1950s, tip leakage flow was lumped into what was and is still known as secondary flow losses, and experiments on full axial fans/compressors/pumps were carried out to study the inception and effects of tip clearance flow [Rains, 1954; Ruden, 1944; Ryan and Ohashi, 1955]. With measurement techniques used at the time however, only relatively base and global information about the flow could be collected (e.g. flow rate, head rise, efficiency, approximative flow angle behind the rotor trailing edge) in addition to mostly qualitative observations. This early research was however more concerned with developing empirical or semi-empirical models able to predict the fan efficiency/pressure rise as a function of the tip clearance gap, although Rains [Rains, 1954] tried to model the tip leakage vortex formation and allowed for a satisfactory prediction of the tip leakage losses incurred in an axial pump as well as a compressor geomery to which the model was applied.

One of the simplest representations of a rotor is arguably the linear cascade configuration. It is also easier to inspect the flow inside a stationary blade cascade than it is in a moving rotor assembly. Different authors, whose work is presented hereafter, have thus opted for this configuration to investigate tip gap flow effects on a more fundamental level. However, this configuration clearly has some differences with usual rotor setups: the solidity of the blades, which varies in a real rotor setup from hub to tip is fixed on a blade cascade model; the radial deviation of the flow that might be seen in real rotors due to centrifugal effects is not reproduced in such experiments; shear effects in the flow affected by the relative motion between the rotor blades and the shroud are not taken into account in most experiments; shroud curvature might have an effect on tip flow formation. It is, however an interesting way to investigate the basic mechanics of tip flow formation in a controlled environment for fixed parameters.

Kang and Hirsch ([Kang and Hirsch, 1993, 1994]) performed measurements on a 7 blade linear compressor cascade using five-hole probes and oil flow visualizations (Reynolds number of 290 000 based on a 200 mm chord). They observed the formation of a tip cross-flow perpendicular to the blade, rolling up at the suction side to form the tip vortex structure when encountering the free-flow. A short distance after the midchord point, the tip flow is seen separating from the blade, rolling up into a smaller vortex structure (tip

separation vortex). They also observed a horseshoe vortex forming near the tip leading edge in close proximity to the tip leakage vortex on the suction side of the blade; this vortical structure could be related to the induced vortex observed by You et al. [You *et al.*, 2007] whose work will be detailed shortly. In all, three main vortical structures are seen appearing from the tip leakage flow. They identified the tip leakage vortex as the main source of vorticity near the passage endwall, with its area of dominance moving away from the blades and inwards spanwise as it is convected downstream. Intense mixing loss is also identified in the aft portion of the profile.

A more complex series of experiments was carried out at Virginia Tech on a linear cascade in order to investigate the inception of tip gap flow features. Work was carried out on a 8 blade compressor cascade at a Reynolds number around 450 000 based on a 254 mm chord length, corresponding to a Mach number of 0.08. Muthanna [Muthanna, 1998], using hotwire sensors, pressure taps and surface oil visualizations, observed the formation of the aforementioned cross-flow perpendicular to the chord across the tip clearance of the blade cascade. The cross-flow then rolled up into the so-called tip leakage vortex (TLV) when encountering the free-stream at the suction side and peeling away towards the pressure side of the following blade. A secondary vortex structure with opposing but relatively lower vorticity when compared to the tip vortex also formed near the suction side tip edge. Varying the tip clearance also influenced the observed vortices, with a larger gap increasing the TLV strength and zone of influence, and moving its detachment point along the blade chord. On the opposite side of the spectrum, a small enough gap prevents the formation of the TLV, instead leading to the formation of a high shear flow layer along the shroud casing originating from the clearance gap. It was observed, however, that with the TLV present, it becomes the main source of turbulence in the flowfield, dominating even the blade wakes downstream of the blade cascade. Wang [Wang, 2000] investigated the effect of adding a moving shroud wall to simulate the relative movement between the blades and the shroud casing in a functional rotor assembly. It was found that it only served to flatten the TLV in the spanwise direction, but did not interfere with the mechanisms behind the formation of the structures. Their findings were also confirmed by laser Doppler velocimetry measurements [Tang, 2004].

The effect of increased upstream general turbulence was also investigated [de la Riva, 2001; Muthanna, 2002]. It was found that a 3% turbulence intensity at the inlet of the cascade had some effect on the tip clearance flow. A decrease in the blade loading was readily observed, as well as a diminution of the vorticity levels inside the TLV by about 20% combined with an increased vortex core size of around 30%. It is interesting to note that

this is in phase with Lakshminaraya's conclusions [Lakshminaraya *et al.*, 1995] regarding the absence of a tip leakage vortex in his own investigations, wherein the authors postured that additional parameters such as inflow turbulence might have affected its formation. This was taken one step further by Ma [Ma, 2003] who added vortex generators to study the influence of inlet vortical flow due to upstream obstructions (e.g. inlet guide vane wakes). He showed that the vortical flow from the generators, which had a total circulation one to two orders inferior to the typical circulation of observed TLV, could influence the tip clearance flow and TLV formation to a potentially large degree. For smaller tip clearances, an apparent superposition of the inlet vorticity with the TLV seems to be the interference mechanism, whereas with increasing clearance and increasingly strong TLV, interference of the inlet vortices with circulation shedding from the clearance gap is postulated as the mechanism. This is highlighted by a meandering TLV structure at higher clearances as a result of vortical inflow which is lessened at smaller clearances.

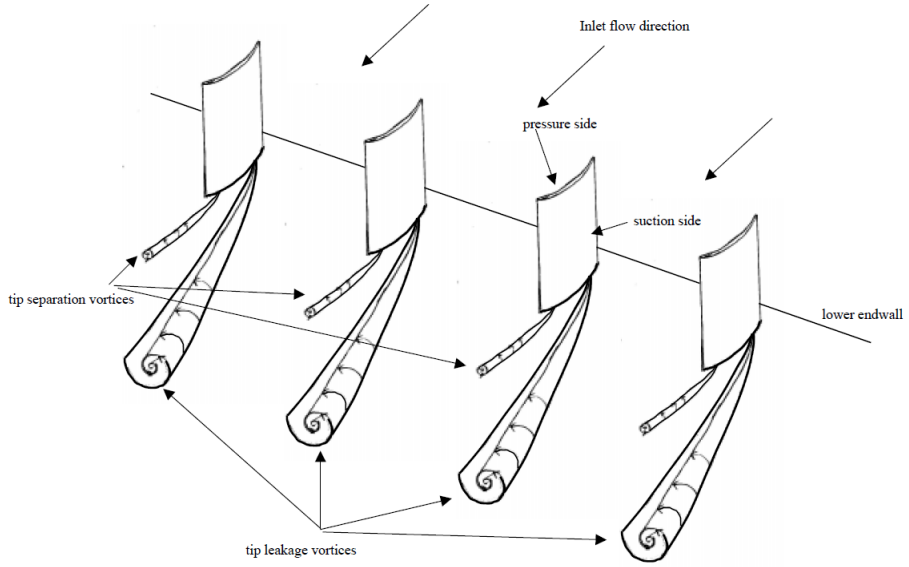

Figure 2.1 Illustration of the Virginia Tech blade cascade and observed vortex structures [Muthanna, 1998].

You et al. [You *et al.*, 2007], in 2007, performed LES calculations mimicking the experimental Virginia Tech setup with a moving endwall [Wang, 2000] at a Reynolds number of 400 000 based on blade chord. They managed to correctly reproduce the upstream flow conditions as evidenced by the mean streamwise velocity and Reynolds stress profiles near the leading edge of the blades near the moving endwall. The authors identified three distinct vortical structures, namely the tip leakage vortex formed by the interaction of the tip leakage jet with the main flow, a tip separation vortex formed due to separation of the

flow in the tip gap and an induced vortex generated by the tip leakage vortex near the leading edge of the blade (see Fig. 2.2). They also managed to correctly identify the tip leakage vortex, and blade wake trajectories when compared to the experimental results. They found that the tip leakage vortex and tip leakage jet are the main sources of turbulence in the endwall region, echoing the Virginia Tech experiment observations. They also attempted to quantify the losses incurred along the length of the blades and found that the trend followed the linear approximation proposed by Bindon ([Bindon, 1989]) for turbine cascades. The correspondance of these LES results with experimental observations demonstrates that unsteady simulations allow for the reproduction of physical phenomena (e.g. vortex structure, secondary flows, 3D effects) in the flowfield; such an investigation would impossible in similar configurations with experimental techniques.

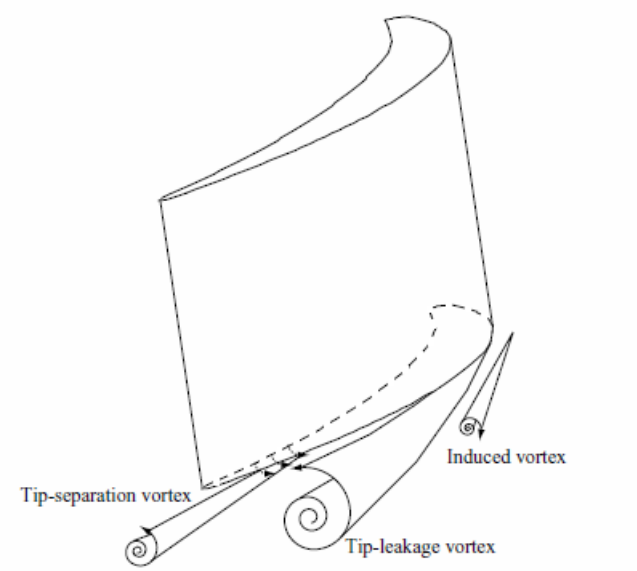

Figure 2.2 Illustration of the tip flow structures identified [You *et al.*, 2007].

In parallel to research using linear blade cascade representations of turbomachine applications, some authors studied complete turbomachine geometries. It is sensible, as it was shown by some authors [Tang, 2004; Wang, 2000] that relative motion effects for example can have a significant effect on the flowfield.

Inoue and Kuroumaru [Inoue and Kuroumaru, 1989] carried out hotwire measurements in the tip gap of an isolated axial compressor rotor with tip clearances varying from 0.5 to 5 mm (0.4% to 4.3% of the blade chord) and a Reynolds number based on a 117.5 mm chord of around 260 000. They observed that the leakage jet flow interacts with the main flow near the leading edge for small clearances, forming up into a vortex that convects downstream. A scraping vortex is also seen forming near the trailing edge. Increase of the

clearance gap leads to the formation of a stronger leakage vortex at increasingly downstream locations on the blade. According to their observations on a second compressor with increased solidity, blade solidity does not modify the flow pattern observed in the tip clearance region, other than the possible interaction of the vortex with the following blades with increasing solidity.

Lakshminaraya et al. [Lakshminaraya *et al.*, 1995] performed measurements of the three-dimensional flowfield in the tip region of an axial flow compressor (Reynolds number of 575 000 based on a 154 mm blade chord) complete with inlet and outlet vanes and a 3.5 mm (2.27% blade height) tip clearance using a rotating 5-hole probe. They however failed to observe the formation of a coherent tip vortex. The author postulated that it may have been due to one or a combination of different factors (inlet swirl, high blade loading and turbulence) causing intense mixing of the tip clearance flow before it could form up into a discrete vortex, thus allowing for rapid mixing with the free-stream flow. This behavior is also seen appearing in previous work where measurements were performed on an isolated compressor [Hunter and Cumpsty, 1982] wherein the tip vortex is not seen forming. It is infered that this would be more representative of a multistage turbomachine environment than a stationary cascade flow experiment.

More recently, Weichert [Weichert, 2011] performed overtip experimental measurements on a 1.52 m (5 ft) diameter research compressor (Deverson compressor) at the University of Cambridge using pressure sensors and miniature hot-wire probes to study stall inception. The study was carried out on a flow at a Reynolds number of 310 000 based on a 167 mm blade chord. She observed the general complexity of the tip clearance flowfield, with changes in flow direction by a full 360° in the blade-to-blade passage. Tip vortex formation was also observed, with the effect of flowrate being visible in the inception and trajectory of the structure, lower flowrates tending to modify the trajectory of the tip vortex towards the leading edge of the following blade. She also found a very complex flowfield that seemed to change widely from blade passage to blade passage, with the largest differences being observed near the exit point of the tip vortex where the tip flow is strongest. She also correlated the unique behavior of some blade passages with the effect of eccentricity of the rotor. Her measurement methodology contrasts with others that have used hot-wire probes and pressure sensors in that she actually measured the flowfield along the whole chord of the blades using moveable miniature hot-wire probe system combined with Pitot total pressure measurements to get a global image of the flowfield across the rotor, both in amplitude and direction, allowing for detailed measurement of the tip clearance flow (see Fig. 2.3).

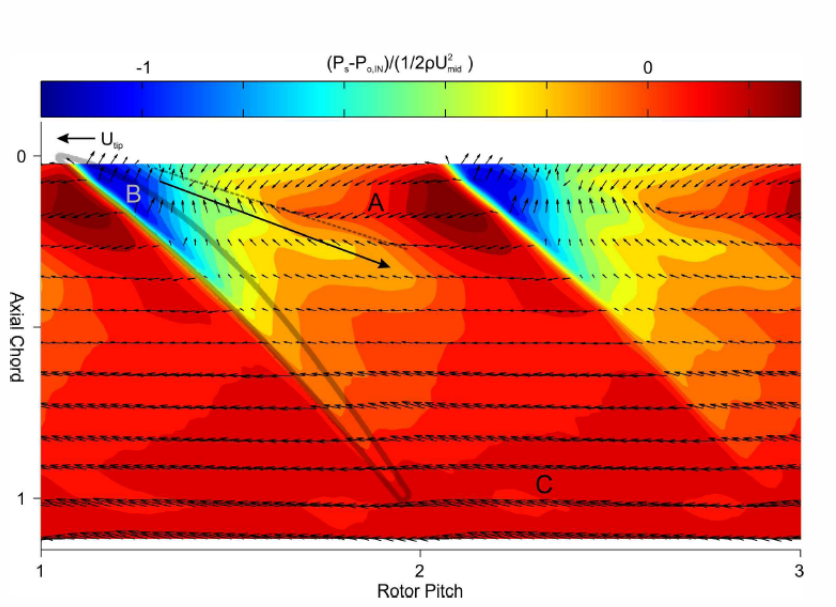

Figure 2.3 Illustration of overtip maps measured on the Deverson compressor. The arrow represents the trajectory of the tip leakage vortex. [Weichert, 2011]

Wu et al. ([Wu *et al.*, 2011a,b]) also used a rather unique method to collect PIV measurements on the flowfield (with specific interest in the tip leakage flow) of a waterjet pump, using a transparent pump mock-up that matches the refraction index of the encompassing fluid, allowing unobstructed flow measurements within the entirety of the experimental pump (Reynolds number of 3 500 000 based on a 267.2 mm chord). They observed the rollup process of the backward tip leakage flow into the tip vortex structure. Contrary to the observations of Bindon ([Bindon, 1989]), Wu et al. did not observe any flow separation at the entrance of the tip gap (separation bubble). Their observations also showed that once the tip vortex was detached from the blade shortly after the rollup process, the leakage flow exited the gap as a wall jet that fed it; the shear layers are either entrained directly by the tip vortex core to form a series of secondary structures surrounding it. The vortex core itself, however, is not a uniform structure but rather an amalgam of vortex filaments closely located as seen in Fig. 2.4. As the tip vortex peels away to the pressure side of the next blade, however, it stops entraining vorticity, reaching a peak in its inherent circulation, and begins coming undone, with core pressure increasing; in this region, the leakage flow from one blade is seen covering the entire blade-to-blade circumference arc and merges with the following blade leakage flow. The operating point of the pump is seen to have a large influence on the rollup/migration/destruction process of the tip vortex. At high loading, the tip vortex is seen to impact the following blades, even reaching the leading edge of the following blade where the tip vortex is chopped into vortex filaments

that are generated vortex structures at the leading edge of the immersed blade. The work of Wu et al. provides precise spatial and temporal insight into the formation of tip leakage flow in turbomachinery applications and allows for measurement data to be collected in typically hard to reach locations. Their measurements also include turbulence information of the flow, giving a very complete picture of the instantaneous as well as mean flow, which would be a good experimental basis for numerical simulations.

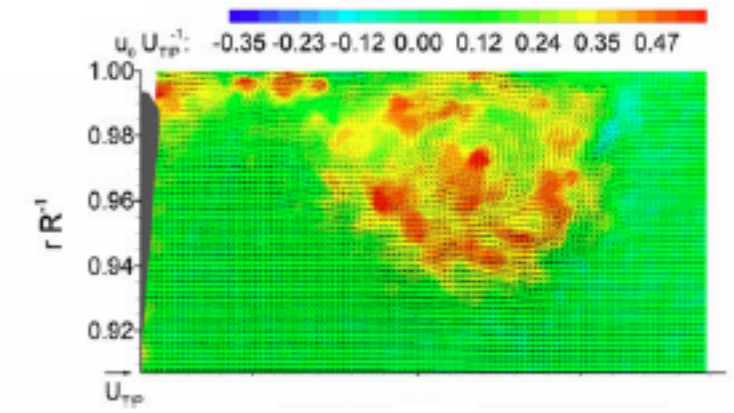

Figure 2.4 Composition of the tip vortex as viewed by instantaneous vorticity. The tip vortex is seen to be composed from several vortex filaments highlighted by the red spots. [Wu *et al.*, 2011b].

In 2003, Lee et al. [Lee *et al.*, 2003] investigated the flow in a very skewed axial fan using laser Doppler velocimetry and RANS CFD analysis for a single operation point on a complete 3-bladed fan assembly (Reynolds number of around 250 000 based on a 21 cm chord). The turbulence model used in their calculations was the Reynolds Stress Model (RSM) in order to alleviate numerical overproduction of turbulent kinetic energy near and in the tip gap where large strain rates are observed. They used a coarse mesh near the blades ($y^+ = 30 - 60$) and a wall function, which while saving on grid size, might not allow for accurate resolution of the flow if it is not attached to the blades. However, a comparison of the experimental velocimetry data and the numerical simulation show that the authors are able to capture the topology of the flow patterns inside the tip gap as well as the location and trajectory of the tip leakage vortex formed on the suction side of the blade with good accuracy. However, a RANS model, while providing insight into the formation mechanics of tip clearance flow, is not adequate to investigate in detail such an unsteady flow given the ensemble-averaging it performs on flow quantities and the steady-state hypothesis. Steady-state RANS simulations are also unsuitable for the prediction of acoustic noise emanating from the flow, as no temporal fluctuations of the flow are simulated.

More recently, Taghavi-Zenouz and Eslami [Taghavi-Zenouz and Eslami, 2011] performed incompressible LES calculations in order to investigate tip clearance flow in a low-speed axial compressor for two different gap sizes and the flowfield measurements compared with experimental results from Inoue et al. [Inoue *et al.*, 1986] for the same compressor. The Reynolds number of the simulated flow was 380 000 based on the blade chord. Their basic aim was to capture the flow frequencies associated with tip clearance flow. Comparison of the LES data with experiments showed good agreements with regards to global performance evaluation and circumferentially averaged velocity profiles along the span. From their visualisations, it is shown that the strength and size of the tip vortex is dependent on tip gap size, larger clearances producing stronger, more unsteady vortices having larger area of effects on the flow. Flowrate is also seen to have an effect as to the trajectory of the tip vortex shed from the rotor blades, diminishing flowrate forcing the shed tip vortex into a more azimuthal trajectory. From a frequency standpoint, tip clearance flow and the associated tip vortex are shown to have an oscillatory nature, which is characterized by large pressure fluctuations over a large domain. There is a main frequency component around the blade passing frequency (60-75 % of the blade passing frequency, or BPF, near the design point) which is related to the tip clearance vortex effects as well as large band oscillations that are due to the generally turbulent flow associated with tip clearance. A larger tip gap produces a more unstable flow, especially near the design point, whereas a decrease in flow rate tends to lower the frequency at which the main tip vortex related unsteadiness occurs as well as generate additional unsteady effects.

Pogorelov et al. [Pogorelov *et al.*, 2015, 2016] also studied tip leakage flow in a low-speed axial fan using a single-blade LES model with periodic boundary conditions at a Reynolds number of around 500 000 based on blade chord. They simulated a single operating point but showed that the simulated fan reproduced the global performance measured through experimentation accurately on their finest grid. They were able to study the formation of the the tip leakage flow in fine detail for two different tip clearances (1% and 0.5%). First, their observations highlighted the fact that the large clearance case favoured the formation of a large wandering tip leakage vortex propagating in an almost circumferential manner, decaying into a turbulent wake across the blade passage that strongly interacts with the following blade. This causes increased pressure fluctuations on the blade as well as a cyclic turbulent transition on the suction side of the blade near the tip at the leading edge. In the case of the smaller clearance, however, the TLV and the turbulent wake resulting from its decay in the blade passage are much smaller and are convected downstream and do not interact with the leading edge of the following blade. The trajectory is also more consistent than in the large clearance case. The cyclic turbulent transition on the suction side of

the blade near the tip leading edge disappears as a result and is replaced by a continuous turbulent transition at the cusp of the blade near the tip. Using auto-correlation analysis on the temporal fluctuations of the numerical flowfield near the suction side of the blade in the tip region, the authors were able to show the occurrence of high energy peaks in the near-field spectra at frequencies that corresponded accurately with tonal noise elements in the experimental far-field sound spectra.

2.3.2 Tip Leakage Flow Noise Investigations

The previous section presented a brief overview of research work on the formation physics, from a fluid mechanics point of view, of tip leakage flow and its impact on turbomachinery operation. It was seen that the phenomenon appears highly turbulent and unsteady at its core. This can contribute to a potentially high degree to increase the acoustic footprint of a given turbomachine application if this secondary flow is not understood and controlled. This becomes a matter of importance as the efficiency of a given turbomachinery system may be overshadowed by its noise production in real life applications and can mean the difference between a successful endeavor in design and a failed product.

Studies regarding the acoustic effect of tip leakage flow were purposefully left out of the previous review section and will be covered here. Even more so than with tip clearance flow topology investigation, distinguishing the effects of tip flow noise from the overall effects of the chaotic flowfields in a turbomachine can be arduous, requiring original methods to be used in order to investigate and quantify its effects. In early research dating back to 1953, Marcinowski [Marcinowski, 1953] attempted to investigate tip clearance noise with far-field acoustic measurements, recording that increases in tip clearance produced increasingly elevated broadband noise levels and the formation of a narrowband hump in the spectra. Several researchers have since followed suit; this section aims at providing a glance at the research effort observed in literature.

Longhouse's research effort [Longhouse, 1978] was aimed at evaluating and optimizing the tip flow of an axial fan used for engine cooling in the automotive industry with the implementation of a ring shroud configuration (Reynolds number of 280 000 based on a 57 mm blade chord at the tip). He first illustrates the tip flow mecanism observed on the static shroud/rotor configuration, which concords with the typical cross-flow tip gap stream and tip vortex formation reported by other authors. The tip vortex is seen to largely and adversely affect the subsequent blades as the blade loading increases, impinging on the trailing edge and eventually the whole blade, which ultimately leads to a rotating stall at critically low flow rates. The tip gap size is seen to largely affect the formation of the

tip flow and thus noise production, as comparisons between a 0.76 mm and 0.05 mm tip clearance show that the larger clearance produces up to 15 dB(A) more noise over a large range of operation points (50 to 100% nominal flow rate) with a clean inflow; analysis of a single sound pressure spectrum at 78% of nominal flow rate shows a general attenuation of noise over the whole frequency spectrum, and especially in the lower range. Tip vortex formation and the effect of tip clearance on turbomachine noise as observed by Longhouse are presented in Fig. 2.5.

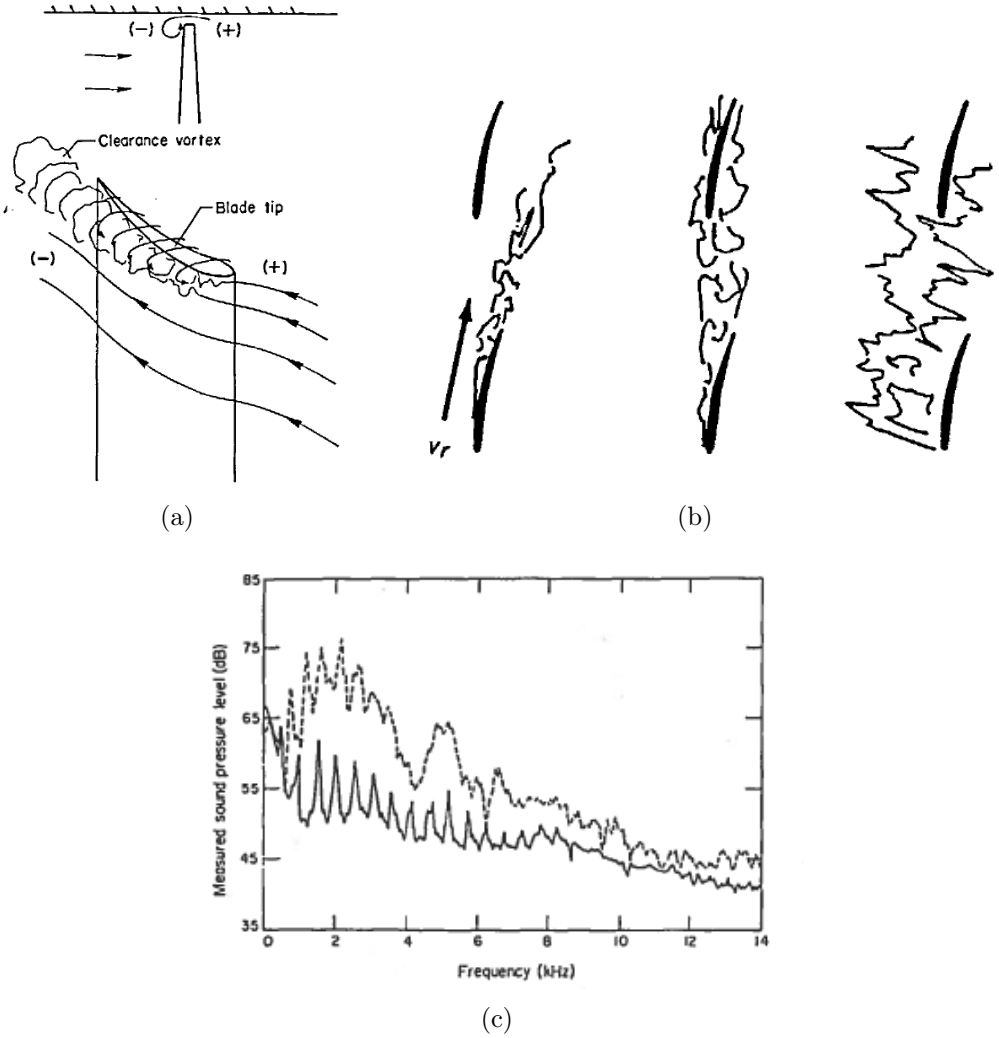

Figure 2.5 Illustration of Longhouse's observations [Longhouse, 1978] (a) Illustration of the tip vortex formation, (b) Tip flow pattern from lightly loaded to highly loaded conditions (c) Effect of tip clearance on turbomachine noise;; - - - 1.33%, — 0.09% chord tip clearance.

Longhouse then proposed a rotating ring-shroud at the tip of the blades in an attempt to eliminate the influence of tip leakage flow in the blade passage (see Fig. 2.6). His study

of the configuration showed that a properly designed ring shroud could lower noise levels as well as increase the efficiency and stall characteristics of a given fan when compared to a similarly operating fixed shroud fan as seen in Fig. 2.7. He however pointed out that a poorly conceived ring shroud can in fact decrease efficiency and increase noise production; this is mainly due to the fact that the rotating shroud produced additional viscous drag as the surface added causes additional friction with the flow, thus requiring additional power to entrain the rotor. However, bad contouring can also cause inlet flow disturbances and affect the efficiency of the machine by deteriorating the flow in the upper blade region. Also, while a rotating ring shroud eliminates the tip clearance near the blades themselves, there still exists a tip clearance in-between the rotating and fixed shroud where a tip flow can still be observed. The rotating ring-shroud configuration outperformed the classic free-tip configuration by several decibels regarding generated noise levels (up to 12 dB) for the largest tip clearances over the full operating range. Rotating ring shrouds are widely used in low-speed (automotive cooling fans, naval propellers) as well as high-speed (jet engine compressors and turbines) modern applications both for their aerodynamic properties as stated above as well as their structural reinforcement effect, effectively strengthening the blade rows and minimizing blade deflections.

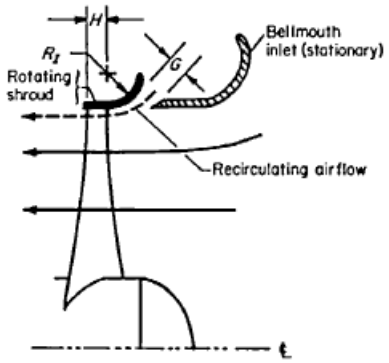

Figure 2.6 Illustration of the rotating shroud of the fan [Longhouse, 1978].

Fukano et al. [Fukano *et al.*, 1986] presented an experimental investigation of the effects of tip clearance on both performance and noise of 4 commercial free-tipped fans (3 axial, 1 mixed flow) with Reynolds numbers based on blade chord varying from 200 000 to 350 000 approximately at the tip. The study takes into account eccentricity of the fan and duct axes. It is shown that aerodynamic performance increases with diminishing clearance until a minimum is achieved. This is mainly due to the fact that the tip profile works increasingly well as the influence from the tip flow diminishes along the span. However, the effect is relatively low when compared to the acoustic impact, as a reduction of the

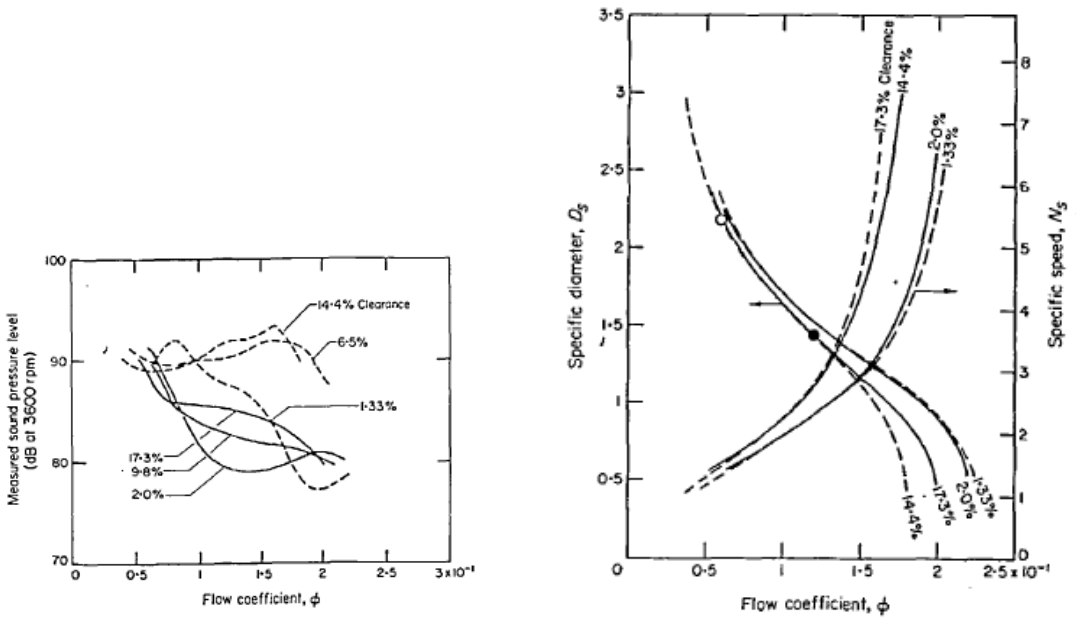

(a) (b)

Figure 2.7 Comparison of the performances of an axial fan with (—) and without (- - -) a well designed ringshroud at different tip clearance value for (a) Noise levels (b) Aerodynamic performance. [Longhouse, 1978].

tip clearance leads to an overall decrease of sound pressure levels over most or all of the frequency ranges by several dB for operating conditions well outside nominal flow rates. Eccentricity of the rotor in relation to the duct also leads to the generation of pure tonal noise by the interaction of the blades with the duct wall as well as a decrease in fan efficiency. This noise can become very annoying to a human listener as Fukano et al. [Fukano *et al.*, 1986] show that it is generated as a plane wave and thus doesn't decay in the duct and due to the fact that tonal noise is usually felt as noisy from a psychological perspective. However, the important factor to take into account as presented by the author is the ratio of eccentricity over tip clearance, meaning that the larger the tip clearance, the lower the increase in sound pressure level (SPL) and decrease in efficiency for a given eccentricity. This means that in order to have a tip clearance as small as possible for performance reasons, eccentricity must be tightly controlled. In real applications, this presents a problem to minimizing the tip clearance in order to minimize tip flow noise, as perfect alignment of rotor and outer shroud axes in a fan assembly is all but impossible even without even taking into account that a turbomachine in normal operation will surely show some eccentricity due to uneven physical deformation of the blades, vibration or small imperfections in the blade or shroud surfaces.

More recently, Fukano and Jang [Fukano and Jang, 2004] and Jang et al. [Jang *et al.*, 2003] presented the study of tip clearance noise in axial fans using a rotating twin hot wire setup. They experimented on an axial fan with two different tip clearances (2 mm and 4.5 mm, respectively 1.6% and 3.5% chord) at different flow rates (Reynolds number based on blade chord is of the order of 260 000) for a constant rotational speed (1000 rotations per minute, or RPM). They also compared the resulting experimental flowfield with a single blade steady-state RANS calculation, showing good agreement regarding the topology of the tip flow features. The authors inferred that broadband noise increases with the reduction of the flowrate (increased blade loading) is mainly caused by the increased interaction of the velocity fluctuations with the duct and following blades due to the fact that the tip vortex moves towards the leading edge with decreasing flowrate and that an increase in tip gap enlarges the vortex both in strength and size, both facts having been observed by other authors. They also identified narrow band peaks in the frequency spectra of the velocity fluctuations that are present in the vortex flow region and reverse flow region near the case. These spectral peaks in the velocity fluctuations are clearly visible in noise recordings and are dependant on rotational speed as well as flowrate. Depending on the configuration and operating point, these tonal effects can be important and can overtake broadband noise in terms of annoyance.

Hamakawa et al. [Hamakawa *et al.*, 2012] used a similar technique with a rotating hot-wire probe and a far-field microphone to investigate the correlation between the aerodynamic fluctuations spectra near the pressure side of one of the blades in the tip region of a 9-blade axial fan (Reynolds number based on a 131 mm chord of 250 000) and the far-field noise spectra. The authors, with no surprise, observed a general increase in broadband noise with decreasing flowrates. The authors also observed, in a fashion similar to Fukano and Jang et al. [Fukano and Jang, 2004; Jang *et al.*, 2003], that the velocity fluctuations associated with tip flow displayed a spectral peak, which showed a positive correlation with flowrate throttling. For the high loading case, this frequency corresponds well with one of the duct modes. This, coupled with the fact that the tip flow impinges on the following blade pressure side, reflects in the cross-spectra as a high correlation between the far-field noise and the velocity fluctuations at this discrete frequency. A lower frequency peak of high correlation observed also corresponds to a duct propagation mode.

Kameier and Neise [Kameier and Neise, 1997a,b], performed an experimental investigation into the aeroacoustic noise mechanisms in relation to tip clearance on an axial compressor (Reynolds number of 100 000 based on blade chord) using microphones, pressure sensors and a hot-wire probe. In addition to increasing broadband noise levels being observed with

enlarging tip clearance as in other cited authors' research ([Fukano *et al.*, 1986; Longhouse, 1978; Marcinowski, 1953], a tone just below the blade passing frequency linked to tip gap flow effects was also identified for the larger clearances tested; the tone all but vanished at the smallest tip clearance. The observed tone level was also shown to increase, when present, with blade loading at lower flowrates. From observations of pressure spectra collected on the rotating blades and at the tip casing wall, they surmised that the identified tone was created as a result of the interaction of the rotor blades with a rotating flow instability generated by the tip leakage flow (which they dubbed rotational instability, or RI). The presence of this rotating instability was found to be dependant on the tip clearance gap size and throttling of the machine and to produce a very specific spectral signature in the near-field spectra as shown in Fig. 2.8. Liu et al. [Liu *et al.*, 1996] further highlighted the appearance of the RI along the circumference of the rotor using cross-spectra for different rotational speeds on the same setup for the largest clearance gap, whereas Kameier and Neise [Kameier and Neise, 1997a,b] only studied one rotational velocity. Baumgartner et al. [Baumgartner *et al.*, 1996] also observed the same RI spectral signature on a high-speed multi-stage compressor. Mailach [Mailach *et al.*, 2001], using laser Doppler anemometry (Reynolds of 680 000), and Marz [Marz *et al.*, 2002], using URANS calculations, finally investigated the physics of the flow in the tip region to conclude that what has been coined the RI appears to be induced by the interference of the tip leakage flow with the passage flow, creating a periodic reverse flow condition rotating at a portion of the blade speed that affects the blade loading.

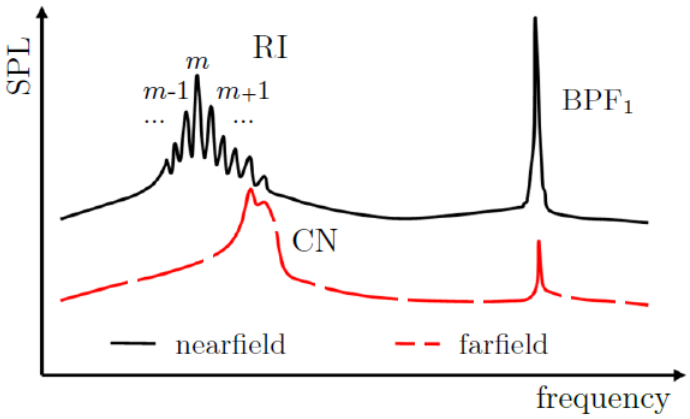

Figure 2.8 Schematic representation of the RI spectral feature in the near-field and its acoustic impact in the far-field [Pardowitz *et al.*, 2012]. (RI=Rotating Instability, CN=Clearance Noise)

However, a more recent publication by Pardowitz et al. [Pardowitz *et al.*, 2012] proposes a new interpretation of the RI, with as a basis previous findings by Kameier [Kameier, 1993] wherein the signature spectral feature was identified in a shrouded rotor without a typical tip clearance. Using cross-spectral analysis, he identified the presence of modal structure along the circumference with a wide range of azimuthal orders. This represented a significant advancement of the theory when compared to the single-passage structures assumed by previous RI investigations, and a more complete characterization of the modes. The new hypothesis proposed is that shear layer instabilities are generated in the tip region as a result of the perturbations perpetuated by the reversed flow observed, spawning stochastic azimuthal modes and the generation of vortical structures in the tip region. Detailed stereoscopic PIV by Pardowitz et al. [Pardowitz *et al.*, 2015b] also achieved an interesting visualization of some of the identified modes. The occurrence of the RI was also shown by Pardowitz et al. [Pardowitz *et al.*, 2015a] on a ring-shrouded version of Kameier and Neise's [Kameier and Neise, 1997a,b] test compressor.

The occurrence of the sub-BPF harmonic tones have also been observed by other authors in recent years on shrouded and unshrouded rotors and linked to tip region flow mechanisms using computational methods.

A series of simulations were run using a ring-shrouded rotor design typically used in automotive engine cooling applications. Magne et al. [Magne *et al.*, 2015] simulated a single blade passage of fan (Reynolds of 150 000 at midspan) in a rotor-only configuration using a URANS code with a $k-\omega$ turbulence model. The simulation was meant to be representative of the plenum-mounted testbed on which the fan was tested experimentally [Foss *et al.*, 2001], which provides a basis for comparisons, and was similar to previous numerical studies of the geometry ([Moreau *et al.*, 2011b; Soulat, 2010]). In ring-shrouded axial fan configurations like this one, recirculation flow is observed in the tip region ahead of the blades (see Fig. 2.9(a)). This recirculating flow is created as a result of the interference of a reverse flow coming from the shroud clearance gap, driven by the pressure differential across the fan, with the oncoming fluid being sucked through the fan blades from upstream. This creates large coherent vortices that can be viewed using proper techniques (Q-Factor and λ_2 isosurfaces), as shown in Fig. 2.9(b), and are seen to rotate at a slightly different speed than the fan (estimated at 580 RPM by Magne et al. by surmising a number of structures multiple of the number of blades). These vortices are likely culprits for the appearance of sub-harmonic tones below the BPF in this kind of configuration. Whilst the simulation method used did not allow for direct acoustic prediction, two hybrid methods were used to evaluate the noise radiated from the fan using the available unsteady pressure

measurements: a frequency-domain analytical formulation for a compact rotating dipole and the Ffowcs Williams and Hawking (FWH) acoustic analogy. The authors showed that the hybrid methods used succeeded in predicting the appearance in both level and frequency range of the experimentally observed sub-harmonic humps (see Fig. 2.10), with the FWH method providing an accurate way of pinpointing the noise sources on the fan.

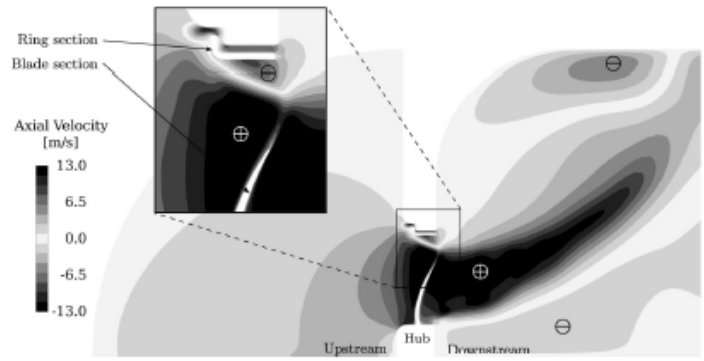

(a)

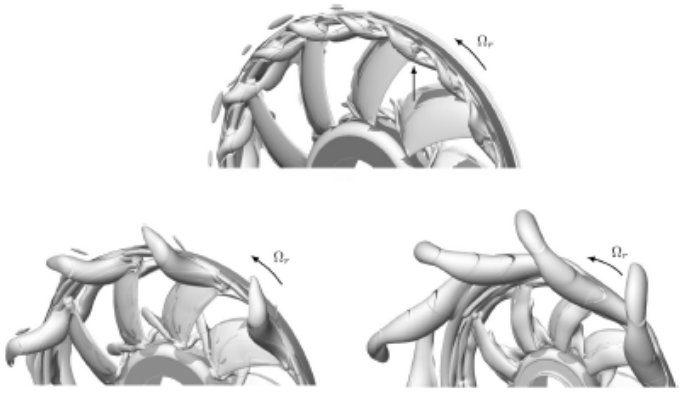

(b)

Figure 2.9 Illustration of the tip region recirculation pattern in a ring-shrouded fan (a) Axial velocity field (b) Coherent vortex structures highlighted by Q-factor contours in the rotor frame of reference and their evolution with increasing loading (top to bottom, left to right). [Magne *et al.*, 2015]

A very recent publication by Moreau and Sanjosé [Moreau and Sanjose, 2016] compared several single-blade channel URANS simulations, including a Scale-Adaptative Simulation (SAS) case, with a full 360 degrees Lattice-Boltzmann method (LBM) simulation on the same setup. From an aerodynamic standpoint, the LBM simulation shows a rather important improvement in the prediction of the velocity field in the wake of the fan, and is in part explained by the full azimuthal nature of the simulation as well as a more accu-

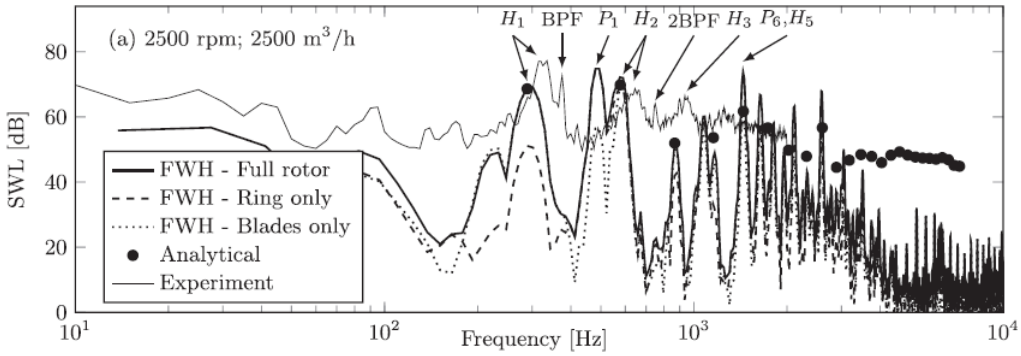

Figure 2.10 Sound spectra obtained through hybrid methods for a ring-shrouded fan compared to the experiment. [Magne *et al.*, 2015]

rate representation of the fan hub (internal ribs). For acoustic predictions, the URANS methods are coupled with the FWH analogy. However, use of the LBM allows for direct acoustic evaluation concurrently with the aerodynamic calculations. The authors observe that, while the URANS models seem able to predict the occurrence of the rotating tip structures and their impact on the noise spectrum regarding their frequency of occurrence, the SAS and LBM simulations are the only ones able to accurately predict the level as a result of a better resolution of the large scale turbulent features of the flow.

A parallel study of a similar ring-shrouded automotive cooling fan geometry using the LBM was carried out by Piellard et al. [Piellard *et al.*, 2014]. The study, however, included not only the fan geometry, but simulated the entire cooling module, complete with the simulation of the all elements such as the driving motor and a modelization of the heat exchanger grids to accurately reproduce the experimental setup. The study further showcased the ability of LBM simulations to accurately represent the acoustic performance of the installed fan system when compared to experimental results. In addition, Piellard et al. studied the effect of modifications to the tip clearance geometry on the acoustic footprint of the fan by adding a stationary acoustic ring (see Fig. 2.11(a)), which effectively lowered the overall noise level by around 2 dB(A), both broadband and tonal (BPF). The authors also noticed the appearance of large BPF sub-harmonic humps as in the case of Magne et al. and Moreau and Sanjosé similar ring-shrouded configuration, especially under the second BPF, where a particularly prominent tonal hump is visible and present up to the fourth harmonic. The origin of this tonal hump was found to be exclusive to the tip region of the blades. The sub-harmonic noise level was also affected by the addition of the static acoustic ring. Piellard et al., through a quantitative analysis of the rotational speed of coherent structures exiting the gap, found that their velocity matched very well with the observed tonal humps, with a range of velocities mainly situated from 5 to 24% of the

fan speed (2400 RPM) for the unmodified tip geometry (notably slower than those found by Magne et al.). The same analysis of the modified fan showed a rather important shift in the distribution of the velocity of the structures as seen in Fig. 2.11(b), from a rather smooth repartition to a distinctly modal nature with three preferential velocities (R1, R2 and R3). As a result, the sub-harmonic spectral humps were modified in their shape and frequency of occurrence, as seen in Fig. 2.12. It can be observed that the spectra with the acoustic ring exhibits several peaks absent from the original configuration; for example taking the tonal hump H2, where two sharp peaks appear on the modified configuration, whereas is was relatively more broadband before. New humps are also created as a result of the velocity differences, as highlighted in Fig. 2.12(b).

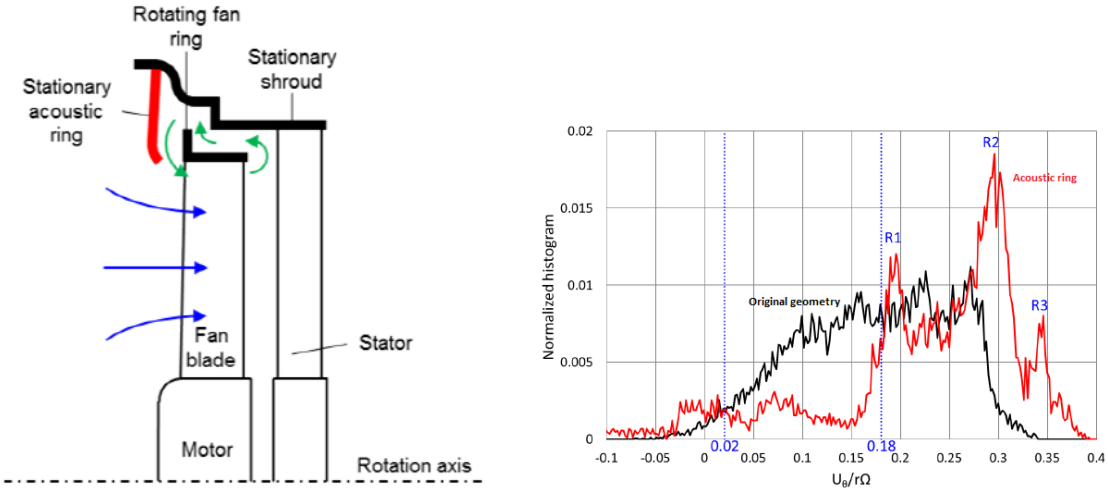

(a) (b)

Figure 2.11 Effect of the modification of a ring-shrouded fan tip clearance (a) Sketch of the static acoustic ring added to the geometry (b) Histogram of coherent structure azimuthal velocity with and without the acoustic ring [Piellard *et al.*, 2014]

The LBM was also used recently to investigate tip leakage flow noise in a free-tipped axial fan (Reynolds number of 500 000 based on chord for a tip radius of 150 mm) [Zhu, 2016; Zhu *et al.*, 2016a]. The fan was designed to have a highly loaded blade near the tip (70% at the root, and 120% in the tip region), making this a fan especially suited to studying tip leakage flow. The simulation was made to mimic the acoustic test rig used experimentally, in which the fan is situated in a duct terminated by an anechoic termination, with the air inflow coming from a large semi-anechoic room. The fan was tested using two tip clearance gap sizes of 0.1 and 1% of the span respectively. The authors observed a general increase in broadband noise as the tip gap similarly to that observed in other research due to the increase in tip leakage flow strength. However, at lower flow

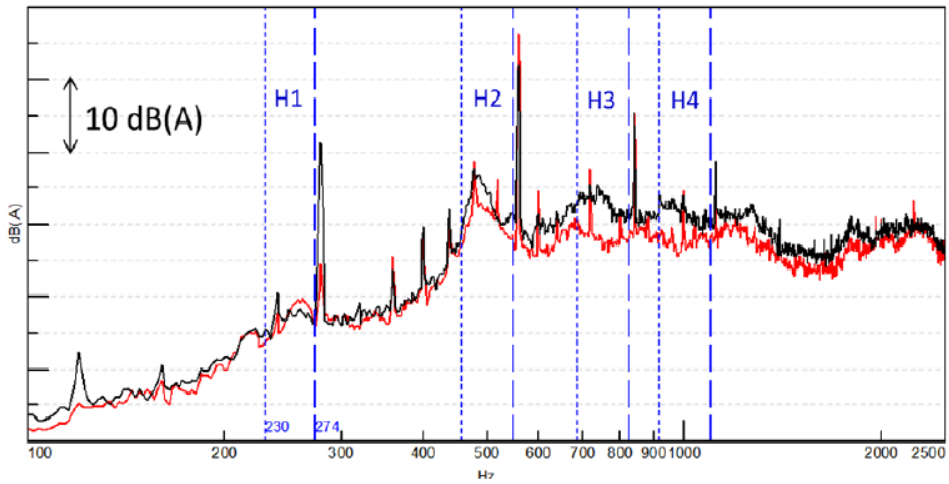

(a)

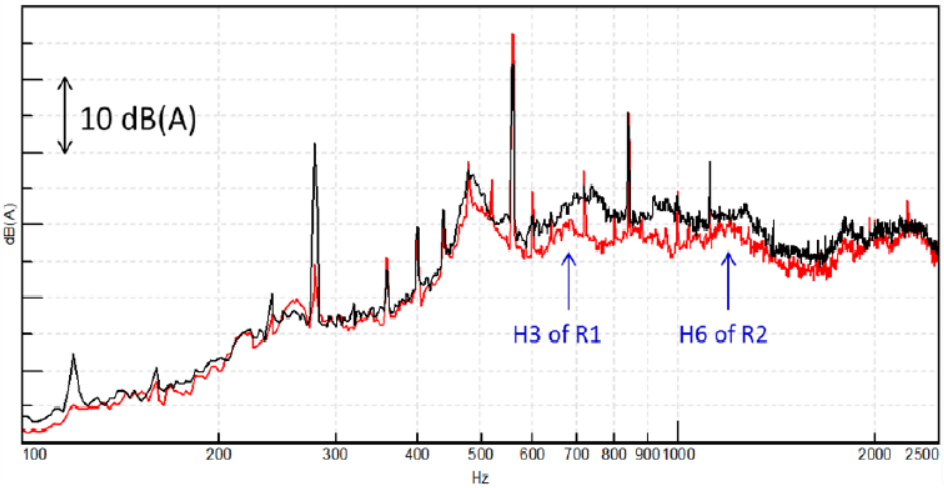

(b)

Figure 2.12 Effect of the acoustic ring on the sound spectra in the experiment. [Piellard *et al.*, 2014]

rates, narrowband humps were also apparent for the larger gap, which could be attributed to the appearance of the so-called RI phenomena introduced by Kameier [Kameier, 1993; Kameier and Neise, 1997a,b] given the appearance of the spectral signature documented by the same author on casing wall pressure measurements in the tip region. The authors proposed the use of a cross-spectral method originally developed to investigate large-scale vortical structures in quiescent flow and used on centrifugal [Bent, 1993; Bent *et al.*, 1993; Mongeau *et al.*, 1993; Tetu, 1993; Wolfram and Carolus, 2008] and axial [Sturm and Carolus, 2012] fans. The method was adapted to investigate the near-field turbulent structures and is similar to the one used by Pardowitz et al. [Pardowitz *et al.*, 2012] in that it attempts to detect coherent structures in the flowfield and model them into

a series of spatially coherent periodic modes possessing a certain rotational velocity. It takes it one step further, however, in that it then records the occurrence of these modes, or 'events', and evaluates their acoustic interaction with the fan blades. The result of the prediction for this particular fan is shown in Fig. 2.13(a) using the cross-spectral method in the 100-600 Hz range, which corresponds to the range where the RI spectral signature appears for this configuration. What is notable is that the three tonal humps are well predicted by the modal method regarding their frequency, shape and the relative levels when comparing to the experimental spectrum superimposed. A spatial study also revealed that the strongest contributors are concentrated in the first 50% of the chord of the blades in the tip region. Frequency filtering of the flowfield using simulation data allows to visualize the corresponding structures in the flow; as an example structures corresponding to mode orders 10 and 15 are illustrated in Fig. 2.13(b). It can be seen that the identified structures all lie in the tip region, represent part of the tip leakage flow structures and indeed seem to interact with the forward part of the blades.

2.4 Literature Review Assessment

The literature review presented in this section reveals that tip leakage flow is a matter of some importance when looking at improving the performance of turbomachinery systems. It was shown that it is a source of significant losses from an aerodynamic point of view. It is also shown to have an important effect on the global noise spectra, as indicated by global increases in broadband sound levels with increases in tip gap clearance or eccentricity for example, and the appearance of tip-related tonal noise components.

From a physical standpoint, however, it is easy to observe that the formation of the secondary flows associated with the tip gap clearances in rotating machines are dependant on a multitude of parameters: to name a few, machine configuration (e.g. single rotor, inlet or outlet vanes), inlet flow, boundary layer formation, flowrate, rotational speed and blade stagger all have an effect on the formation of tip leakage flow. A comprehensive investigation of tip clearance flow thus requires the evaluation of several of these aspects; practically, this is achievable by studying different fans of varying sizes, operating points and tip clearance configurations and it was the option considered in the course of this study.

Experimental investigation of these flows is also problematic because in part of the small clearances usually encountered in turbomachine applications and the possible interference of the probes with the turbomachine itself and/or the flow as well as the high rotational

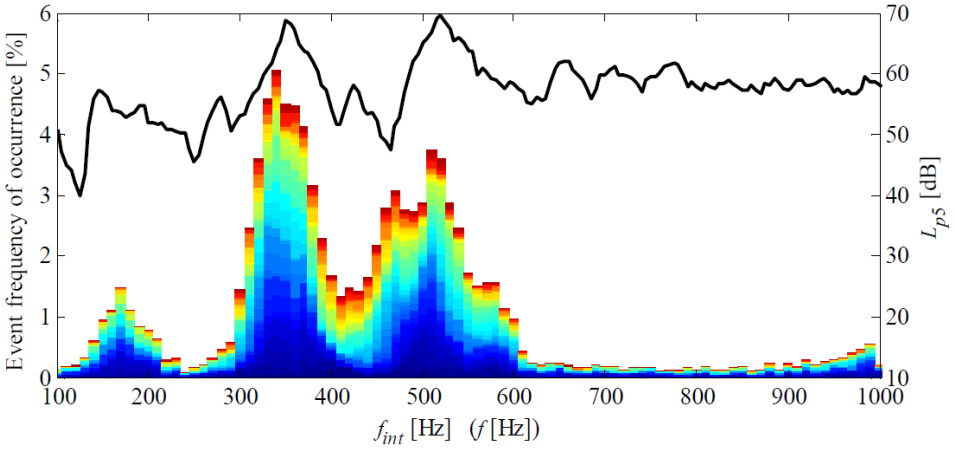

(a)

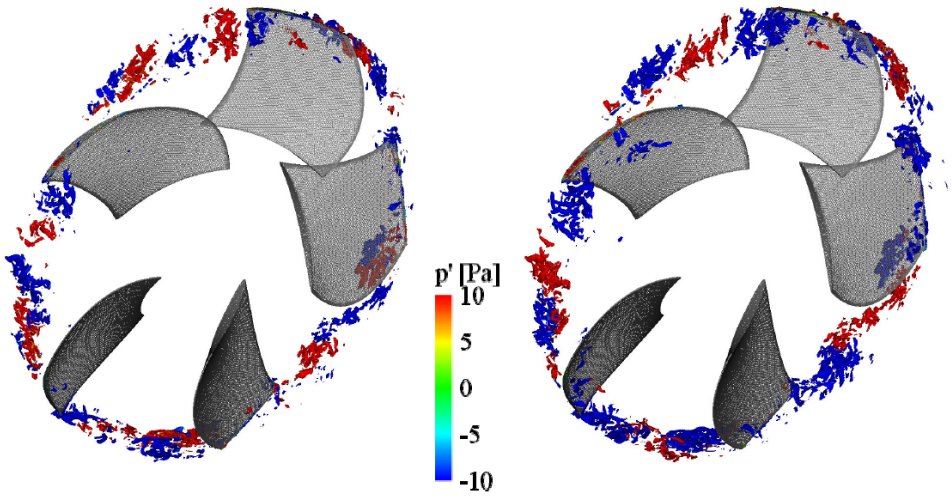

(b)

Figure 2.13 Assessment of a modal prediction tool for tonal tip leakage flow noise from coherent structures (a) Prediction of the acoustic effect from the coherent structures (b) Visualization of pressure fluctuations associated with modes of order 10 (left) and 15 (right)

speeds inherent to turbomachine applications, which limit the collection of data or force the experimenter to resort to alternative configurations (linear cascades), scaled models ([Weichert, 2011]) or advanced data collection apparatus ([Pardowitz *et al.*, 2015a; Wu *et al.*, 2011a,b]) in order to acquire detailed data. This is especially critical when considering that correlation analysis techniques using joint near-field aerodynamic measurements together with far-field acoustic measurements appear to be key to identifying and understanding the aerodynamic and linking it to the aeroacoustic influence of tip leakage flow in turbomachinery applications, as evidenced by some of the recent studies covered in this chapter [Pardowitz *et al.*, 2012; Pogorelov *et al.*, 2015, 2016; Zhu *et al.*, 2016b].

Numerical studies show great promise to alleviate the experimental shortcomings that come with tip clearance flow and more generally turbomachinery flowfield investigation as a whole. However, the small tip clearances encountered and the highly turbulent and unsteady nature of tip clearance flows (and overall turbomachinery flowfields) also become a problem in the case of CFD calculations, as the meshes needed to achieve sufficient resolution in the tip gap and for the subsequent flow phenomena are quite fine and must often be applied to full annular simulations of the turbomachines, which results in large grid point counts that require large amounts of computing power. Also, while steady-state Reynolds Averaged Navier-Stokes (RANS) approaches can provide some insight into the flow features, ultimately unsteady calculations are required to obtain complete information regarding the flowfields involved due to the nature of tip leakage flow and ultimately obtain the associated acoustics. Large differences can also be observed for a given configuration between steady and unsteady simulations [Moreau *et al.*, 2011a], with the latter providing better flowfield predictions when compared to experimental data. It was also seen that RANS simulations can predict flow separations whereas unsteady Large Eddy Simulations (LES) do not [Gourdain, 2013] for example. Moreau and Sanjosé [Moreau and Sanjose, 2016] further showed that, in order to accurately predict turbomachinery noise levels, LES, or at least hybrid, quasi-LES simulations are required in conjunction with acoustic propagation methods. Observations from this and other studies also showed that an emerging class of simulations, the Lattice-Boltzmann Method (LBM), with its ability to conduct direct acoustic simulations and accurately model complex installations and their effect on acoustic propagation, shows great promise for the concurrent investigation of aerodynamics and aeroacoustics and the development of insight into noise mechanisms (diagnostic or prediction tools).

The current work was thus oriented towards performing a numerical study of tip leakage flow in low-speed axial fans using the LBM class of simulation tools, with a particular

emphasis on the identification of the impact of this secondary flow on the overall acoustic spectra of such turbomachines. This allowed for the concurrent evaluation of the aerodynamic field as well as the associated propagating acoustics in realistic environments, providing an invaluable database for the identification of noise mechanisms through flow vizualisations and the application of correlation based analysis techniques. A selection of axial fans was retained for investigation in order to make it as extensive as possible with regards to the wide array of parameters seen to influence the formation of tip leakage flow; a description of the selected configurations is presented in the following chapter. The final aim of this study was to properly identify the noise mechanisms related to tip leakage flow and if possible to try and develop a way to model them; the elusive *Holy Grail* with regards to acoustic modeling lies in the determination of a way to predict the radiated noise *a priori* for a given turbomachine design, and this research was a way to make strides toward that goal.

CHAPTER 3

Test Cases

3.1 Context

From the literature review in the previous chapter, it was seen that tip leakage flow physics and the associated acoustic effects in axial turbomachinery applications were highly dependant on several parameters. The first parameter that comes to mind is of course the tip configuration; from the literature review in the previous chapter, a relatively wide range of tip clearance sizes as well as different configurations (e.g. typical free-tip, ring-shrouded fans) were observed. The importance of the tip clearance size was highlighted by several studies cited in the literature review as having an effect on the TLV and associated flow phenomena. The effect of a non-orthodox tip configuration was also shown to be a decidedly major factor when it comes to fan performance and acoustics ([Longhouse, 1978; Piellard *et al.*, 2014]).

From an operational point of view, it was also shown that blade loading had a marked effect on the formation of tip leakage flow, with the strength increasing as flowrate is throttled down and the blade loading increases and the release point and trajectory of the coherent vortical structures being altered.

However, even for a similar tip configuration and operating point, not all fan designs are equal on that front, so while the basic mechanisms behind tip leakage flow remain the same, it can either be favored or impeded by some design choices (e.g. skewed blades [Corsini and Rispoli, 2004; Wadia *et al.*, 1998] and the modification of the radial equilibrium). Furthermore, installation effects also have the potential to influence tip leakage flow formation. This last parameter, however, is a rather broad one, as the term 'installation effect' refers to environmental interference from the fan surroundings during normal operation, from potentially negligible effects in a plenum-mounted fan system (relatively free-field environment) to a largely environment dependant system such as an aircraft engine compressor (ducted geometry complete with inlet and outlet guide vanes with multiple in-line stages).

In addition to throttling effects, a complete investigation of tip leakage flow noise inception in axial fans thus requires to look at fans with differing tip configurations and requires

the inclusion of installation effects in order to insure results representative of real-life environments.

In order to carry out such an investigation, it was decided to carry out Lattice-Boltzmann simulations on several fan geometries in order to investigate a wide range of tip configurations with varying operating points and designs. Use of the LBM also allows for the concurrent investigation of aerodynamic phenomena along with the associated acoustics through direct acoustic simulation. The LBM has the added incentive of being able to accurately and quickly simulate complex environmental effects which are taken into account for the acoustic results. The method, which will be detailed in the next chapter, is however limited to the simulation of low-Mach flows (on the order of Mach=0.4-0.5 in the upper limit), which is why the current study was also limited to low-speed fans.

In order to investigate as wide a spectrum of configurations as possible, a series of 5 axial fans were selected as test cases for the study of tip clearance flow mechanisms and their acoustic impact, covering 3 different configurations with regards to the tip clearance shape. The cases selected all had extensive aerodynamic and aeroacoustic experimental data available for the purpose of validating simulation results.

The following sections are aimed at presenting the chosen geometries and their test conditions as well as the data made available for each chase.

3.2 Axial Free-Tipped Fan

The first configuration investigated in the course of this study, which represents the simplest and perhaps most common form of axial fan, is the free-tipped axial fan with a cylindrical tip clearance gap. Two fans from this category were investigated.

3.2.1 Rotating Controlled Diffusion Blade Fan

The first geometry, dubbed Rotating Controlled Diffusion Blade (RCDB) fan, is a rotor-only research fan which was designed to allow for the study of differences between a stationary airfoil and the same airfoil when placed in a rotating frame. It is shown in Fig. 3.1.

The fan blades were designed using the so-called controlled diffusion (CD) airfoil designed by Valeo and used in their fan designs, the stationary version of which has been studied extensively both from an experimental and a numerical perspective [Moreau *et al.*, 2016].

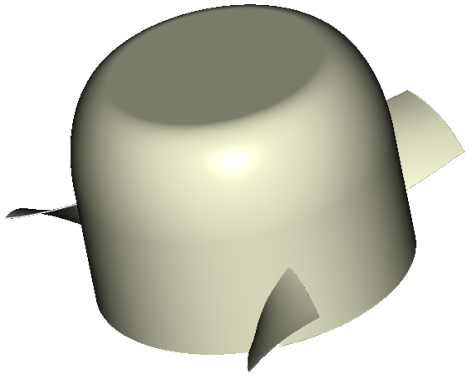

Figure 3.1 RCDB impeller in the 3-blade configuration.

The fan is 732 mm in diameter, with a blade span of 126 mm. The blades themselves, as stated above, are designed using a single airfoil shape (CD airfoil); the blades exhibit no sweep or lean, with the profiles stacked along their chord center, and a constant chord length of 133.9 mm equal to that used for the stationary CD airfoil. The RCDB was designed to be modular and is able to accomodate anywhere from 2 to 9 blades. The design flow rate of the fan is 2.31 kg/s and the design rotational speed is 437 RPM; for this operating condition, the mid-span profile is at an angle of incidence of 8 degrees with a relative velocity at the fan inlet of 16 m/s to reproduce the nominal test conditions on the stationary CD airfoil.

The fan was studied experimentally in the Axial Fan Research and Development (AFRD) test facility at MSU, with regard to both the aerodynamic and aeroacoustic perspectives [Barrent, 2015; Cawood, 2012; Davoudi, 2014; Foss *et al.*, 2001; Neal, 2010]. The AFRD facility consists in a large plenum of 3x3x2 m large, the test fan beeing mounted in an opening on the ceiling wall in a short ducted section; there is a 4 mm annular clearance between the fan blade and the shroud surface (740 mm duct diameter). An inlet bellmouth was also designed to insure a flat inlet velocity profile along the span of the blades. A schematic of the experimental setup is shown in Fig. 3.2. Flowrate through the system is measured using the calibrated turning vanes, while the static pressure rise across the fan plane is determined using a pressure tap located in the ceiling panel of the plenum.

In addition to the overall characteristics of the fan, near-field wake measurements were also carried out. Two methods were used, namely hot-wire anemometry (HWA) and particle image velocimetry (PIV).

For the HWA measurements, a traverse system was designed and integrated in the AFRD facility. Measurements were carried out using both a rotating traverse ([Cawood, 2012;

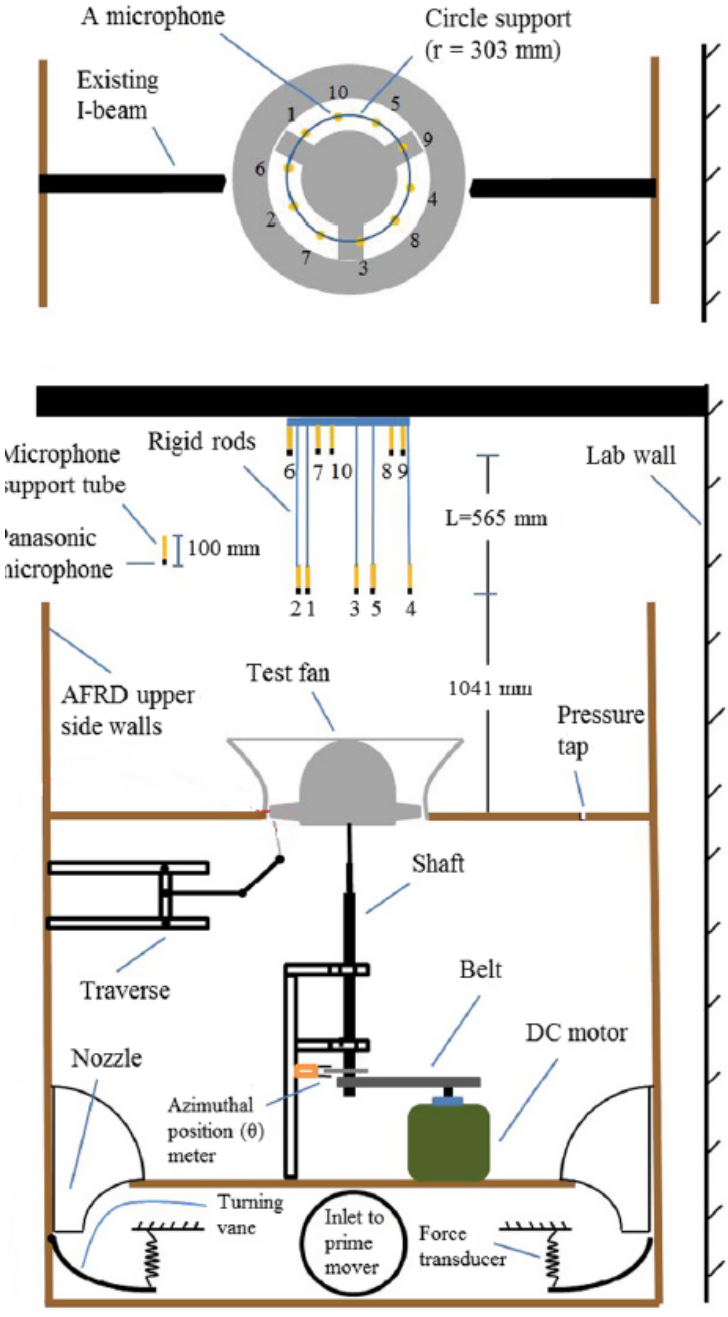

Figure 3.2 Schematic view of the AFRD facility at MSU [Davoudi *et al.*, 2016b]

Neal, 2010] which allowed for measurements to be carried out at a fixed position relative to one of the RCDB blades and a fixed traverse system ([Barrent, 2015]) to evaluate the phase averaged velocity profiles downstream of the RCDB rotor at midspan for different axial positions. The rotating HWA anemometry setup is illustrated for reference in Fig. 3.3.

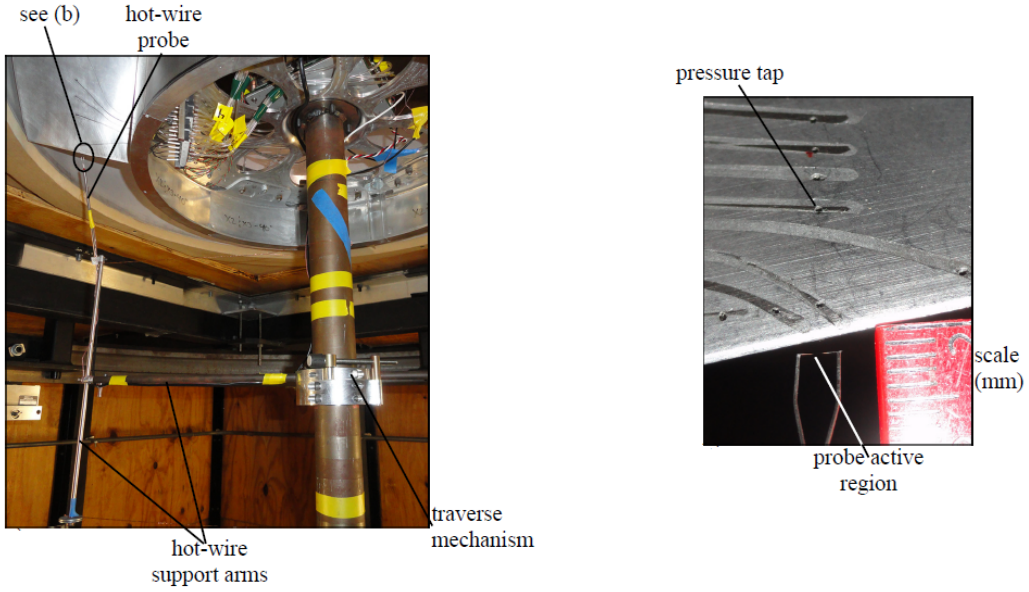

Figure 3.3 Rotating HWA near-wake measurement system for the RCDB fan (a) Hot-wire traverse system overview (b) Close-up view of the hot-wire measurement probe [Cawood, 2012]

Phase-averaged PIV measurements were also conducted to provide an in-depth description of the flowfield encountered downstream of the fan. Two types of measurement were carried out, namely fixed radius $\theta - Z$ plane measurements at midspan as well as radial evaluations at fixed $r - Z$ positions, as shown in Fig. 3.4.

Finally, the RCDB fan blades themselves were also instrumented to allow for the evaluation of wall-pressure fluctuations along the chord on both the pressure and suction sides. A total of 18 chordwise pressure taps were thus incorporated to the fan blade design, as illustrated in Fig. 3.5. A total of 5 blades were instrumented at different spanwise locations (11.9, 30.2, 50, 60.3 and 86.5 % span).

More recently, aeroacoustic measurements were also carried out within the non-anechoic AFRD facility [Davoudi, 2014; Davoudi *et al.*, 2016a,b] with a delay and sum beamforming technique. The technique employed a series of ten microphones located in circular arrays

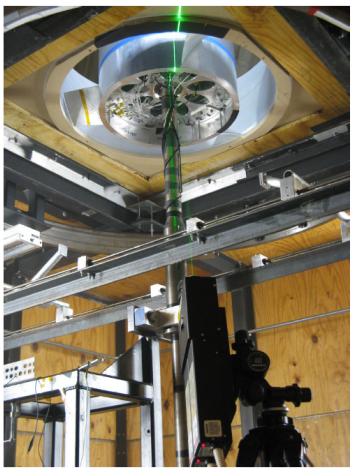

(a)

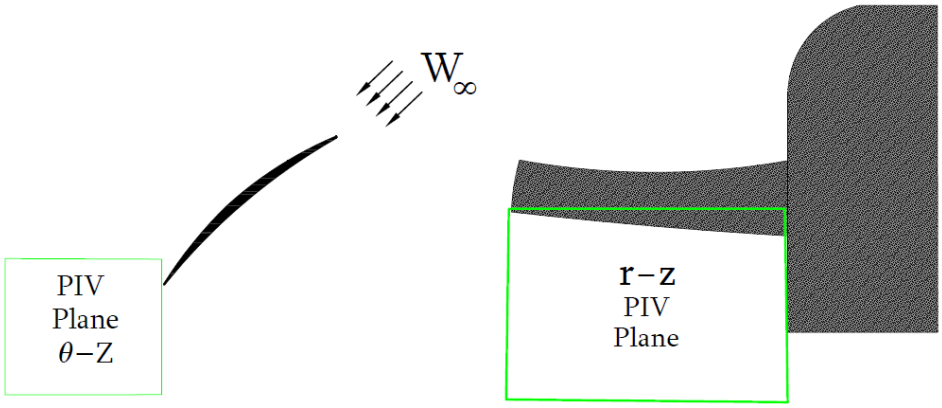

(b)

Figure 3.4 PIV measurements carried out on the RCDB fan in the AFRD facility (a) PIV measurement setup (b) Illustration of the PIV measurement planes [Neal, 2010]

at two upstream locations, with 5 microphones at each axial position above the RCDB midspan, for signal denoising.

3.2.2 USI7 Test Fan

The second free-tipped geometry with a cylindrical tip clearance gap investigated in the course of this study is a test fan dubbed USI7 designed at Siegen Universitat, Germany, whose design methodology was described in Carolus et al. [Carolus *et al.*, 2015]. It was recently the subject of a thesis investigating tip clearance noise in a parallel study [Zhu, 2016]. A collaboration between the Université de Sherbrooke and Siegen Universitat included sharing of pertinent data, both numerical and experimental.

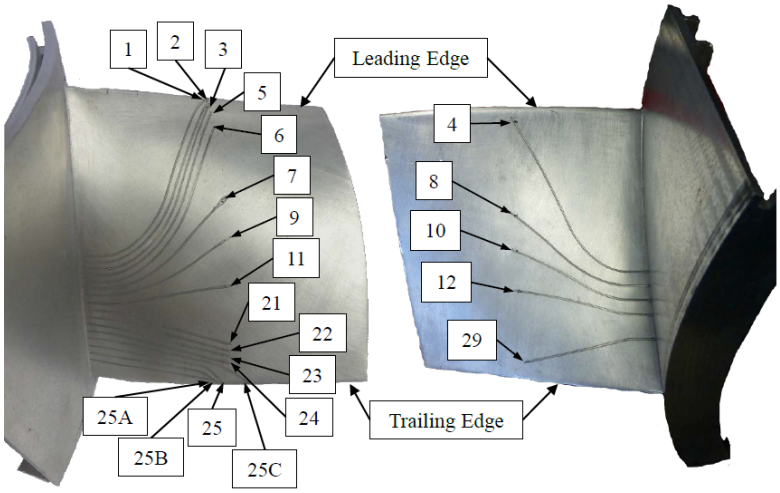

Figure 3.5 Location of the imbedded pressure taps on the RCDB blades. Probes 1-25 are located chordwise, with probes 25A-B-C located at the trailing edge and spread out spanwise. [Barrent, 2015]

The USI7 is a low-pressure rotor-only fan designed to be representative of a large class of mass-produced fans with regards to flowrate and effective pressure rise. The blades were designed using Blade Element Momentum (BEM) theory code coupled with the free-source code XFOIL for the prediction of airfoil lift and drag properties of blade profiles selected at different radial stations.

The rotor is 300 mm in diameter, with a 135 mm hub - less than half the size of the RCDB fan - and is composed of 5 equally spaced blades (see Fig. 3.6). In contrast to the RCDB, the USI7 blades are skewed and have varying profiles from the 4-digit NACA profile family along the span with varying chord and thickness (86 to 68 mm and 8 to 7 % from hub

Figure 3.6 USI7 impeller.

to tip respectively). The fan has a design flowrate of 0.65 m^3/s and an impeller speed of 3000 RPM.

During experimentation, the USI7 rotor is inserted in a 300 mm diameter duct (see Fig. 3.7), and the nominal fan diameter is modified through milling to introduce a tip clearance gap with respect to the duct wall. Two clearances were considered, namely 0.1 % and 1 % of the nominal rotor diameter (0.3 and 3 mm). An inlet bellmouth is also included to allow for clean inflow conditions to the fan. The rotor assembly is maintained in the duct by two sets of three thin cylindrical struts located downstream of the fan.

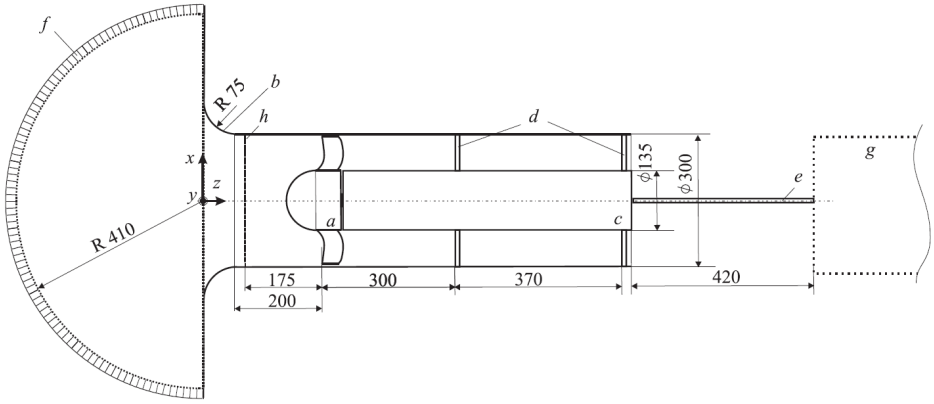

Figure 3.7 Schematic view of the ducted USI7 fan assembly a) USI7 impeller with its hemispherical hub nose b) inlet bellmouth c) bearing and electric drive d) support struts (M8 threaded rods) e) optional external drive shaft f) hemispherical flow conditioner g) optional electric motor with integrated torque meter. Dimensions in mm. [Carolus *et al.*, 2015]

Two different test rigs were utilized in order to gather data on the USI7 geometry. First, the global aerodynamic performance of the fan (pressure rise and efficiency with regards to flowrate) were evaluated in a DIN 24163 compliant test rig shown in Fig. 3.8 which consists of two main sections. The first section is meant to measure and control the flow rate for the test rig and settle the flow: ambient air is taken from the room surrounding the test rig into a calibrated nozzle; the air then passes through flow-straighteners and an auxiliary fan and throttling section. The air from the first section is then exhausted into a settling chamber forming the air intake reservoir for the test fan assembly. The total-to-static pressure rise is given by the pressure differential between the settling chamber and the ambient atmospheric pressure outside the rig. The volumetric flow rate is determined from pressure measurements at the calibrated nozzle relative to the ambient pressure outside the rig. In this test rig, the fan is driven by an external electrical drive with an integrated torquemeter, with the output torque used to calculate the fan efficiency.

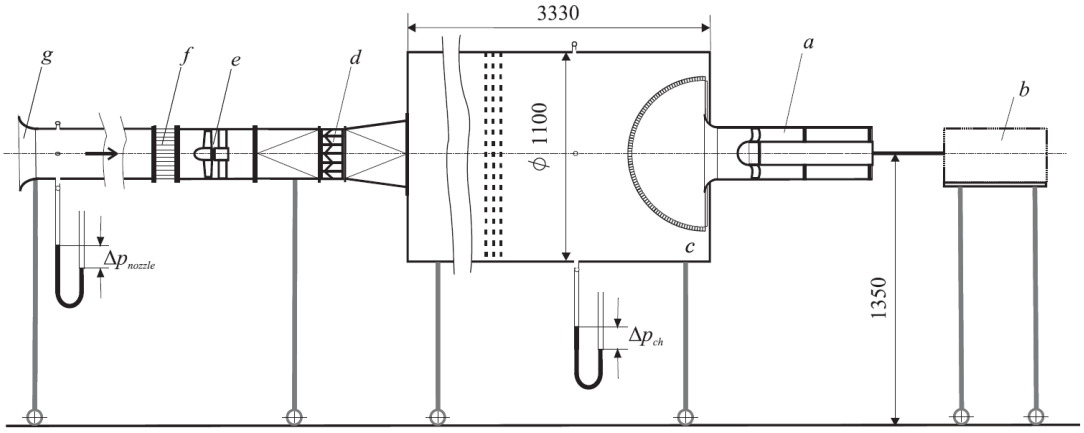

Figure 3.8 Schematic view of the aerodynamic test rig for the USI7 fan as seen from the side a) ducted fan assembly b) electric motor with integrated torque meter c) settling chamber with filter screens d) adjustable throttle e) auxiliary fan f) flow straighteners g) calibrated nozzle inlet. Dimensions in mm. [Zhu, 2016]

Acoustic measurements were carried out on a second ISO 5136 compliant rig shown in Fig. 3.9 for the determination of sound power radiated by fans in a ducted configuration. In essence, the test fan assembly takes the air from a large semi-anechoic room; the air then moves through flow straighteners downstream of the assembly and it is finally exhausted into an anechoic termination. Four half-inch Bruel et Kjaer type 4190 microphones are used to evaluate the acoustic footprint of the system. One microphone is located 4 m downstream of the rotor at 80% of the duct radius to measure the downstream radiated noise levels. The other three microphones are located on a virtual horizontal semi-circular line 1.3 m ahead of the fan in the semi-anechoic room, with one microphone on the rotational axis and the others spaced 35 degrees from the centerline. The fan rotational axis was situated 1.35 m from the semi-anechoic chamber floor.

In addition to sound pressure measurements, pressure measurements were carried out in the near-field using Knowles FG-23329-P07 miniature pressure transducers. A first series of sensors was located on the duct inner-wall in the tip clearance gap of the rotor, as illustrated in Fig. 3.10. The sensor array is composed of three rows of 10 transducers with 25 degree spacing in the azimuthal direction between the rows, with the transducers measuring the pressure through 0.5 mm pinholes in the inertial frame. In each row, the sensors are arranged to coincide with the blade tip profile mean chord location and thus cover the whole blade from leading to trailing edge.

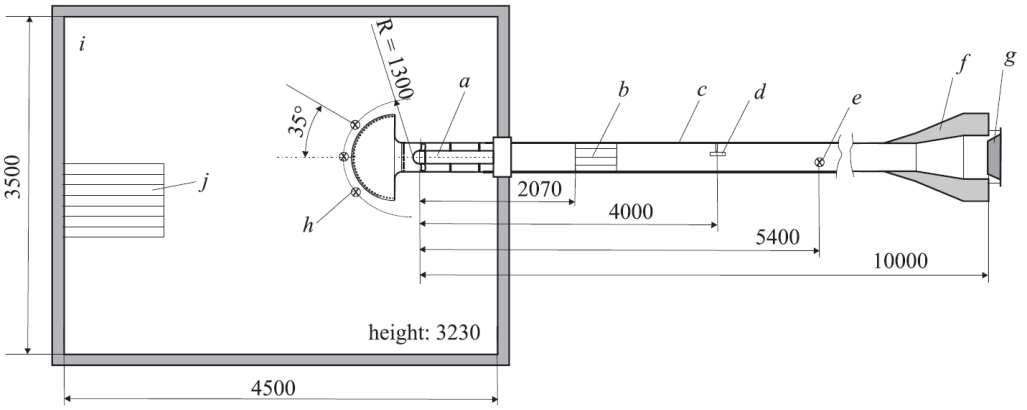

Figure 3.9 Schematic view of the acoustic test rig for the USI7 fan viewed from the top; a) ducted fan assembly b) flow straightener c) flow chamber duct d) downstream microphone with slit tube and nose cone e) hot-film flow meter f) anechoic duct termination g) adjustable throttle h) upstream microphones i) semi-anechoic chamber j) air inlet floor aperture. Dimensions in mm. [Zhu, 2016]

A second set of 16 transducers was integrated into the blades themselves to allow for wall-pressure measurements in the relative frame. The transducers are installed on only two subsequent blades of the rotor. Seven sensors are located at the *Sxx* positions (see Fig. 3.11) on each blade of a single blade passage, with the leading blade having the sensors installed on the pressure side (denoted P_{xx}) and the following blade on the suction side. The remaining two transducers were installed at the tip of the blades (position *T01*). Therefore, wall-pressure measurements were made available for the pressure and suction sides for a set of two blades covering a single blade passage.

3.3 Free-Tipped Fan with Complex Tip Geometry

As an extension of the previously described free-tipped cylindrical tip clearance fan configurations, a more complex design with regard to the tip shape was considered as a test case. The fan is a Bosch design for the purpose of automotive engine cooling. It was recently studied from both experimental [Sampath *et al.*, 2015] and numerical [Chumakov *et al.*, 2015a,b] points of views.

The rotor is composed of 5 equally spaced blades with an outer diameter of 320 mm with a hub radius of 60 mm. The blades are highly skewed and have a variable profile and angle of attack along the span. Whilst the rotor is free-tipped, as opposed to often seen ring-shroud configurations fans for similar applications, it also differs from the test cases

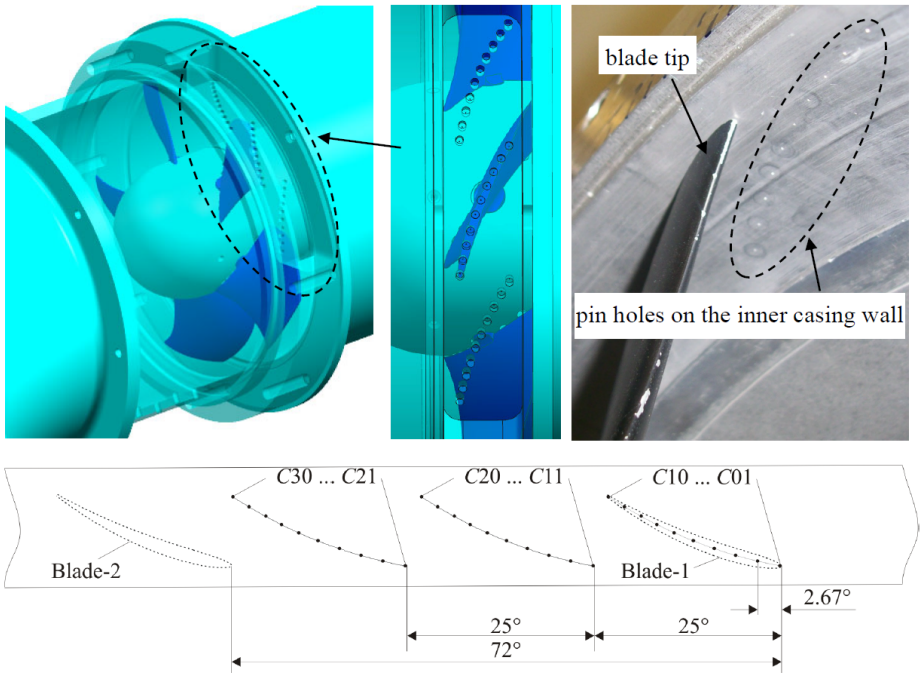

Figure 3.10 Pressure transducers incorporated on the shroud casing wall in the tip region of the blades for the USI7 acoustic test rig. The transducers are numbered $C01$ to $C30$. [Zhu, 2016]

presented in the previous section in that it has a variable radius blade tip in conjunction with a convergent static shroud geometry. The tip clearance, however, is maintained constant at 3 mm along the chord, normal to the blade tip surface. The fan and shroud geometries are illustrated in Fig. 3.12. The design flowrate for this configuration is 0.43 m^3/s for a rotor speed of 2630 RPM. However, detailed testing was carried out at a higher flowrate of 0.53 m^3/s.

During testing, the fan was inserted in a 700 mm diameter duct, with a static shroud assembly inserted along with the rotor. An inlet bellmouth was also added to allow for a more uniform upstream velocity profile. The duct assembly was terminated with a perforated plate (200 mm diameter). The complete rotor/stator/duct assembly is schematically shown in Fig. 3.13.

Fan characterization was carried out internally at Bosch using two different setups for the aerodynamic and aeroacoustic properties. The first rig was used to collect aerodynamic performance data conforming with the ANSI/AMCA 230-12 standards. A schematic view of the AMCA flow chamber is presented in Fig. 3.14. The duct assembly described above was inserted through the fan mount surface for the test.

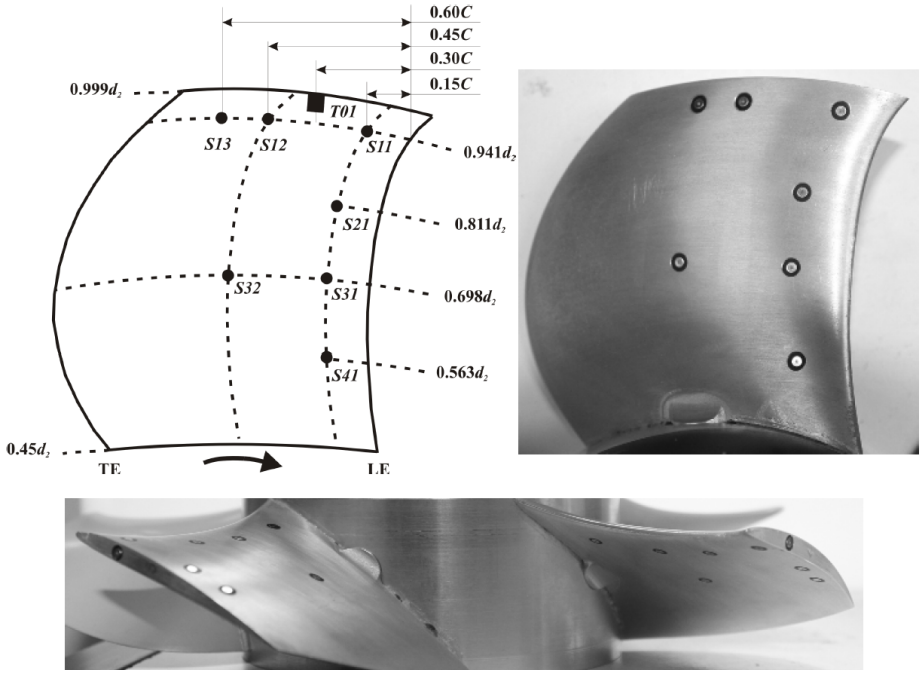

Figure 3.11 Illustration of the blade-imbedded pressure transducers on the USI7 fan. [Zhu, 2016]

The performance curve of the fan (pressure rise as a function of flowrate) was measured on this setup through the use of two series of 4 static pressure wall taps located at 90^o from each other located respectively 25 mm upstream and 35 mm downstream of the fan to measure the pressure differential across the fan plane. The pressure difference was measured using a Baratron 220CD differential capacitance manometer with a 0.15% accuracy. The torque applied to the fan was also measured using a Himmelstein & co. MCRT 3-08TLS torquemeter with a 0.01356 Nm accuracy. Additionally, a 5-hole probe was used to measure the spanwise time-averaged velocity profiles 30 mm behind the trailing edge of the fan blades.

The second rig was setup to evaluate the acoustic performance of the fan in an anechoic environment. The duct assembly containing the fan/shroud, similarly to the AMCA setup, was suspended and centered in an anechoic room with a length of 4.8 m, a width of 3.5 m and a height of 2.6 m to the end of the acoustic lining of the chamber. The flowrate through the fan was controlled through the use of a damper plate. A schematic of the test rig is presented in Fig. 3.15.

In the experiment, acoustic pressure was recorded at 81 locations located upstream of the fan, as illustrated in Fig 3.16. The microphones were situated to allow for the evaluation

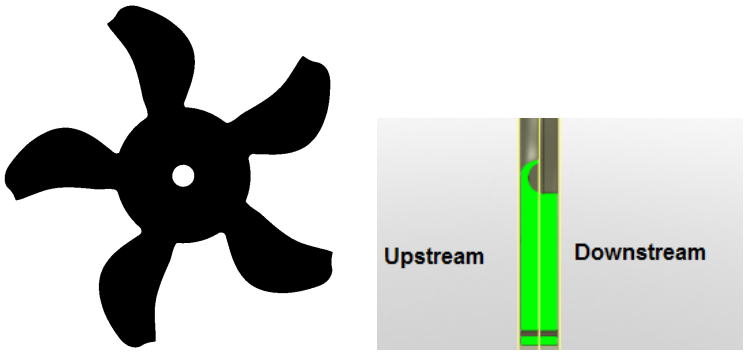

(a) (b)

Figure 3.12 Illustration of the geometry of the automotive cooling fan (a) Fan rotor (b) Axis cut of the shroud.

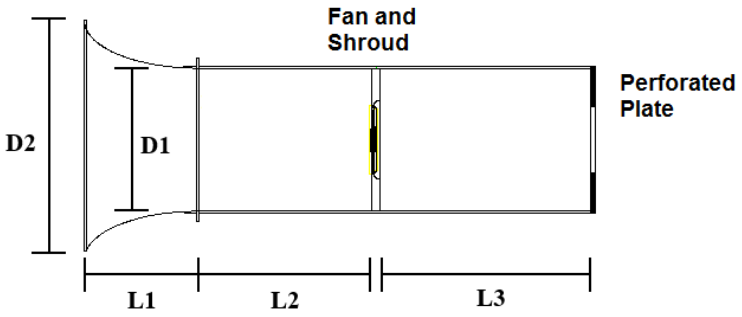

Figure 3.13 Schematic view of the Bosch test case duct assembly.

of the acoustic performance of the fan over a large area ahead of the bellmouth entrance, with a series of 78 measurement points spread out over 6 equally spaced (200 mm) axial positions with 13 equally spaced (50.8 mm) radial evaluation points starting from the fan axis at each. In addition, three measurement locations located on the fan axis were situated inside the duct to a distance of 600 mm. The data was recorded using a sampling rate of 24 kHz over 20 s. The microphones used were BSWA Tech model MPA201 half-inch microphones.

The main differences in the described experimental setups mainly pertain to the acoustic properties of the test environment. The AMCA experimental setup was used as a means to investigate the aerodynamic performance of the fan and was thus not placed in anechoic conditions, whereas the anechoic chamber setup was concerned with obtaining the acoustic pressure upstream of the fan using an array of microphones, as illustrated in Fig. 3.16.

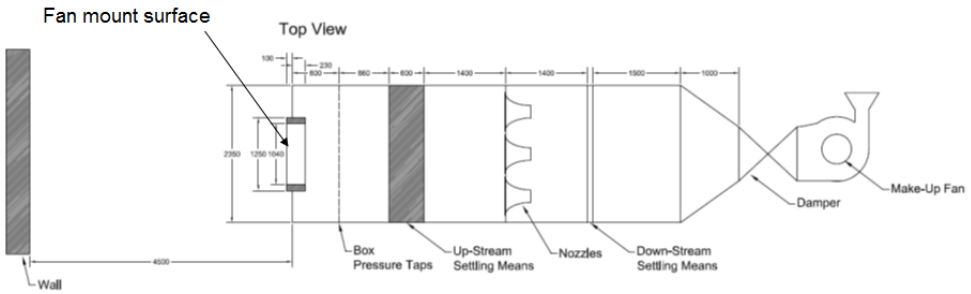

(a)

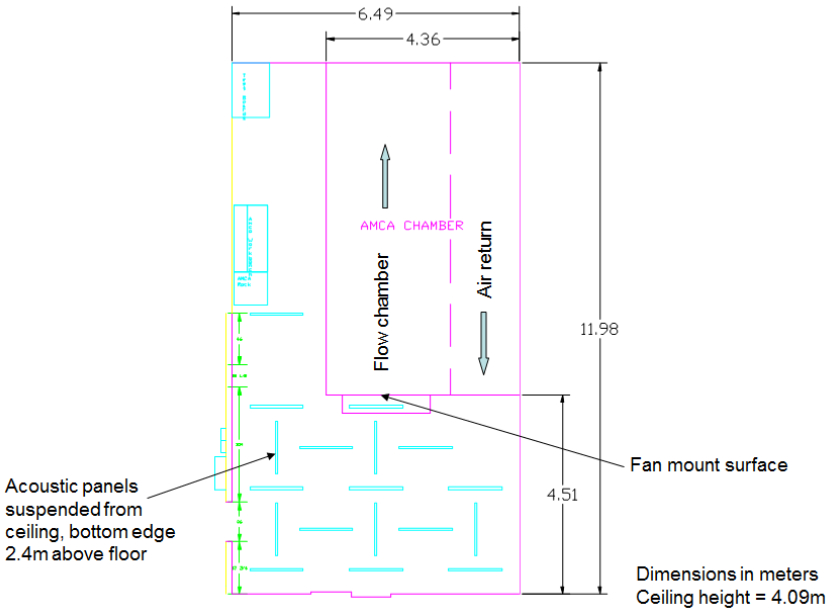

(b)

Figure 3.14 Schematic view of the AMCA test rig used for the experimental aerodynamic evaluation of the Bosch test case (a) Details of the AMCA flow chamber make-up (b) Surroundings of the AMCA flow chamber.

However, there are some geometric differences in the two setups. First of all, the test duct termination was different between the two cases; the AMCA experiment used a simple perforated plate, as the flowrate through the fan was driven through the use of an auxiliary fan whereas in the acoustic setup, flowrate had to be controlled through a sliding plate used to set the system resistance.

The length of the test ducts were also a little different between the two cases with the AMCA setup having a longer constant radius duct portion following the bellmouth, as highlighted in Tab. 3.1; the dimensions refer to those present in Figs. 3.13 and 3.15.

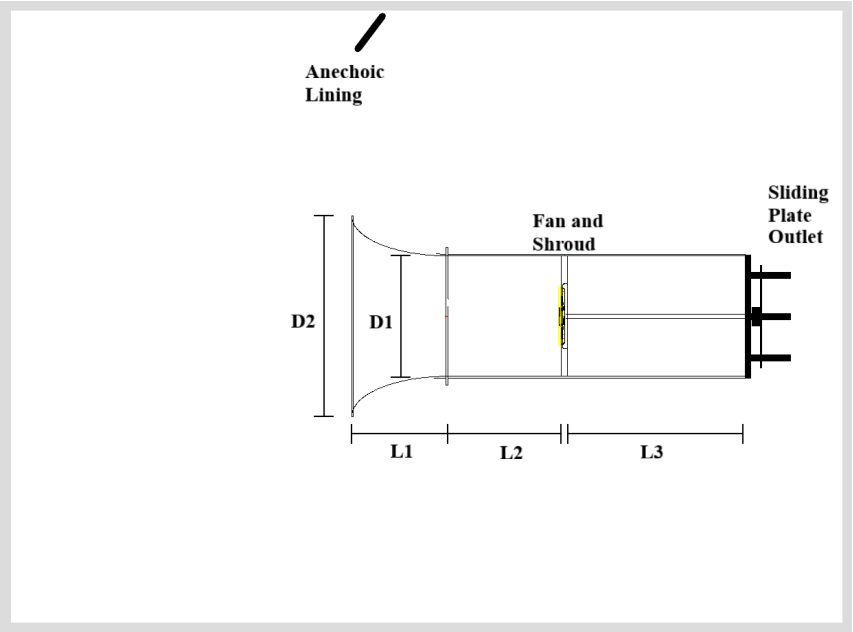

Figure 3.15 Schematic view of the anechoic test chamber setup for the Bosch test case.

Table 3.1 Dimensions of the Test Duct Assembly for the Bosch Fan Experimental Rigs

Case	D1 (mm)	D2 (mm)	L1 (mm)	L2 (mm)	L3 (mm)
AMCA	1167	700	560	870	1050
Anechoic	1167	700	560	650	1050

3.4 Ring-Shrouded Fan Configuration

The final low-speed axial fan configuration that was investigated as a part of the current study was the ring-shroud rotor configuration, as introduced by Longhouse [Longhouse, 1978]. This type of rotor system is typically used in engine cooling application as the air moving system for the radiator heat exchangers. The ring-shroud serves a dual purpose in this case. The first purpose is to solidify the rotor, as these fans are often injection moulded from plastic for mass-production; the linking ring then serves to limit the warping that can occur during operation as a result of the forces exerted by the flow, the heat produced by the surroundings or centrifugal forces resulting from the high-speed rotation of the rotor. The second reason, highlighted by Longhouse [Longhouse, 1978], is that the addition of a tip ring typically improves the aerodynamic efficiency of a given axial fan as well as the stall characteristics, a very important fact given that such fans are exposed to varied and

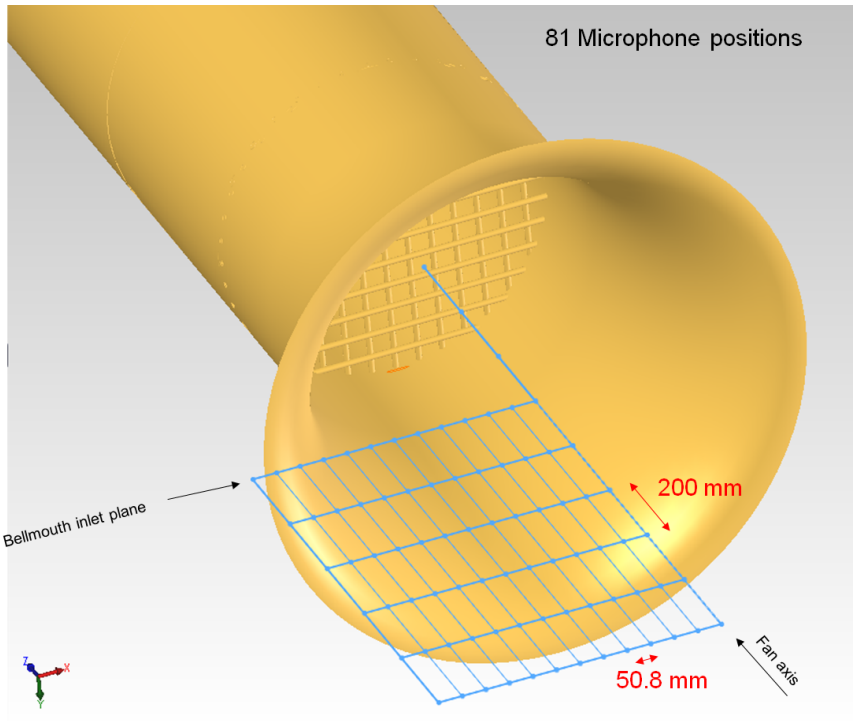

Figure 3.16 Microphone array for the acoustic measurements on the Bosch test case.

often less than ideal inlet and outlet flow conditions. Additionally, an important decrease in overall noise levels can be achieved compared to a free-tip baseline.

However, while this configuration does away with the typical tip leakage mechanism where the pressure differential between the pressure and suction side at the blade tip drives the tip leakage flow, a clearance gap is still present between the rotating ring-shroud and the static shroud surface; a backflow is thus observed through this channel on such machines, driven by the pressure differential across the fan plane. This generates a recirculating flow ahead of the fan leading edge in the tip region and leads to the formation of large coherent vortex structures affecting both the performance and the acoustic footprint of the fan.

Investigation of this class of tip clearance geometry thus complements the free-tipped configurations presented previously in the chapter. Two ring-shrouded fan geometries were evaluated in the course of this study, both engine cooling fans designed by Valeo and Mahle-BEHR respectively. Additionally, the impact of installation effects on ring-shrouded fans were investigated by considering three test configurations: plenum and duct test configurations for the Valeo fan and a realistic module configuration representative of a real-life engine cooling application for the Mahle-Behr fan.

3.4.1 Valeo Ring-Shrouded Fan

The first ring fan that was studied is an engine cooling radiator fan designed by the company Valeo. The fan, designated H380EC1, was investigated in previously cited studies [Foss *et al.*, 2001; Magne *et al.*, 2015; Moreau and Roger, 2007; Moreau *et al.*, 2011b; Moreau and Sanjose, 2016; Soulat, 2010].

The rotor is 380 mm in diameter (hence the H380 designation) and possesses 9 equally spaced blades. The blades are highly skewed, and have a varying profile, chord and angle of attack along the span. The blades are linked together at the tip by an L-shaped rotating ring, namesake of the ring-shroud configuration. The installed fan showcases a 2.5 mm (0.66 % of diameter) tip clearance gap between the ring and the shroud casing. The rotor geometry is shown in Fig 3.17. At peak efficiency operating conditions, the fan rotates at a speed of 2500 RPM and outputs 0.69 m^3/s (2500 m^3/h) of air.

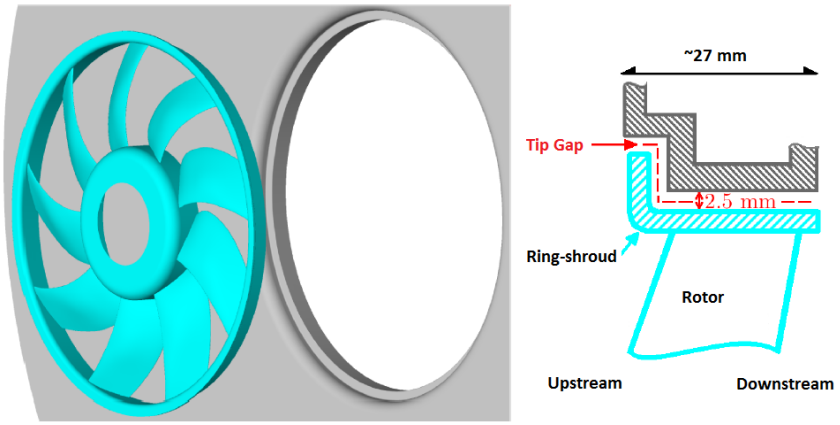

Figure 3.17 Representation of the H380 Valeo fan geometry and associated fixed shroud geometry.[Soulat, 2010]

The fan has been studied in several installed configurations over the past 16 years. The first configuration consisted of the fan being wall-mounted on a plenum, as shown in Fig. 3.17. Experiments were carried using three different testbeds. First is the MSU AFRD facility [Foss *et al.*, 2001] described in more details in section 3.2.1, where a hot-wire measurement campaign was carried out to measure the flow velocities in the wake of the rotor-only fan in addition to a global performance measurements (flow rate and pressure differential). In the H380

The H380 fan performance was also investigated in the Valeo Engine Cooling lab in La Verrière (LVR) [Foss *et al.*, 2001; Moreau and Sanjose, 2016] using a horizontal plenum rig roughly similar to the MSU experiment. The flow direction was inverted compared

to the AFRD facility however, with fan pulling air from the control plenum; the airflow through the system was measured using a calibrated Venturi nozzle integrated in the plenum. An auxiliary fan was used in both the AFRD and LVR setups to control the flow rate through the system with the pressure rise measured as the dependant variable. The fan performance was measured using the average pressure measurement from three differential static pressure taps from the plenum in the LVR. The acoustic power radiated from the fan was also measured using a typical three microphone technique in the former Valeo reverberant wind-tunnel. The Valeo facilities are shown in Fig. 3.18.

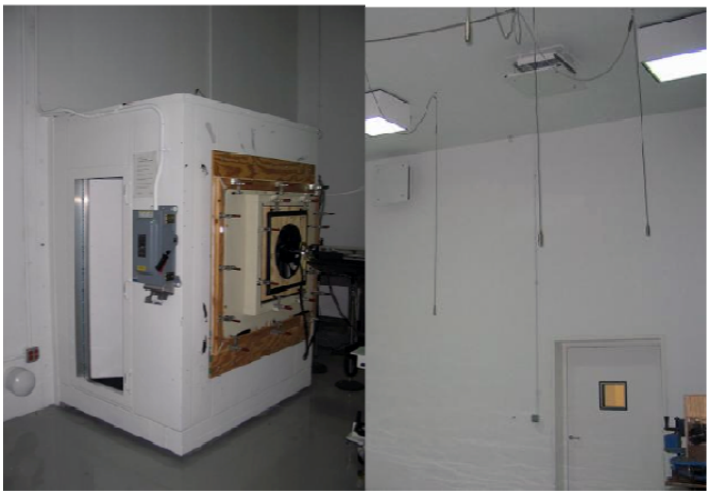

Figure 3.18 Illustration of the Valeo flow facility (left) and reverberant room (right).

Another configuration investigated in the course of this study was designed by Magne [Magne, 2015; Magne *et al.*, 2014] during his PhD. Contrary to the free-field plenum configuration, the fan was inserted in a duct assembly similar to those used for the USI7 and Bosch fans, as shown in Fig. 3.19(a), complete with an inlet bellmouth to insure a smooth inflow profile and a sliding 90^o opening conical termination plug used to control the flow rate through the system. In Magne's study, who studied the control of blade passing frequency tones in axial fans, a stator was specifically designed to increase the tonal noise level. However, for the current study, a stator designed to avoid exciting the BPF tones was designed in order to make it possible to study tip clearance noise mechanisms. This setup was tested in the fully anechoic wind tunnel outflow chamber at the Université de Sherbrooke. Both aerodynamic and aeroacoustic measurements were carried out concurrently on the same setup in the course of the experiments.

In order to measure flowrate, a Prandtl probe tube was used to measure the velocity profiles through the opening between the conical plug and the duct exit wall. The probe

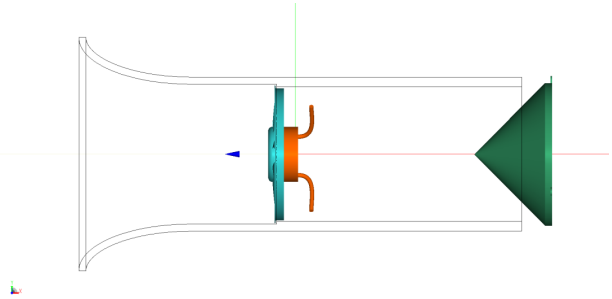

(a)

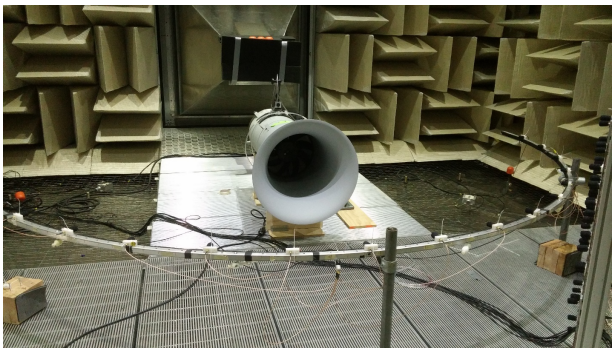

(b)

Figure 3.19 Illustration of the H380 test rig for the ducted configuration (a) Numerical model of the duct assembly with the H380 rotor, stator and conical plug presented in solid (b) Test rig in the anechoic wind tunnel chamber, with the semi-circular microphone array used for acoustic measurements visible in the forefront.

was mounted on a motorized micrometer screw to allow for accurate positioning and it was carefully aligned with the exiting flow; an assumption of axisymetric flow was made to calculate the flow rate. The outflow measurement rig is illustrated in Fig. 3.20. Additionally, a series of 5 pinholes equally spaced azimuthally on the duct wall and located 150 mm behind the fan were used to measure the average static pressure rise relative to the ambient atmosphere using an oil manometer.

Finally, a series of 19 half-inch Bruel et Kjaer type 4190 microphones were used in a semi-circular array, as shown in Fig 3.19(b), to measure the noise emissions upstream of the test rig. The array was centered on the fan and had a radius of 1.9 m.

3.4.2 Mahle-Behr Ring-Shrouded Fan

The second ring-shrouded fan investigated in this thesis is the aforementioned Mahle-Behr engine cooling fan, illustrated in Fig. 3.21 as installed on the engine cooling module

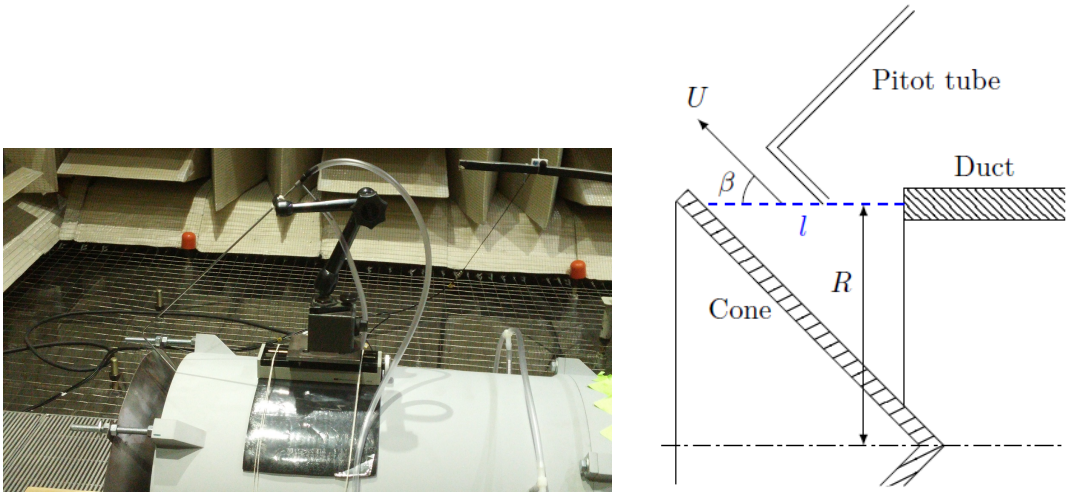

(a) (b)

Figure 3.20 Flow metering Prandtl probe setup for the H380 duct configuration (a) experimental setup (b) schematic view of the pitot configuration with regards to the duct termination plug.

(Condenser, Radiator and Fan Module, CRFM). The rotor has a similar design to the previously described H380 Valeo rotor, with the same L-shaped tip clearance channel configuration, but possesses only 7 blades. Other than the rotational speed of 2535 RPM, however, the specific data pertaining to the tip gap clearance, diameter, flow rate and pressure rise cannot be disclosed here due to confidentiality. The fan was tested using two separate rigs for aerodynamic performance and acoustic emissions internally at the then Delphi Luxembourg plant, now Mahle-Behr.

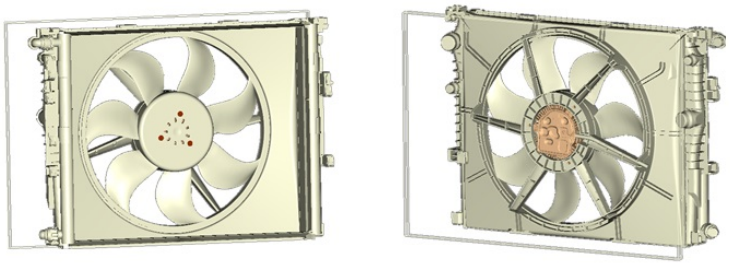

(a) (b)

Figure 3.21 Mahle CRFM geometry (a) View from upstream (b) View from downstream

As reported by Piellard et al. [Piellard *et al.*, 2013] the CRFM was subjected to aerodynamic testing using different fan geometries on an AMCA 210-07 compliant rig (see Fig. 3.22) for a zero pressure rise (free-flow condition) across the fan plane. The complete

engine cooling module constituted of the fan, the electrical motor, shroud as well as all heat exchangers was mounted on the plenum wall for testing. The obtained flowrates from the calibrated nozzles compared well to the LBM simulation flowrates achieved for the transparency condition across all tested geometries, to within 3%; the details of the simulation setup will be discussed in chapter 5.

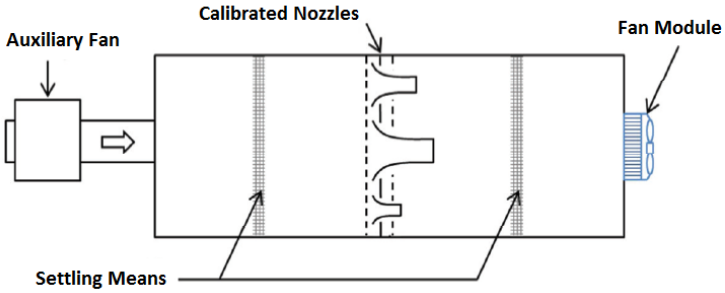

Figure 3.22 Schematic representation of the AMCA test rig used for the Mahle fan tests.

The acoustic emissions by the fan were also measured in a semi-anechoic chamber environment using a 20 microphone array arranged in 4 rows of 5 microphones (Brüel & Kjaer type 4190 and G.R.A.S. 46AE 1/2" microphones). The microphone array is centered on the fan and located 0.5 m upstream of the module. During testing, the CRFM is suspended in the room so that the fan axis is located 0.5 m above the hard floor surface. A wooden plate is also situated behind the module to simulate the proximity of the engine block in a realistic environment. The acoustic test rig is shown in Fig. 3.23.

3.5 Wrap-Up on the Test Cases

The array of low-speed axial fan configurations forming the framework of the current study on the inception of tip clearance flow noise was presented in this chapter; a total of five fan geometries were considered in order to investigate various parameters affecting the formation of tip leakage flow. The first case, the RCDB fan, is a large, free-tipped, tube-axial fan with a low rotational speed (437.22 RPM) and associated blade loading; it was tested in the MSU AFRD facility's plenum test rig. The RCDB blade is a rather simple design, as it was meant to be an academic case study of the Valeo CD airfoil in a rotating frame. A second tube-axial free-tipped fan, the USI7, was also investigated and exhibits characteristics representative of a large swath of mass-produced low-speed fans

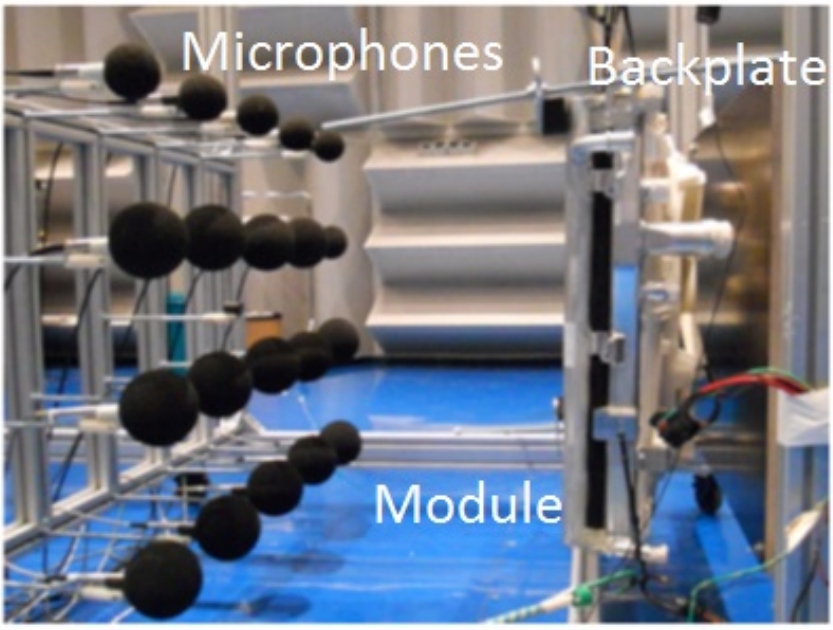

Figure 3.23 Experimental test rig for the Mahle CRFM for the measurement of acoustic emissions.

employed commercially in everyday life applications (e.g. ventilation systems, automotive engine cooling); this fan was tested in a ducted environment experimentally. The last three fan geometries are actual commercial designs employed in automotive engine cooling modules from three different companies (Bosch LLC, Valeo and Mahle-Behr) with similar diameters and operating points. The Bosch design is a free-tipped fan with a convergent tip configuration, as opposed to the previous tube-axial cases; it was also tested in a ducted configuration for performance evaluation purposes. The Valeo and Mahle-Behr fans, however, are ring-shrouded designs commonly seen in automotive engine cooling applications. The Valeo design was experimented on in both plenum and ducted test rigs; it provided an opportunity to investigate the impact of a different installation on the fan operational characteristics, and especially the formation of the tip clearance flow, for similar operating conditions. Finally, the Mahle-Behr design was a little peculias, as it was tested in free-flow conditions, but mounted with the entire cooling module assembly and an approximation of the downstream engine block to investigate installation effects on both the aerodynamic and aeroacoustic performance of the fan.

Three rather different global tip clearance configurations in axial fans are represented among the five geometries: 1) a typical annular clearance, which is observed in the RCDB and USI7 fans 2) a variable radius tip clearance gap, observed in the Bosch design 3) L-shaped tip clearance gap associated with rotating ring-shroud fan configurations, observed

on the Valeo H380 and Mahle fans. All cases considered exhibited a constant clearance (not unique across the configurations however) along the chord of the blades. The USI7 configuration furthermore investigated the influence of the size of the tip clearance gap on the formation of tip leakage flow noise. A large variety of differing installations are also indirectly investigated across all the geometries, with some specific configurations complicating things with regards to the evaluation of tip leakage flow noise because of interfering acoustic propagation mechanics as it will be shown in Chaps. 5 and 6.

The influence flowrate throttling has on tip clearance flow formation was also investigated numerically on the RCDB and USI7 test cases.

The LBM computational method was chosen for this study due to several factors: 1) the capacity of the method to properly simulate the aerodynamic performance of turbomachinery in realistic setups as well as the associated propagation of acoustic waves for low-speed flows 2) given the fact that tip clearance flow is essentially an unsteady phenomenon and that correlation analysis techniques appear to be key in properly analyzing its aerodynamic and acoustic impacts, as it was mentioned at the end of Chap. 2, a requirement of the simulations was that it be able to provide ample physical simulation time to allow for accurate assessments; in that regard, the LBM stands alone with its ability to rapidly simulate several seconds of physical time on complex configurations when compared to traditional Navier-Stokes CFD methods 3) for the study to serve as a test-bench for the application of the LBM towards the investigation of a still ill-understood and complex flow problematic. For those unfamiliar with the LBM class of flow simulations, a brief primer is presented in the next chapter, including a comparison with the aforementioned more *traditional* CFD methods. Since the heart of the problem that this study seeks to address is fundamentally acoustic in nature, the chapter also touches on the subject of computational aeroacoustics (CAA).

CHAPTER 4

Numerical Methods

4.1 Context

The previous chapter presented the quintet of low-speed fan geometries selected for the current tip leakage flow noise study. It was also mentioned that the LBM was selected for the numerical study, on the basis of results from other research on low-speed fans and the ability of this simulation method to carry out direct acoustic simulation in complex geometries including the actual experimental setup. An overview of CFD simulation methods with an emphasis on the presentation of the LBM is presented in this chapter.

Auxiliary methods for the computation of aeroacoustic effects are also briefly presented in this chapter, as other Computational Aeroacoustics (CAA) methods aside from direct acoustic simulation were also used to study the aforementioned geometries.

4.2 Equations Governing Fluid Flow

The fundamental physics of fluid flow are governed by a well-known series of continuum equations called the Navier-Stokes (NS) equations. They are the basis for the current knowledge possessed by the scientific community in the field of fluid mechanics and aeroacoustics alike. They describe the dynamics of 3D compressible, unsteady and viscous fluid flow through three equations describing the conservation of mass, momentum and energy in the system. The instantaneous conservation of mass is described by the differential continuity equation, shown using Einstein's notations in the conservative form

$$\frac{\partial \rho}{\partial t} + \frac{\partial (\rho u_i)}{\partial x_i} = 0 \tag{4.1}$$

with ρ the fluid density, $u_i, i = 1, 2, 3$ the fluid velocity components in 3D space, $x_i, i = 1, 2, 3$ the spatial coordinates and t the time. The momentum conservation equation is in

turn decribed by Eq. 4.2 describing the changes in momentum of a fluid element in space and time

$$\frac{\partial(\rho u_i)}{\partial t} + \frac{\partial(\rho u_i u_j)}{\partial x_j} = -\frac{\partial p}{\partial x_i} + \frac{\partial \tau_{ij}}{\partial x_j} \tag{4.2}$$

where the additional variables p describing the static pressure of the fluid and τ_{ij} the viscous stress tensor of the fluid are the driving forces of momentum changes. For a Newtonian fluid, the viscous stress tensor is itself described as

$$\tau_{ij} = \mu(\frac{\partial(u_i)}{\partial x_j} + \frac{\partial(u_j)}{\partial x_i}) + \lambda(-p\delta_{ij}) \tag{4.3}$$

with δ_{ij} representing the Kroenecker Delta function. The parameters λ and μ are the Lamé coefficients used in continuum mechanics. In the case of a Newtonian fluid, the parameter μ is the dynamic fluid viscosity and is related to the λ value through the Stokes hypothesis that at rest the stress is equal to the hydrostatic pressure, hence $2\mu + 3\lambda = 0$. Finally the energy conservation equation can be written as

$$\frac{\partial(\rho E)}{\partial t} + \frac{\partial(\rho E u_i)}{\partial x_i} + \frac{\partial(p u_i)}{\partial x_i} - \frac{\partial \tau_{ij} u_i}{\partial x_j} = -\frac{\partial q_i}{\partial x_i} \tag{4.4}$$

where E is the total energy of the fluid and q_i is the heat flux parameter, which is a function of the spatial distribution of static temperature. The equations thus defined cannot be solved directly, and as of yet it hasn't been proven that solutions do exist and are unique in the general case; the answer to that question is subject to a 1M$ prize by the Clay Mathematical Institute [1]. In practice, however, the equations can be solved using spatial and temporal discretization schemes numerically, which is the field of application of Computational Fluid Dynamics (CFD) methods.

There exists several CFD methods, however, and it becomes important to be able to choose a suitable method that would allow to capture the highly unsteady and turbulent flow features associated with tip clearance flow in order to be able to capture the associated aeroacoustics. In this section, an overview of the more classical CFD methods encoutered in current numerical simulations is proposed (Reynolds-Averaged Navier Stokes, Large Eddy Simulation and Direct Numerical Simulation), with emphasis on a more recent method named the Lattice-Boltzmann Method, which was introduced in chapter 2 that

1. http://www.claymath.org/millennium-problems

has seen heavy development in the past 20 years and is showing great promise as a powerful CFD tool, especially in the field of direct acoustic simulations at low Mach number which is of particular interest when trying to investigate noise mechanisms from low-speed rotating machinery.

4.2.1 Reynolds Averaged Navier-Stokes (RANS)

RANS simulations are based on the ergodic hypothesis that any instantaneous flowfield can be decomposed in two separate components, namely a mean ensemble-averaged flow $\overline{u}_i$ and a series of highly unsteady flow perturbations u'_i. This, however, results in an open equation system, as the so-called Reynolds stress tensor $\overline{\rho u'_i u'_j}$ being created by the fluctuating flowfield components is impossible to resolve directly and is only created as a result of modelization of the flow components into mean and fluctuating fields. Turbulence models are used to close the system and resolve the Reynolds stress, thus allowing to solve the flowfield [Groth, 2010]. This modelization, however, comes with a price, as turbulence models are manifold and are often based on theoretical and empirical studies and are often tuned to particular flow solutions, thus including an additional uncertainty in the resulting flowfield calculations, as it can dictate the topology of the global solution.

While the RANS approach in its initial form is stationary, there is an unsteady form of the RANS equations where the mean flow component maintains a temporal dependance and is marched in time. It is commonly refered to as URANS for Unsteady-RANS.

4.2.2 Large Eddy Simulation (LES)

LES calculations are based upon the idea that the larger scales of turbulence in a flow are the main source of energy and must be resolved through the spatially filtered Navier-Stokes equations as they are dependant on the modeled geometry and the overall nature of the flow. The turbulent scales smaller than the filter size are considered to be a byproduct of the larger scales, draining the energy from them, and can hence be modeled as they are considered to have a more homogeneous and isotropic universal behavior. LES simulations are in essence transient, as opposed to the ensemble-averaging performed in RANS calculations. However, the grids required to resolve enough of the turbulence to obtain a suitable solution are finer than those for RANS simulations for a given application. It is widely acknowledged that the computing power needed for a calculation grows with the Reynolds number as Re^2 [Pope, 2000]; as an indication, most of the fans considered as test cases in Chap. 3 exhibit a Reynolds number based on chord Re_c of around $5x10^5$. The number of

required grid points can also be evaluated as being proportional to $N_{WM,LES} \sim Re_c$ for a wall-modeled LES, but this number quickly jumps to $N_{WR,LES} \sim Re_c^{13/7}$ in cases when a wall-resolved model is required according to Choi and Moin [Choi and Moin, 2012], who revisited previous estimates made by Chapman [Chapman, 1979]. For the Re_c range of interest in this study, this strikes somewhere in the ballpark of $N_{WM,LES} \sim 5x10^5$ and $N_{WR,LES} \sim 3.84x10^{10}$. However, the transient nature of the calculations allows for the resolution of the instantaneous flowfield and provides, in the case of aeroacoustic applications for example, pressure fluctuations in the flowfield and consequently allows the evaluation of sound propagation on a proper grid. The subgrid scale models that are used to solve the smaller scales of turbulence in the flow are however still semi-empirical models and must be carefully selected for a given application.

4.2.3 Direct Numerical Simulation (DNS)

In DNS calculations, all scales of the flowfield are resolved through the Navier-Stokes equations, including all turbulence scales. The number of scales to be resolved grows exponentially with the Reynolds number of the flows involved; for a 3D simulation, the number of grid points needed N is approximately given by $N_{DNS} \sim Re_c^{37/14}$, which for the Reynolds values of $5x10^5$ encountered in this study yields $N_{DNS} \sim 1.15x10^{15}$ [Choi and Moin, 2012]. In addition, the time steps must be adjusted to resolve the different scales, resulting in the number of operations and hence required computing power growing as a function of Re^3 based on an analysis of the Kolmogorov scales [Coleman and Sandberg, 2010; Rogallo and Moin, 1984; Tennekes and Lumley, 1972]. The critical timestep value also scales with the Mach number through a CFL condition to ensure numerical stability when acoustic waves are concerned [Volpe, 1993]. Hence, typical usage of DNS simulations is often restricted to relatively simple flow calculations at low Reynolds (airfoils, $Re_c \sim 2 - 3x10^5$ for state-of-the-art calculations) and turbulence research for the development of turbulence models for RANS and LES simulations. However, as the computing power capabilities of modern computers grow, it is not impossible that we should see the advent of DNS simulations becoming the norm for the modelization of typical real life applications such as turbomachinery in our lifetime.

4.2.4 Lattice-Boltzmann Method (LBM)

The LBM is a different class of CFD tool when compared to the classical CFD trifecta (RANS, LES and DNS), as it does not rely on the discretization of the Navier-Stokes equations but rather on the statistical distribution of particles in a given fluid and their

interaction derived from the original equation proposed by Boltzmann in 1872 (commonly referred to as the Boltzmann equation).This highlights a fundamentally different approach to the resolution of the flowfield, as we are no longer trying to resolve directly the main flow features (density, velocity and pressure) but are rather trying to get the layout and calculate the probability density function of the velocity of groups of particles in the fluid, from which the macroscopic properties can be calculated.

This CFD method is relatively new even though the basic equation has been known for more than 100 years; the development of the equations using a proper collision model in such a way that the Navier-Stokes equations could be recovered (Chapman-Enskog) didn't come until the mid-1910s whereas the more current lattice Boltzmann models didn't arrive until the beginning of the 1990s. Those interested in the more detailed developmental chronology of the LBM are referred to Marié's work [Marié, 2008].

In the next section a brief overview of the development of the LBM from the Boltzmann equation is presented.

4.3 Presentation of the Lattice-Boltzmann Method

As exposed before, the lattice-Boltzmann method uses a fairly different approach compared to the traditionally used NS codes (RANS, LES, DNS) currently currying favor in the industry, basing itself on probabilistic physics rather than on a discretization of the continuum Navier-Stokes equations. This section of the thesis is meant to provide a summary of the method and is by no means an exhaustive presentation of the subject; for a more complete overview of the subject, the reader is directed to Chen and Doolen's work for example [Chen and Doolen, 1998].

Drawing from kinetic dynamics, the lattice Boltzmann equation is derived from the continuous Boltzmann equation which can be written as

$$\frac{\partial f}{\partial t} + c_i \frac{\partial f}{\partial x_i} + \frac{F_i}{m} \frac{\partial f}{\partial c_i} = \left(\frac{\partial f}{\partial t} \right)_{coll} \tag{4.5}$$

where $f = f(\vec{x}, \vec{c}, t)$ is the probability density function of particle velocities at spatial coordinates $\vec{x}$ and time t possessing a speed $\vec{c}$, F_i corresponds to external forces and m is the molecular weight of the gas considered. The term $\left(\frac{\partial f}{\partial t}\right)_{coll}$ in Eq. 4.5 is the collision term describing the interaction of the particles. The collision operator, describing elastic collisions between the particles, must therefore satisfy the conservation of mass,

momentum and kinetic energy of the particles during the collision itself. A simple operator being used in current models is the Bhatnagar-Gross-Krook (BGK) collision operator ([Bhatnagar *et al.*, 1954]), given by

$$\left(\frac{\partial f}{\partial t}\right)_{coll,BGK} = -\frac{1}{\tau}[f - f^{eq}] \tag{4.6}$$

where τ is a relaxation time parameter and f^{eq} is the thermodynamic equilibrium distribution function known as the Maxwell-Boltzmann distribution.

However, the direct resolution of the continuous Boltzmann equation and its collision operator, as with the Navier-Stokes equations, is still a daunting task, as it requires the integration of a function of 6 variables (3 spatial coordinates and 3 velocities) in a 3D space and a relatively complex collision operator. In 1964, a discrete velocity model was proposed by Broadwell [Broadwell, 1964] in the form of a 3D model with 8 discrete velocities. He and Luo [He and Luo, 1997], in 1997, presented a formal method to obtain discrete velocity models from the Boltzmann-BGK equation, also presented in [Marié, 2008]. The recent versions of the commercial LBM solver PowerFLOW uses a more recent model initially presented by Qian [Qian *et al.*, 1992], which is a 3D isothermal model with 19 discrete velocities on a cubic lattice (D3Q19). The performances of the D3Q15 , D3Q19 and D3Q27 models were evaluated by Mei et al. [Mei *et al.*, 2000] on several simple fluid flow cases; the authors concluded that the D3Q19 model was the better one due to the D3Q15 being prone to computational instability and to the fact that the D3Q27, whilst more complex, do not necessarily provide better flow solutions with equivalent spatial resolution.

The Boltzmann equation (Eq. 4.5) combined with the BGK collision operator in Eq. 4.6 and the discrete velocity model can be processed with a Chapman-Enskog development [Chapman and Cowling, 1990], making it possible to recover the Navier-Stokes equations from Eq. 4.5 in the limit of low Mach numbers [Chen *et al.*, 1992; Frisch *et al.*, 1986] (Mach 0.2 to 0.5 is cited as the limit in the literature); readers interested in the *a priori* development from the Boltzmann equation can refer to Marié's [Marié, 2008] or He and Luo's [He and Luo, 1997] work.

The velocity-discretized form of Eq. 4.5 named the discrete velocity Boltzmann equation (DVBE) with α discrete velocities can be written as

$$\frac{\partial f_\alpha}{\partial t} + c_{\alpha,i}\frac{\partial f_\alpha}{\partial x_i} = -\frac{1}{\tau}[f_\alpha - f_\alpha^{eq}] \tag{4.7}$$

Equation 4.7 can be represented in a space/time first-order discretized form along the particle trajectory ([He and Luo, 1997]) as

$$f_\alpha(x_i + c_\alpha \Delta t, t + \Delta t) - f_\alpha(x_i, t) = -\frac{1}{\tau}[f_\alpha(x_i, t) - f_\alpha^{eq}(x_i, t)] \tag{4.8}$$

Note that the external force term has been removed in equations 4.7 and 4.8 when comparing to the original Boltzmann Eq. 4.5, noting an absence of external forces. However, in order to solve flows with the presence of rotating elements in PowerFLOW, a local reference frame including the fluid around rotating geometrical elements is put into rotating motion with the solid geometry. The result is the modified Eq. 4.8, wherein a pseudo external body force is introduced ([Pérot *et al.*, 2010a])

$$f_\alpha(x_i + c_\alpha \Delta t, t + \Delta t) - f_\alpha(x_i, t) = -\frac{1}{\tau}[f_\alpha(x_i, t) - f_\alpha^{eq}(x_i, t)] + F_\alpha(x_i, t) \tag{4.9}$$

This body force F_α corresponds to the Coriolis, centrifugal and Euler pseudo-forces normally found in a rotating non-inertial reference frame as evidenced in Eq. 4.10 (for more details, see [Guo *et al.*, 2002])

$$F_\alpha(x_i, t) \propto A(x, t) = \overbrace{-\Omega(t) \times (\Omega(t) \times r(x, t))}^{\text{centrifugal}} \overbrace{-2\Omega(t) \times u(x, t)}^{\text{Coriolis}} \overbrace{-\frac{d\Omega(t)}{dt} \times r(x, t)}^{\text{Euler}} \tag{4.10}$$

The code PowerFLOW also utilizes a modified relaxation time $\tau \rightarrow \tau_{turb}$ derived from the renormalization group $k - \epsilon$ transport equations ([Chen *et al.*, 2003], [Chen *et al.*, 2004]) in order to model the unresolved turbulent small scales in the LBM calculations. This has a direct effect on the viscosity of the fluid, as it can be shown that the kinematic viscosity ν of the fluid is related to the relaxation time as [Li *et al.*, 2004]

$$\nu = (\tau - 1/2)T \tag{4.11}$$

with T the temperature of the fluid. This forms the basis of the LBM as used in the commercial solver PowerFLOW, generating a reliable solver for low Mach flows (under 0.5 is usually considered); using the turbulence modeling, the code behaves as a Very Large Eddy Simulation (VLES) method. The resulting equations are the fruit of the restriction of

particle velocity subspace (D3Q19 model) and proper time/space first-order discretization along the particle trajectory of the Boltzmann equation.

The macroscopic features (density, linear momentum and kinetic energy) of the fluid can be recovered from the particle density distribution function f from the calculation of the first three moments of said equation, as evidenced by relations 4.12, 4.13 and 4.14 below

$$\rho = \int_{\Re^3} f dc \tag{4.12}$$

$$\rho u = \int_{\Re^3} c f dc \tag{4.13}$$

$$\rho e + 1/2\rho|u|^2 = \int_{\Re^3} |c|^2 f dc \tag{4.14}$$

4.4 Computational Aeroacoustics (CAA)

Contemporary research into CFD has given rise to an interest in also computing the sound generation by studied flows. This broad area of research is coined Computational Aeroacoustics (CAA) and covers any and all computational efforts focused at resolving the sound associated with fluid flow, which is a branch in the field of aeroacoustics. Two families of methods exist depending on the strategy used to attain this goal: direct and hybrid approaches.

In this section, a succinct overview of CAA methods is proposed. Complete scientific reviews of CAA can be found in the literature however [Colonius and Lele, 2004; Wang *et al.*, 2006], whereas only broad elements pertinent to a general understanding are presented here.

A specific hybrid method for computing the aeroacoustics of turbomachinery elements, the Ffowcs Williams and Hawkings' analogy, is however presented in more details, as it was used in the course of this study specifically.

4.4.1 Direct Acoustic Simulation

Direct acoustic simulation refers, as the name entails, to computational methods aimed at trying to solve both the aerodynamic unsteady flow features and the generated sound waves concurrently from the basic physical equations of fluid flow. To accurately represent

both the unsteady flow features as well as the resultant sound, a necessary condition to such a simulation requires that the physical domain simulated be as accurate and realistic as possible. This includes both the dynamical flow region, or near-field, where aerodynamic fluctuations occur, as well as what could be referred to as the acoustic radiative region, or far-field, of the domain where the flow is rather quiescent and acoustic pressure fluctuations are propagated.

Secondly, accurate simulation of the flow features requires the use of a high-fidelity compressible CFD method able to resolve the different scales of the unsteady aerodynamic flowfield and propagate the significantly weaker acoustic pressure fluctuations into the far-field. As an indication of the orders of magnitude involved, a very elevated noise level of 120dB (the threshold of pain for the human ear) is equivalent to 20 Pa of acoustic pressure, which is 10 to 100 times weaker than aerodynamic fluctuations caused by turbulent eddies in the flow. Thus, the CFD method used needs to display low numerical dissipative and dispersive properties in order to reproduce the acoustics correctly. In practice, this requires a very large, finely meshed simulation domain as well as the use of specific numerical schemes for the discretization of the governing equations of fluid flow. Also, while DNS would be the preferred method to obtain detailed, realistic descriptions of a modeled flow both from an aerodynamic perspective and the resultant acoustics, in practice LES, which resolves only the larger scales of the flow whilst the smaller scales are modeled, is probably the method most likely to be utilized for the foreseeable future as the basis for direct acoustic simulations of realistic (high Reynolds number) flows, as coined by Wang [Wang *et al.*, 2006] due to the restrictions inherent to DNS with regards to required computing power. DNS, however, still represent a powerful tool for the investigation of relatively *simpler* flows.

An alternative emerging right now for complex and large geometries of low Mach number flows is the lattice-Boltzmann method. The performance of the LBM with regards to generation and propagation of acoustic waves has been the subject of recent studies, as highlighted below.

Direct Acoustic Simulation - Advantages of the LBM Over Classical NS Schemes

The numerical properties of the lattice-Boltzmann method (LBM) have been studied recently by Marié (first in his thesis [Marié, 2008], with the results also reported in [Marié *et al.*, 2009]) and [Brès *et al.*, 2009]. Both studies were focused into analysing the properties of the LBM with regards in particular to acoustic propagation error due to the numerical schemes employed.

[Marié, 2008] first presented the results of a comparison of LBM calculations of a standing planar wave against Navier-Stokes simulations using three centered finite difference (FD) spatial schemes (2^{nd}, 3^{rd} and 6^{th} order) and Runge-Kutta (RK) temporal schemes (3-step RK for the 2^{nd} and 3^{rd} order spatial simulations and 6-step RK for the 6^{th} order simulation). The standing planar wave simulations were run with a quiescent flow condition and with a mean flow with a Mach number of Ma=0.2. He studied the dispersion and dissipation properties of the various schemes.

They observed that the LBM calculations, which are of global 1^{st} order accuracy, offer better dispersion and dissipation than a centered FD 2^{nd} order Navier-Stokes scheme and is actually close to the 3^{rd} order method presented here in terms of dispersion of both the acoustic waves and shear mode. However, at higher $k\Delta x \geq 3\pi/4$, where the number of points per wavelength drops under 2.6, the LBM method shows lower dispersion than all the NS cases due to the inability of the centered schemes to resolve the flow with 2 points per wavelength. Regarding dissipation of the acoustic waves, the LBM performs better than the 6^{th} order NS scheme. It should be noted however that for the quiescent case, the LBM dissipation of the shear mode is still evaluated as being between the 2^{nd} and 3^{rd} order NS schemes whereas for the uniform flow case it shows a slightly higher dissipation of the shear mode than the 6^{th} order NS scheme. They also showed that the LBM calculations are usually faster than the high-order NS schemes when trying to attain a given dispersion error.

Brès *et al.* [Brès *et al.*, 2009] also studied the dispersive and dissipative properties of the LBM in its DNS form and with turbulence modeling (used for high Reynolds number flows) on a planar standing wave test case as well as a Gaussian pulse. His results, similar to those presented for a standing planar wave in quiescent flow [Marié, 2008], showed that the turbulence model did not produce any additional dispersion when compared to the DNS version of the code but that there was additional dissipation, with the dissipation increasing with the size of the voxels used. Brès *et al.* evaluated, however, that using 12-16 points per wavelength would only amount to a 0.068 dB loss per wavelength (1 dB loss at 5 kHz, 1 m away).

Therefore it could be said that while the LBM shows dispersion properties similar to 2^{nd} and 3^{rd} order NS schemes, it shows acoustic dissipation properties that are better or equivalent to a 6^{th} FD centered NS scheme whilst using a more efficient algorithm due to its reliance on 1^{st} order neighbouring cells for calculations (2^{nd} order global accuracy) [Marié, 2008]. While it is not impossible that other types of NS numerical schemes (only explicit centered FD schemes were studied here) or new developments in NS simulation

research should allow for equivalent or better acoustic dissipation than the LBM, it is clear that the LBM shows promise in the field of computational acoustics, for which it was not initially designed.

4.4.2 Hybrid Acoustic Methods

The second category of CAA methods includes what are commonly called *hybrid* methods. Unlike direct acoustic simulation, this family of methods isn't concerned with computing the acoustics concomitantly with the full-scale aerodynamics of the flow in the whole domain of interest. Rather, such methods aim to separate the problem by considering a split-domain approach: a source region where unsteady aerodynamics responsible for the production of flow noise dominate and the more settled surrounding region where mainly acoustic waves are propagated. It relies on the use of accurate methods for modeling the near-field aerodynamic and acoustic fields, but alleviates the need for a large physical region to be accurately modeled and resolved, thus lowering the necessary computational resources. However, in-between direct acoustic simulation and the full-decoupling of the aerodynamic and acoustic portions of the flow, there exists a plethora of methods than can be used.

A first example of such hybrid methods would be the *extension* of the near-field, nonlinear aerodynamic/acoustic field of the *source* into the less-disturbed region in the immediate vicinity using a set of simplified differential equations derived from the fundamental NS equations and a finite element method approach [Marburg and Nolte, 2008]. For example the Euler or Linearized Euler Equations [Bailly and Bogey, 2004; Bogey *et al.*, 2002] or similar Acoustic Perturbation Equations (or their linearized form) [Ewert and Schroeder, 2003; Munz *et al.*, 2007; Seo and Moon, 2006] could be used to solve the acoustic field in the intermediate region between the non-linear aerodynamic domain and the aerodynamically undisturbed far-field using source tems from the accurate high-accuracy aerodynamic simulation of the source flow. This category of methods is especially useful when the acoustic field involves complex solid boundaries and possibly still perturbed flow in the case of an *interior* domain; they provide an acoustic solution for a complex propagation environment one-step removed from direct acoustic simulation with the attached decrease in necessary computational resources.

Another category of hybrid methods, pioneered by Lighthill [Lighthill, 1952, 1954], is dubbed the acoustic analogy. In this category of methods, the NS equations are rewritten in the form of an inhomogeneous wave equation outside a source region, with the source terms derived from the non-linear aerodynamics within this source region as measured

on the control surface. An integral form is obtained using a compact source hypothesis and a tailored Green's function. The original development by Lighthill was concerned with the case of a source region contained in a uniform fluid at rest and used a porous control/integral surface. Curle [Curle, 1955] extended Lighthill's analogy to the case of stationary solid boundary surface sources. Lighthill's and Curle's work were further generalized by Ffowcs Williams and Hawkings (FWH) [Ffowcs Williams and Hawkings, 1968] to take into account moving boundary surfaces (and sources) in a uniform medium. This last analogy is of particular interest in the case of turbomachinery, as the primary noise sources (rotor blades) are in motion and will be presented in more detail in the following section.

However, acoustic analogy formulae are of specific interest when the Green's function is analytically derivable (typically the free-space form will be used); in the case of complex propagation domain, including the effects of solid boundary walls for example, the use of a numerical method to compute the Green's function is necessary. The Boundary Element Method [Kirkup, 2007; Marburg and Nolte, 2008] can thus be used to solve the wave-form equations spawning from acoustic problems.

Yet another integral formulation would be the Kirchoff method [Lyrintzis, 1994, 2002], which uses the simple linear wave equation as a basis. In contrast to the more general acoustic analogy formulations, it then requires all of the non-linear flow region to be included in the control surface. Developments made to the original Kirchoff method also allow for moving surfaces to be taken into account.

Ffowcs Williams and Hawkings Analogy

The FWH analogy based on Farassat's 1A formulation of the FWH equation [Brentner, 1986; Farassat, 2007; Farassat and Succi, 1980; Ffowcs Williams and Hawkings, 1968] is covered here. As explained above, it fits a special purpose in the case of acoustic problems in turbomachinery applications, where the main sources of noise are located on the rotor blades most often. The formulation supposes a permeable surface $f(x,t) = 0$ with outward surface normal $\hat{n} = \nabla f$. The surface encloses a volume V defined by $f(x,t) < 0$. The surface is defined as having a certain velocity in 3D space.

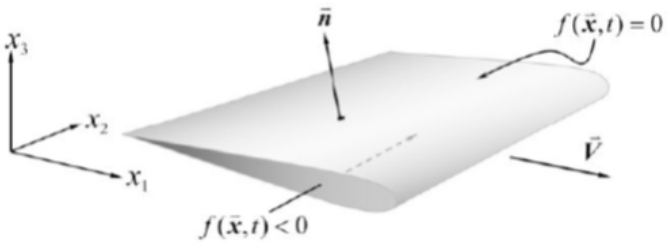

Figure 4.1 Representation of a possible permeable moving surface $f(x,t)=0$ in the FWH equation. [Farassat, 2007]

The original FWH equation is given here as

$$\Box^2 c^2(\rho-\rho_0) = \frac{\partial}{\partial t}[Q_n\delta(f)] - \frac{\partial}{\partial x_i}[L_i\delta(f)] + \frac{\partial^2}{\partial x_i x_j}[T_{ij}H(f)] \tag{4.15}$$

with the components Q_n and L_i defined as

$$Q_n = [\rho_0 v_i + \rho(u_i - v_i)]\hat{n}_i \tag{4.16}$$

and

$$L_i = [(p-p_0)\delta_{ij} - \tau_{ij} + \rho u_i(u_j - v_j)]\hat{n}_j \tag{4.17}$$

In Eq. 4.15, the notation $\Box$ is the d'Alembert wave operator ($\Box = (1/c^2)(\partial^2/\partial t^2) - \nabla^2$), u_i is the fluid velocity at the surface, v_i is the surface velocity, c is the speed of sound, ρ is the fluid density, p the pressure, T_{ij} is Lighthill's stress tensor and τ_{ij} is the shear stress tensor. The functions δ and H represent the Dirac delta and Heaviside functions whilst δ_{ij} is the Kronecker delta function.

The τ_{ij} term is usually neglected from the L_i term [Brès *et al.*, 2010; Farassat, 2007; Ffowcs Williams and Hawkings, 1968]. The three terms from Eq. 4.15 can be respectively identified as thickness noise (monopolar source), loading noise (dipolar source) and the quadrupolar source term containing all the non-linearities from the flowfield. A specific case of the FWH equation occurs when the permeable surface is set to correspond to a solid boundary wall; in that case the equality $u_i = v_i$ simplifies the equation.

For the solid formulation, the Exa suite uses, as mentioned before, Farassat's 1A formulation of the FWH equation. The complete development is quite lengthy and not reproduced here; the reader is directed to Farassat's and Brentner's work for full reference [Brentner, 1986; Farassat, 2007; Farassat and Succi, 1980; Ffowcs Williams and Hawkings, 1968]. The formulation is concerned with the calculation of the acoustic pressure radiated from the source region. It uses a free-field Green's function for a quiescent medium to solve the wave equations for the monopolar and dipolar terms whilst neglecting the quadrupolar source term from the FWH equation. The acoustic pressure p' is thus given at an observer position $\mathbf{x}$ from the source terms emanating at position $\mathbf{y}$ from the monopolar (thickness, T) and dipolar (loading, L) terms in Eq. 4.18;

$$\begin{aligned} 4\pi p'_T(\mathbf{x},t) = \int_{f=0} [\frac{\rho_0 \dot{v}_n}{R(1-M_r)^2} + \frac{\rho_0 v_n \hat{r}_i \dot{M}_i}{R(1-M_r)^3}]_{ret} dS \\ + \int_{f=0} [\frac{\rho_0 c v_n (M_r - M^2)}{R^2(1-M_r)^3}]_{ret} dS \end{aligned} \tag{4.18}$$

$$\begin{aligned} 4\pi p'_L(\mathbf{x},t) = \int_{f=0} [\frac{\dot{P} cos\theta}{cR(1-M_r)^2} + \frac{\hat{r}_i \dot{M}_i P cos\theta}{cR(1-M_r)^3}]_{ret} dS \\ + \int_{f=0} [\frac{P(cos\theta - M_i \hat{n}_i)}{R^2(1-M_r)^2} + \frac{P cos\theta (M_r - M^2)}{R^2(1-M_r)^3}]_{ret} dS \end{aligned} \tag{4.19}$$

Where v_n is the surface velocity aligned with the local normal vector, $\hat{r}_i$ is the component of the unit radiation vector ($\mathbf{x}$-$\mathbf{y}$)/R, M_i is i^{th} component of the Mach number of the source, P is the gauge pressure at the surfaces, θ is the local radiation angle defined by $cos\theta = \hat{n}_i \hat{r}_i$ and the relative Mach along the radiation direction is given by $M_r = M_i \hat{r}_i$. The $[]_{ret}$ notation indicated that contribution is evaluated at the source *retarded* time. The acoustic pressure is thus defined as the sum of the two contributions as

$$p'(\mathbf{x},t) = p'_T(\mathbf{x},t) + p'_L(\mathbf{x},t) \tag{4.20}$$

A special formulation of the FWH equation which is suited for example for wind tunnel applications wherein both observer and source are stationary but immersed in a uniformly moving medium. The formulation can be recovered by redeveloping the original FWH equation [Najafi-Yazdi *et al.*, 2010] or by retaking formulation 1A but considering now the

observer and source to be moving at constant speed in a quiescent medium, modifying the thickness and loading terms as well as the radiative distance [Wells and Han, 1995].

It can also be recovered by solving the convective wave equation [Najafi-Yazdi *et al.*, 2010], leading to the convective FWH equation, and using a convective Green's function. The formulation presented by Najafi-Yazdi et al., which includes source motion, is shown to recover Farassat's 1A formulation with a quiescent medium. The wind tunnel formulation is obtained by setting the source and observer at rest, thus negating all temporal derivatives.

The source terms are evaluated using an advanced time approach [Brès *et al.*, 2010; Casalino *et al.*, 2003], taking advantage of the regularly sampled numerical data measured at the retarded time τ_{ret}. The acoustic pressure is then propagated into the farfield to designated observer points at a time t. This will likely result in unevenly spaced observer time; this is resolved by using interpolation of the given pressure signal at the observer to restore the received signal sampling rate to that of the source term.

4.5 Conclusion on Numerical Methods

The present chapter was aimed at presenting the framework of numerical methods available for the purpose of carrying out the aeroacoustic investigation proposed in this document. It showed that while direct acoustic simulations should be sought after, they are impractical using standard true unsteady Navier-Stokes methods (LES, DNS) for high Reynolds number applications and particularly complex environments for the moment due to the required computational power. However, such simulations in which the near-field (i.e. acoustic sources) is properly resolved can be coupled with propagative models to create so-called *hybrid* CAA methods to alleviate the required calculation effort.

It was also shown that an emerging CFD tool, the lattice-Boltzmann method, shows significant promise for direct acoustic simulations in complex environments such in the case of low Mach number flow simulations and was chosen as the numerical investigation tool for the purposes of the current study into tip leakage flow noise. The ability of the LBM to accurately predict the acoustic signature for a given case, however, is reliant on the proper prediction of the aerodynamic field first and foremost. In the next chapter, a thorough investigation of the performance of the LBM for the simulation of the selected test cases will be shown, both from an aerodynamic and aeroacoustic point of view.

CHAPTER 5

Validation of Simulation Cases

5.1 Context

Chap. 3 presented the turbomachinery test cases selected for the current study of tip leakage flow noise. As well, the properties proposed numerical method for the numerical investigation, namely the lattice-Boltzmann method, was described in Chap. 4 along with other methods for CAA. One of the main advantages of this simulation method is that it allows for the resolution of both the aerodynamic and the direct far-field aeroacoustic field simultaneously on realistic representations of complex geometries. This paves paving the way for a more complete aeroacoustic investigation of complex geometries without the need for broad simplifications necessary using typical CFD methods and the use of hybrid acoustic methods for the propagation of sound. This is especially useful when trying to evaluate installation effects on the acoustic footprint of turbomachinery applications.

However, before going forward with a detailed aeroacoustic investigation of the noise sources on the basis of simulations, it is important to validate the numerically predicted performance against their experimental counterparts which were described in Chap. 3. The test cases selected for this study were in part chosen on the merits of the available experimental database for each of the geometries to compare the LBM simulations. The current chapter is aimed at presenting the results of this validation effort for each of the previously presented geometries. The simulations were compared against their respective experiments from both the aerodynamic and aeroacoustic points of view.

5.2 Technical Considerations for the Validation of Turbomachinery Simulation Cases

With the avowed goal of the current chapter being the validation of the LBM simulations used to model the various turbomachinery test cases detailed in Chap. 3, it was deemed necessary to formally detail some of the terms and post-processing techniques employed in the following sections. This is to provide a certain level of transparency as to the definitions and methods utilized and eliminate any ambiguity.

5.2.1 Dimensionless Coefficients for the Characterization of Turbomachinery

As the chapter primarily deals with the characterization of turbomachinery, the introduction of the dimensionless coefficients that can be derived formally derived using the Π-theorem for the description of turbomachine performance becomes necessary. Their form depends on the choice of the initial variables and thus a large range of minute variations can be found in the coefficients used in different studies. They are used to present the typical characteristics of a turbomachine (e.g. flowrate, pressure rise) in a normalized form, allowing for the comparison of machines with different operating points and sizes. The form of the flow and pressure coefficients used in the course of this study is shown in Eqs 5.1 and 5.2.

$$\phi = \frac{Q}{\omega(D^3/2)} \tag{5.1}$$

$$\psi = \frac{\Delta p}{\rho(\omega D/2)^2} \tag{5.2}$$

With the flowrate Q in cubic meters per second, the diameter of the fan D in meters and the rotational speed of the rotor ω in radians per second. These dimensionless coefficients can be used to define scaling laws for *similar* machines (i.e. constant coefficient value) and evaluate for example the expected performance of a given fan if the rotational speed is modified, assuming a *similar* flow behavior. Typically, measuring the performance curves of a given machine according to variations in the rotor speed and plotting the results in normalized (ϕ, ψ) form will yield a collapse of the curves into a single curve assuming the machine stays in a more or less stable operating range.

In addition to the aforementioned similitude coefficients, another dimensionless factor of importance is the wall-pressure coefficient C_p, which is used to normalize the pressure on aerodynamic surfaces with the dynamic pressure of the surrounding flow, and is defined as shown in Eq. 5.3.

$$C_p = \frac{p - p_{ref}}{0.5\rho_{ref}V_{ref}^2} \tag{5.3}$$

The variables p_{ref}, ρ_{ref} and V_{ref} are the reference pressure, fluid density and velocity respectively. In the case of turbomachinery, the reference pressure will often be taken to

be the absolute pressure downstream of the fan or the ambient value. The fluid density and velocity will be evaluated in the flow surrounding the rotor blades, with the velocity measure in the rotating frame of reference fixed with the blade.

5.2.2 Spectral Analysis

The results presented in this chapter involve a fair amount of spectral analysis involving timeseries. All frequency domain post-processing is done using Welch's modified periodogram method for the estimation the power spectral density (PSD) of a temporal signal [Welch, 1967] included in the *Matlab* signal processing toolbox (function *pwelch* for power spectral density S_{xx} of a single signal and *cpsd* for the cross-power spectral density S_{xy} between two signals). The timeseries segments are windowed using a Hanning function with a 50% overlap between the segments. The length of the segments is adjusted on a case by case basis to obtain a suitable frequency resolution for the different cases covered depending on the sampling frequency; the resolution is specified for each presented spectra in the figure caption throughout this document.

The PSD (or CPSD) level in decibels is calculated as in Eq. 5.4

$$PSD_{dB}(f) = 10\ \log_{10}\left(S_{xx}(f) * \Delta f_{ref}/p_{ref}^2\right) \tag{5.4}$$

Where the standard acoustic reference pressure $p_{ref} = 2 \times 10^{-5}$ Pa is used throughout this document unless otherwise specified and the reference frequency band Δf_{ref} is set to 1 Hz.

The acoustic sound power level SWL through a virtual surface A is calculated from the estimated PSD spectra as in Eq. 5.5

$$SWL_{dB}(f) = 10\ \log_{10}\left(\frac{\Delta f_{PSD}}{\rho_0 c_0 W_{ref}^2}\int S_{xx}(f)dA\right) \tag{5.5}$$

With ρ_0 the fluid density in kilograms per cubic meter, c_0 the velocity of sound in the fluid, Δf_{PSD} the frequency resolution of S_{xx} (or S_{xy}) and W_{ref} the reference acoustic power (1×10^{-12} W). This metric was required in part to compare numerical results against some experimental data for which only acoustic power measurements were made available. Acoustic power measurements are usually carried out to do away with observer dependant variations in the measured spectra. In the current work, however, the *raw*

noise estimates obtained using the power spectral density spectra of the acoustic signals at given points in space are preferred as a metric for the evaluation of the direct acoustic prediction capabilities of the LBM method.

5.3 RCDB

5.3.1 Presentation of the Numerical Setup

The numerical simulation for the RCDB test fan was made to mimic the experimental conditions of the AFRD facility previously presented in Sec. 3.2.1, where the fan is mounted on the ceiling of a large plenum chamber, with the air being taken from the surrounding room where the fluid is at rest. The simulation case is based on a previous study by Pérot et al. [Pérot *et al.*, 2010b] of the RCDB geometry. The simulation domain, shown in Fig. 5.1, is 130 X 130 m in width and 65 m in height in total. The side walls and ceiling have static pressure freeflow boundary conditions imposed to represent a large quiescent room, whilst a solid wall condition is imposed to represent the plenum surfaces and the *floor* surface. The test plenum inlet is centered along the width of the simulation domain. A wireframe view of the plenum volume is shown in Fig. 5.1, with the fan also visible as a solid in the inlet duct. The flow rate through the system was regulated through the use of an outflow boundary condition at the exit surface of the outlet duct. Two types of boundary conditions were tested in the course of this study to investigate the effect of the performance of the simulation: a mass-flow boundary condition, as with the study by [Pérot *et al.*, 2010b] and a velocity outlet condition. Damping regions are defined in the outlet duct to try and avoid acoustic reflections.

The simulation domain is discretized in the LBM code PowerFLOW using a structured grid composed of several imbedded Variable Resolution (VR) regions; the mesh resolution around the RCDB fan is 1 mm (VR10), with the VR region envelopping the fan geometry. The mesh resolution decreases two-fold in each subsequent adjacent region to the edge of the simulation domain. A rotating local reference frame (LRF) is defined within the VR10 region, encompassing the fan blades and hub; the reference frame cuts off at half of the tip clearance gap, leaving the shroud wall in the inertial frame of reference.

In order to monitor the simulation from both an aerodynamic and aeroacoustic perspective, a series of measurement points were setup. For the aerodynamic performance evaluation, a series of 4 probes was included at the 4 opposite corners of the plenum along its centerline to monitor the pressure inside the chamber; the probes are located 0.8 m from the fan

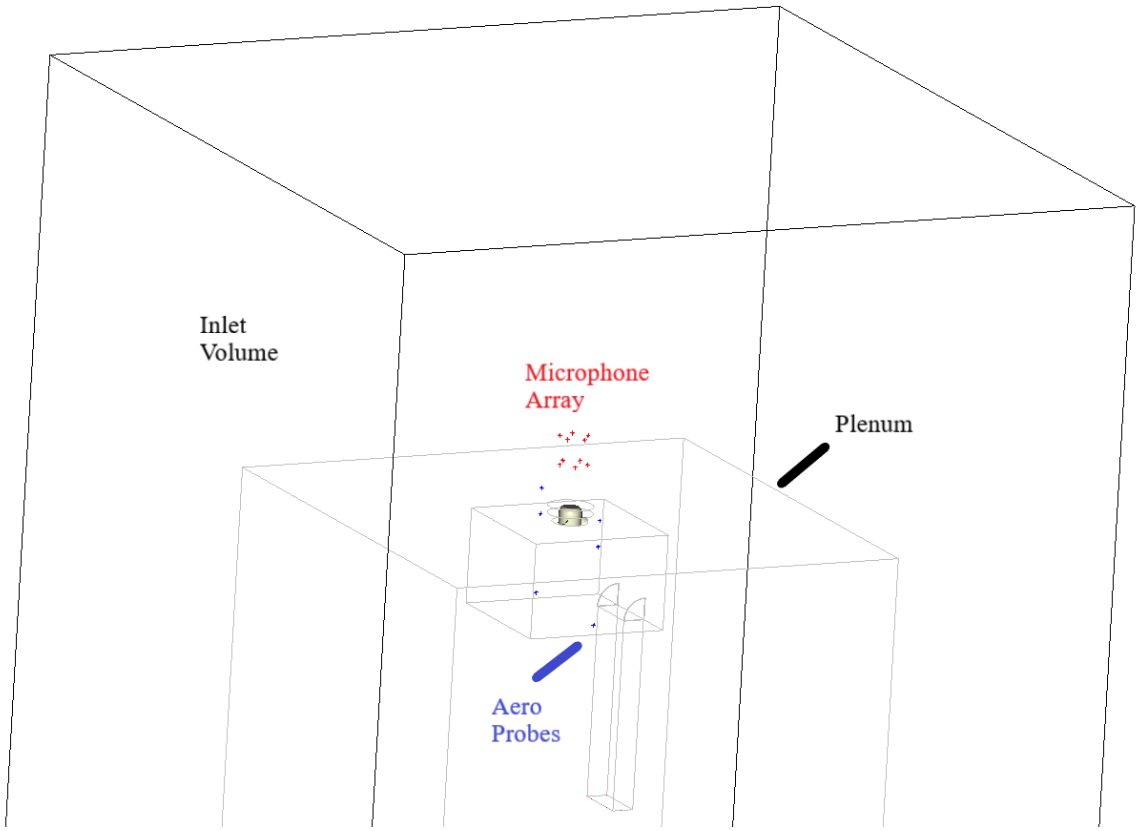

Figure 5.1 Computational domain for the RCDB in the AFRD facility; not to scale.

axis, with one pair located 150 mm behind the fan and the second at 1800 mm. Two additional probes situated 180 mm over the plenum wall upstream of the fan were used to monitor the pressure in the room.

Additionally, a series of 10 probes situated at midspan in circular arrays arrays of 5 sensors was included in the simulation to simulate the acoustic measurements carried out by Davoudi [Davoudi, 2014; Davoudi *et al.*, 2016a,b] at the AFRD facility. These sensors were located in the VR6 region, where the resolution is Δx_{grid} =16 mm. This yields a maximum frequency resolution of 2361 Hz, assuming a required number of 10 grid points per wavelength (N_{ppw}) for the capture of acoustic waves. The maximum frequency resolution attainable for a given grid level can be approximated through the use of Eq. 5.6 if the soundspeed c_0 is known.

$$f_{max} = \frac{c_0}{(N_{ppw} - 1)\Delta x_{grid}} \tag{5.6}$$

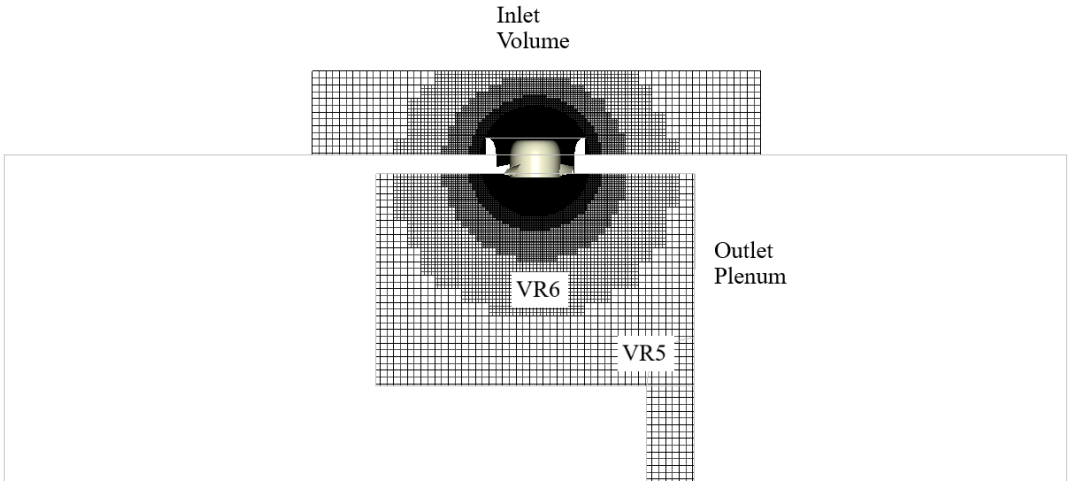

(a)

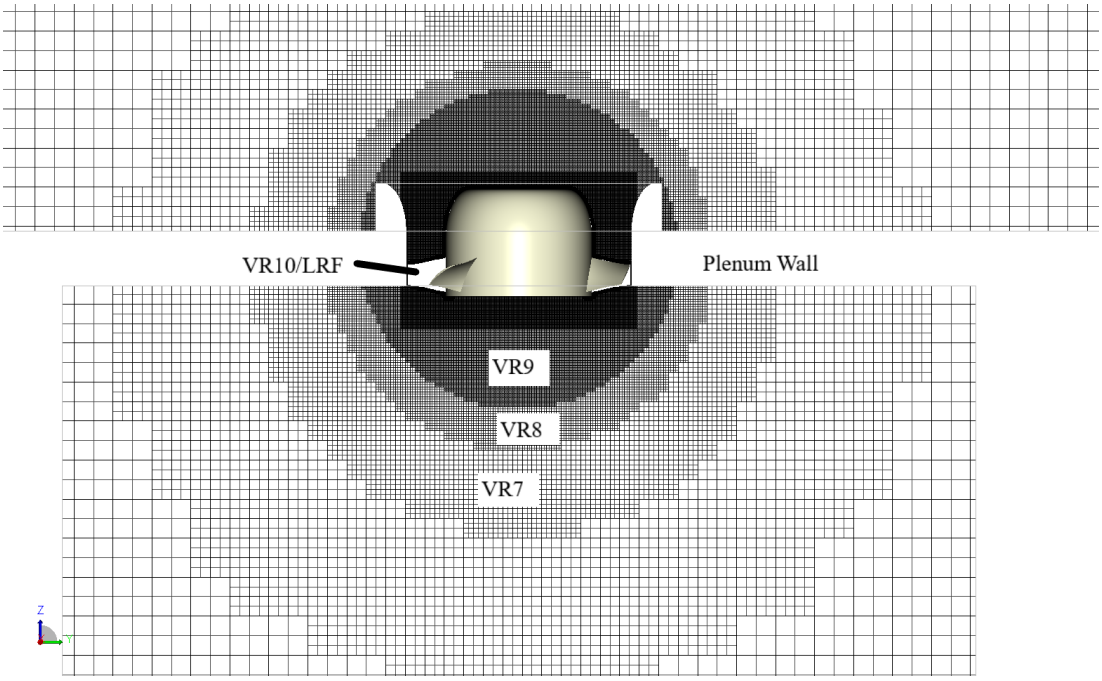

(b)

Figure 5.2 Mesh topology for the RCDB simulation (a) Overall view of the mesh (b) Focus on the fan region

Finally, two sensor locations located along the fan axis upstream and downstream of the rotor and situated exactly 1 m from the rear of the fan hub (the front probe is located 0.6 m in front of the fan hub). The described sensor locations are illustrated in Fig. 5.1.

In the course of this study, three operating points were simulated using the described simulation setup. First, the nominal operating condition of 2.31 kg/s used to reproduce the test conditions for the stationary CD airfoil, as exposed in section 3.2.1, and covered at length in Neal's thesis [Neal, 2010] was considered the reference point. In addition, the near-transparency flow condition at 1.73 kg/s and a point of operation just before stall at 1.01 kg/s were also covered as they were the focus of additional studies [Barrent, 2015; Davoudi, 2014]. These three operating points are hereby dubbed OC1, OC3 and OC5. This was done to numerically explore the largest range possible of flow conditions for this particular fan and its effect on the acoustic footprint of the fan and tip gap flow in particular in parallel with experiments carried out at MSU for validation purposes.

Simulation efforts were carried out in three separate steps, with three distinct simulations having been run. The initial simulation effort [Pérot *et al.*, 2010b] was conducted using the described grid and an imposed simulated Mach number of 0.3 to evaluate the flow characteristics for the three selected operating points. This is an option in the PowerFLOW software that allows for the imposition of a higher Mach number than the real experimental value to reduce the simulation run time, relying on the fact that the flow for a given geometry will be the same at low Mach number for a given Reynolds number value. This has an effect on the propagation of acoustic pressure waves however, and thus cannot be relied on for evaluating the acoustic footprint of a system. This set of simulations was run using the mass-flow boundary condition at the exit of the outlet duct.

A second set of simulations was run on the same grid with the same mass-flow boundary condition for the outlet duct, but this time using the realistic (i.e. actual experimental) Mach number value for the acoustic evaluation of the fan geometry.

Finally, a third set of simulations was run at the realistic Mach number value, but this time imposing the flowrate through the fan by imposing a constant velocity outlet condition instead of an imposed mass-flow outflow condition to investigate its effect on the simulation performance. The three simulation runs will hereby be defined as Cases 1-3.

The following sections are aimed at providing the validation results for the described simulations with the available experimental data described in section 3.2.1.

5.3.2 Global Aerodynamic Performance Evaluation

The first element of validation between the simulations and the experiments was the comparison of the aerodynamic performance of the fan system. Three main items were used for the comparison: the global aerodynamic performance curve, the average pressure coefficient at midchord on the fan blades as well as the velocity profiles downstream of the fan.

The global performance curve is shown in Fig. 5.3 for the three distinct simulation steps. A good agreement between the simulation results and the experimental performance curve collected in the MSU AFRD facility [Neal, 2010]. Whilst there are discrepancies in the levels presented for the selected flowrates, the maximum error is 5.3 Pa for OC3 for Case 3, with the absolute error being relatively low.

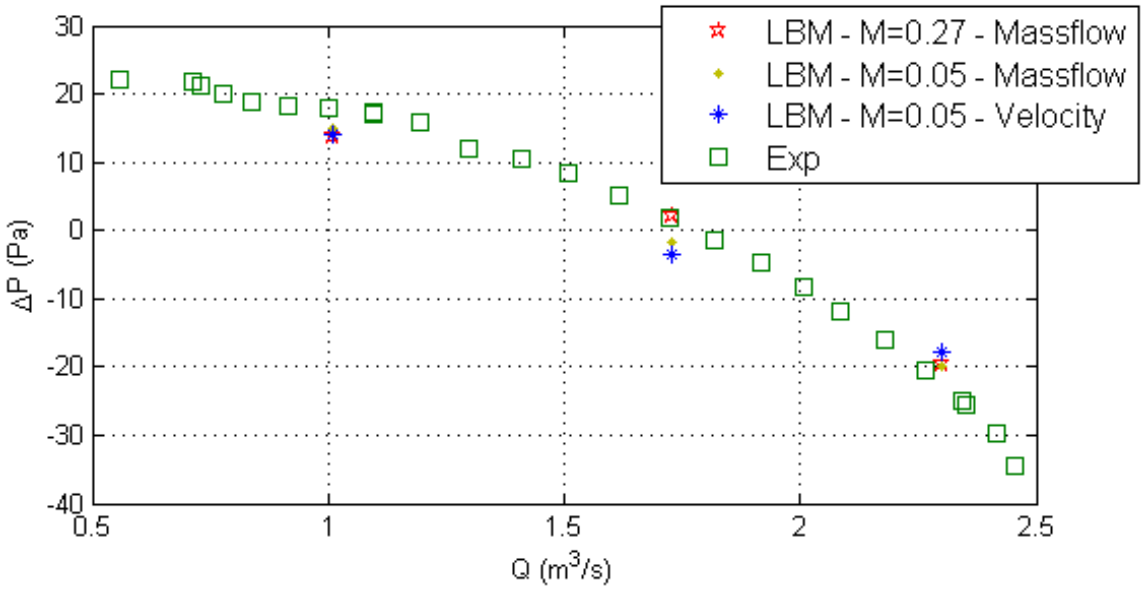

Figure 5.3 Performance characteristic curve for the RCDB fan (3-blades). Experimental data from [Neal, 2010].

The numerical average pressure rise is evaluated over a statistically converged interval of time, with the convergence of the pressure rise for each of the simulated cases presented in Fig. 5.4. The convergence of the pressure rise over time for Cases 1 and 2 indicates a rather high variation of the pressure levels at the point of measurement inside the AFRD chamber. For the OC1 case, a cyclical fluctuation of around 30 Pa in amplitude is observed around the mean, falling off to around 10-15 Pa for OC3 and OC5. This was a preliminary indication of instabilities in the dynamic behavior of the flow. This was made more evident when looking at the acoustic properties of the simulations, which are presented in the next

section, and led to a modification of the outlet boundary condition for Case 3 from a mass-flow outlet condition to a velocity outlet condition. As it can be seen from the convergence of the pressure rise, however, it had a large stabilizing effect observed fluctuations, with the amplitude having been lowered to less than 2 Pa for all operating conditions. As the reader will observe, the simulations were run for long periods of time (with the exception of OC1 for Case 1); this was done due to the low rotational frequency of the fan (7.3 Hz) making it mandatory to collect longer samples to obtain significant frequency analysis results on the order of the rotational frequency.

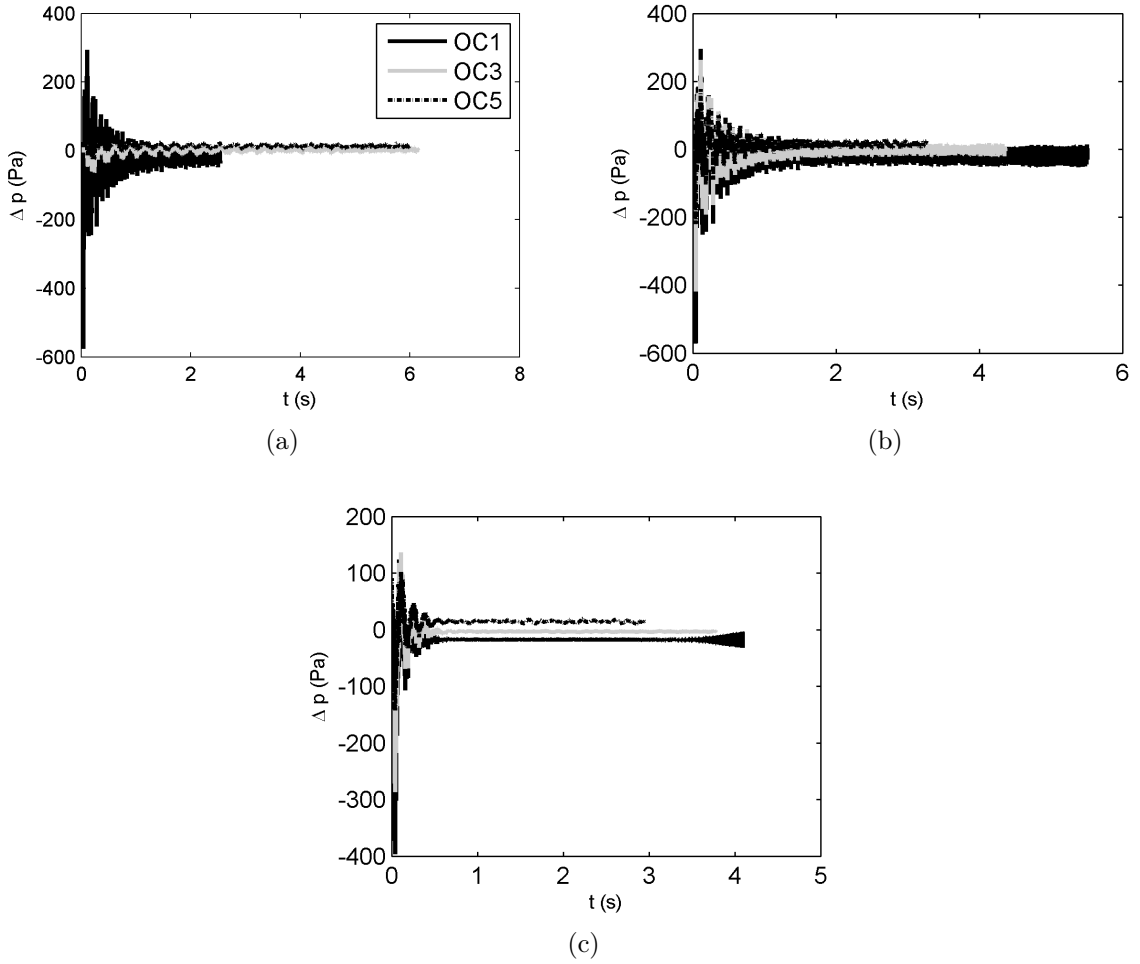

Figure 5.4 Convergence of the pressure rise across the simulated RCDB cases (a) Case 1 (b) Case 2 (c) Case 3

In addition to the global performance of the fan, the pressure coefficient collected at midspan on a single RCDB blade was compared to the experimental results from the MSU studies on the OC1 [Neal, 2010] as well as OC3 and OC5 [Barrent, 2015], as shown

in Fig. 5.5. Numerical data was averaged over 10 fan rotations to obtain average pressure coefficient plots.

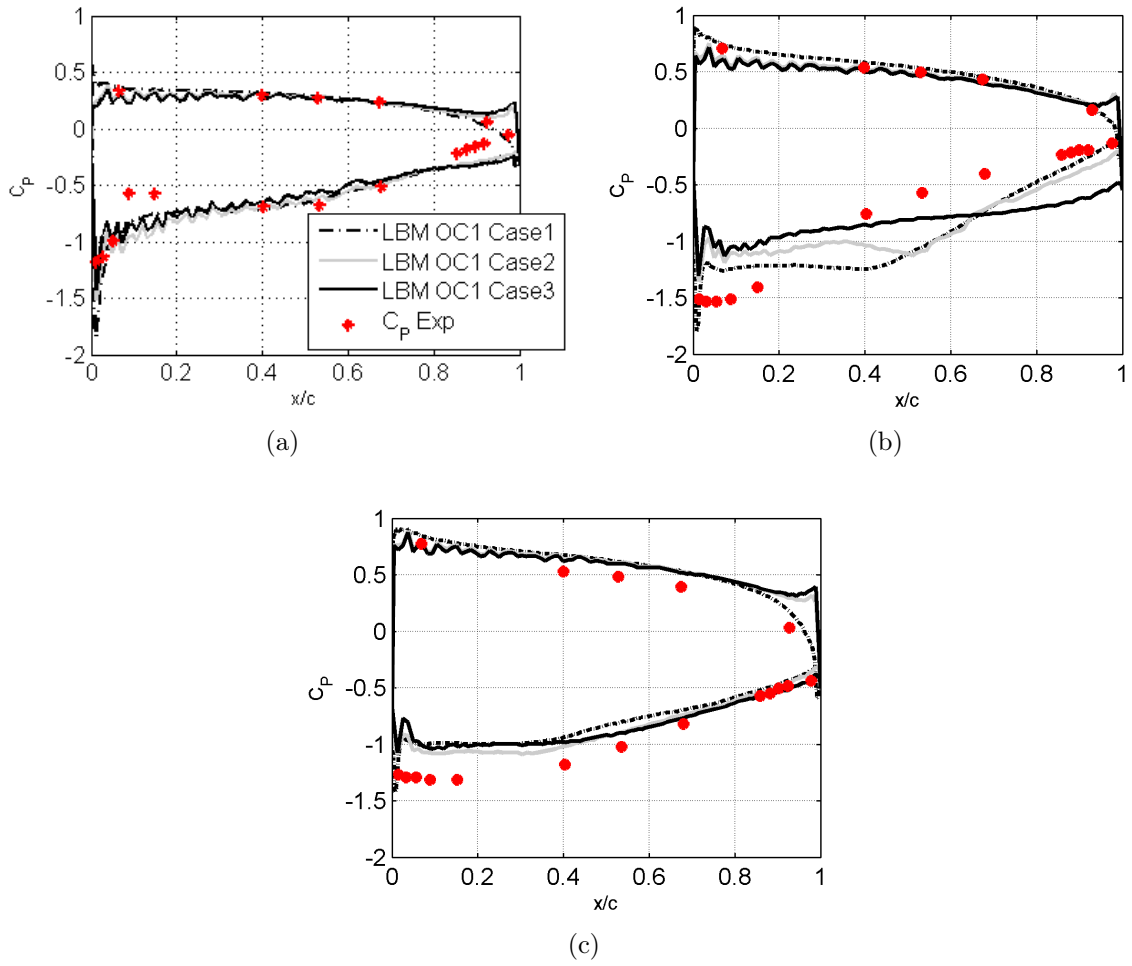

Figure 5.5 Pressure coefficient profile at midspan for the RCDB along the normalized chord $\frac{x}{c}$ at different operating conditions (a) OC1 (b) OC3 (c) OC5

For the design point (OC1), it can be observed that the three simulation cases agree fairly well with the experimental data on the pressure side (positive C_p) with the exception of the trailing edge portion where Cases 2 and 3 show signs of an adverse pressure gradient near the trailing edge. This adverse pressure gradient is also seen on OC3 and OC5 for the experimental Mach number simulations. There is however little difference qualitatively as to the flow around the blade between Case 1 and Cases 2-3 when looking at contours of velocity magnitude around the blade in Fig. 5.6. On the suction side, the simulation agrees well with the experimental data over the median portion of the normalized chord interval ($\frac{x}{c}$ =0.4-0.7); near the trailing and leading edge, however, the simulation results predict a lower C_p value when compared to the experiment. In particular, the laminar

recirculation bubble at the leading edge evidenced in the experiments by the plateau near the leading edge on the suction side ($\frac{x}{c}$ =0-0.05) is not captured in the current simulation. Similarly, at the trailing edge the adverse pressure gradient seems to have a stronger effect in the simulation, which shows a C_p on the verge of flow separation on the suction side. When looking at the contours of chordwise velocity in Fig. 5.6 for all three Cases at OC1,the separation at the trailing edge is visible through the thickness of the wakes. The simulation being unable to capture the laminar separation bubble that was observed on this fan experimentally leads to problems in reproducing the transition from laminar to turbulent flow that occurs over the chord length with the observed results. A more refined simulation (0.5 mm resolution) was run for the OC1 flowrate where a significant improvement was noticed in the behaviour of the flow around the blades [Marsan *et al.*, 2018], but a global refinement of the simulations could not be carried out in the course of this study due time constraints.

For the near-transparency point (OC3), a trend similar to OC1 can be observed on the pressure side. However, the correlation is less conclusive when looking at the suction side results; the general slope and levels of the C_p are not well reproduced by the simulations. In fact, the observed separation of the flow for the OC1 condition becomes generalized over the chord at OC3, leading to larges variations in the surface pressure levels between the simulations due to the formation of instabilities.

For the lower flowrate (OC5), all three simulation cases exhibit a slope that correlates well with the experimental data on the pressure side, with all three simulations however over-predicting the pressure levels by approximately 0.1 and the low Mach number simulations (Cases 2-3) once again showcasing an adverse pressure gradient near the trailing edge. For the suction side, the simulations correlate well with the experiment in the last 50% of the chord; however, the plateau seen in the first 30% of the chord on the simulation data isn't in line with the experimental trend. Overall, the simulations seem to underestimate the lift at midspan, which is once again coherent with the global performance curve. At this point, the profile is nearing a stalled condition, and the flow is largely separated over the entire chord.

5.3.3 Blade Wake Velocity Data

In addition to the overall aerodynamic characteristics, the experimental campaign at the MSU facility provided detailed data pertaining to the phase-averaged velocity profiles directly behind the fan blades with which to compare the simulations. However, the Case 1

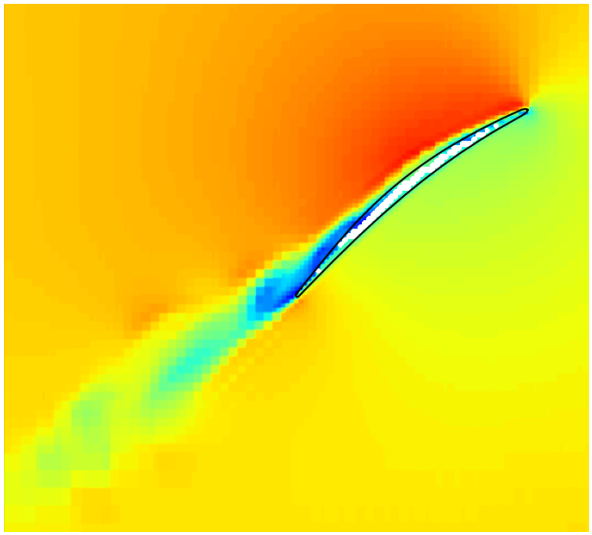

(a)

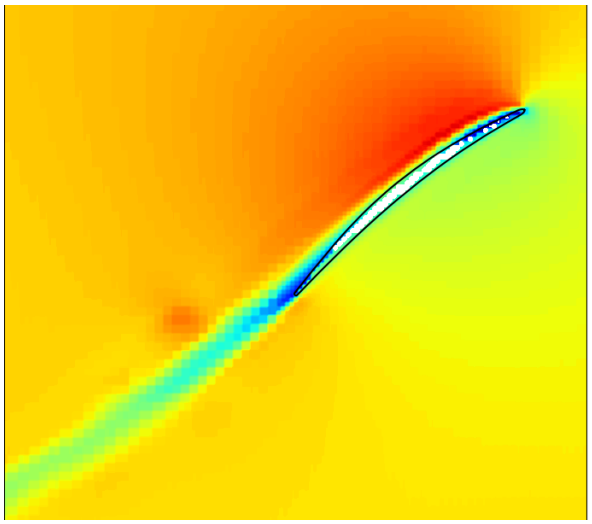

(b)

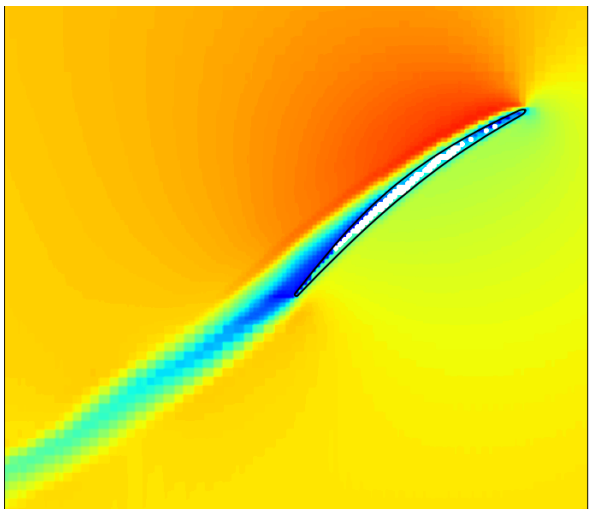

(c)

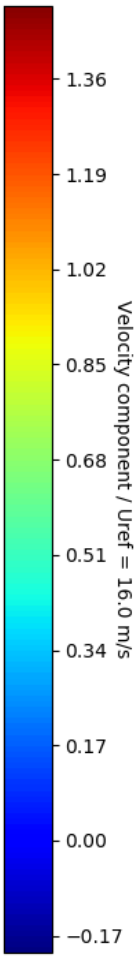

Figure 5.6 Instantaneous contours of chordwise velocity U around the midspan for the RCDB at OC1 (a) Case 1 (b) Case 2 (c) Case 3

simulations did not have sufficient recording data to allow for proper phase-averaging, and is not presented here.

The initial study on the RCDB fan [Neal, 2010] provided data for OC1; the author investigated the velocity profiles at midspan at distances ranging from 5 to 50% of the chord behind the fan blades. The velocity profiles were measured using a rotating hot-wire method, and the velocity components were forrmulated in a coordinate system u, v, w aligned with inflow velocity, as shown in Fig. 5.7.

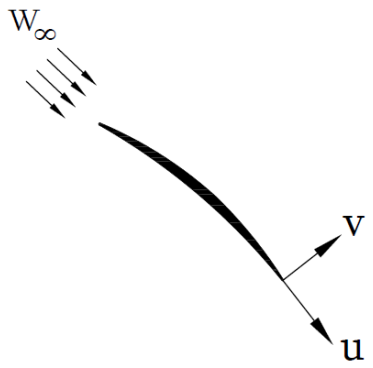

Figure 5.7 Schematic representation of the UVW coordinate system used for the evaluation of the wake velocity.

It is important to note here that while the experiment made use of data sampled at 50 kHz and measured over several minutes (several thousands of rotations), in the simulation data was sampled at 2400 Hz over the course of 15-20 revolutions' worth of statistically converged time.

Fig. 5.8 presents the phase-averaged velocity profiles located 5% chord downstream of the RCDB fan as extracted from the experimental Mach number simulations when compared to the experimental data from the MSU campaign. The abscissa of the plots are normalized by the freestream relative inlet velocity V_0 of 16 m/s for OC1 and are presented as a function of the circumferential position normalized by the blade chord ($r\theta/c$).

Observing the results for the normalized streamwise u/V_0 velocity, both simulations are able to predict the shape of the wake fairly well, but it can be observed that the simulated wake of the blade appears to be approximately twice as thick as those measured in the experiment. The velocity deficit is also much more pronounced, with the maximum deficit reaching 20% of the freestream velocity for Case 3 whilst the hot-wire results show a deficit of 65% freestream velocity. This is in line with the observations made on the simulation in the previous section, where it was seen that the flow at the trailing edge of the blade for

Cases 2 and 3 was nearly or lightly separated, as it would lead to the formation of wider wakes.

Looking now at the v/V_0 velocity normal to the chord, the general shape of the experimental profile is fairly well represented by both simulations, although Case 3 shows a relative decrease of the velocity values in the blade passage, which compares better with the experimental values. The positive v/V_0 values encountered in the simulated wake (towards the suction side) as opposed to negative values (towards the pressure side) in the experiment is a further indicator of the possible flow separation at the trailing edge in the simulations.

In the case of the radial velocity w/V_0, the two simulation cases once again represent the experimental velocity profile shape fairly well. However, Case 3 predicts the overall experimental velocity levels much better than Case 2.

A subsequent study [Barrent, 2015] expanded to cover several operating conditions at flowrates equal to or below the transparency point (OC3) using a stationary hot-wire system for the measurement campaign. As opposed to the blade-aligned velocity coordinate system used by Neal, however, the author opted to present the measured velocity in the cylindrical frame of reference $r - \theta - z$, and only measured the axial V_z and tangential V_θ velocity components, omitting the radial component. A comparison of the collected wake velocity components for OC3 is presented in Fig 5.9. From the axial velocity graph, a trend similar to that observed for OC1 is confirmed, where the numerical wake thickness is increased twofold when compared to the experimental value. A much stronger velocity deficit is also observed.

In the case of the tangential velocity, it can be seen that Case 2 largely underestimates the experimental data over the entire circumferential range evaluated, with even the baseline value in the blade passage shown to be off by 10-20% of the freestream velocity. However, once again Case 3 presents a wake component profile that is much closer in shape and level to the experiment, although the peak velocity value is more elevated by approximately 35% of the freestream velocity value.

The same analysis could however not be performed for OC5, as the simulations yielded noisy velocity profiles from which the blade wake centers could not be appropriately extracted for phase-averaging purposes and yielded no positive comparison to the experiment. However, from the results gathered on both OC1 and OC3, it can be postulated that simulation Case 3 appears to offer a much more realistic comparison when comparing the fine wake velocity data for both operating conditions. In addition, it was shown

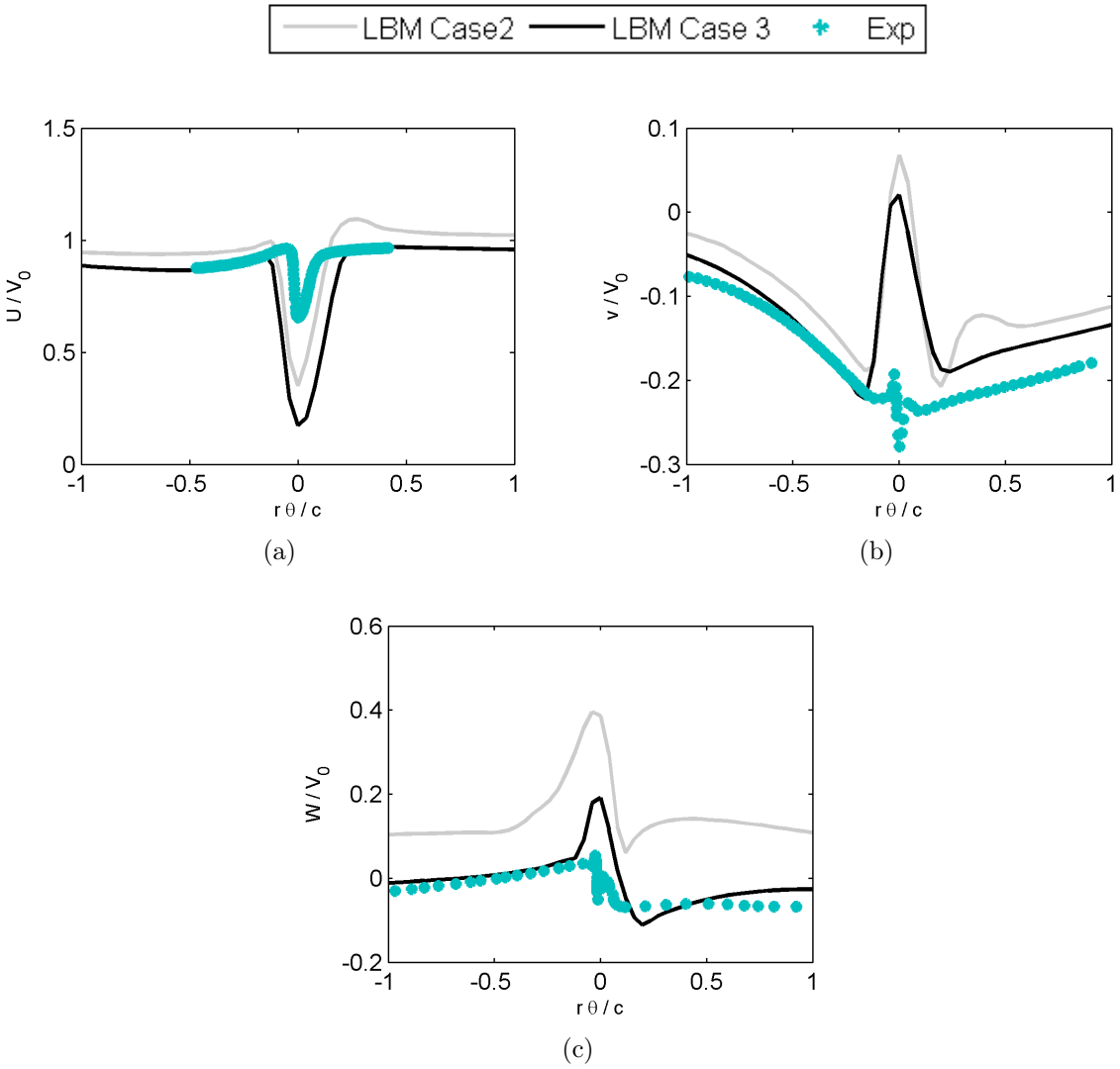

Figure 5.8 Single-blade phase-averaged wake velocity profiles for the RCDB fan in the UVW frame of reference for OC1.

from Fig. 5.4 that the convergence of the pressure characteristic was more stable with the modification of the massflow outlet condition in Cases 1-2 to a velocity outlet condition in Case 3.

5.3.4 Acoustic Performance

The previous section having covered exclusively the validation of the aerodynamic performance of the RCDB geometry, it was however mentioned that the effect of the modification of the outlet boundary condition to a velocity outlet was very noticeable on the acoustic properties of the fan. Fig. 5.10 shows the acoustic spectra as recorded 0.6 m upstream

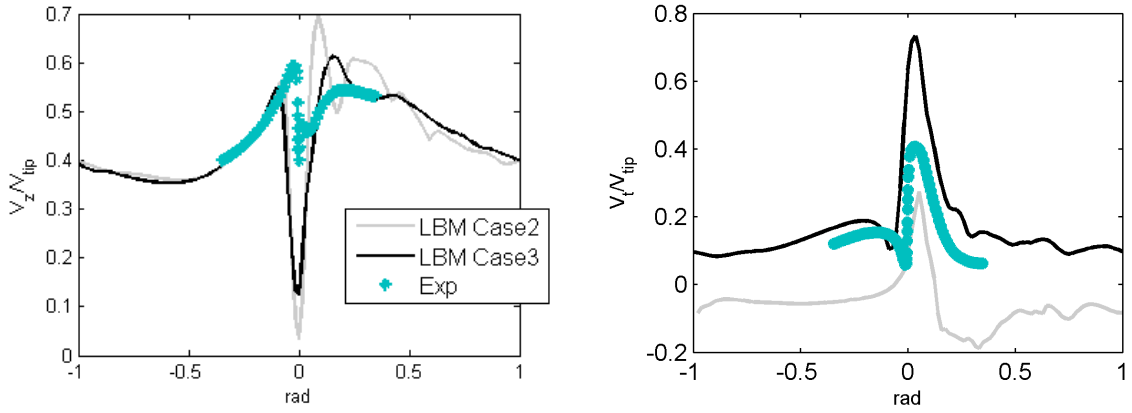

(a) (b)

Figure 5.9 Single-blade phase-averaged wake velocity profiles for the RCDB fan in the cylindrical frame of reference for OC3.

of the fan hub along the rotational axis for all three operating conditions (OC1-OC5). The plots show the power spectral density of the acoustic signals as computed by Welch's periodogram method (*pwelch* function in Matlab) using a Hanning window and a 50% overlap between the data segments. The numerical data was sampled at 9478 Hz and periodogram segment lengths were set to obtain a frequency resolution of $\Delta f = 2.1$ Hz. Whilst only Cases 2 and 3 are valid representations of reality from an acoustic standpoint, having been simulated with the realistic Mach number, Fig. 5.10(a) nevertheless includes the spectra from Case 1 to highlight the large effect the outlet boundary condition effected on the differing simulations; Cases 1 and 2 show an acoustic spectra exhibiting high peaks at 21 Hz, 53 Hz and 86 Hz, with a maximum level discrepancy of around 7 dB between the two simulations. However, with the modification of the outlet boundary condition in Case 3, these high peaks disappear and what was a highly tonal spectra becomes very characteristicly broadband.

The same trend is visible in the case of OC3 between the two realistic Mach simulations, with the peak frequencies having shifted to 21 Hz, 56 Hz and 88 Hz for the Case 2 simulation. The differences in the spectra for OC5, however, are more interesting. Looking at Case 2, the peaks from OC3 are still visible but are much less predominant above the broadband noise level, which has substantially increased. Comparing with the spectra for Case 3, a clear broadband hump is this time visible at 28 Hz, whereas other operating conditions showcased a predominantly broadband spectra. The hump has a level comparable to the 21 Hz hump observed on the Case 2 spectra, with a frequency shift. In addition,

the broadband noise levels are comparable between the two simulations over the whole frequency range exception made of the tonal peaks on Case 2.

The rather tonal behavior observed in the acoustic spectra of Cases 1 and 2 was linked to instabilities forming inside the downstream flow chamber, causing the large fluctuations in the pressure rise across the fan pictured in Fig. 5.4 for Cases 1 and 2. This resulted in an increased tonal acoustic footprint. The modification of the mass-flow outlet condition to a velocity outlet eliminated the behavior.

Whilst the initial experimental foray at MSU was focused on aerodynamic study of the RCDB geometry [Barrent, 2015; Cawood, 2012; Neal, 2010], an evaluation of the acoustic performance of the system was also more recently performed in the AFRD facility [Davoudi, 2014]. However, due to the reflective nature of the test environment, a high-pass filter with a threshold of 200 Hz was applied when investigating the acoustic performance of the fan system in the experiment. Moreover, the higher flowrates (OC1 chief among them) could not be investigated acoustically as the use of the noisy make-up fan was necessary to reach the required negative relative pressure in the pressure side plenum. Although the semi-anechoic domain from the simulation provides an acoustically *clean* environment, in the experiment a denoising method was applied. The delay-and-sum method employed by Davoudi [Davoudi *et al.*, 2016a] for use with the 10-microphone array installed in the AFRD facility (and replicated in the simulation) was also applied to the numerical measurements to provide a suitable basis for comparison. Furthermore, as the experimental acoustics were collected using a minimum rotor speed of 540 RPM for the three-blades rotor configuration, a dipolar source assumption was used to rescale the experimental noise levels to the nominal 437 RPM rotor speed for the RCDB fan used in the simulation. The comparison of the rescaled acoustic emissions from the simulation with the experimental spectra for OC3 and OC5 are shown in Fig. 5.11. Overall, the trend is good up to 850 Hz for both operating conditions in both level and shape of the spectra, although differences of up to 7 dB are observed for OC3 whereas OC5 shows a much closer agreement. At higher frequency, however, a divergence is observed, with the simulation exhibiting a higher noise level when compared to the experiment.

With the combined results from the aerodynamic and aeroacoustic analysis, it becomes clear that simulation Case 3 with the velocity outlet boundary condition modification provides a fairly better representation of the experimental behavior of the RCDB fan as investigated in the MSU facilities, especially regarding the acoustic radiation. In the next chapter, a more in-depth analysis of the noise mechanisms will be provided on the basis of the results issued from simulation Case 3.

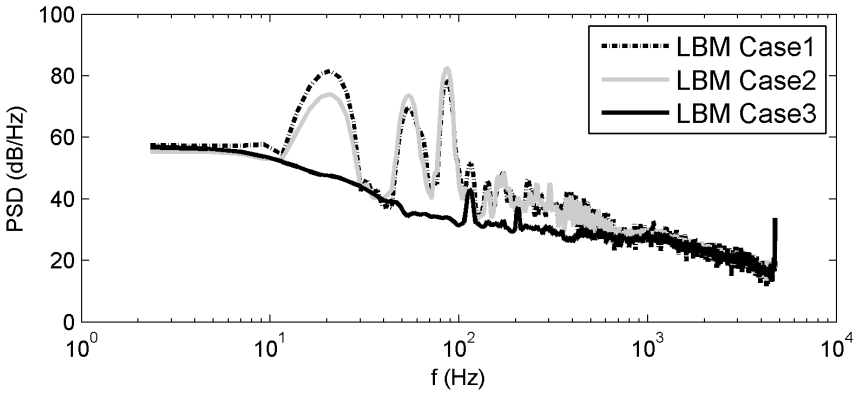

(a)

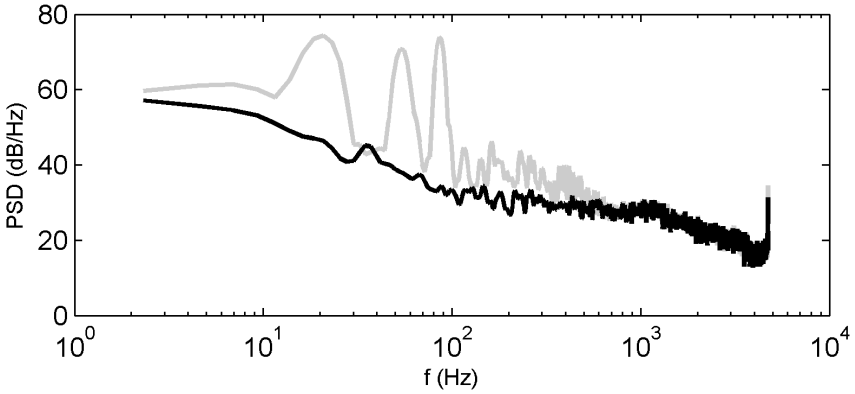

(b)

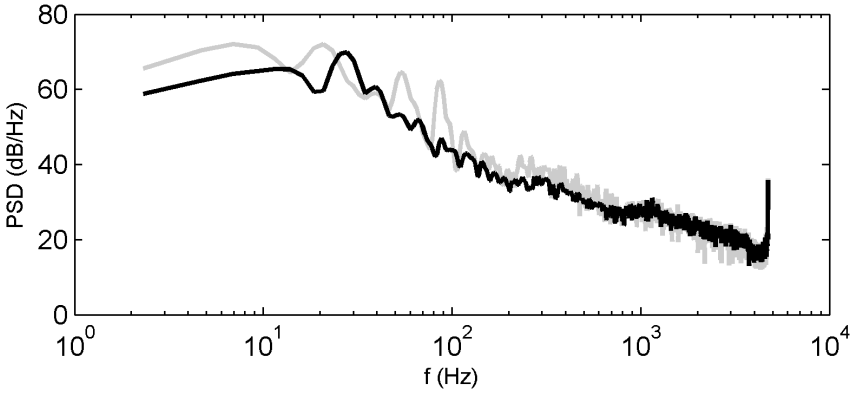

(c)

Figure 5.10 Acoustic radiation measured along the fan axis upstream of the RCDB fan for operating point (a) OC1 (b) OC3 (c) OC5. $\Delta f = 2.1$ Hz

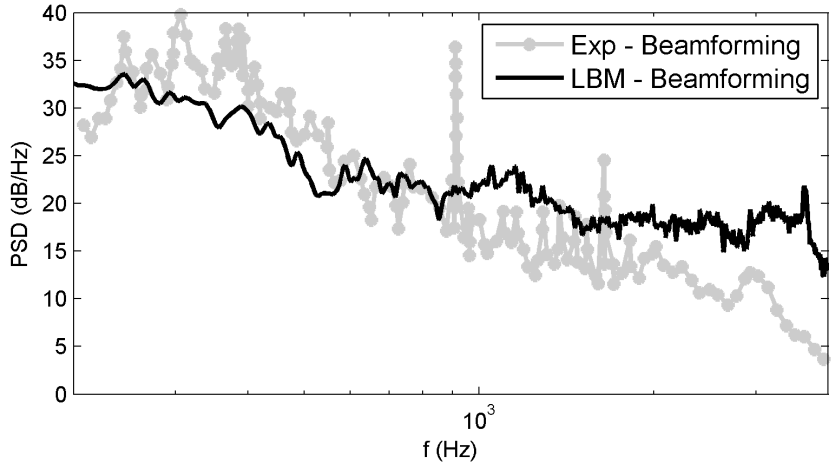

(a)

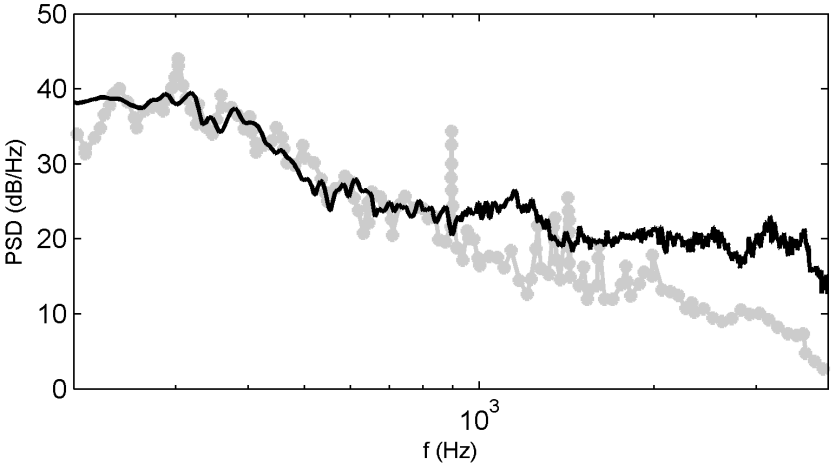

(b)

Figure 5.11 Comparison of the acoustic performance of the RCDB fan between the LBM simulation direct results (Case 3) and experiment at (a) OC3 (b) OC5. The beamforming technique utilized by Davoudi [Davoudi *et al.*, 2016a] was applied to the LBM microphone data for a proper comparison.

5.4 USI7 Test Fan

The USI7 fan system is the second free-tip fan configuration which was investigated in this study. Like the previously covered RCDB fan, this is a test rotor which was specifically built for research purposes at Siegen University, as described in Sec. 3.2.2, and subjected to an extensive experimental measurement campaign as well as numerical investigation using several methods including the LBM [Sturm *et al.*, 2013; Zhu, 2016; Zhu *et al.*, 2016a]. In opposition to the RCDB fan, however, it was made to be representative of a large class of mass-produced fans for applications such as automotive engine cooling with regard to the attainable flowrate and pressure ranges. The original data both experimental and numerical used in the current study pertaining to this geometry is a result of the work carried out in Siegen but was made available as part of a collaboration effort between the Université de Sherbrooke and Siegen University. The data presented in this section is a direct byproduct of Zhu's thesis work.

5.4.1 Presentation of the numerical setup

Although in reality the USI7 rotor was characterized using two separate test rigs for the aerodynamic and aeroacoustic properties, the LBM simulations setup by Zhu only modeled the acoustic test rig, although in great detail. The simulation domain is presented in Fig. 5.12(a). In the simulation, the inlet semi-anechoic chamber was modeled as a fully anechoic room, with the side walls defined as porous medium zones with very high viscous resistance to absorb incoming acoustic pressure waves. All other surfaces are specified as fully rigid walls. The massflow is specified at the inlet surface, whereas the outlet is defined as a free-flow surface at constant atmospheric pressure. Damping regions are applied near the inlet and outlet boundary conditions to avoid spurious acoustic reflections, as was done with the RCDB case in the outlet duct.

The domain was discretized using 11 VR regions, with a maximum refinement level of 0.5 mm in the region of the fan; an overview of the meshing grid in close vicinity to the fan rotor is shown in Fig. 5.12(b). The maximum refinement of 0.5 mm was deemed sufficient based on the LBM grid independance study carried out by Moreau and Sanjosé [Moreau and Sanjose, 2016] for a fan with a similar diameter and operating conditions.

The fan performance was simulated for the nominal operating condition of the fan (flowrate of 0.65 m^3/s) as well as a part-load point (flowrate of 0.55 m^3/s), or $\phi_{nom} = 0.154$ and $\phi_{part-load} = 0.131$ in terms of the dimensionless flowrate coefficient ϕ defined in Eq. 5.1. The reader will note that the fan performance coefficients used in Zhu's work differ from

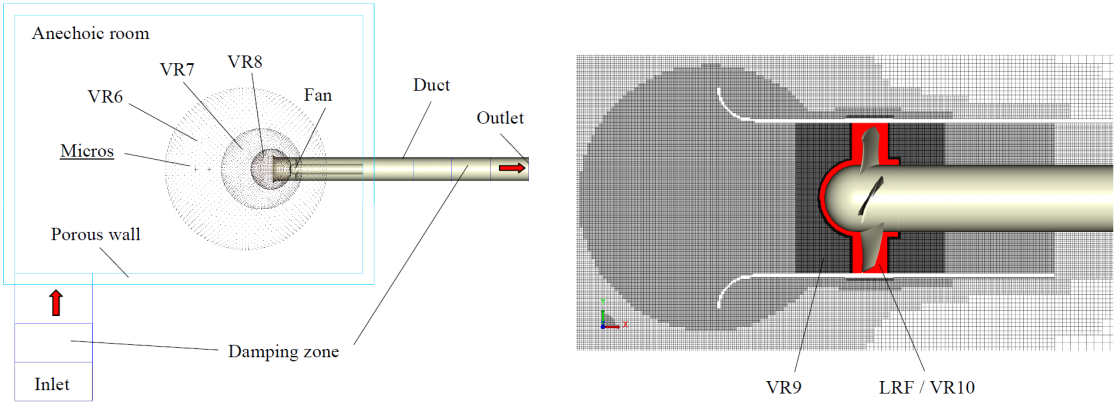

Figure 5.12 Simulation domain for USI7

those presented here as they used a differing definition and were also based on the use of the fan rotational speed in rotations per second rather than radians for the normalization, leading to a flawed coefficient definition; this was corrected here. The effect of varying the tip gap clearance was also investigated in the simulation. The nominal tip clearance of s =3 mm (1%) was modeled and resolved directly on the 0.5 mm grid, leading to a resolution of 6 voxels across the tip clearance. However, in the case of the tighter s =0.3 mm (0.1%) tip clearance, it was decided that the tip clearance would be entirely neglected in the simulation as it would lead to extreme grid requirements for a proper resolution of the flow in the tip region of the blades; the tip profile of the blade was thus extruded radially to intersect with the duct wall. In total a number of 4 simulations were carried out (2 flowrates with 2 differing tip clearance gaps).

In order to compare the simulated and experimental characteristics of the fan system, a series of measurement points and regions were included in the simulation. First of all, the evaluation of the static pressure rise across the fan was done using the differential of time and area-averaged static pressure from two planes located one diameter upstream and downstream of the fan rotor in the duct over ten rotor revolutions. Aeroacoustic measurements in the anechoic room were carried out using three sensor probe measurement points located at a radius of 1.3 m on the suction side of the fan rotor to mimic the location of the physical microphones in the experiment; they are located in the VR8 region with a resolution of 8 mm, allowing for a maximum frequency resolution of 4800 Hz assuming a requirement of 10 grid points per wavelength for proper evaluation. The near-field pressure measurements locations from the experiment were also reproduced accurately by including surface measurement points on the rotor blade and shroud whose locations and size correspond to the sensor locations in the experiment. The following sections show a

detailed comparison of the simulation results with the USI7 experimental database. The data reported here is identical to that presented by Zhu in his thesis work, but were reproduced here from the raw data to provide all necessary information to the reader without the need for him to refer to outside sources and to validate the post-processing of the data.

5.4.2 Aerodynamic Performance Evaluation

In the case of the USI7, the simulated aerodynamic performance of the system was evaluated using two main elements of comparison with the experiment. The first element consists of the global aerodynamic performance curve of the system. The characteristic curve of the system predicted by the LBM from the four simulation cases is presented in Fig. 5.13 against the experimental curves for the two tip clearances considered. Overall a very good agreement is found, with the simulation however consistently underpredicting the experimentally obtained pressure rise. For small clearance case (s =0.1%) the maximum error is 3.5% of the experimental value. However, the maximum error more than doubles when looking at the larger clearance gap, with a value of 7.7% observed for the lower flowrate. The increasing relative error for the larger tip clearance might indicate that further refinement might have been required to better resolve the flow features in the tip region, but the simulation results nevertheless show a satisfactory agreement with the experiment taking into account the difference in the measuring method used to evaluate the static pressure rise in the numerical model comparatively with the measurement method employed on the aerodynamic test rig in the experiment.

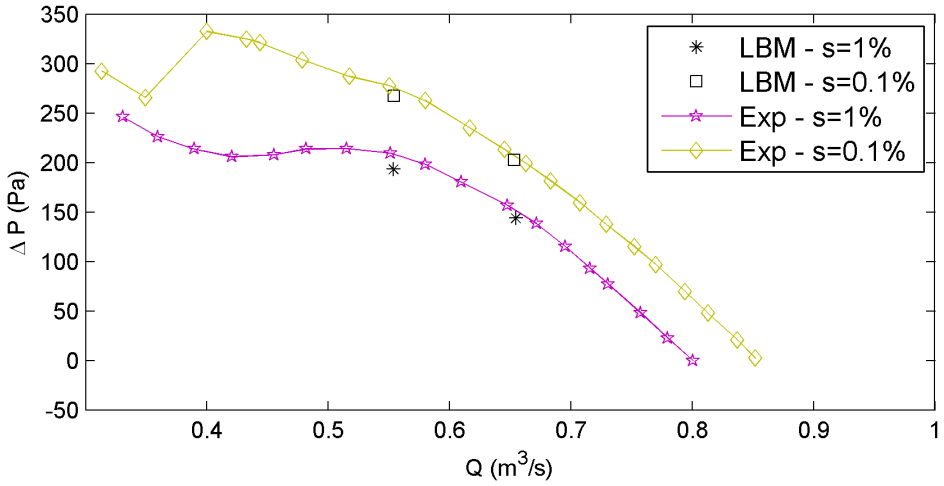

Figure 5.13 Performance characteristic curve for the USI7 fan.

The second element of aerodynamic comparison between simulation and experiment is based on the experimental near-field pressure sensor measurements from the acoustic test rig. Whilst the characteristic curve comparison from Fig. 5.13 indicates a satisfactory similar time-averaged global performance of the fan system, the evaluation of the time-dependant wall-pressure spectra at the surface of the rotor blades provides insight into the spectral signature of the flow features in the vicinity of the fan. The spectra for the wall-pressure sensors located on the rotating blades in the tip region on both the pressure side (sensors S11, S12, S13) and the pressure side (sensors P11, P12, P13) as well as in the tip gap (sensor T01) of two subsequent blades are shown for the nominal and partial load flowrates in Figs. 5.14 and 5.15. Note that in the $s = 0\%$ simulation case, the tip gap sensor on the blade is absent and is thus not reported on the graphs.

Globally, a base level discrepancy between the experimental and numerical spectra is observed across all locations for a given tip clearance, with routine differences of up to 10 dB apparent on the pressure and suction side sensors; larger discrepancies of around 30 dB are observed for the T01 sensor for the larger tip clearance. This discrepancy is observed most notably for the $s = 1\%$ clearance case, with the smaller clearance case exhibiting a more tenuous level difference. Generally, for the larger tip clearance, the simulation overpredicts the wall-pressure fluctuations whilst the trend is inverted for the small clearance.

Regarding the spectral features, however, several observations have to be pointed out. First, as a general rule, wall-pressure fluctuation levels are increased when looking at the large tip clearance case when compared to the equivalent case for a given sensor position. The simulated pressure fluctuation levels also differ from the experiment; globally, a base level discrepancy is observed across all locations for the large tip clearance case, with routine overpredictions of to 10+ dB apparent on the pressure and suction side sensors, whilst larger discrepancies of around 30+ dB are observed for the T01 sensor. In the case of the smaller tip clearance case, the differences are much smaller, but the comparison is also less significant as the simulation does away with the tip leakage flow as a whole, leading to a less disturbed flow.

Most notably, the spectral shape between the two clearances is notably different for a given flowrate on the pressure/suction side sensors, with the larger tip clearance exhibiting large broadband hump shape whilst the smaller clearance shows more of a typically broadband noise spectra. The large clearance spectral hump is especially well-defined for the $\phi_{part-load}$ flow point, where the spectral signature closely resembles the rotating instability (RI) signature for clearance noise initially coined by Kameier and Neise [Kameier and Neise,

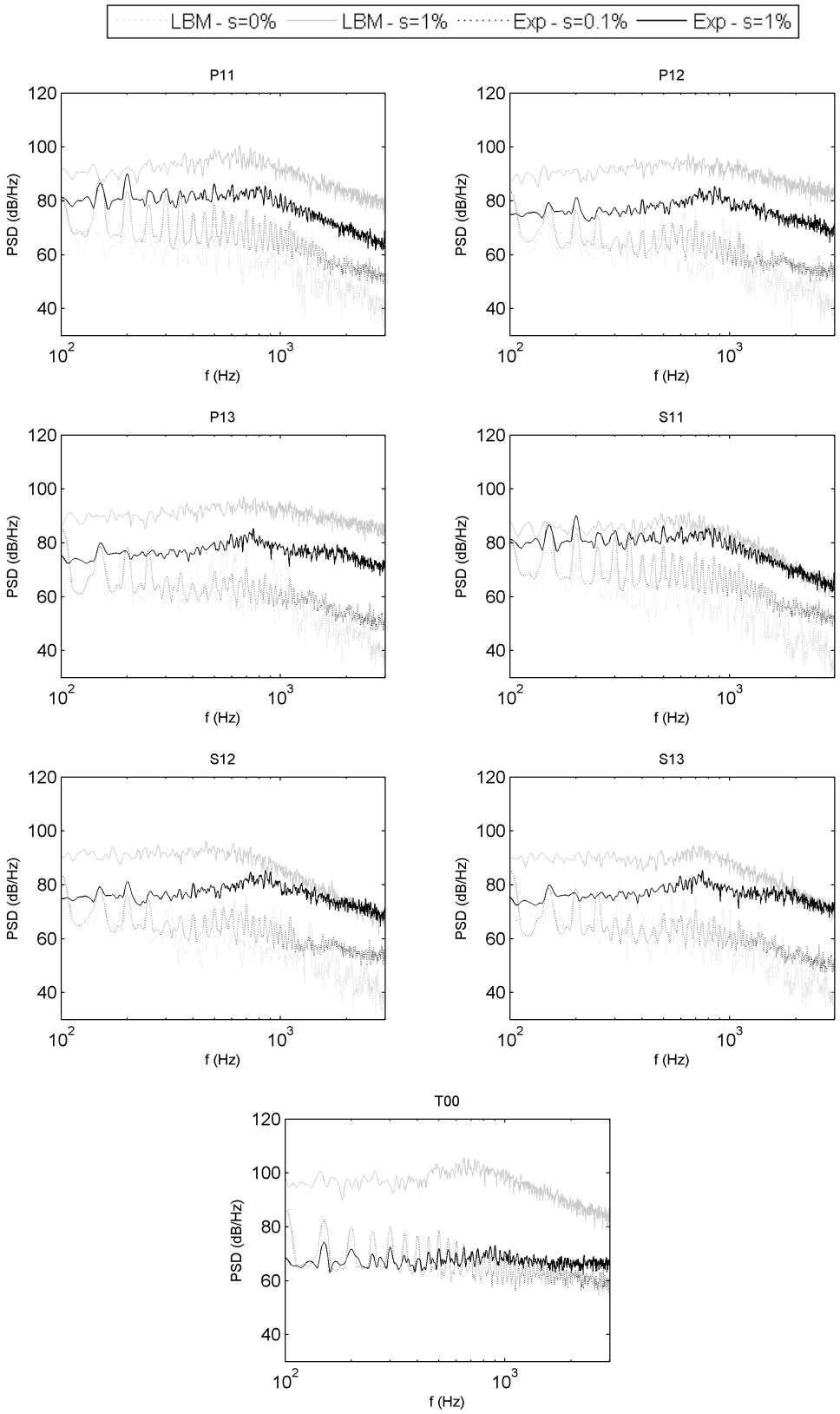

Figure 5.14 Wall-pressure spectra issued from the sensors imbedded in the rotating blades in the tip region for the nominal flowrate case ($\phi_{nom} = 0.154$) $\Delta f = 2$ Hz

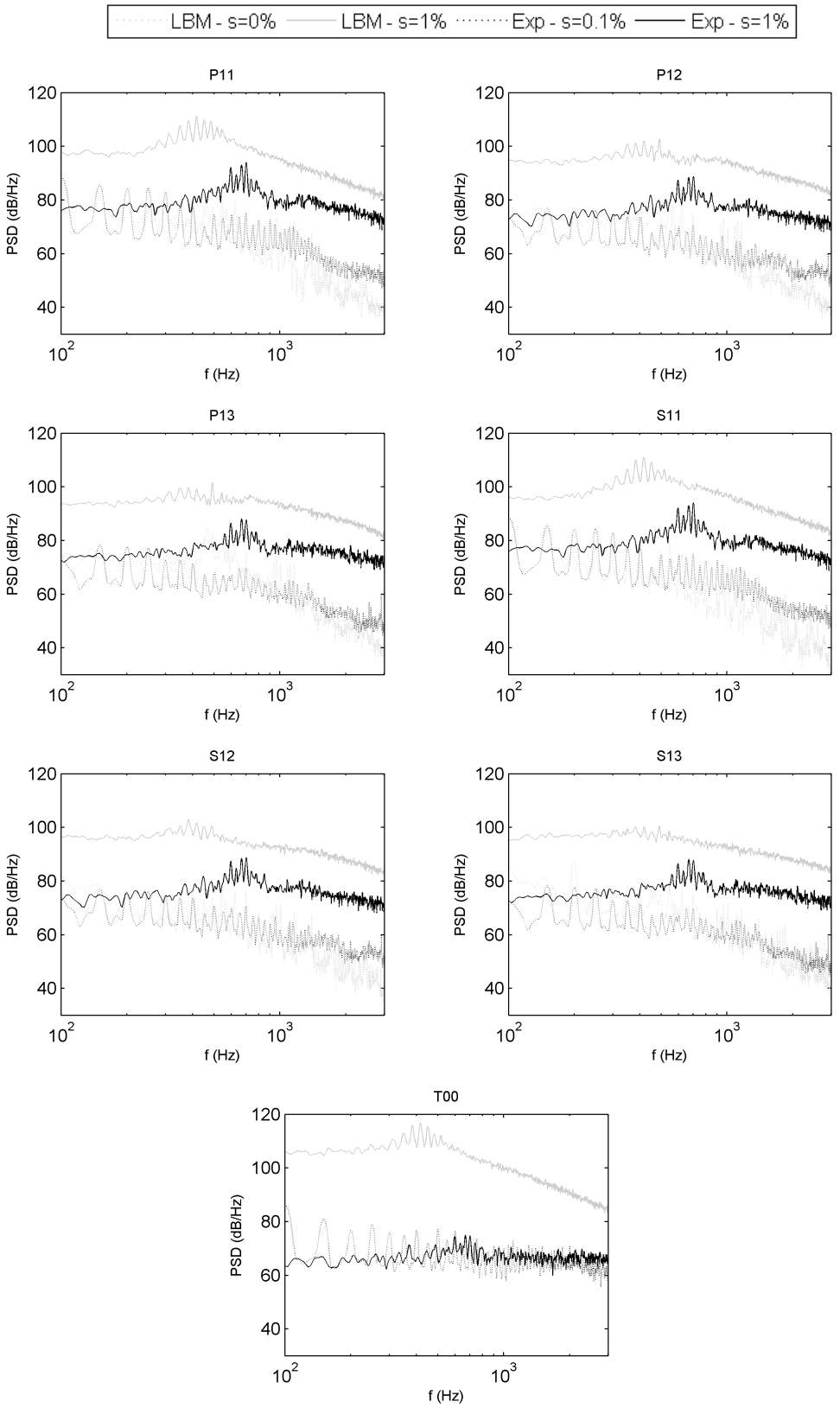

Figure 5.15 Wall-pressure spectra issued from the sensors imbedded in the rotating blades in the tip region for the nominal flowrate case ($\phi_{part-load} = 0.131$) $\Delta f = 2$ Hz

1997a,b]. The central frequency of occurrence of this hump differs between the experiment (600 Hz) and the simulation (400 Hz). This item will be the focus of a specific investigation in the following chapter.

Pronounced peaks at harmonics of the fan rotational frequency (50 Hz) are also observable in the experimental spectra that are not reproduced in the simulation; they were shown to most likely be due to the formation of large-scale distortions being formed in the plenum room over long periods of time (hundreds of seconds), causing an inhomogeneous inflow condition in the duct and affecting the production of BPF tones [Sturm and Carolus, 2012; Zhu, 2016]. The simulations do not cover enough physical time for these distortions to form and affect the results.

The joint comparison of the USI7's global performance curve as well as the detailed wall-pressure fluctuation spectra on the rotor blades recorded in the rotating reference frame confirms the fact that the LBM simulation is able to accurately reproduce the overall aerodynamic behavior observed in the course of the experiment. However, there is a fluctuating pressure level disparity noted in the blade sensor spectra, indicating differences as to the strength of the simulated flowfield when compared to the experiment. To complete the comparison, the aeroacoustic radiation from the fan was also evaluated and is presented in the next section, supplementing the near-field analysis carried out using the blade-imbedded sensor locations.

5.4.3 Acoustic Performance Evaluation

The acoustic radiation from the fan was measured using an array of three microphones located upstream of the test duct, as explained in Sec. 5.4.1 in both the simulation and experiment. The acoustic spectra issued from a single microphone located 35° off the fan axis are presented in Fig. 5.16 for both operating points ($\phi_{part-load}$ and ϕ_{nom}) as well as both clearance sizes $s = [0.1, 1.0]\%$.

The LBM direct acoustic results compare fairly well with the experimental data as far as noise levels and general spectral shape are concerned. The general trend of broadband noise levels increasing with tip clearance size for a given operating point is well reproduced by the simulation. Once again, the reader is however reminded that the simulation actually simulates the absence of a tip clearance, comparatively with the 0.1 % small clearance present in the experiment.The appearance of harmonic humps at a frequency related to the BPF tones (approximately 74 % of the BPF) is also observed up to fourth order for the large clearance at part-load in the experiment. These sub-harmonic tones were shown to

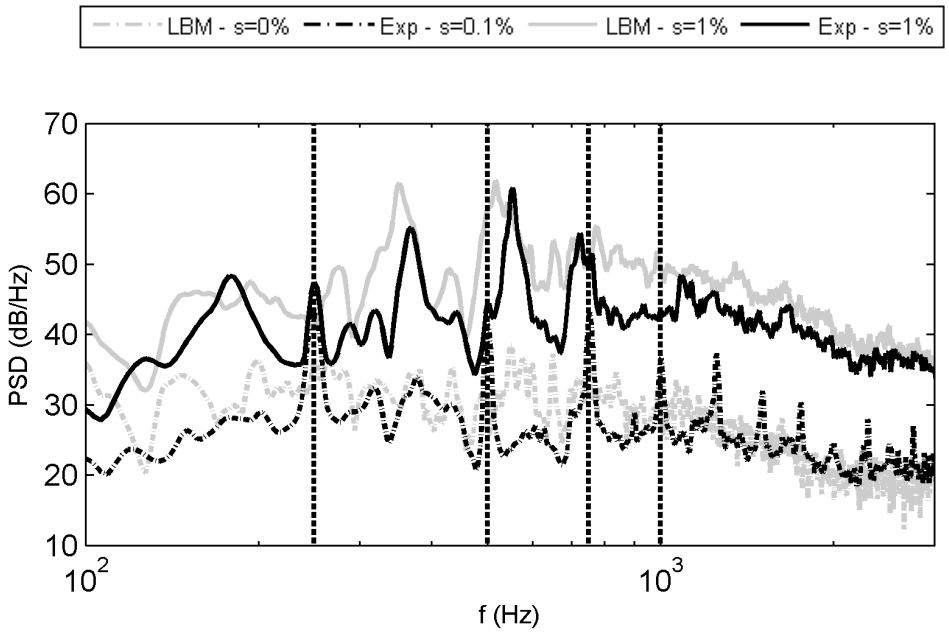

(a)

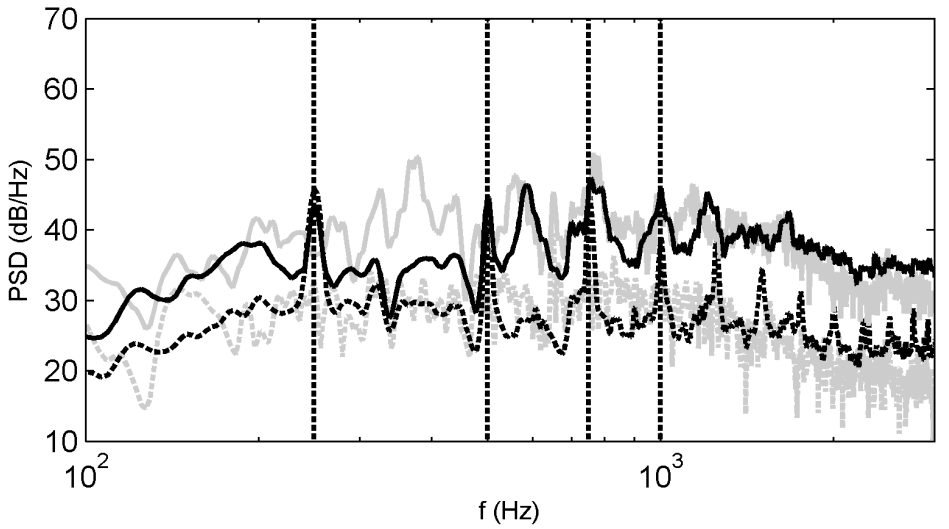

(b)

Figure 5.16 Acoustic sound power spectra for one of the off-axis microphone locations for the USI7 fan for the considered operating points (a) $\phi_{part-load} = 0.131$ (b) $\phi_{nom} = 0.154$. BPF harmonics are highlighted using vertical dashed lines.

be caused by the interaction of coherent turbulent structures generated in the tip region of the fan with the rotor blades themselves. This was confirmed using a correlation method devised in the current work to attempts to quantify coherent tip leakage flow structures in a more rigorous manner which will be presented in the next chapter. These sub-harmonic humps are reproduced fairly well up to third order in the simulation, although their frequency is shifted to approximately 70 % of the BPF harmonics; the fourth order harmonic cannot be distinguished from among the broadband fluctuations if it even is present.

There are, however, level discrepancies that can be observed between the experiment and the numerical results. This is especially true for the large clearance configuration, where differences between 5-10 dB overall are observed. These discrepancies are coherent with those observed from the blade pressure sensors in Figs. 5.14 and 5.15, wherein higher broadband levels are observed for the large clearance cases in the simulations whilst for the small gap case the spectral levels are closer together.

All in all the simulation tend to provide a fair representation of the experiment from the comparison aspects available. However, whilst the global fan performance is accurately represented, the near-field and acoustic results do indicate differences in the LBM predicted flowfield when compared to the experiment, where general behavioral trends observed in the experiment are reproduced in the simulation with some spectral shift and level discrepancies.

5.5 Free-Tipped Fan with Complex Tip Geometry

The last configuration investigated from the free tip fan family was the Bosch designed engine cooling fan. As explained previously, the prototype fan was experimentally investigated using a duct configuration. However, the aerodynamic and aeroacoustic properties were investigated on wholly different platforms; the aerodynamic performance was thoroughly evaluated on an AMCA compliant but non-anechoic test rig, whilst the acoustic performance of the fan was appraised in an anechoic environment. In addition to the test environment, significant differences in the test duct assembly geometry were also apparent in the form of the duct length and flowrate control devices at the exit aperture.

In order to correctly represent both test rigs, two simulations were setup to validate the experimental results. The following section covers the numerical domains used for the lattice-Boltzmann simulations of the two cases as well as the ensuing results when compared to the experiments.

5.5.1 Presentation of the AMCA Numerical Setup

The simulation was designed to be a simplified representation of the experimental setup, where the duct assembly was mounted on an ANSI/AMCA 230-12 compliant flow chamber (shown in Fig 3.14) and necessary to limit the intricacy of the simulation (e.g. honeycomb flow straighteners, flow nozzles and make-up fan). The AMCA test rig was modeled in the lattice-Boltzmann simulation by placing the duct assembly in a large simulation domain acting as both inlet and outlet volume to the fan system as seen in Fig. 5.17; this is in opposition to the relatively confined room volume in the experiment. The domain boundaries were defined as freeflow surfaces to accurately model a quiescent domain, with the duct assembly located 2 m above a solid wall boundary as in the experiment. This simulation is hereafter referred to as the *Aerodynamic* setup.

The detail of the duct assembly as modeled in the LBM simulation is shown in Fig. 5.17; the fan-and-shroud assembly is inserted in a 700 mm diameter duct, with the air flowing from the inlet bellmouth towards the outlet diaphragm. In opposition to the RCDB simulation, the flow rate through the fan was not imposed artificially through an outlet boundary condition; the mass-flow through the fan system was instead regulated by varying the size of the diaphragm opening in the simulation and the rotational speed of the fan rotor.

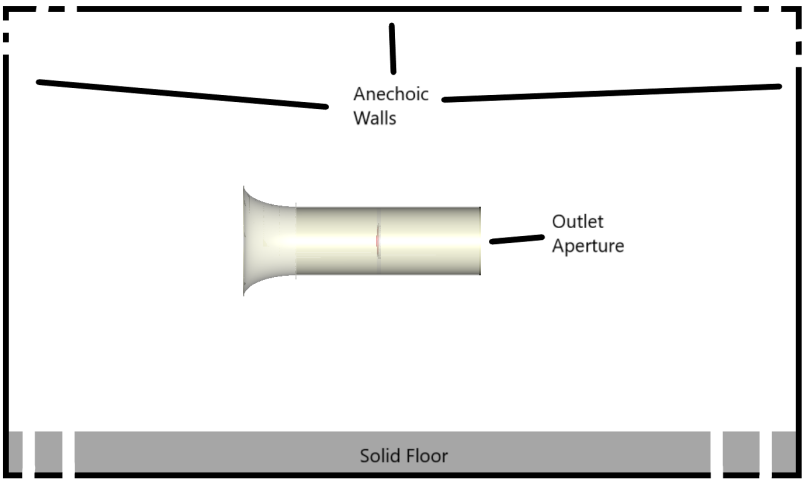

Figure 5.17 Computational domain for the Bosch fan in the AMCA configuration; not to scale

The simulation domain was discretized using a total of 10 VR regions for the finest mesh employed, with a minimum voxel size of 0.5 mm around the rotor for the most refined simulation. The VR regions down to VR3 are shown in Fig. 5.18, with the exception

the finest region VR10, which is a volume created from an offset of the fan surface and comprises a refinement zone in the tip region of the blades.

In order to validate the simulation, two sets of measurement probes were set in the simulation. First of all, two series of 24 evenly spaced circumferential probes located at the duct wall, respectively 25 mm upstream and 35 mm downstream of the rotor, to evaluate the pressure rise across the fan plane through static pressure measurements; this was done to mimic the pressure taps used in the experiment. The pressure rise value was taken as the differential value between the average upstream and downstream static pressure at the wall. Second, a series of 50 radial probes (from the fan axis to the duct wall) located 30 mm behind the fan trailing edge was used to collect velocity data in order to correlate with the 5-hole probe data from the experimental campaign measurements.

5.5.2 Presentation of the Anechoic Numerical Setup

Whereas the AMCA simulation of the Bosch geometry presented in the previous section was aimed primarily at validating the numerical aerodynamic performance of the system against those from the AMCA rig experiment, a second simulation was setup to evaluate acoustic performance. As explained in Sec. 3.3, differences in the duct assembly configuration were present, with the anechoic setup having a shorter inlet length and the flow rate controlled through a sliding plate on the acoustic rig. This is in addition to the acoustic testing having been carried out in an anechoic room as opposed to the reflective conditions found in the AMCA test rig.

Thus, a second simulation to more accurately represent the anechoic rig was setup on the heels of the previous one. It will hereafter be referred to as the *Acoustic* setup. The computational domain is shown in Fig. 5.19 and was tailored to accurately represent the dimensions of the test chamber (4.8 x 3.5 2.6 m to the acoustic lining). The duct assembly was centered along the height and width of the chamber, whilst the bellmouth inlet aperture is situated 3 m from the acoustic lining. In the simulation, the acoustic lining was modeled using porous media to avoid the reflection of acoustic waves into the free fluid volume. The location of all 81 microphone probe locations meant to mimic the experimental microphone grid used to measure the acoustic pressure in the experiment is also shown.

The domain was discretized using 11 VR regions for the finest mesh, with a maximum resolution of 0.5 mm, as shown in Fig. 5.20. The finest resolution region (VR11) consists of an offset of the rotor volume as well as a refinement zone in the tip region. The microphone

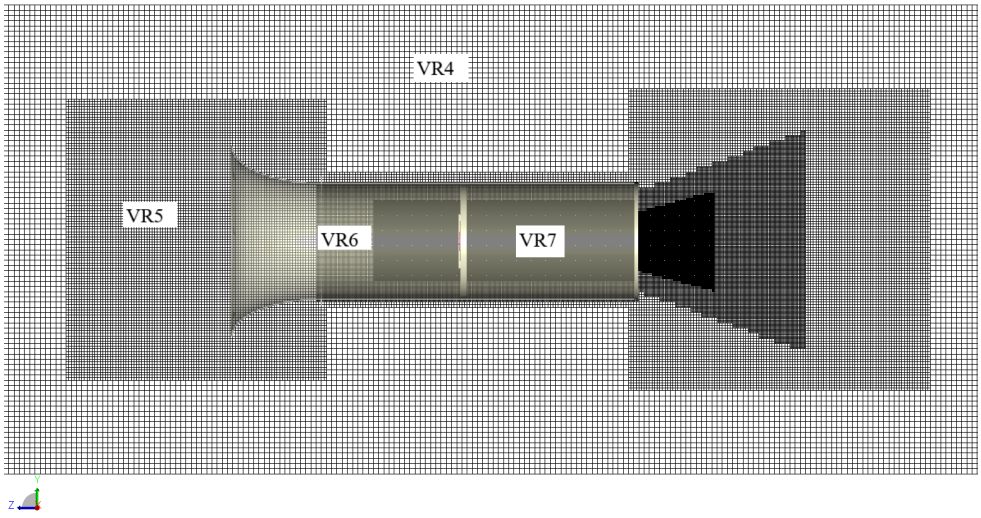

(a)

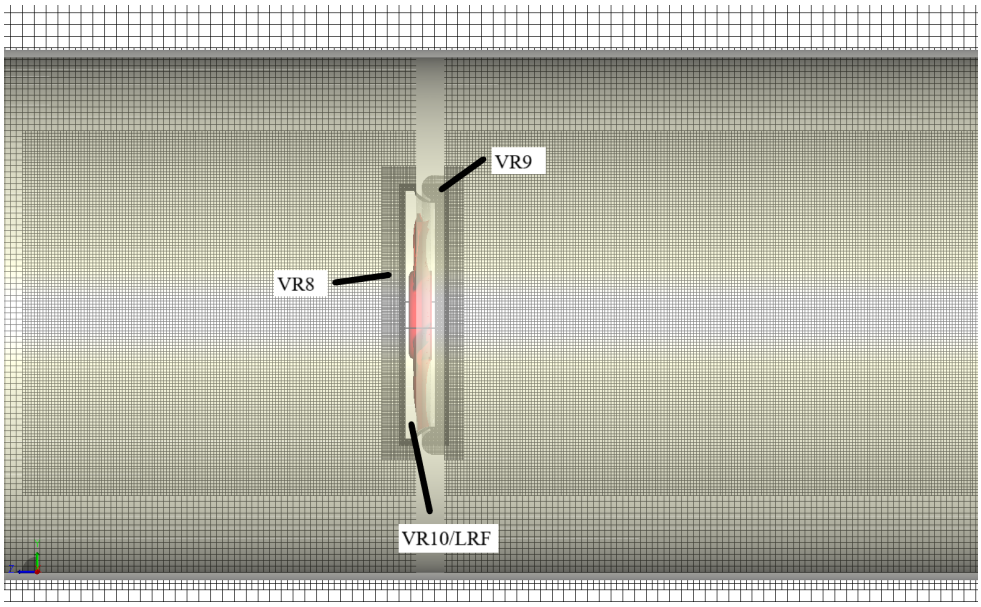

(b)

Figure 5.18 Mesh topology for the Bosch fan in its AMCA configuration (a) around the test duct (b) in the fan region

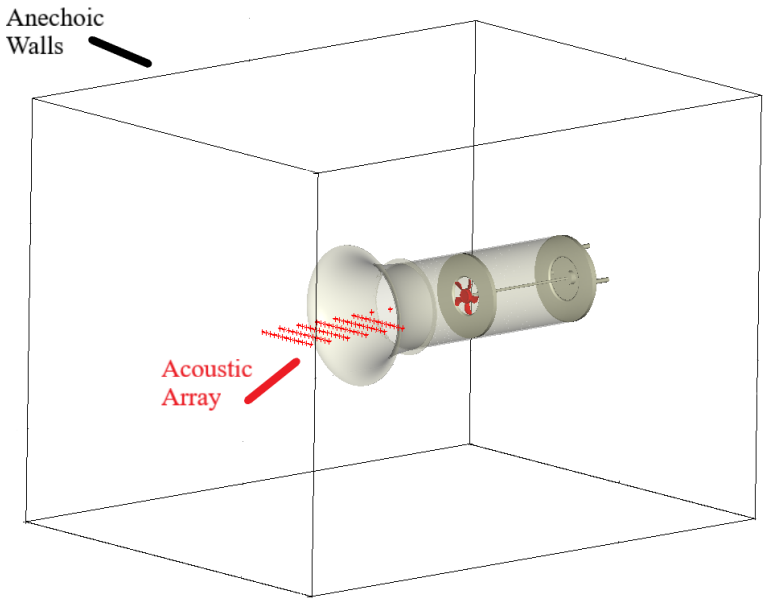

Figure 5.19 Computational domain for the Bosch fan in the anechoic configuration

probe locations shown in Fig. 5.19 are located in the VR region with a 16 mm resolution, allowing for a maximum frequency resolution of 2361 Hz assuming a required number of 10 grid points per wavelength for proper evaluation. Henceforth, references to the microphone positions will be made with regard to the axial position (*Pos*) of the microphone as well as the radial column (*Col*) of evaluation, with the reference position *Pos0* situated at the duct bellmouth inlet plane (down to *Pos(-3)* and up to *Pos5*) and the column number increasing from 1 to 13 from the fan axis to the outer radial position of evaluation.

5.5.3 Aerodynamic Performance Evaluation

A coarse case with a 1 mm resolution, omitting the finest VR region, was used to initiate the simulations and define the required diaphragm opening size or slider plate position to obtain a flow rate of 0.53 m^3/s on either simulation setup. It was also used to compare the pressure rise across the fan obtained numerically across several operating conditions with the extensive experimental performance curve. A grid refinement was then carried out to 0.5 mm for both cases for the grid independance study. The performance curve is shown in Fig. 5.21. It becomes obvious that the *Aerodynamic* simulations largely underpredict the

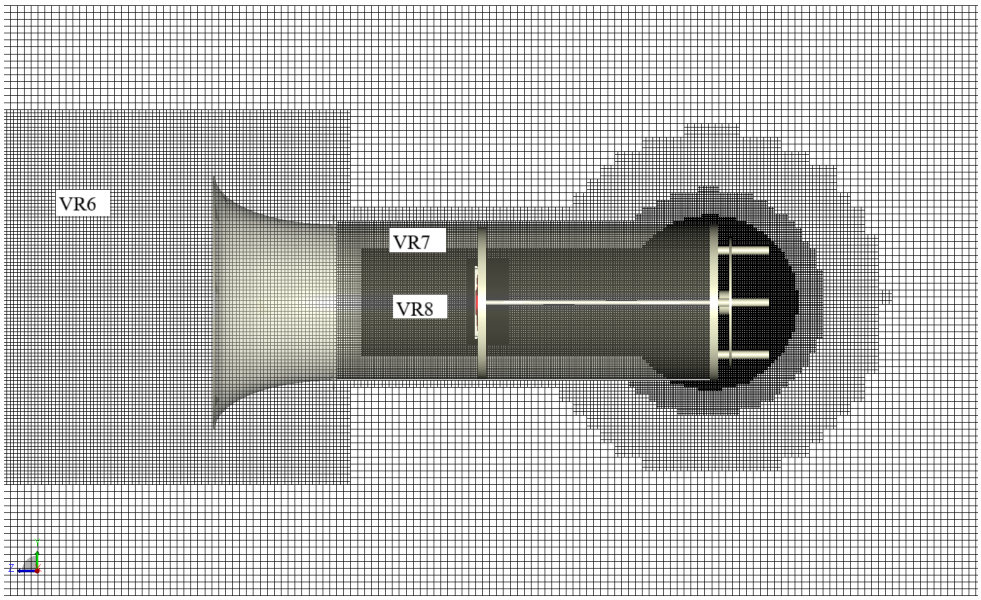

(a)

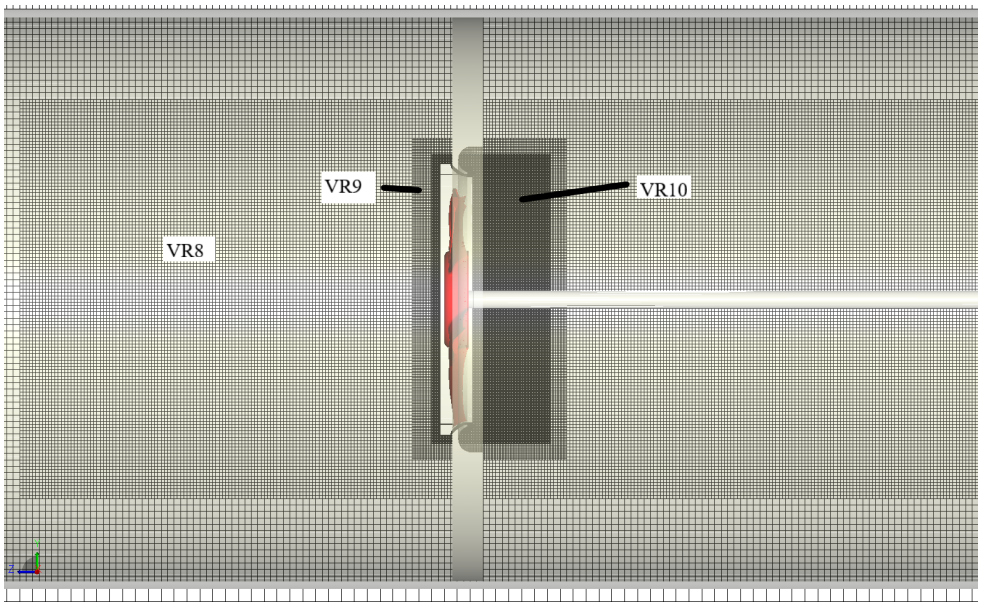

(b)

Figure 5.20 Mesh topology for the Bosch fan in the anechoic configuration (a) around the test duct (b) in the region around the fan

experimental pressure rise (around 20% at the study-specific $Q = 0.53\ m^3/s$ flow rate). However, the slope of the experimental curve is fairly well represented in the 0.35-0.55 m^3/s, with the exception higher flowrate simulated falling almost on the experimental curve breaking the trend. Moreover, refinement of the grid in the rotor region does not modify the predicted pressure rise, indicating a certain level of convergence.

The *Acoustic* setup performance is similar with respect to the average pressure rise across the fan when compared to the *Aerodynamic* simulation. Refinement also seems largely ineffective at modifying the predicted performance, with a difference of around 2 Pa at the study-specific flow rate.

The reader will note that the simulations did not quite reach the required flowrate, having reached values between 0.51-0.52 m^3/s, or a maximum deficit of 4%; this was deemed a small enough difference that it did not warrant running new simulations to set the outlet geometry through further trial and error.

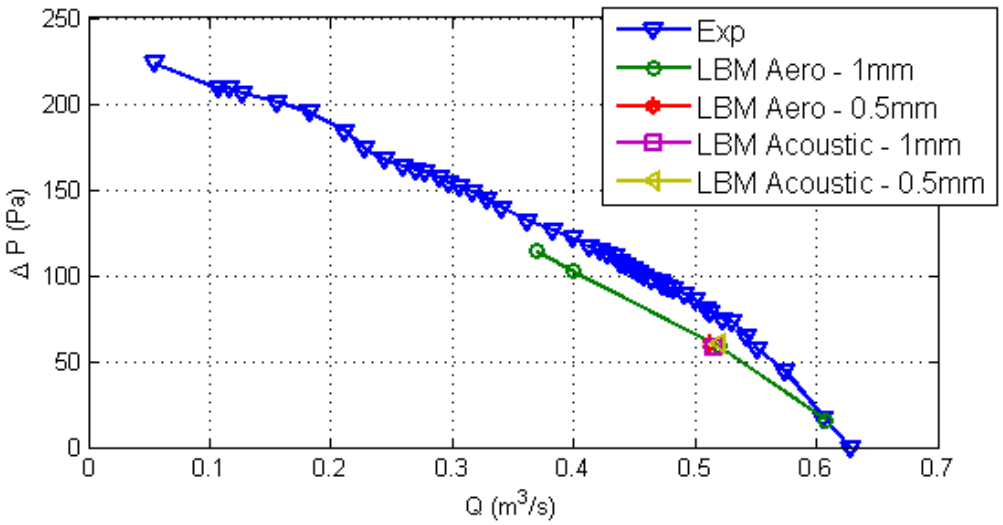

Figure 5.21 Performance characteristic curve for the Bosch fan.

For full transparency, the timeseries of the pressure rise for the different simulations for the study-specific flow rate are shown in Fig.5.22. For the *Aerodynamic* setup, Fig. 5.22(a) confirms the nearly unchanged average pressure rise between the two refinement levels. The initial coarse simulation was run for a long amount of physical time (6.6 s), but the measurement files were only initialized after 2.5 s of physical simulation time, which explains the missing data; this was corrected for the refined mesh. Note that the refined mesh was seeded with the final solution from the coarse simulation in order to shorten the transient settling of the flow.

Fig. 5.22(b) shows the whole range of the timeseries associated with the *Acoustic* simulations at the coarse and refined level; the coarse simulation has a difficult transient startup, with pressure spikes reaching 10 000 Pa, until it 'settles' after roughly 1 s of physical simulation time. Whilst the average pressure rise is comparable between the two, Fig. 5.22(c) focusing on a converged portion of the signal shows that the coarse simulation exhibits high levels of instability in its time signal, with amplitudes reaching 30 Pa. However, the refined simulation is somewhat more settled, with fluctuations on the order of 2-3 Pa around the mean. This indicates a notable change in the behavior of the flow in the downstream portion of the duct.

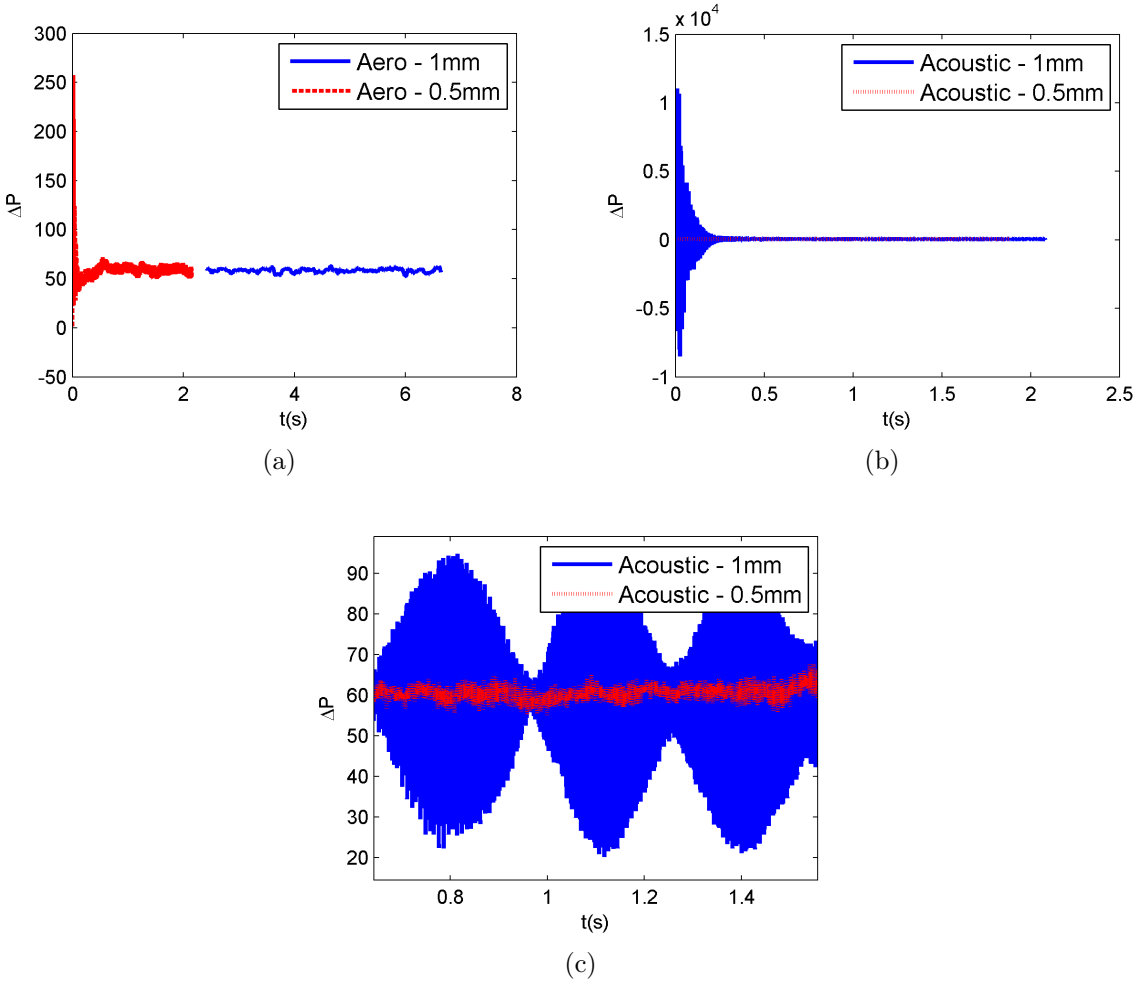

Figure 5.22 Convergence of the pressure rise across the different Bosch fan simulations (a) AMCA configuration (b) Anechoic configuration (c) Detailed view of a portion of the anechoic configuration pressure rise convergence

Finally, for further comparison of the *Aerodynamic* simulation with the experiment, the time-averaged velocity profiles 30 mm behind the fan rotor at a fixed azimuthal position as

a function of the radius of evaluation were also recorded and are shown in Fig. 5.23, with the abscissa showing the velocity levels in m/s and the ordinate in the radius normalized by the leading edge tip radius ($r_{tip} = 0.151$ m). The correlation is fairly good with regard to the axial velocity profile in Fig. 5.23(a); the small deficits observed are coherent with the lower flow rate obtained in the simulations. When looking at the radial velocity in Fig.5.23(b), it can be seen that the velocity profile is similar in the 45-75% normalized radius range. However, larger differences are observed between the simulations and the experimental data in the root and tip regions of the blades.

First, in the hub region, the experimental data shows a negative radial velocity, whilst the simulations predict positive radial velocities in this region. When looking at the tangential velocity profile in Fig. 5.23(c), we see that the experiment also showcases a velocity which is close to double the ones predicted in the simulations near the hub. This is thought to be coherent with the fact that the hollow rotor hub was left open during the experiment, whereas it was closed off in the simulation model. It might also explain in part the pressure rise prediction difference between the experiment and simulation. The experimental radial velocity levels near the tip are also very high when compared to the simulations; the flow in the tip region expectedly fairly turbulent, it is possible that the 5-hole probe could provide exaggerated readings due to a limited directional sensitivity. However, the tangential velocity in the tip region compares fairly well between the experimental and simulation data, with the refined mesh showing a better correlation with the experiment; this is most probably due to the refinement zone in the tip region that allows for a better resolution of the turbulent flow features.

5.5.4 Aeroacoustic Performance Evaluation

The final validation aspect for the Bosch fan rests with the experimental acoustic pressure measurements carried out in the anechoic chamber using a planar grid of 81 microphones on the Bosch fan. The *Acoustic* simulation setup incorporated a series of microphone probe locations to mimic those measurements and provide a suitable basis for comparison. The acoustic spectra for the *Pos0-Col1* microphone is presented in Fig. 5.24, with both the coarse and refined simulations present on the graph. The coarse simulation exhibits significantly lower broadband levels of up to around 10 dB when compared to the experimental acoustics. The refined mesh better shows a marked improvement in the base level prediction up to the second BPF and with regard to the peak levels around 90 Hz and at the first and second BPF, which are however deformed and slightly shifted in the simulation. Definitely higher noise levels are however observed in the inter-BPF frequency

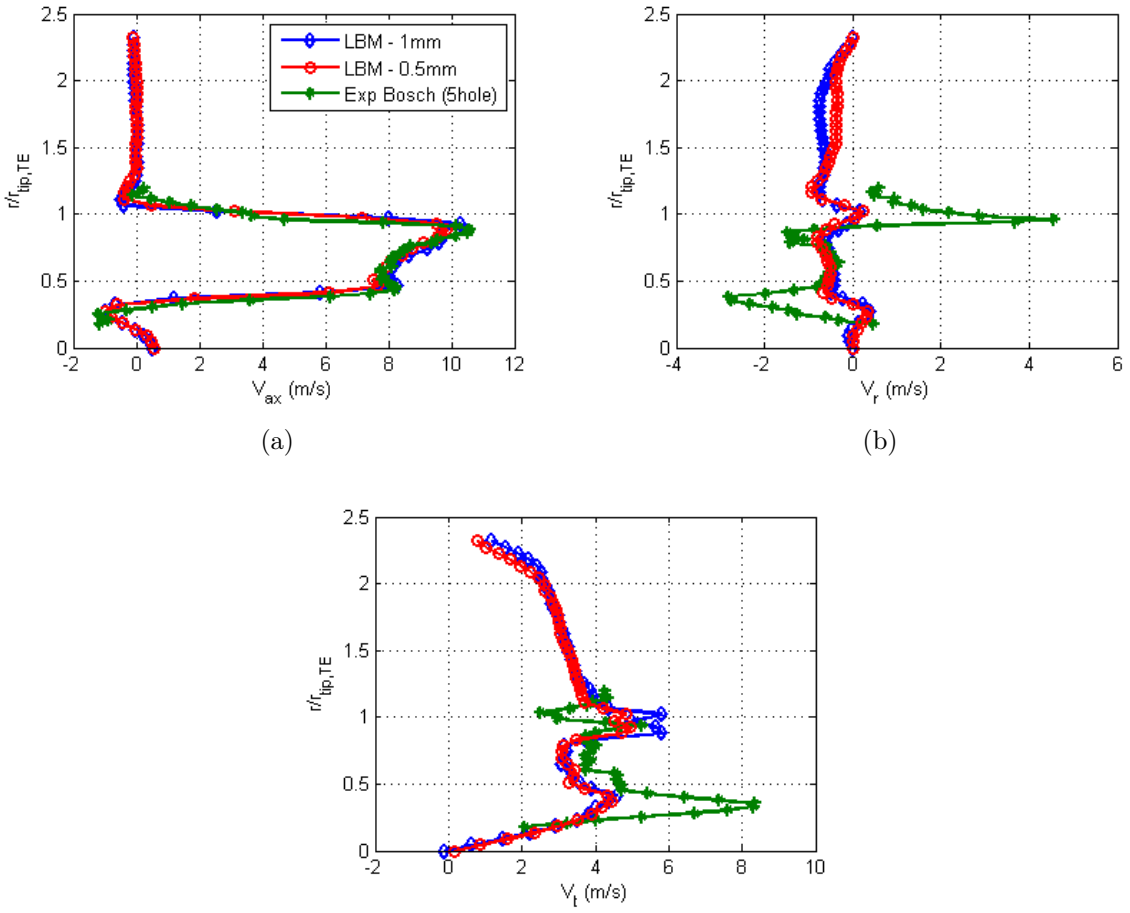

(a) (b)

(c)

Figure 5.23 Time-averaged velocity profiles in the wake of the Bosch fan rotor according to the normalized radius in the cylindrical reference frame for the AMCA setup (a) Axial velocity (b) Radial velocity (c) Azimuthal velocity.

ranges between the first and fourth harmonics on the simulation, with differences of up to 30 dB. A similar behavior is observed at difference microphone locations, indicating the simulation largely overpredicts the acoustic footprint of the fan when compared to the experiment.

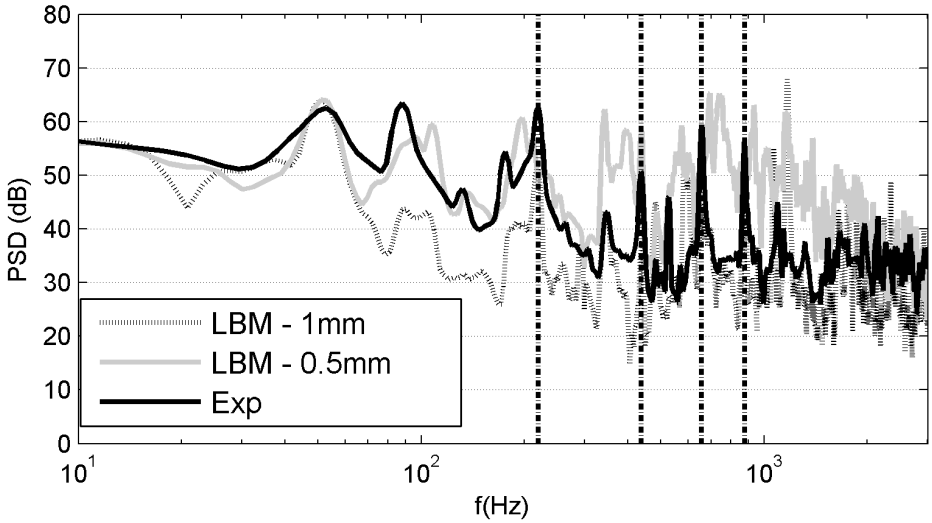

Figure 5.24 Acoustic sound power spectra for the Bosch fan anechoic setup for a microphone located at *Pos(0)/Col(1)* . The BPF harmonics are highlighted using vertical dashed lines.

As a more global comparative measure of the acoustic levels measured, the root-mean-square (RMS) values of the acoustic pressure gathered at each microphone location upstream of the bellmouth inlet plane are reported in Fig. 5.25. The data presents the RMS sound pressure level of the acoustic pressure according to the axial position (*Pos0-Pos5*) of evaluation on the microphone grid, with the abscissa representing the normalized bellmouth radius. The noise level discrepancy observed in the single acoustic spectra is confirmed, and it becomes also apparent that the acoustic directivity of the experimental setup is not properly reproduced in the simulation. The experimental RMS values indicate a hemispherical directivity pattern originating at the fan axis, indicating that plane wave patterns are mainly propagated in the duct. This is coherent with the fact that the experimental spectra is largely dominated by the appearance of strong tonal peaks at the BPF harmonics, which should propagate as plane waves assuming the rotor blades are the source. The numerical results exhibit higher levels at the outer radii, however. Examination of the filtered pressure field in the numerical setup provides some measure of explanation to this behavior. Fig. 5.26 presents the filtered acoustic pressure levels in Pascals according to three frequency ranges corresponding to the inter-BPF frequency tufts with elevated levels observed in the numerical spectra (Fig. 5.24), namely the 330-360 Hz,

510-630 Hz and 710-800 Hz ranges. An axial cross-cut of the simulation domain in the immediate vicinity of the test duct as well as transversal cuts located 300 mm upstream and downstream of the fan are presented for each frequency range.

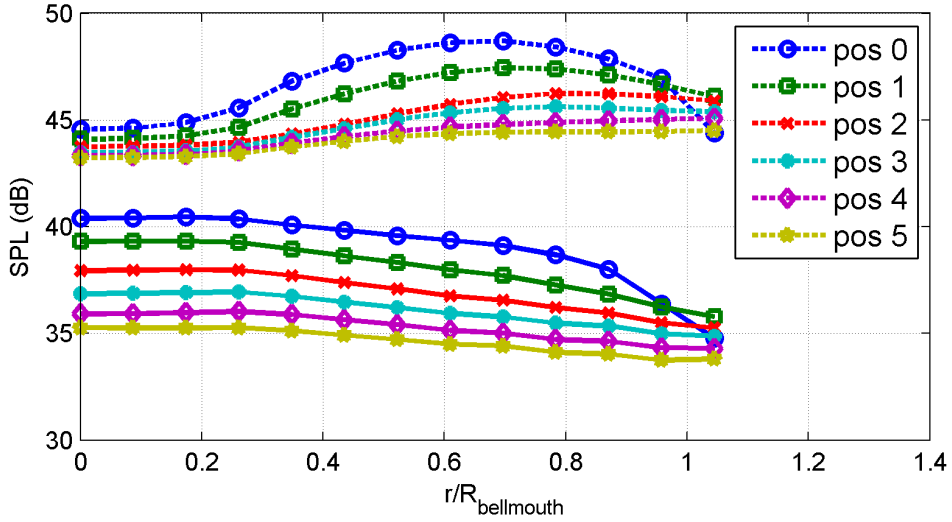

Figure 5.25 Overall RMS acoustic pressure measured at microphone positions upstream of the bellmouth inlet for the Bosch case. The numerical data is presented in dashed lines.

The inception of strong acoustic resonance in the aft chamber, with the apparition of (1,0), (2,0) and (3,0) standing duct modes for the respective studied frequencies. This in turns drive strong acoustic waves in the upstream portion of the test rig and the appearance of strong propagating azimuthal duct modes. The experimental rig would seem to prevent the apparition of these strong modes, whereas the numerical simulation becomes saturated with them. This provides a physical explanation to the discrepancy, but it highlights a fundamental difference between the simulated and experimental rigs. Some of the discrepancy can be explained by the fact that whilst in the simulation solid boundaries are infinitely rigid and provide a perfectly reflective environment, the actual real-life rig is composed of materials with a certain impedance, in effect dampening the modes. However, the effect should not be this radical and does not explain the differences fully.

5.6 Valeo Ring-Shrouded Fan Geometry

Presenting a break in the continuity with the free-tip fan geometries presented previously in this chapter, the following section adresses the validation of the Valeo ring-shrouded

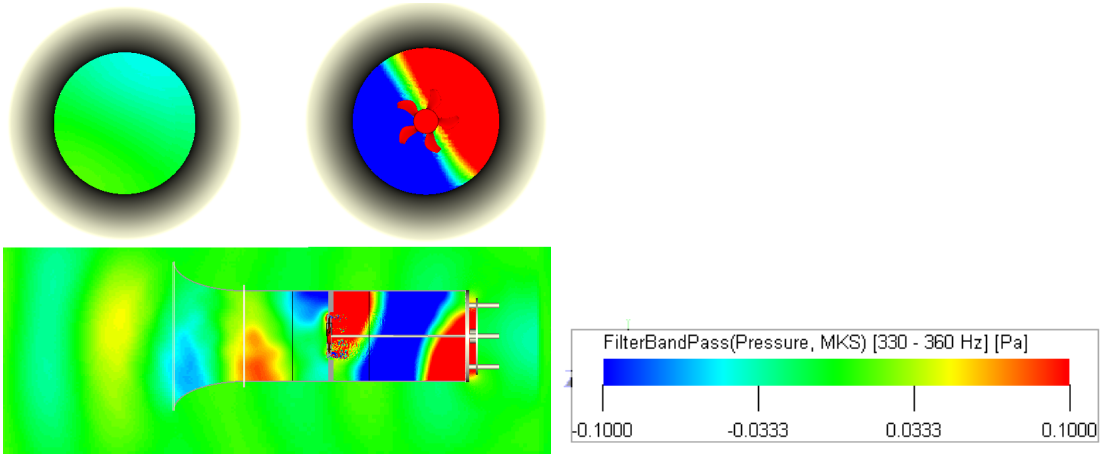

(a)

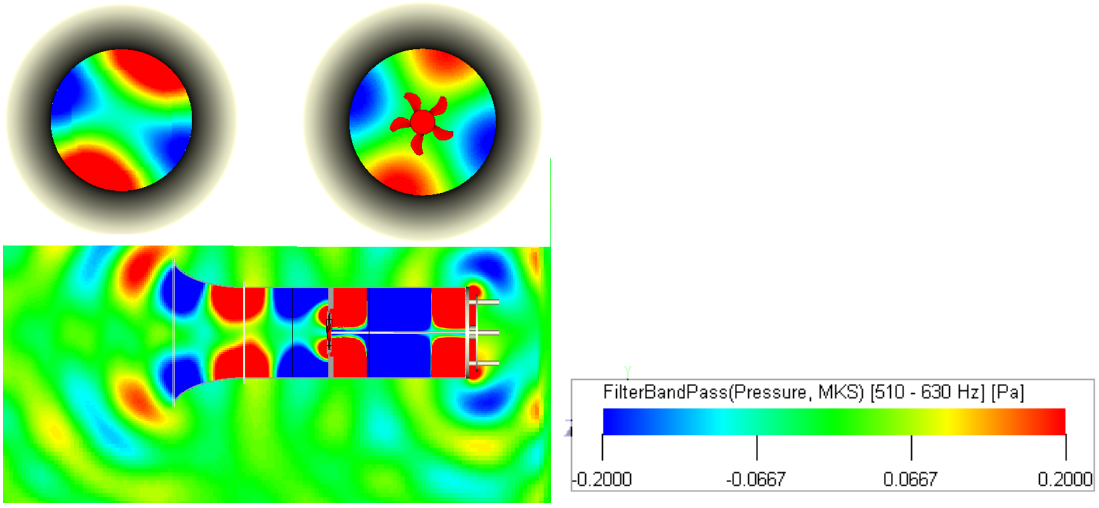

(b)

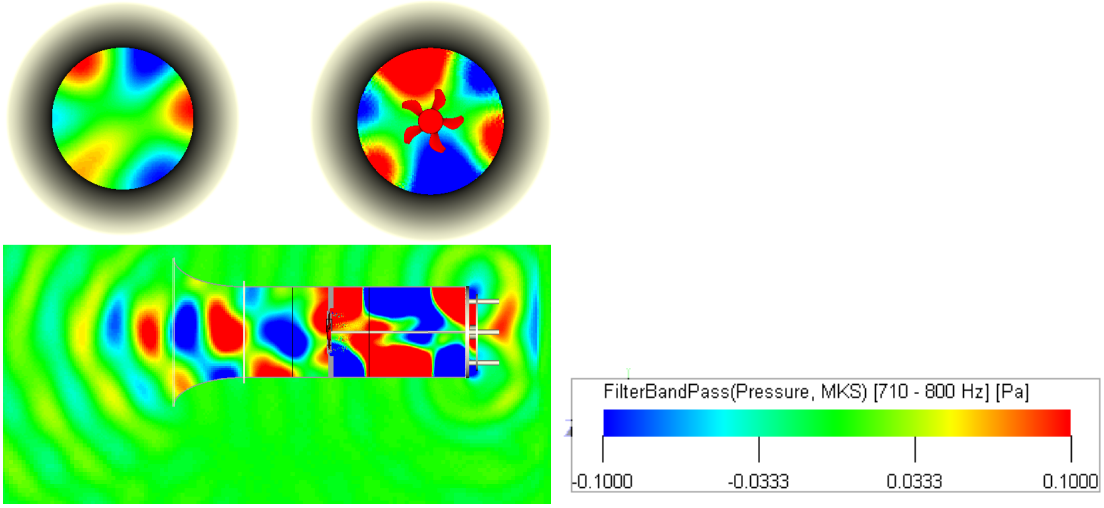

(c)

Figure 5.26 Filtered pressure field in the Bosch anechoic configuration simulation for different inter-BPF frequency ranges (a) 330-360 Hz (b) 510-630 Hz (c) 710-800 Hz.

fan presented in Sec. 3.4.1. The H380 configuration was initially investigated in a plenum-mounted configuration [Foss *et al.*, 2001; Moreau and Bakir, 2003, 2004; Moreau and Sanjose, 2016], but was recently also studied in a ducted configuration [Magne, 2015; Magne *et al.*, 2014]. This provided the opportunity to evaluate the impact of the different installations on the H380 fan performance, both aerodynamic and aeroacoustic. In the following sections, the numerical setups used to replicate the experimental test beds are presented and a comparison of the fan characteristics between the LBM simulations and the experiments is carried out from both the aerodynamic and aeroacoustic point of views.

5.6.1 Presentation of the Flush-Mounted Numerical Setup

The flush-mounted setup was previously numerically investigated using a wide range of methods (from RANS to LBM) [Magne, 2015; Magne *et al.*, 2014; Moreau and Sanjose, 2016; Pérot *et al.*, 2010a]. The LBM simulation used in the current work to represent the flush-mounted setup is virtually identical to the one described by Pérot et al. [Pérot *et al.*, 2010a]. The simulation domain is presented in Fig 5.27 and is meant to loosely reproduce the aerodynamic test conditions in the AFRD facility (described in Sec 3.4.1); the fan intakes the air from a large room volume wherein the test plenum is located. The test plenum is 2.8 m long along the fan axis and has a 1.9 m wide cross-section, compared to the 3x3x2 m dimensions in the AFRD facility. A rectangular duct is modeled in the simulation to direct the outflow; an outlet boundary condition is imposed at the end surface in order to control the flowrate through the system. In the original simulation, the massflow was imposed in order to impose the flowrate; however following the observations made as to the impact of such an outflow condition in the RCDB simulation, as shown previously in this chapter, it was decided to switch it to a velocity outlet boundary condition in the current work. This allowed for further investigation of the effect of the outflow boundary condition on a different fan geometry. In the experiment, aeroacoustic measurements were mainly carried out in the former Valeo reverberant wind tunnel; to model this properly, the intake room volume is bounded by solid wall surfaces, except for the surfaces located directly upstream and downstream which are defined as free-flow conditions, with the fan axis located exactly 1 m above the floor surface as in the experiment. This is in stark contrast to the previous simulations wherein an anechoic or semi-anechoic propagation domain was modeled.

The simulation domain was decomposed using 12 VR regions, with the finest resolution in close proximity to the fan being 0.5 mm having been found to be sufficient for grid

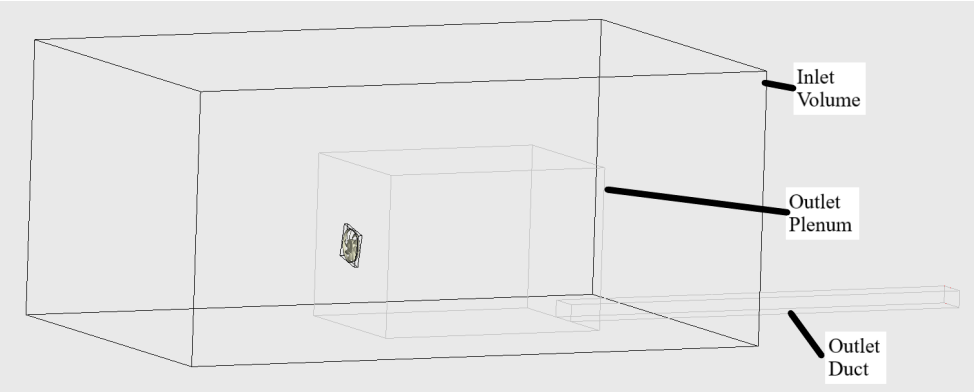

Figure 5.27 Computational domain for the H380 fan in the plenum configuration

independant results [Moreau and Sanjose, 2016]. The mesh topology in the fan general vicinity of the fan is shown in Fig. 5.28.

The pressure rise across the fan plane was measured using two pressure probes located near the fan plane wall respectively inside the intake volume and test plenum, as highlighted in Fig. 5.28(a). A series of 33 probes located on a virtual hemispherical surface with a radius of 1 m and centered on the fan was also used to record the acoustic pressure ahead of the fan in order to calculate the acoustic power radiated from the fan to compare with the experiment. The acoustic probe array spans spans VR regions 6-8, with the minimum voxel size reached 16 mm, leading to a maximum frequency resolution of 8425 Hz assuming a minimum required number of 10 points per wavelength for proper evaluation.

5.6.2 Presentation of the Ducted Numerical Setup

The second numerical setup used for the H380 fan is identical to the one described in Magne's work [Magne, 2015; Magne *et al.*, 2014], where the fan is inserted in a test duct assembly similar to those used for the USI7 and Bosch fans. The simulation domain is shown in Fig. 5.29. In the simulation, the duct assembly is centered in a large volume from which the air is ingested at the bellmouth inlet; the air is then recirculated into the room through the plug termination outlet. The outer boundaries of the inlet volume are defined as free-flow surfaces with high damping properties to prevent the reflection of acoustic waves into the domain.

The simulation domain was decomposed in 12 VR regions, with resolution of 0.5 mm in the vicinity of the fan, which was shown to be sufficient for grid independence by Magne

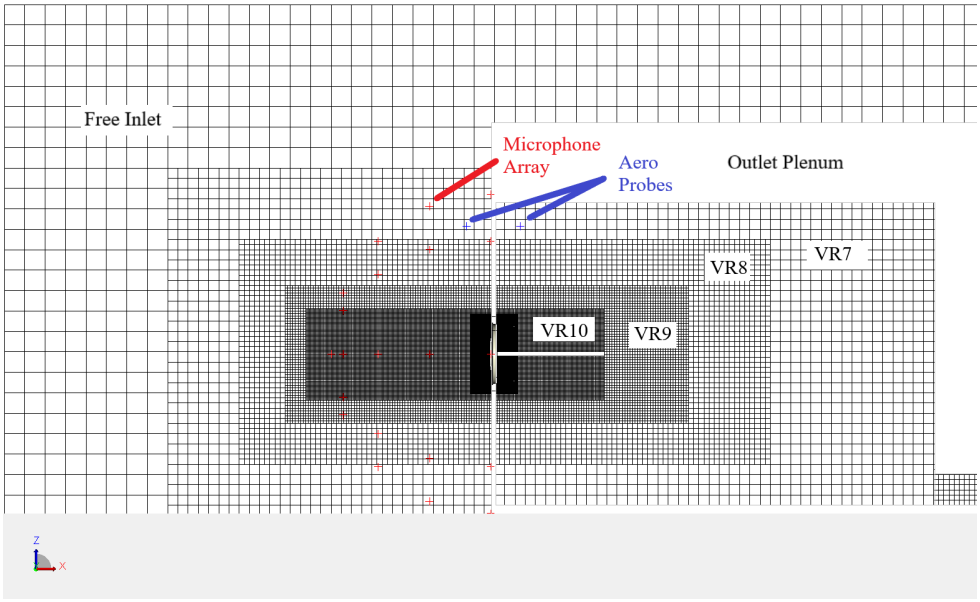

(a)

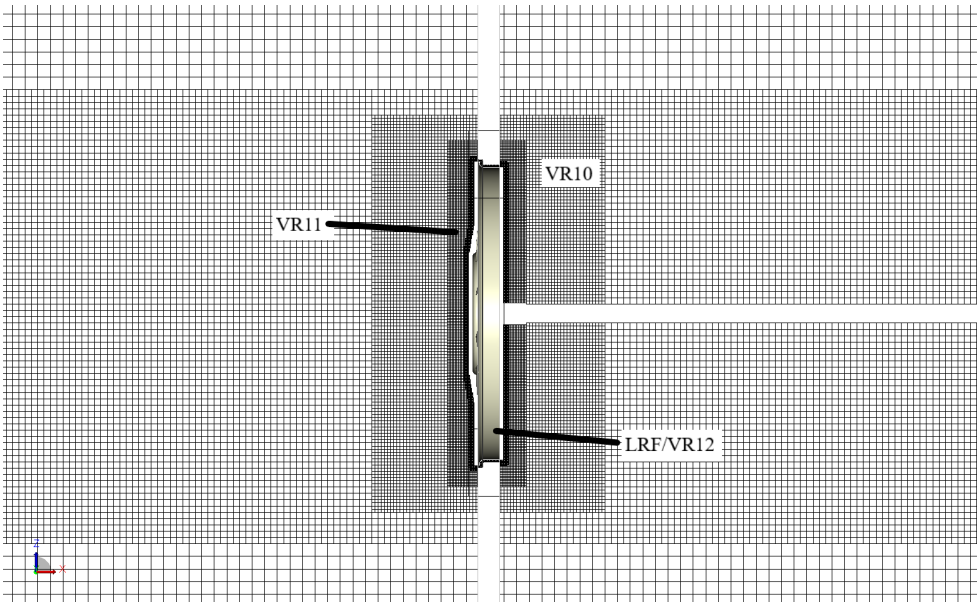

(b)

Figure 5.28 Computational mesh for the H380 fan plenum configuration (a) around the test plenum (b) in the region around the fan

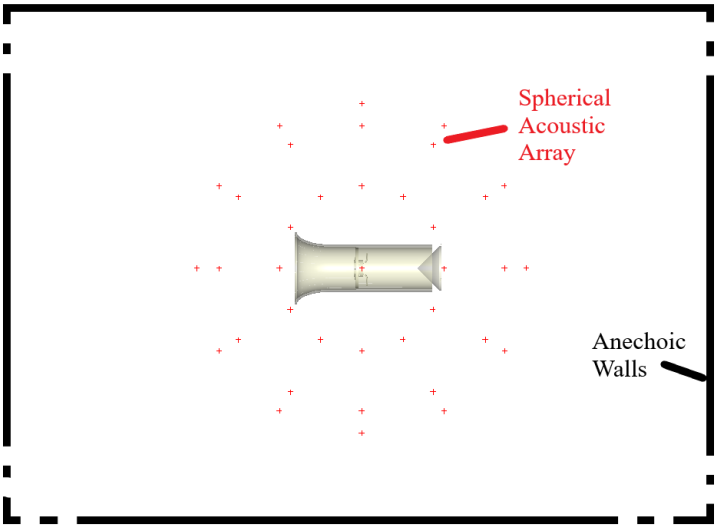

Figure 5.29 Computational domain for the H380 fan duct configuration; not to scale

for this configuration. The grid topology in the immediate proximity of the duct assembly is shown in Fig. 5.30.

The acoustic pressure around was measured using a series of 67 evenly-spaced probes on a full hemisphere with a radius of 1.5 m centered on the fan (see Fig. 5.29) and located in VR region 4 (64 mm voxel grid size), allowing for a maximum frequency resolution of 1060 Hz assuming a required 10 points per wavelength for proper evaluation.

5.6.3 Aerodynamic Performance Evaluation

As with the previous machines, the first step in evaluating the aerodynamic behavior of the Valeo fan was to compare the numerical and experimental overall performances obtained for the system on the two setups considered. To start off, the performance curve of the plenum mounted H380 fan is presented in Fig. 5.31. As mentioned previously, the plenum configuration simulation used for this study is virtually identical to that run by Moreau and Sanjosé [Moreau and Sanjose, 2016], with the exception of the fact that the outlet boundary condition used to regulate the flow rate through the fan was modified from mass flow to a velocity outlet condition to investigate whether it impacted the results as with the RCDB fan (see Sec. 5.3). The previous simulation results from Moreau and Sanjosé are included in the graph. Overall the agreement of both simulations with the experimental data is more than satisfactory; it should be noted that the current work only simulated the fan at the design flowrate of 2500 m^3/h, and that it predicts a pressure rise of 226 Pa

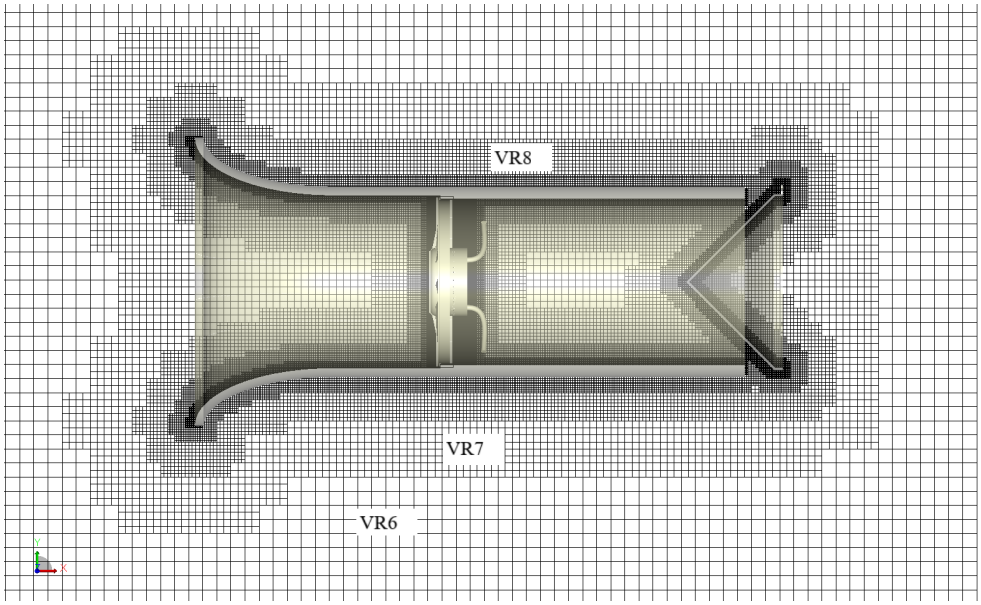

(a)

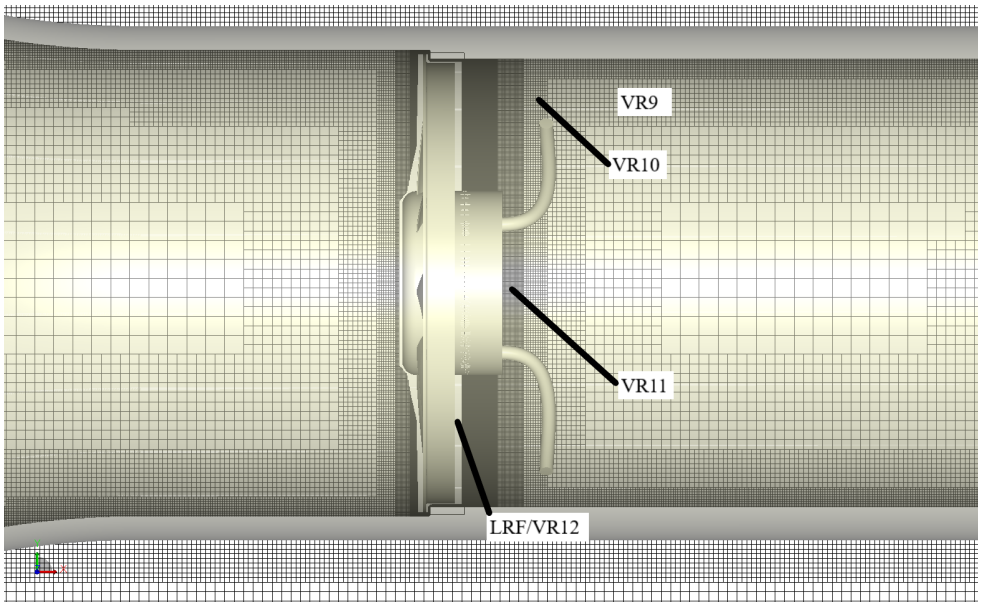

(b)

Figure 5.30 Computational mesh for the H380 fan duct configuration (a) around the test duck (b) in the region around the fan

compared to the previous 209 Pa obtained by Moreau and Sanjosé. However, it is still well within the experimental scatter range.

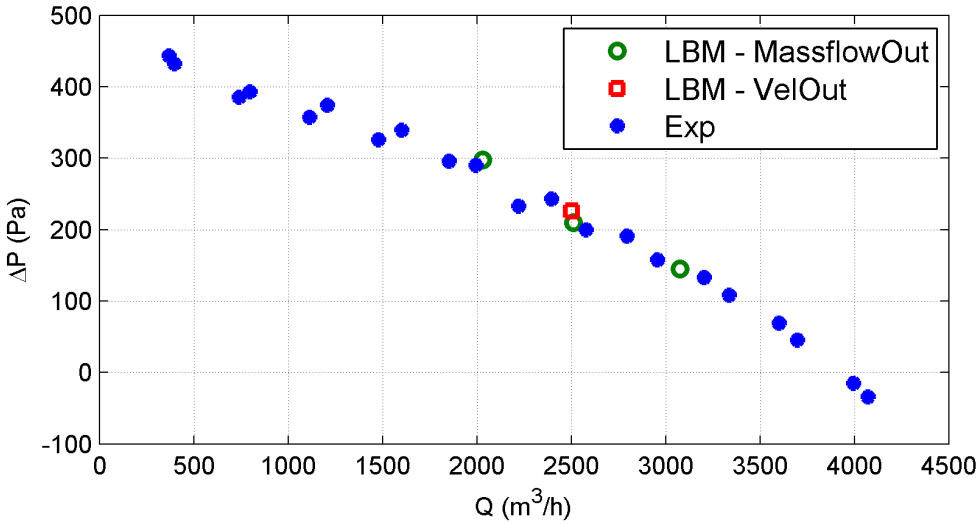

Figure 5.31 Performance characteristic curve for the H380 fan in the plenum configuration.

In similar fashion, the ducted configuration performance curve is presented in Fig. 5.32. Three measurement campaigns were carried out in the experimental test rig. In the first (*Exp 1*) that was performed immediately after receiving the newly manufactured stator/fan mount section of the rig, a sharp discontinuity is observable in the recorded pressure rise around the 1500 m^3/h mark; this was caused by a hairline fracture of one of the stator arms for the motor mount, modifying the rigidness of the setup and thus leading to a decrease in the performance of the fan (the high flow rates were the first to be tested).

Note that in the experiment, the maximum attainable rotational speed was 2450 RPM due to power supply limitations, as opposed to the design 2500 RPM used in the simulations, and often exhibited fluctuations of 20-30 RPM during operation. In most cases at full power, the attainable speed neared 2400 RPM.

To verify this, the normalized performance curves in terms of the dimensionless flow rate and pressure rise coefficients ϕ and ψ, respectively defined in Eqs. 5.1 and 5.2, were examined.

The normalized curves for rotational speeds spanning from the 2400 RPM ranged down to 1600 RPM in 100 RPM increments during *Exp 1* are shown in Fig. 5.33. With the exception of the higher flow rate points from the 2400 RPM curve before the stator arm failure and an outlier in the 2300 RPM series of points at $\phi = 0.33$, all the curves merge

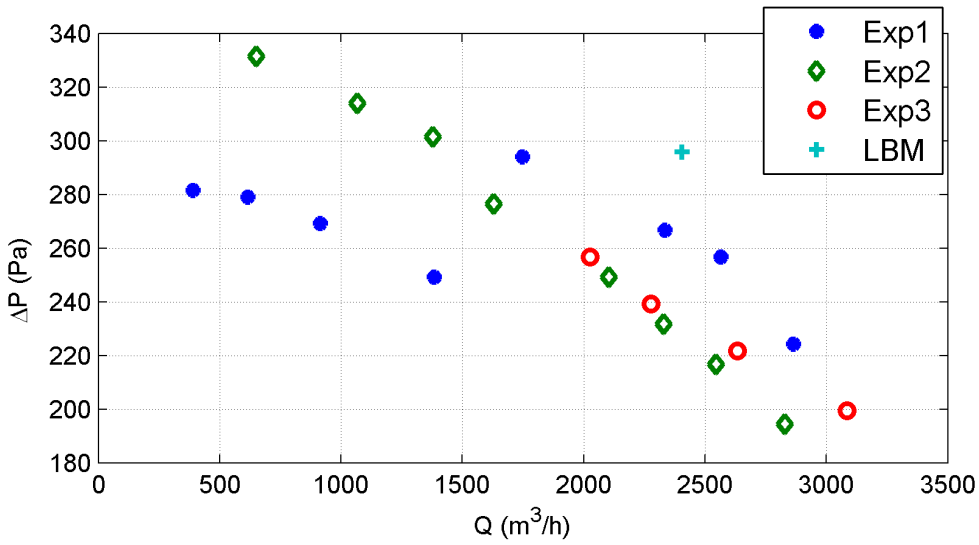

Figure 5.32 Performance characteristic curve for the H380 fan in the ducted configuration.

together fairly accurately, indicating similar flow conditions according to fan similarity laws.

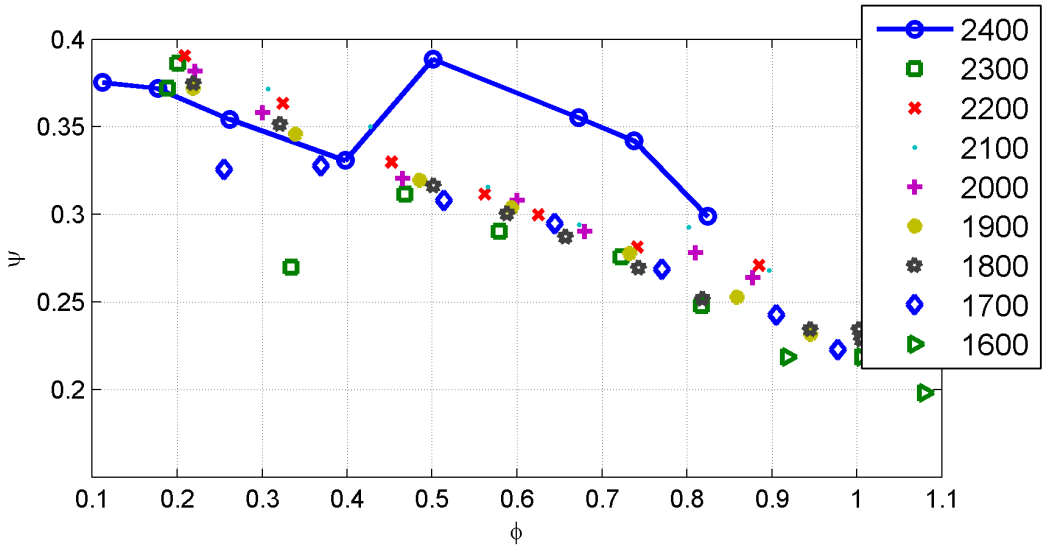

Figure 5.33 Dimensionless performance characteristic curve of H380 fan in the ducted configuration in *Exp 1*.

Repairs were affected to the damaged arm, and two more rounds of measurements were carried out at the maximum attainable speed (curves *Exp 2* and *Exp 3* from Fig 5.32). Representing them using the aforementioned dimensionless coefficients, Fig. 5.34 is obtained. Whilst a measure of stiffness is restored compared to the initial tests, the similarity curves from the second and third rounds of experiment do not quite merge with the

initial curve (around 12% difference in the pressure rise coefficient). This helps explain the higher pressure rise predicted by the LBM simulation, which can be credited to the numerical setup using infinitely rigid solid conditions.

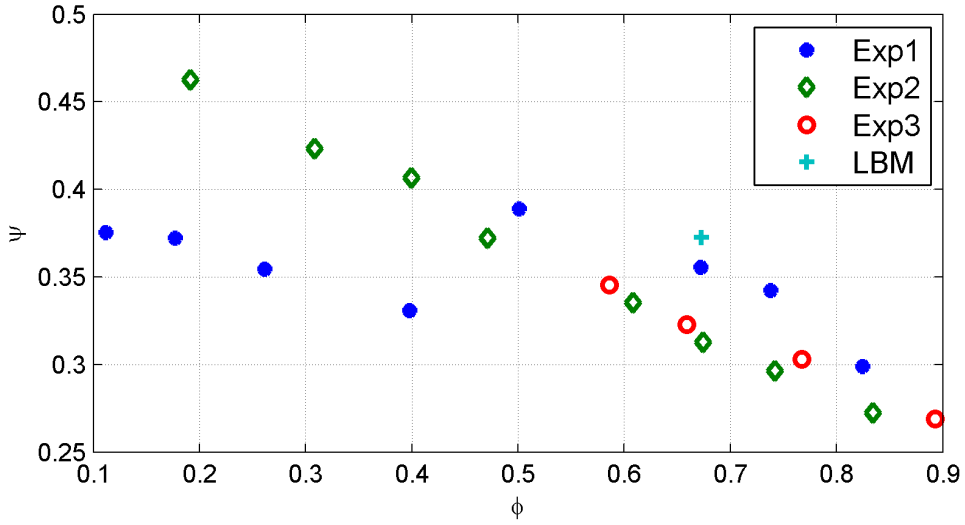

Figure 5.34 Dimensionless performance characteristic curve for the H380 fan in the ducted configuration fort he nominal rotor speed.

Further quantitative assessment of the performance of the simulation was performed using hot-wire anemometry measurements carried out at Michigan State University's AFRD facility where the flow velocity components were measured 33 mm behind the fan trailing edge [Foss *et al.*, 2001]. In the experiment, measurements were phase-averaged to obtain the velocity components for a fixed orientation of the rotor. The phase-averaging methodology was replicated in the simulations to provide a suitable basis for comparison. The azimuthally averaged radial velocity profiles for both the experiment and simulations, including the previous H380 plenum simulation by Sanjosé [Moreau and Sanjose, 2016], are shown in Fig. 5.35. The current plenum configuration simulation results are very similar to Sanjosé's simulation results, with the differences being attributable to the longer physical time used for the phase-averaging process in the current simulation, and show a reasonable agreement with the experiment.

Whilst the experimental results are not meant to validate the ducted configuration, comparing it to the plenum simulations yields some interesting information. Note here that while the plenum configuration simulations had a flowrate around 2500 m^3/h, the duct simulation had a 2405 m^3/h flowrate, which accounts for the level discrepancies in the axial velocity profiles that are very similar otherwise between all simulations. However, the duct configuration exhibits overall higher tangential velocities, with this phenomena

being exacerbated near the tip and root of the blades. This is in line with the higher pressure rise observed on the configuration, although differences in the measuring method between the configuration somewhat obfuscate this fact by looking at the performance curves alone.

The radial velocity profile is also very different in both shape and level between the two simulations, with the radial velocity visibly close to zero over 40% of the span for the ducted configuration and a much weaker deviation near the tip. Two factors contribute to this dissemblance. First off, the plenum configuration models the hollow plastic model, including the molded ribs inside the hub, which, as Moreau and Sanjosé pointed out [Moreau and Sanjose, 2016], act as a centrifugal fan would and induce strong radial velocities at the hub whereas the duct simulation rotor is in effect sealed by the stator hub. This naturally leads to the second factor, which is that the flow is strongly restricted in the radial direction by the annulus walls of the ducted configuration comparatively to the more free-field domain of the plenum mounted configuration; the latter thus exhibits a strong radial deviation of the throughflow, as highlighted in Fig. 5.36.

5.6.4 Aeroacoustic Performance Evaluation

Once again in similar fashion to the previous sections, the final quantitative assessment of the detailed ring-shrouded Valeo fan simulations was concerned with comparing the numerical acoustic footprint obtained in the simulations with those measured during experiments. Both simulations were run to allow for at least 1 s of statistically converged acoustic data. As a reference, Fig. 5.37 presents the time series of the acoustic pressure measured on a probe located upstream on the fan axis for the H380 simulations considered in this section. Both simulations converge fairly rapidly.

As mentioned in the previous sections, the plenum configuration was previously investigated experimentally from an acoustic point of view in the Valeo reverberant wind-tunnel facility, wherein the acoustic power (SWL) radiated towards the suction side of the fan was estimated using a three microphone technique. This is in contrast to the previous test cases which relied on sound pressure level spectra (or the power spectral density estimation) for the validation of their acoustic performance. In order to replicate the Valeo acoustic power measurements in the simulation, a more extensive array of 33 microphone probe locations located on a virtual hemisphere 1 m in radius centered on the fan to better capture the radiated acoustics, allowing for a more discretized integration to be carried out. The resulting SWL spectra is presented in Fig. 5.38. The results from the previous simulation by Moreau and Sanjosé [Moreau and Sanjose, 2016] for the sister 0.5 mm res-

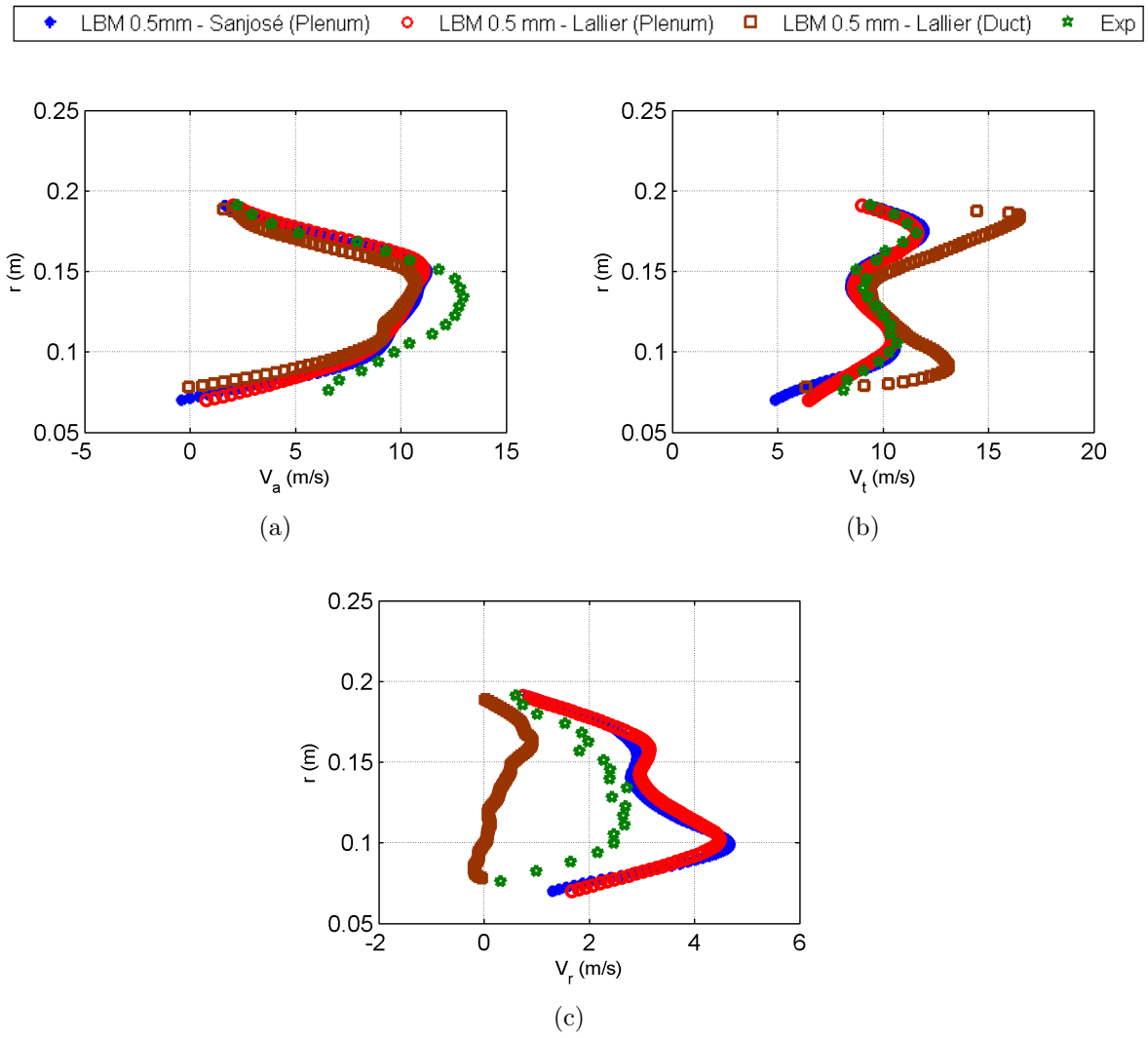

(a) (b) (c)

Figure 5.35 Phase-averaged velocity profiles collected 33 mm downstream of the trailing edge for the H380 fan in the cylindrical reference frame (a) Axial velocity (b) Azimuthal velocity (c) Radial velocity.

olution case of the current work is shown in addition to the experimental SWL levels. It quickly becomes clear that the modification of the outflow boundary condition between the two simulations did not globally improve the prediction when compared to the experimental data, as both show nearly identical spectra in the 100-2000 Hz range. This is in exception of a net decrease of the tonal peaks at 125, 187 and 222 Hz on the lower end of the presented frequency range, which were attributed to spurious modes from the test plenum outlet duct by Moreau and Sanjosé; the lowered levels of these peaks as a result of the modification of the outflow condition would seem to confirm this fact.

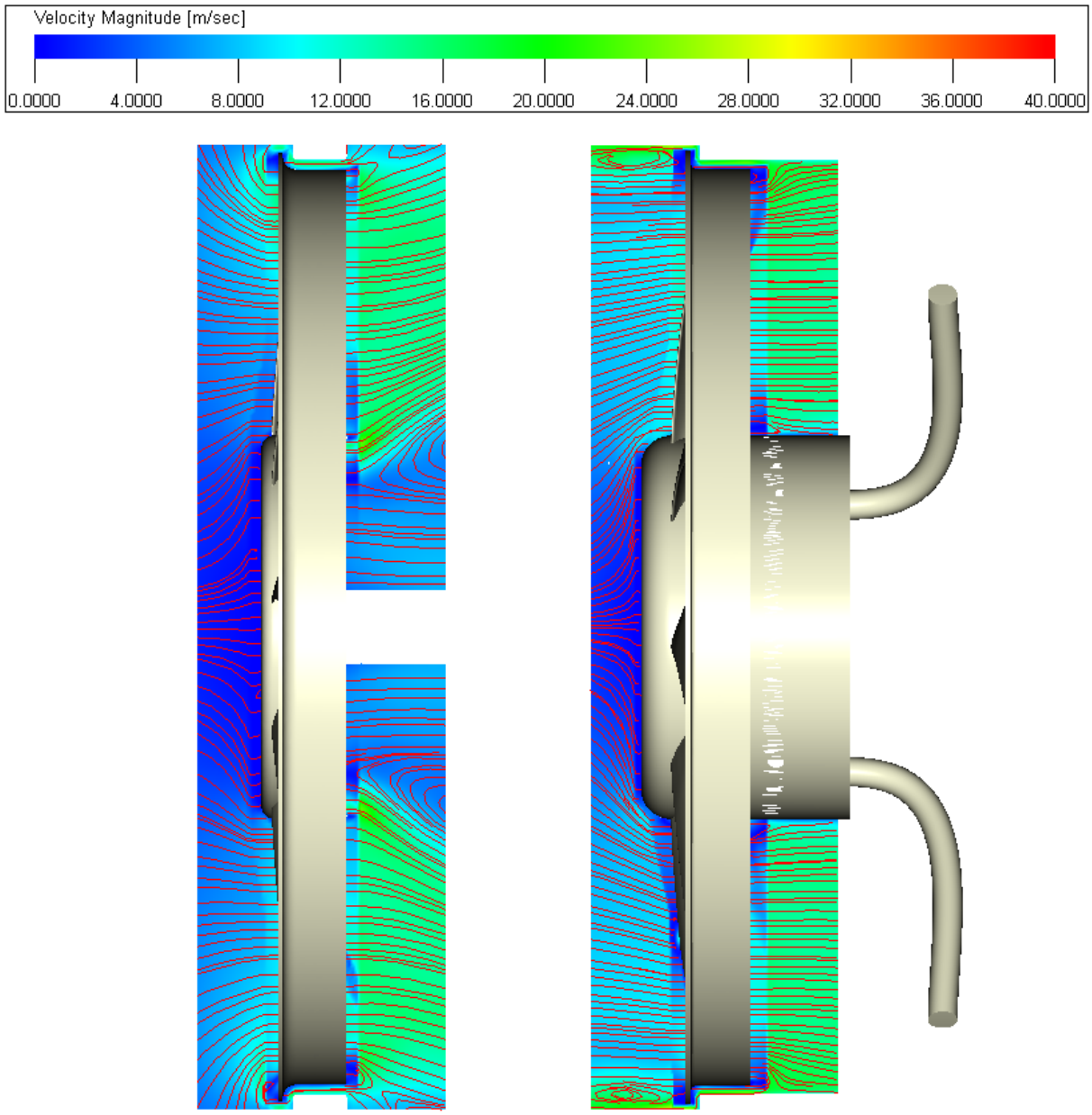

(a) (b)

Figure 5.36 Time-averaged meridional streamlines superimposed on contours of velocity magnitude for the (a) Plenum H380 simulation (b) Ducted H380 simulation

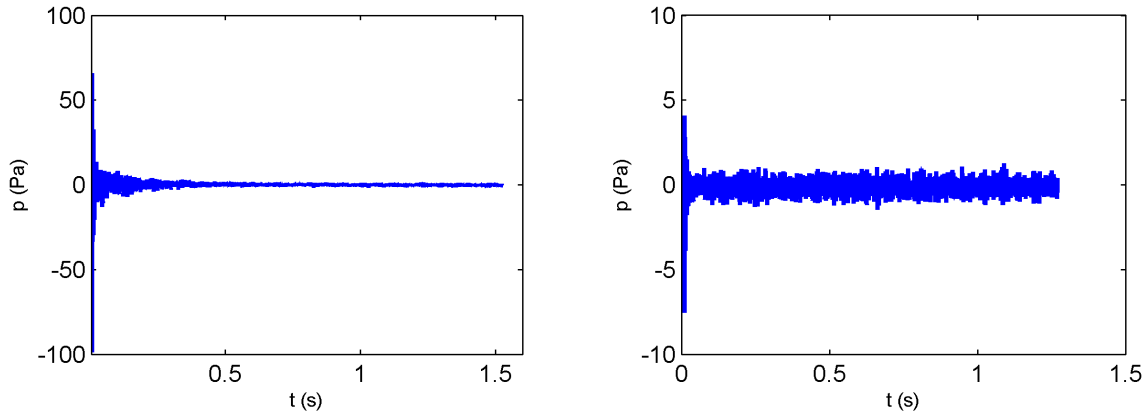

(a) (b)

Figure 5.37 Convergence of the acoustic signal across the H380 simulations (b) Plenum configuration (b) Ducted configuration.

Further delving in the spectral features observed in Fig. 5.38, an important difference that is observed is the absence of the first two harmonics of the BPF tones in the numerical spectra wheras the experiment shows clear peaks at 375 Hz and 750 Hz; the higher order harmonics are indistinguishable from within the other spectral features, most notably the third harmonic which is merged with a broadband hump in the 800-1000 Hz range. This behavior is easily explained by the fact that the physical prototype distorts during operation and causes an eccentric tip clearance, shown to cause the occurrence of these tones [Fukano *et al.*, 1986]. Meanwhile, in the simulation, perfect axisymmetry is maintained at all times.

The broadband hump centered around 320 Hz and its harmonics up to third order in the experiment, linked to the interaction of the rotor blades with coherent structures rotating at a fraction of the rotor speed issued from the backflow through the rotating ring gap [Magne, 2015; Magne *et al.*, 2014; Moreau and Sanjose, 2016; Piellard *et al.*, 2014], are also visible in the simulations, but their central frequency of occurrence is shifted to approximately 285 Hz and harmonics. The need for further identification and characterization of these flow structures is the core of the next chapter.

For the ducted configuration, acoustic measurements were carried out internally at the Université de Sherbrooke using a semi-circular array of 19 microphones, as presented in Sec. 3.4.1. As exposed in the aerodynamic performance evaluation, neither the simulation nor the experiment reached the nominal operating point of 2500 m^3/h at 2500 RPM rotor speed, with the simulation exhibiting a flowrate of 2400 m^3/h at 2500 RPM whilst the experiments failed to reach the nominal rotational speed. However, using the normalized

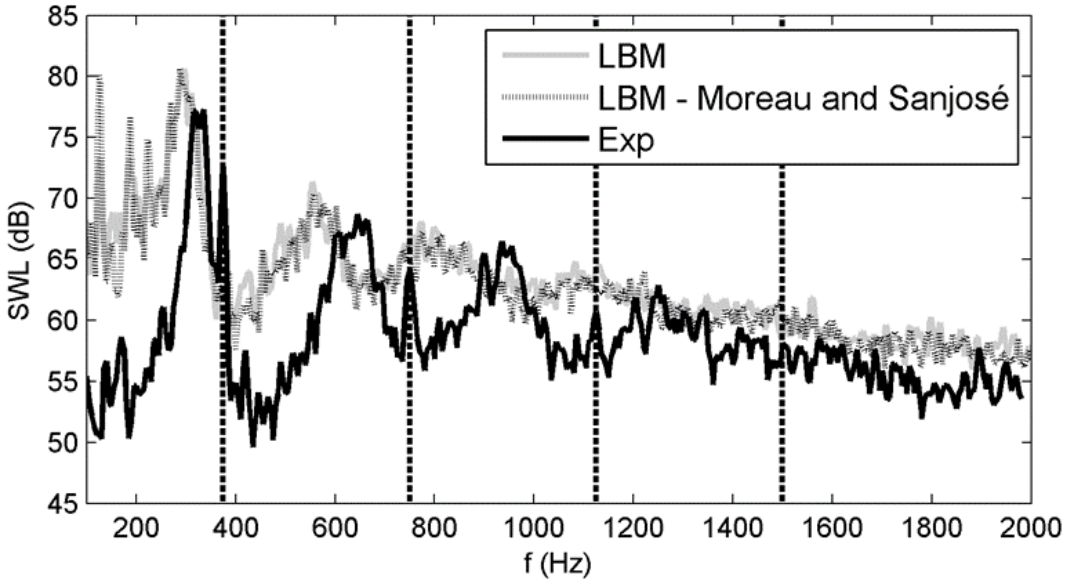

Figure 5.38 Acoustic power spectra (SWL) for the H380 plenum configuration. BPF harmonics are highlighted by vertical dashed lines.

performance curve from Fig. 5.34, the normalized flow coefficient $\phi = 0.66$ was selected as the reference point for the evaluation of the acoustic performance of the setup at a similar flowrate in the sense of the fan similarity laws between the simulation and experiments. The acoustic spectra measured on the fan axis on the suction side at a distance of 1.5 m is shown in Fig. 5.39. The experimental and simulation data were both scaled using a dipolar assumption to represent the levels expected at the nominal operating condition, whilst the experimental spectra were also scaled to the simulated measurement point of 1.5 m (as opposed to 1.9 m on the physical setup). Furthermore, a single experimental spectra is shown, as all three experiments produced a nearly identical acoustic signature both in shape and level (to within 0.5 dB).

Comparing the numerical and experimental results, globally a relatively good agreement is found up to 1100 Hz in the shape of the spectra, whereas the simulation generally underestimates the experimental acoustics. This is especially visible when looking at a directivity plot for the RMS acoustic pressure on a semi-circular array of measurements located at 1.5 m on the suction side of the fan in Fig. 5.40, where the simulation is shown to underestimate the experiment by 3-4 dB over all observer positions; however, the RMS directivity plot is indicative of a dipolar acoustic source, validating the noise rescaling method used. The reader will note the appearance of a high tonal peak at 40 Hz in the experimental spectra; this corresponds with the rotor rotational frequency observed for this case, indicating a rotational speed of 2400 RPM for the experiment. The frequency of

this low frequency tone was also seen to change and match with modifications in the fan rotational frequency at lower speeds, reinforcing this interpretation. The occurrence of this tone is most likely explained by the eccentricity of the fan rotor, which can be imparted to the deformation of the model during operation, the imperfect stiffness of the motor mount as well as to the partial failure of one of the stator arms early in the experimental campaign; the numerical spectra is devoid of this tone. This however confirms the rotational speed measured through optical means in the experiment. The first BPF order, although barely protruding, is also visible at 360 Hz on the presented experimental spectra. The simulated spectra is similarly devoid of strong tonal peaks linked to the BPF tones.

In the 200-2000 Hz range, the spectra is dominated by large broadband humps, with a tonal component also visible at 115 Hz. A parallel study, using the current simulation work as a basis, showed that these humps were caused by the scattering of trailing-edge noise by the ducted geometry using an extension of Amiet's theory in conjunction with a BEM solver [Christophe *et al.*, 2016]. The second tonal component at 258 Hz in the 200-300 Hz range dual peak in the experiment is of particular interest however in the current study as it is not predicted by the trailing-edge noise model. It is however very similar to the BPF sub-harmonic noise mechanism linked to the interaction of coherent structures forming upstream near the tip of the blades as a result of the backflow through the tip gap. The sub-harmonic tone is also visible in the numerical spectra, but the frequency of occurrence is shifted to 274 Hz and the amplitude is much lower. The amplitude difference can easily be explained by the eccentricity of the fan in the physical model, whilst the frequency shift can be a result of different factors including the eccentricity and stiffness difference, but also the difference in the operating point with regards to the rotational speed of the rotor. However, the frequency ratio between the BPF of 360 Hz and the current value of 258 Hz for the sub-harmonic peak in the experiment and BPF of 375 Hz for a sub-harmonic tone of 274 Hz would suggest a faster rotation rate of the turbulent structures of around 30% of the nominal rotor speed in the duct configuration, as opposed to the 20% value suggested by the plenum configuration results and confirmed by Magne through flow observations. The characterization of these structures and the potential differences between the two setups will be covered in the following chapter.

5.7 Mahle-Behr Ring-Shrouded Fan Geometry

The final geometry evaluated in the course of this thesis consisted of a complete engine cooling module constituted of a ring-shrouded fan, an electrical motor, a shroud as well as a series of heat exchangers. It was mentioned that the system was subjected to purely

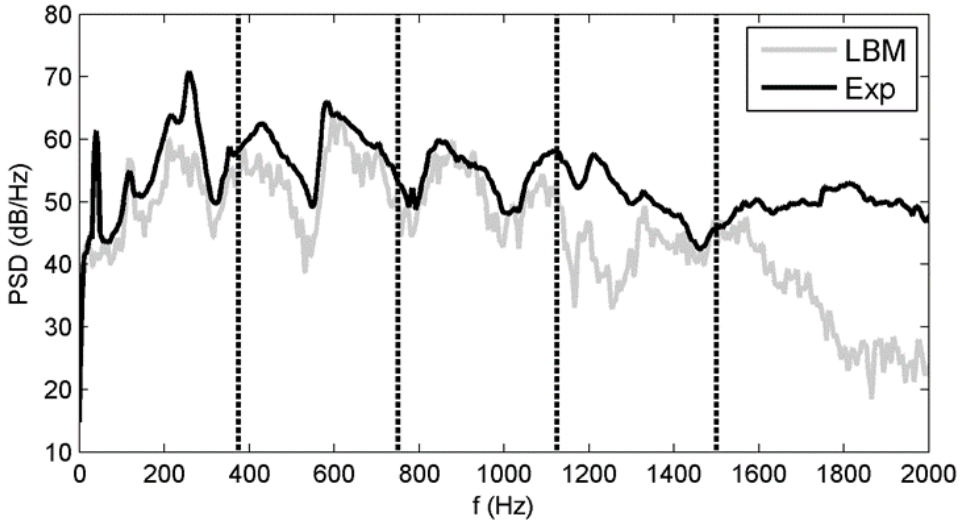

Figure 5.39 Acoustic power spectral density spectra for the H380 ducted configuration recorded 1.5 m upstream of the fan along the rotational axis. Δf =2 Hz. BPF harmonics are highlighted by vertical dashed lines.

aerodynamic testing in Section 3.4.2 in an AMCA 210-07 compliant test rig for the transparency operating condition. It was found that the simulations achieved an accuracy to within 3% to the experimentally measured flowrates for several tested fan geometries [Piellard *et al.*, 2013]. Details about the performance of the system from an aerodynamic standpoint, however, are considered confidential and cannot be published here.

An aeroacoustic study was also carried out internally at Mahle-Behr Luxembourg in a semi-anechoic environment. Details pertaining to the LBM simulation representing this experiment are reported here in this section. The simulated geometry was previously shown in Fig. 3.21. Due to the complexity of the grid refinement that would be required to properly mesh the heat exchangers, they were modeled in the simulation using equivalent porous media regions [Piellard *et al.*, 2014]. The inertial and viscous resistance of the media were set in such a way that it reproduced the pressure loss incurred across the actual heat exchangers. A blockage plate located downstream of the module (outlined in Fig. 3.21) is also modeled in the simulation in order to reproduce the proximity of the engine block when mounted on a car. The electric motor driving the fan was also modeled.

In order to reproduce the semi-anechoic environment from the experiment, the modeled CRFM was inserted in a large simulation domain, as schematically shown in Fig. 5.41 The floor is the solid grey line while all other outer surfaces have free-flow conditions. As mentioned previously, the simulation grid is composed of cubic elements called voxels. A Variable Resolution mesh strategy (VR) is used and the grid size changes by a factor of

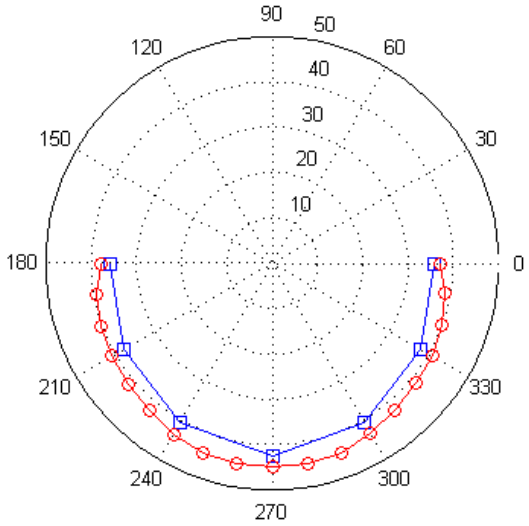

Figure 5.40 RMS acoustic pressure level in dB at 1.5 m on the suction side of the H380 duct configuration.

two for adjacent resolution regions. The circles seen in Fig. 5.41 correspond to the outer refinement zones. High viscosity is artificially imposed in the last outer layers of the fluid domain to prevent the reflection of acoustic waves back to the source. The finest VR zones on the module surface have a 0.35 mm voxel size, which was shown to be sufficient to yield grid-independent solutions by Piellard *et al.* [Piellard *et al.*, 2014]. This is also consistent with previous mimimum grid sizes reported by Moreau and Sanjose on a similar automotive ring fan [Moreau and Sanjose, 2016].

In the simulation, as in the experiment, the CRFM is operating at free-flow conditions (uniform pressure in the room) with the fan rotational speed imposed at 2535 RPM. Time-domain convergence of flow and noise was reached after six complete fan revolutions, and flow and acoustics records were started at this time.

A series of 20 probes located 0.5 m upstream of the CRFM was included in the simulation setup to mimic the experimental microphone array used to collect acoustic data in the semi-anechoic chamber (Fig. 3.23). Experimental acoustic data was sampled at 40960 Hz, while it was sampled at 101580 Hz in the simulation. Note the presence of the downstream backplate in the experimental setup on the right side of Fig. 3.23. In the simulation the microphones are placed in a VR where the grid resolution is smaller than 6 mm, allowing an accurate acoustic waves propagation up to 5600 Hz assuming 10 points per wavelength.

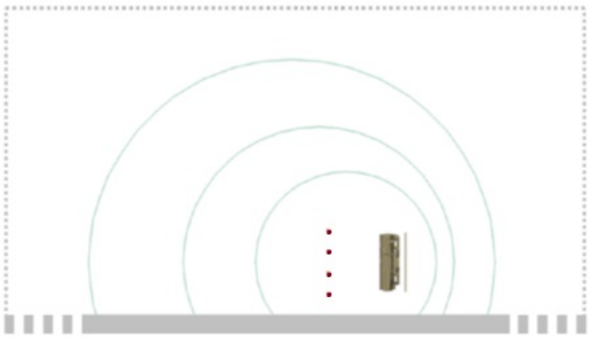

Figure 5.41 Semi-anechoic simulation domain for the Mahle cooling module. [Piellard *et al.*, 2014]

Finally, the installation effects due to the microphone array in the experiment are not represented in the simulation, as it is far enough from the module that also acts as a flow straightener. It is possible however that the additional obstructions may still influence the module inlet flow in the experiment.

5.7.1 Aeroacoustic Performance Evaluation

Direct acoustic signals recorded in the simulation have been compared with the experimental data gathered in the semi-anechoic room through the aforementioned microphone array. As an example, two comparisons of the power spectral density for different microphones are shown in Fig. 5.42 where the frequency is normalized by the rotational frequency of the fan, referred to as order (abbreviated by 'O').

The first numerical spectra are extracted from a simulation with only 0.35 s of physical time available (termed Sim 1). The second simulation had 1 s of available physical time (termed Sim 2). Both simulations have identical geometries, but the second simulation also has a more detailed surface decomposition for the FWH analogy propagation for source identification as explained in the next section. Hardly any change was observed on the acoustic results for longer run times.

Overall, a good correlation between the experiment and simulation is obtained, with some variance between the different evaluation locations. A better agreement with the experimental spectra on both tonal and broadband noise components is also obtained with the longer simulation; this is not particularly surprising as it allows for the flow to settle in the simulation volume [Sturm and Carolus, 2012] and provides longer time data for the Fourier transform, which is carried out using Welch's periodogram method.

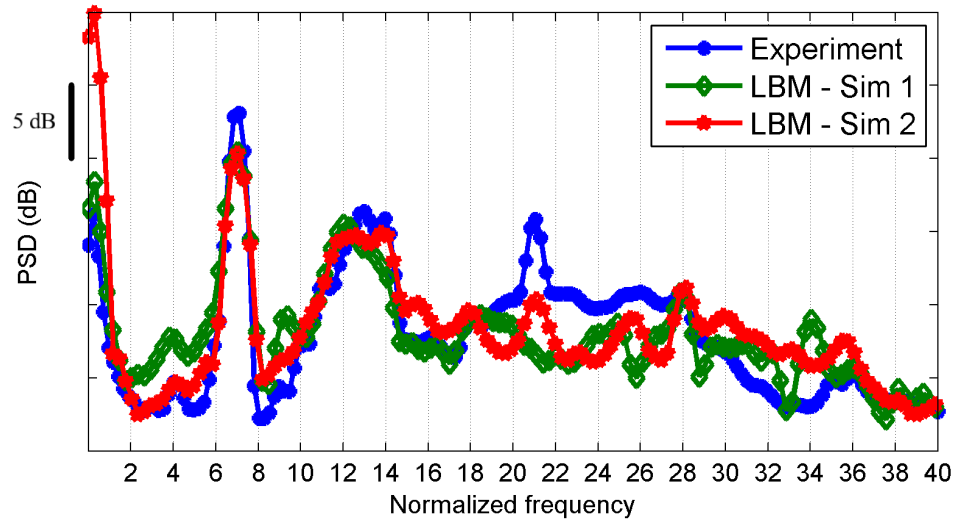

(a)

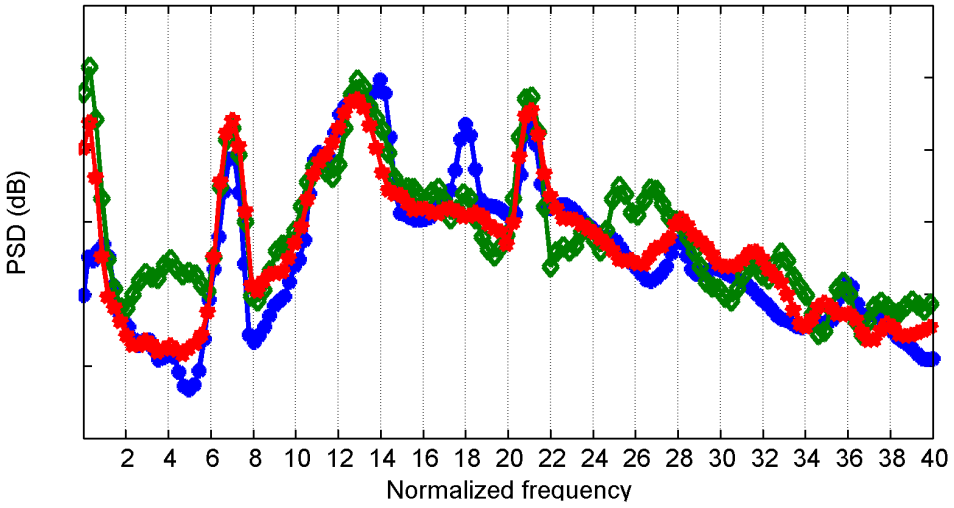

(b)

Figure 5.42 Comparison of the acoustic pressure PSD from the direct CAA with the experiment for two separate microphone locations (a) Microphone 2 (b) Microphone 14

Furthermore, the spectra show that the configuration produces consistent strong tonal noise around the first Blade Passing Frequency (BPF) at O7 and its first two harmonics at O14 and O21, with the levels varying for the considered microphone, indicating an uneven directivity pattern, which is to be expected from a dipolar source. Note that the longest simulation is even able to capture the third and fourth harmonics correctly even though their strength is much weaker. There is also a large broadband hump in the frequency range below the second BPF (O12-14).

This can be attributed to the presence of rotating turbulent structures originating from the tip gap in the flow interacting with the fan blades, causing sub-harmonic humps. This phenomenon was discussed in previous publications for similar axial ring fans [Magne *et al.*, 2015; Moreau and Sanjose, 2016; Piellard *et al.*, 2014]. In this case, however, the fan was isolated and flush-mounted on a plenum; this suggests that the same large coherent structures form in the tip gap in the module configurations and tip noise is also a significant broadband noise contributor when installed in a vehicle. The third BPF also emerges as a discrete tone, although again its emergence level differs from microphone to microphone. A discrete tone at 760 Hz (O18) is also observed in the measured spectra that is only partially captured in the simulation. Its amplitude also varies from microphone to microphone in the experiment. The origin of this particular tone was not found during the initial experimental campaign but was deduced by carrying out a FWH analysis using the LBM results after the fact.

5.8 Conclusion on the Validation of Test Cases

The present chapter was intended to provide an in-depth validation for each of the proposed fan geometries proposed as study cases to establish a baseline upon which to rely for further analysis. The experimental database available for this purpose changed from case to case aside from the performance characteristic curve and the availability of some form of acoustic measurements which were present for most cases. In terms of the global performance characteristic curve evaluation, the simulated test cases compared fairly well with their respective experiments. The same can be said of the direct acoustic predictions from the LBM simulations, as almost all the simulation cases showed good agreement with the experimental acoustics, although some problems regarding boundary conditions had to be solved for the RCDB test geometry to achieve good results. The exception to the norm was the Bosch axial fan case, where the LBM simulations consistently underestimated the measured pressure rise characteristic for a given flowrate but nevertheless approximated the slope of the curve exception made of the higher flowrate simulated. The acoustic predictions from the simulations also showed significant differences with the experimentally obtained spectra, with strong acoustic modes shown to occur in the simulation having been identified as the source of the additional noise apparently being prevented from forming in the experiment.

However, while the validation effort presented in this chapter covered both the aerodynamic and aeroacoustic performance of the simulated test cases, the next chapter will focus on the identification of the noise sources responsible for the spectral signatures on

each of the geometries with an emphasis on the mechanisms associated with tip clearance flow.

CHAPTER 6

Detailed Investigation of Clearance Flowfield and Fan Noise Sources

6.1 Context

The previous chapter was intended to present the validation effort carried out on the LBM simulations. Most of the numerical results compared fairly well, with the exception of the tube-axial fan with the complex tip geometry designed by Bosch that still showed discrepancies in the global performance curve prediction as well as the acoustics, which could be traced to the various setups used in the experiments.

The core of the current study, however, revolves around the investigation of the flow features associated with tip clearance flow in axial fans and the analysis of their impact on the radiated noise. Furthermore, as evidenced in previous chapters of this manuscript, the effect of different tip clearance configurations on the associated flow was investigated by considering a wide range of axial fan configurations, ranging from the typical tube-axial case through to ring-shrouded configurations.

This chapter presents the work done analyzing tip clearance flow on the studied fans.

6.2 Investigation of Tip Clearance Flow Topology

In order to gain a basic understanding of the flow features, the tip clearance flow for the different configurations studied was investigated using flow visualizations made available from the LBM flow simulations described in the previous chapter.

As a form of qualitative analysis, the three-dimensional vortices associated with tip clearance flow can be visually identified using contours of the λ_2 criterion proposed by Jeong and Hussain [Jeong and Hussain, 1995] in the unsteady volumetric data recorded. The criterion is based on taking the gradient of the steady, incompressible and inviscid Navier-Stokes equations, which yields

$$\mathbf{S}^2 + \mathbf{\Omega}^2 = -\frac{1}{\rho}\nabla(\nabla \mathbf{p}) \tag{6.1}$$

where $\boldsymbol{S}$ and $\boldsymbol{\Omega}$ are the symmetric and antisymmetric parts of $\nabla \boldsymbol{u}$ and represent the strain and vorticity tensors, or

$$S_{ij} = \frac{1}{2}\left(\frac{\partial u_i}{\partial x_j} + \frac{\partial u_j}{\partial x_i}\right) \tag{6.2}$$

$$\Omega_{ij} = \frac{1}{2}\left(\frac{\partial u_i}{\partial x_j} - \frac{\partial u_j}{\partial x_i}\right) \tag{6.3}$$

and $\nabla(\nabla \mathbf{p})$ is the pressure Hessian. The criterion is made to take the eigenvalues $\lambda_1 \geq \lambda_2 \geq \lambda_3$ of the matrix $\mathbf{S}^2 + \mathbf{\Omega}^2$ to determine the existence of a local minima in the pressure distribution due to vortical motion when $\mathbf{S}^2 + \mathbf{\Omega}^2$ has two negative eigenvalues i.e. λ_2 is negative, hence the nomenclature of the method. The regions corresponding to this criteria are defined as vortices. It can however prove difficult to separate structures that may be separated but are close together in a simulated flowfield, but it allows for a qualitative comparison of the vortical fields surrounding the various fan configurations studied here.

Additionally, the time-marching of the images issued from volumetric data can also provide a qualitative indication of the evolution of these structures and can help provide a sense of their velocity relative to the rotor blades, as it was carried out by Magne [Magne, 2015] for the H380 configuration.

Given the number of configurations covered in this study, the fans are grouped into two sections according to their type of tip configuration (i.e. free-tipped or ring-shrouded) for ease of reading and to provide an idea of the variations in tip leakage flow topologies between *similar* tip configurations.

6.2.1 Free-Tipped Fan Configurations

The first fan category covered in this section concerns the free-tip configurations. Three among the five fan geometries presented in the previous chapters in this work fit this category, namely the RCDB and USI7 (both classical annular tip clearance tube-axial configurations) as well as the Bosch-designed (variable radius tip clearance) fans. Visualizations using the aforementioned λ_2 criteria were first used to establish a basic understanding of the tip leakage flow topology in the sense of the vortical structures being generated for each of the considered geometries.

The first fan covered in this section is the USI7 configuration. As highlighted before, the simulation data for this configuration was obtained as a result of a cooperation with the

University of Siegen in Germany, as it was the object of a recent parallel study pertaining to tip clearance flow [Zhu, 2016]. The λ_2 contours, as presented by Zhu in his thesis, are shown again here in Fig. 6.1 for ease of reading, showcasing the vortical structures detected in the LBM simulation at $\phi_{nom} = 0.154$ and $\phi_{part-load} = 0.131$ for tip clearances of 1% and 0% (the experimental 0.1% clearance was modeled as a 0% gap in the simulations).

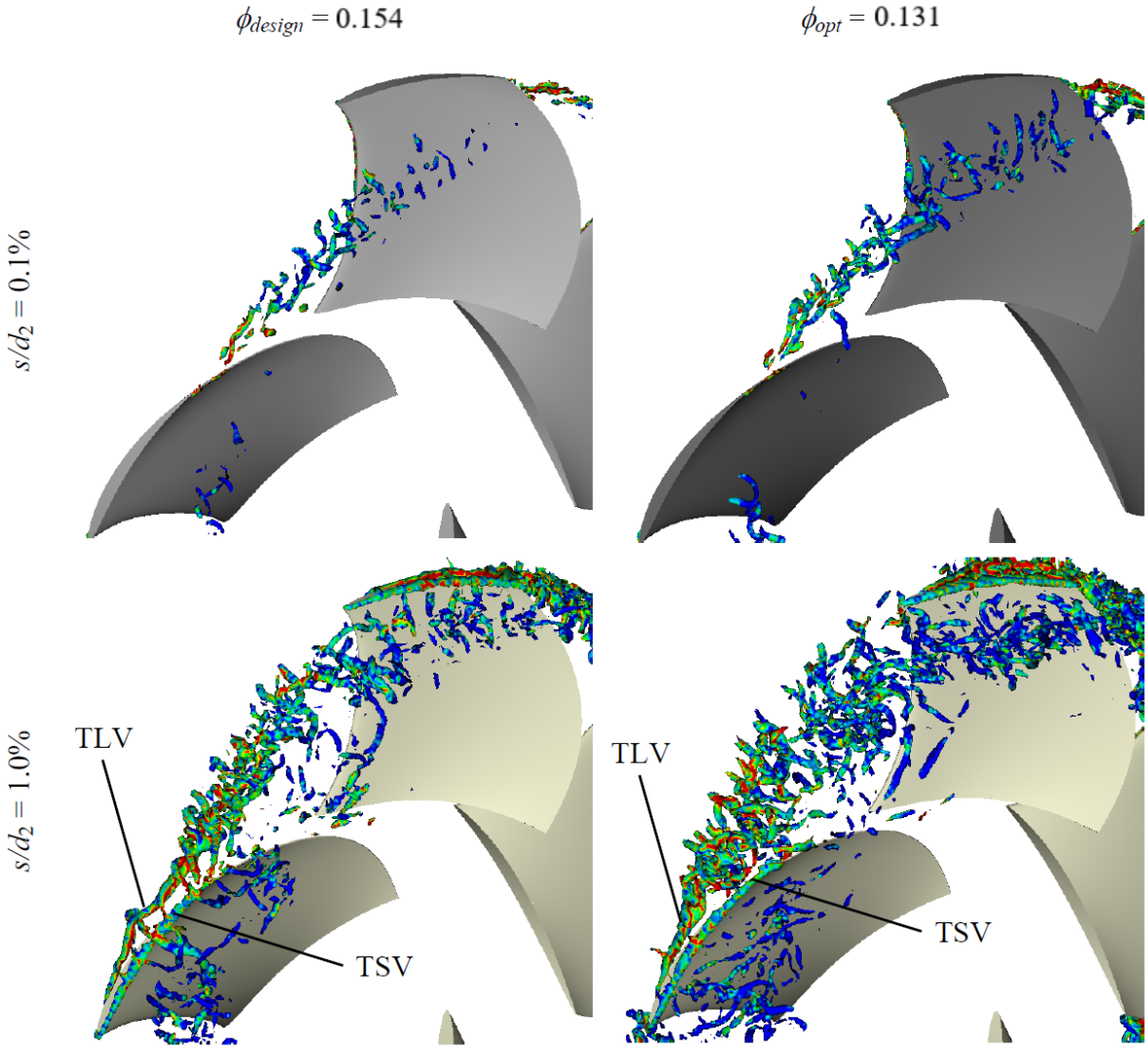

Figure 6.1 Tip clearance flow highlighted by contours of λ_2 for the USI7 colored by vorticity magnitude. [Zhu, 2016]

As observed previously by Zhu, even for the no-clearance case, vortical structures are detected by the λ_2 criterion; they can be attributed to flow separation at the trailing edge of the blade. These structures, however, are convected downstream and only slightly interact with the trailing edge of the following blade. With the addition of the tip clearance gap, however, the inception of an intricate vortex system is observed, with the tip leakage and

tip separation vortices (TLV and TSV) becoming visible. The TLV is highlighted by strong vorticity coming off the blade suction side, and it eventually breaks down into smaller vortical structures with weaker vorticity levels halfway through the blade passage. A shift in the path of the TLV is also visible between the considered operating points, shifting to a more azimuthal direction with a decrease in flowrate. This is coherent with observations from several authors in recent work [Taghavi-Zenouz and Eslami, 2011; Weichert, 2011; Wu *et al.*, 2011a,b]. The vortical system detected strongly interacts with the following blade, leading to increased wall-pressure fluctuation levels in the tip region, as shown by Zhu.

The λ_2 structures in this section are colored by vorticity as it helps both with the spatial visualization of the structures, but also helps identify the primary vortical structures such as the tip leakage vortex which have strong vorticity levels from secondary vortical structures in the flow, usually generated as a result of the breakdown of the main structures.

The second geometry covered in this section is the RCDB test fan, which was investigated numerically as an integral part of the current study for three separate operating conditions corresponding to the design, free-flow (0 Pa pressure rise) and near-stall conditions (respectively OC1, OC3 and OC5). Isosurfaces of λ_2 for each of these operating conditions are presented in Fig 6.2. Note that the tip clearance gap was maintained constant throughout all simulations for this configuration, unlike the USI7 case.

A significant evolution of the tip clearance flow can be observed as the flowrate moves to the lower end of the characteristic curve. At the design flowrate, the tip leakage vortex (TLV) can clearly be seen forming and is rapidly convected downstream. At about a fourth of the blade passage, the TLV shows signs of a breakdown, with instabilities appearing and a sudden drop in the vorticity levels. Hints of the formation of the tip suction vortex (TSV) can also be observed along the suction side edge at the of the blades. However, as the flowrate is throttled down, a much more intricate vortical system appears in the tip region of the blades, originating from the tip clearance gap. At the free-flow point, the TLV rapidly breaks down and merges with structures issued from the tip gap into a complex system of vortices; these distortions, which show lowered average levels of vorticity, are however still convected downstream of the blade row and do not appear to interact very strongly with the following blades. The nature and trajectory of the tip leakage flow structures becomes significantly different at the near-stall condition, where large turbulent structures issued from the tip clearance are convected more azimuthally and impinge strongly on the following blades; the formation of a clear TLV is no longer clearly observed.

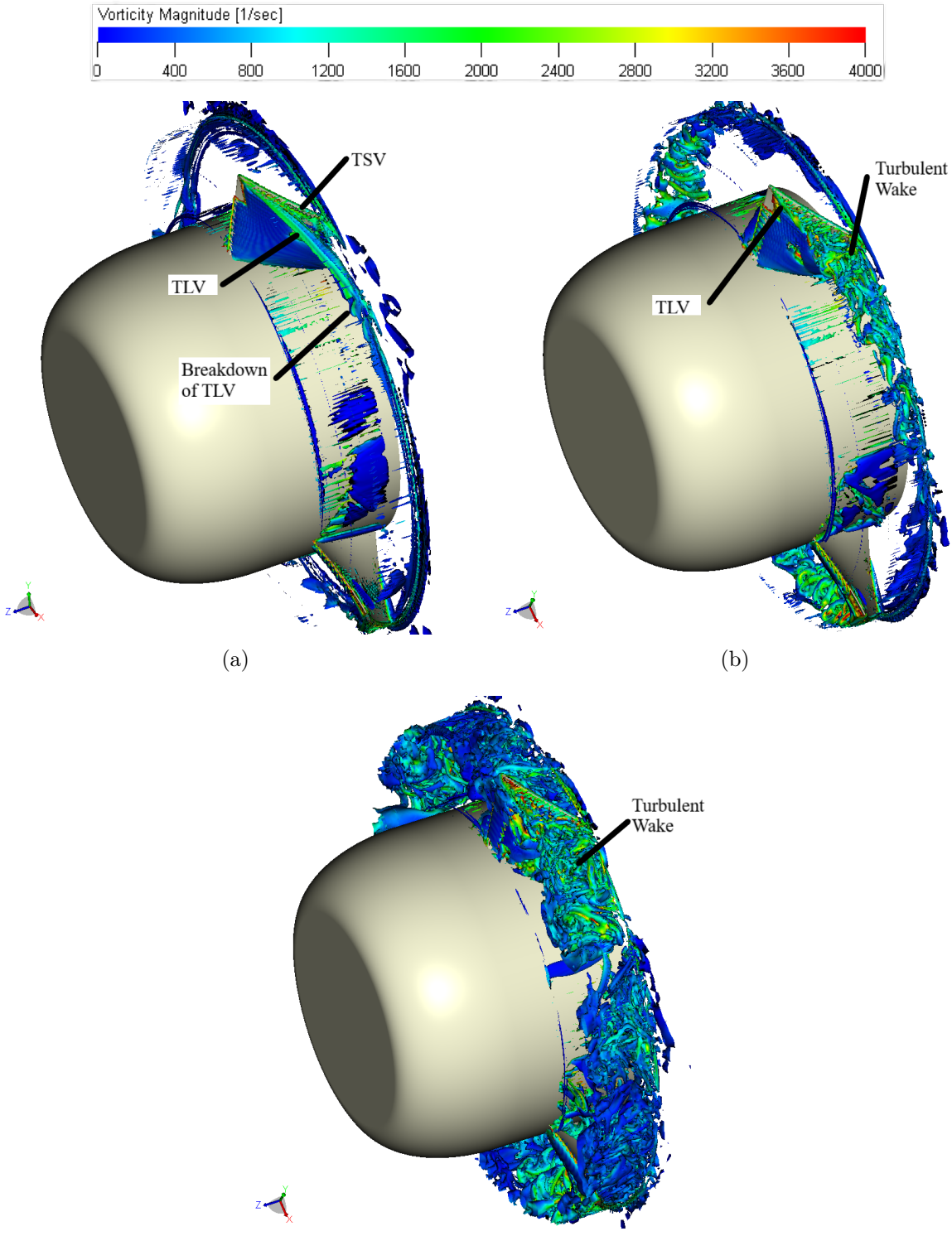

Figure 6.2 Illustration of the tip clearance flow structure for the RCDB simulation (Case 3) highlighted by isosurfaces of λ_2 (colored by vorticity magnitude) at different flowrates (a) Nominal operating point (OC1) (b) Free-flow operating point (OC3) (c) Low flowrate operating point (OC5)

From the perspective of the noise caused by tip clearance flow effect, it becomes apparent that the nominal and free-flow operating conditions show little interest from looking at the highlighted flow topology. Looking at the farfield acoustic spectra of all three flow rates together, as shown in Fig. 6.3, it is fairly apparent that there is little change in the overall noise levels radiated from the fan at OC1 and OC3, exception made from two high tonal peaks in the OC1 spectra at 114 and and 206 Hz, which cannot be linked to tip leakage noise in the current study as shown in the next section. However, the acoustic levels are 15-20 dB higher in the low frequency range (under 100 Hz) and on average 5-10 dB higher in the 100-400 Hz range. Furthermore, clear tonal humps in the frequency range the fan covering the first five harmonics of the BPF tones are observed and could be related to the influence of the aforementioned vortical field on blade loading, producing tonal noise. This is further delved into in the following sections.

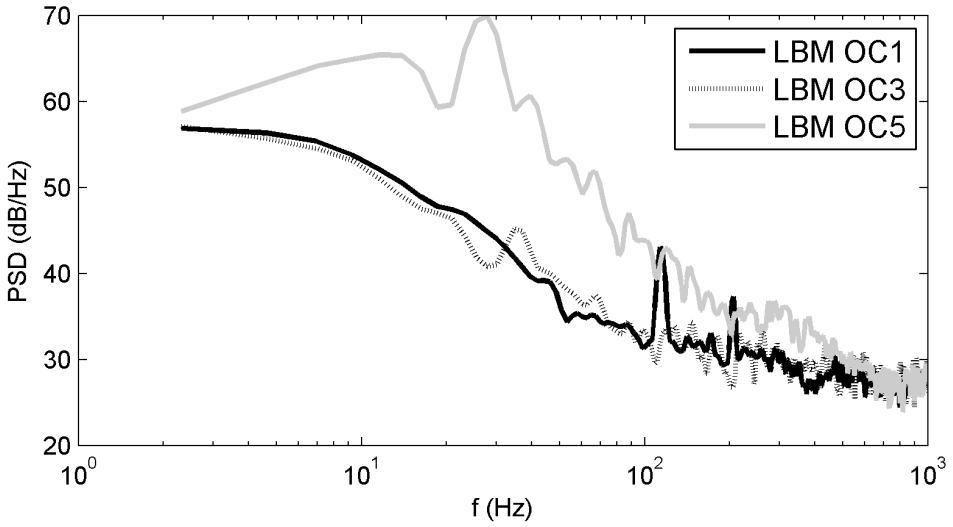

Figure 6.3 Acoustic PSD of the RCDB fan measured at 1 m along the rotational axis for all three simulated operating conditions.

The final configuration comprised in the free-tip axial fan category of this study is a Bosch-designed engine cooling fan. As shown in Sec. 3.3 and repeated at the beginning of the current section, this fan configuration was reportedly different from the RCDB and USI7 with regards to its tip clearance topology. The fan exhibits a constant 3 mm (0.9% of the rotor diameter) clearance gap with the static shroud normal to the tip surface of the blade, but the blade tip radius varies along the flowpath in a convergent manner. As shown in Fig. 6.4, this leads to the formation of a strong tip leakage vortex with high vorticity ($\geq$ 10000 1/s, red region) shedding from the cusp of the blade on the suction side, which quickly devolves a coherent scraping turbulent wake with reduced vorticity ($\sim 4000 - 6000$ 1/s, green region) that propagates from blade to blade along the shroud

wall. A series of secondary thin vortical structures with lower vorticity ($\sim$ 3000 1/s) are seen to form around the main turbulent wake in the blade passage.

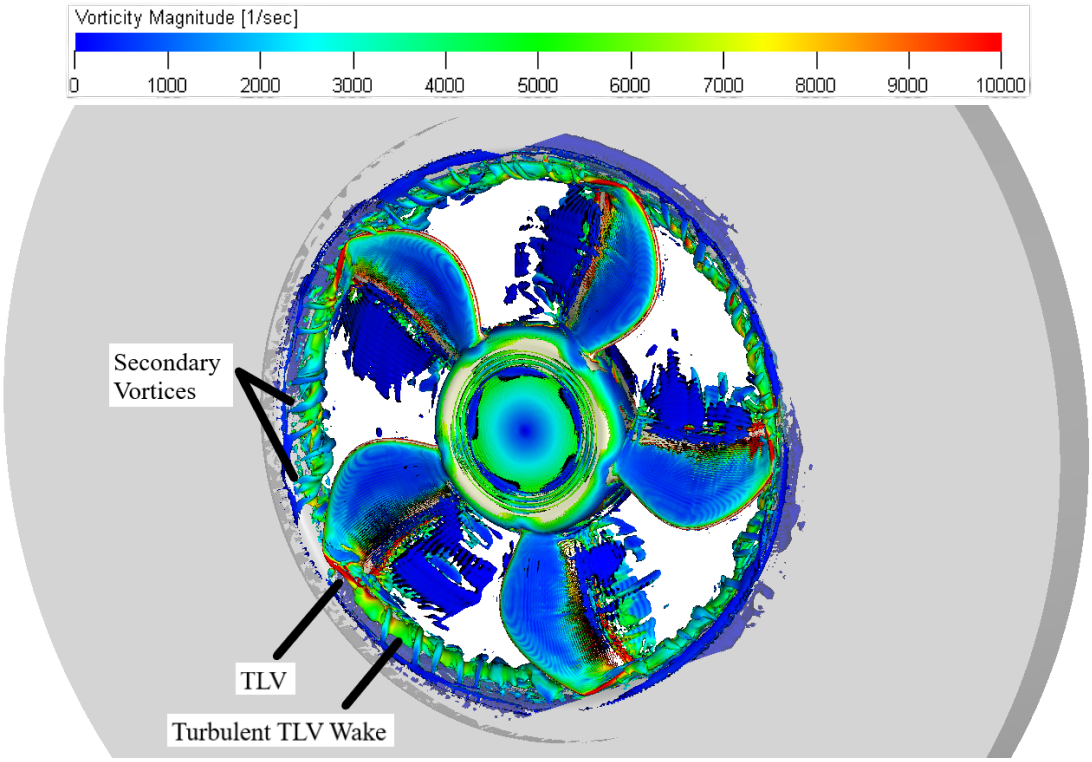

Figure 6.4 Tip clearance flow highlighted by isosurfaces of $\lambda_2 = -50$ colored by vorticity magnitude for the Bosch converging shroud configuration at the nominal flowrate.

All in all, the convergent tip clearance appears detrimental to the operating efficiency of the fan from both an aerodynamic and aeroacoustic perspective, as the converging shroud forcefully keeps the tip leakage vortex and associated tip leakage flow features from convecting downstream, maintaining them in the plane of rotation of the rotor and leading to a strong interaction with the following blades. The impact of theses structures on the acoustic spectra in the LBM simulation is however impossible to evaluate properly at this time because of the large impact of the duct propagation on the propagation of acoustic waves in the setup, as shown in Sec. 5.5.4. The effect of duct propagation is also an item which must be cleared up for the RCDB and USI7 cases for the free-tip fans, and it is adressed in Sec. 6.3.1 using an approach based on the FWH analogy.

However, the various free-tipped fans covered in this section provide some insight into the parameters influencing the formation of tip leakage flow in such configurations. Probably the most obvious factor lies in the operating point of the fan, which largely influences the strength and path of the tip leakage flow, and is illustrated on the USI7 and RCDB fan

geometries in this study. In effect, as the flowrate is throttled down at constant rotational speed, the blade loading increases as a result of the increasing angle of attack; as the TLF is essentially a flow driven by the pressure difference across the tip of the blades, the strength of the flow also increases. With decreasing flow rate, the path of the TLF also shifts to be more azimuthal, leading to more interference with the following rotor blades; in the more extreme cases, as with the near-stall condition for the RCDB fan, it can lead to the generation of a very complex turbulent field that propagates from blade to blade and impacts the entire chord length along with a large portion of the span. Aside from the obvious aerodynamic efficiency drop that ensues, dramatically increased levels of noise, both broadband and tonal, can also be associated with the phenomena. An increasing tip clearance gap also favors the formation of a stronger tip leakage flow, causing much the same effects as a decrease in flowrate, as evidenced by the USI7 investigation.

The third free-tip fan geometry (Bosch) also highlights that a misadapted shroud contouring can potentially lead to a forceful interaction of the TLF with the rotor blades and adversely affect the operating efficiency of the fan.

6.2.2 Ring-Shrouded Fan Configurations

Following the presentation of the tip clearance flow topology of the free-tipped axial fan configurations in the previous section, the ring-shrouded axial fan configurations are similarly covered in this section.

In effect, one fan geometry, the Valeo H380 engine cooling fan, was simulated in-house in both plenum and ducted configurations, as explained in Sec. 3.4.1. The second geometry, the Mahle-Behr engine cooling fan, was effectively studied in a more complex engine cooling module configuration as part of an internship at Mahle-Behr [Lallier-Daniels *et al.*, 2015].

The vortical field around the H380 fan for the nominal operating condition in both the ducted and plenum configurations is shown in Fig. 6.5, colored again by vorticity magnitude.

Whilst the tip clearance configuration is similar for both of the configurations, it becomes immediately apparent that the vortical structures generated upstream of the ring-shroud in the tip region of the blades are fairly different. In the plenum case (Fig. 6.5(b)), a series of thin vortices with vorticity levels between 3000 and 4500 are seen forming along the circumference of the ring-shroud, originating from the tip gap, wrapping closely around the ring and being sucked back into the blade passage. In the ducted configuration (Fig. 6.5(a)) however, the vortical structures are much larger, extending much further upstream of the

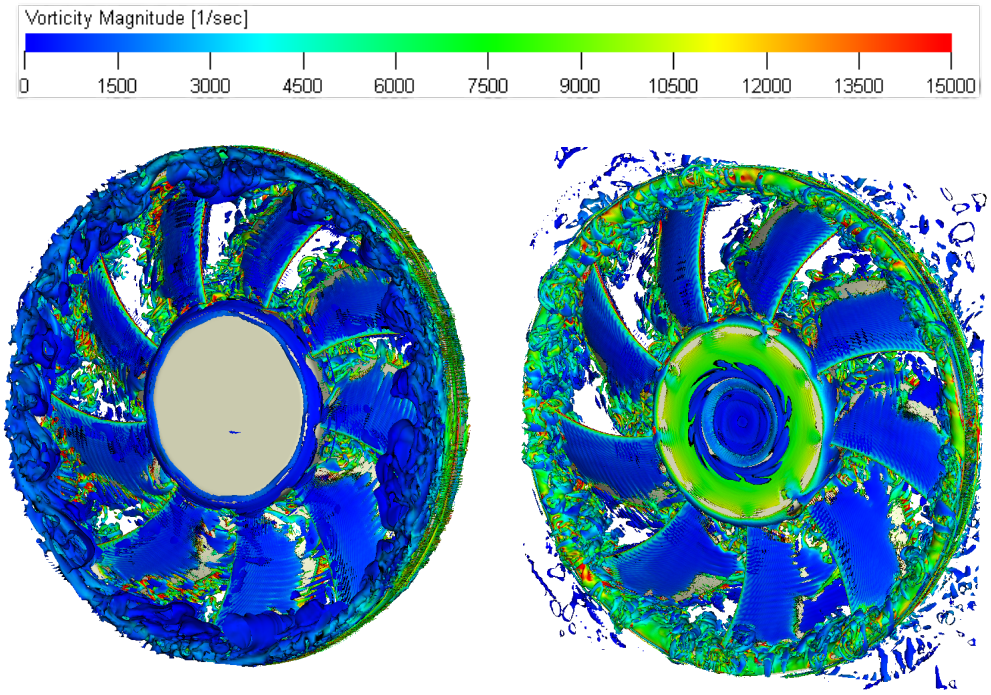

(a) (b)

Figure 6.5 Illustration of the tip clearance flow structure for the H380 simulation highlighted by isosurfaces of $\lambda_2 = -100$ colored by vorticity magnitude for the (a) Ducted configuration (b) Plenum configuration

fan and deeper in radially before being sucked back into the blades; they also exhibit much lower levels of vorticity (≤ 2000 1/s).

The modification of the zone of influence of the tip leakage flow structures in the H380 fan between the two configurations is more readily apparent when looking at the instantaneous throughflow contours of circumferential velocity shown in Fig. 6.6, where elevated levels of circumferential velocity upstream of the fan in the tip region are indicative of the presence of coherent structures rotating with the fan. It can be observed that presence of disturbed flow is visible up to 2 cm ahead of the ringshroud for the ducted configuration, with the tip leakage jet generating a large recirculation and creating a dead zone in the tip region ahead of the fan. In the plenum configuration however, the disturbed flow is restricted to approximately 3 mm ahead of the fan and a much cleaner inflow is observed; in effect, the tip leakage jet is sucked along the ring-shroud surface and back into the fan almost as soon as it exits the tip gap and no large recirculating structures are generated at the inlet unlike the ducted case. A large recirculating flow feature present just under the ring-shroud in the blade passage covering almost the entire blade chord is also observed in Fig. 6.6, whereas its equivalent in the plenum case appears to be more localized to the first

third of the chord. The proximity of the duct wall thus appears to affect the formation of the tip leakage flow features to a large degree.

To conclude this section on the investigation of the tip clearance flow topology, the final ring-shrouded fan designed by Mahle, described in Sec. 3.4.2, was investigated. The fan is very similar to the Valeo H380 design, but the fact that it was simulated as installed on a realistic engine cooling module (which the plenum H380 configuration seeked to mimic) provides additional insight into the influence the operational environment might have on similar automotive engine cooling fans. The vortical field around the Mahle ring-shrouded fan is shown in Fig. 6.7.

As with the H380 in the plenum configuration, a complex system of thin coherent structures with elevated levels of vorticity (more than 5000 1/s) is seen wrapping closely around the ring-shroud surface across most of the circumference. However, larger, more radially penetrating structures with lower vorticity levels ($\sim$2000-3000 1/s) are also seen appearing at 12 and 6 o'clock where the CRFM frame is closest to the fan along the circumference and occur only in those areas. This occurrence might be linked to the appearance of strong BPF harmonics in the acoustic spectra (see Fig. 5.42) as it creates stationary distortions in the flowfield at regular intervals ahead of the rotor blades. The influence of these singular structures on the three components of the velocity field can readily be seen in Fig. 6.8 in a plane just upstream of the fan, where distortions appear at 12 and 6 o'clock.

While all three ring-shrouded fan configurations in this study are fairly similar when looking at their operating conditions and with regard to their tip clearance configuration, the resulting tip leakage flow appears to be easily impacted by the various installation considered. In the presence of a clean inflow, best represented by the H380 plenum configuration, the backflow through the tip leakage flow tends to quickly roll up into a complex field of thin vortical structures along the circumference of the fan rotating shroud. However, the lack of axisymmetry of the module in the Mahle case generates localized disturbances in this field, leading to the formation of larger vortices, while this becomes generalized along the circumference in the ducted H380 configuration.

The H380 in particular provides an interesting opportunity to investigate the impact of such differences on the resulting acoustic contribution of the tip clearance flow. This is however made difficult due the different modal content of the acoustic propagation waves in the ducted case, as explained in Sec. 5.6.4. This was also an issue that is present for the free-tipped configurations presented in the previous section, and a denoising methodology based on the FWH analogy is presented in the following section to address this.

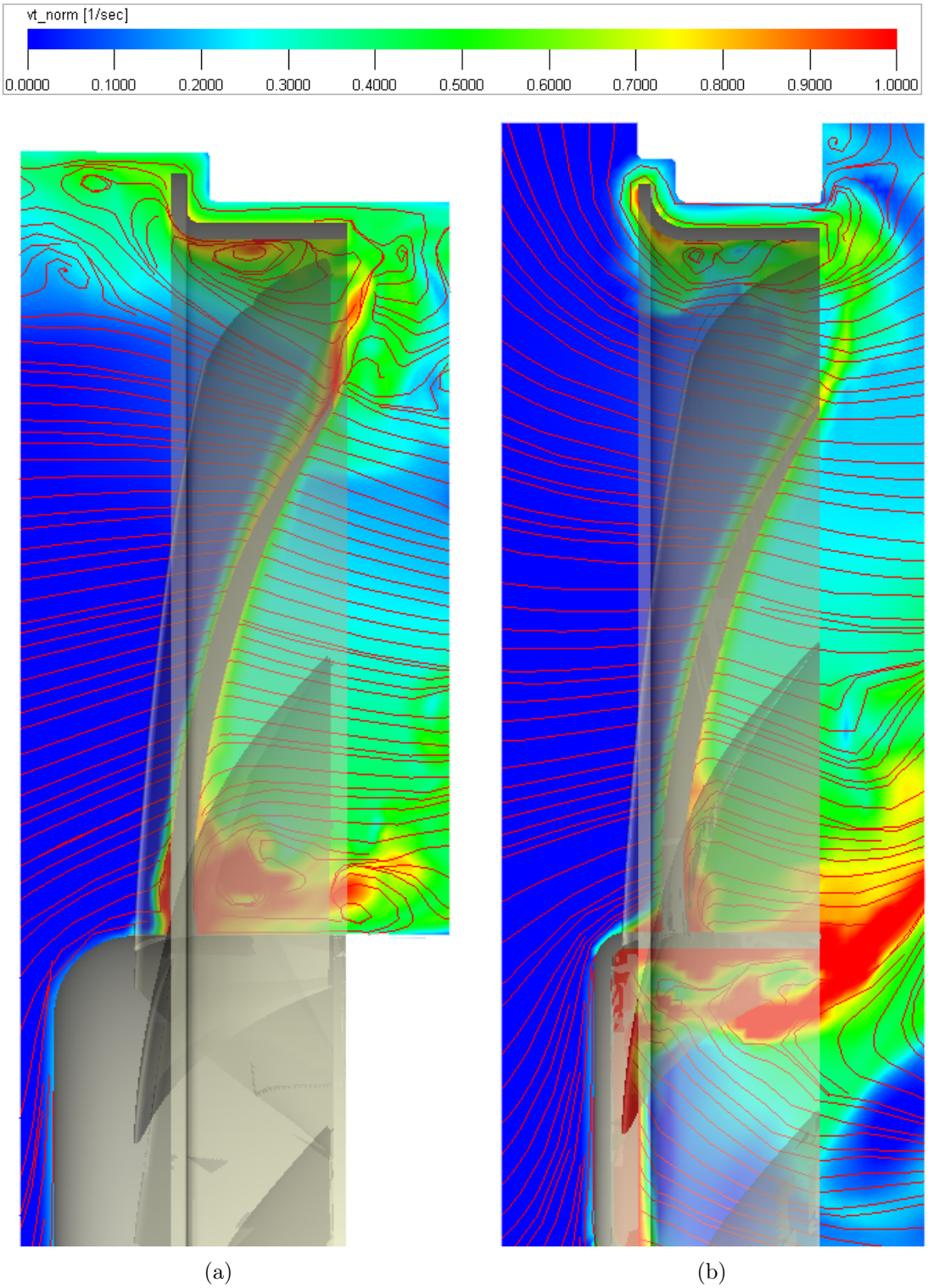

(a) (b)

Figure 6.6 Throughflow view colored by instantaneous contours of circumferential velocity normalized by the local blade speed for the H380 fan for the (a) Ducted configuration (b) Plenum configuration

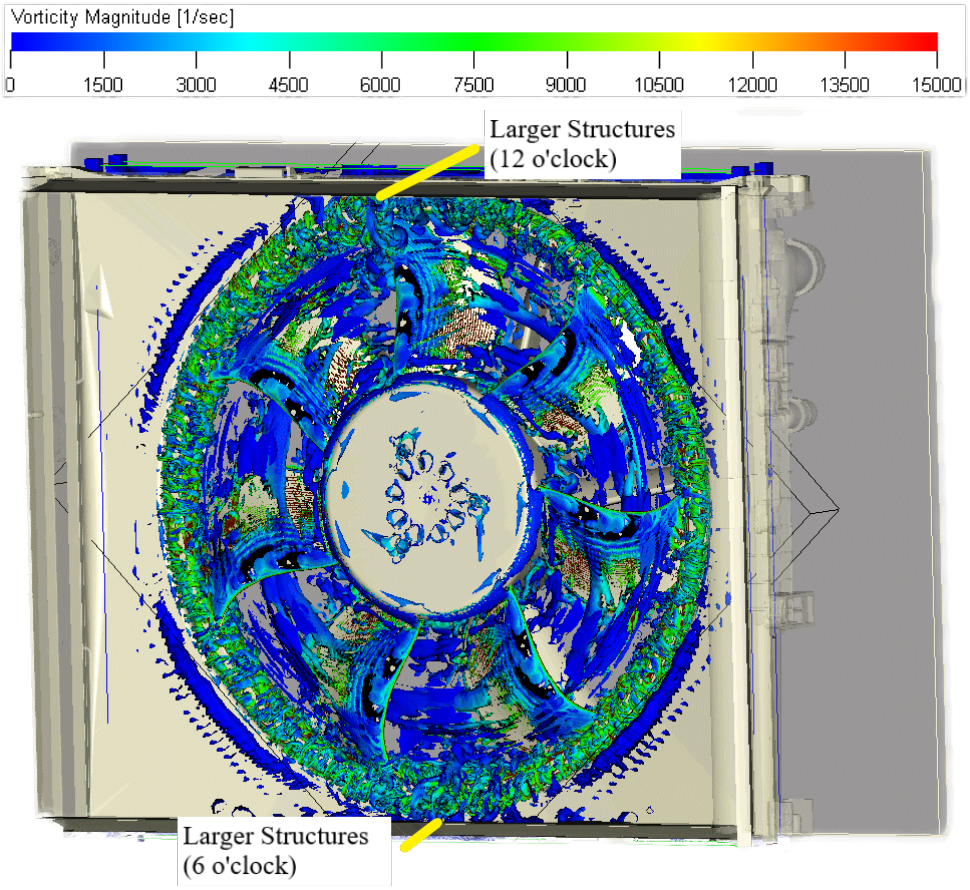

Figure 6.7 Vortical field around the Mahle fan as identified by isosurfaces of $\lambda_2 = -800$, colored by vorticity magnitude.

6.3 Noise Source Identification for the Investigated Rotors

Visualisations of the tip leakage flow topology using mainly λ_2 isosurfaces for the identification of vortical structures generated as a result of tip leakage flow presented in the previous section are a necessary step to gain a physical understanding of their interactions with the blades. However, while it is understood that the aerodynamic distortions caused by the tip leakage flow are expected to result in unsteady loading as they impact the rotor blades and bring an increase in both broadband and tonal noise components radiated by the fan, investigation of the acoustic impact of tip leakage flow on the fan acoustics requires a detailed investigation in and of itself.

This is especially true given the fact that the fan configurations covered in this study were simulated in realistic environments using LBM simulations, further complicating the acoustic propagation of the noise sources associated with the fan (i.e. strong duct modes

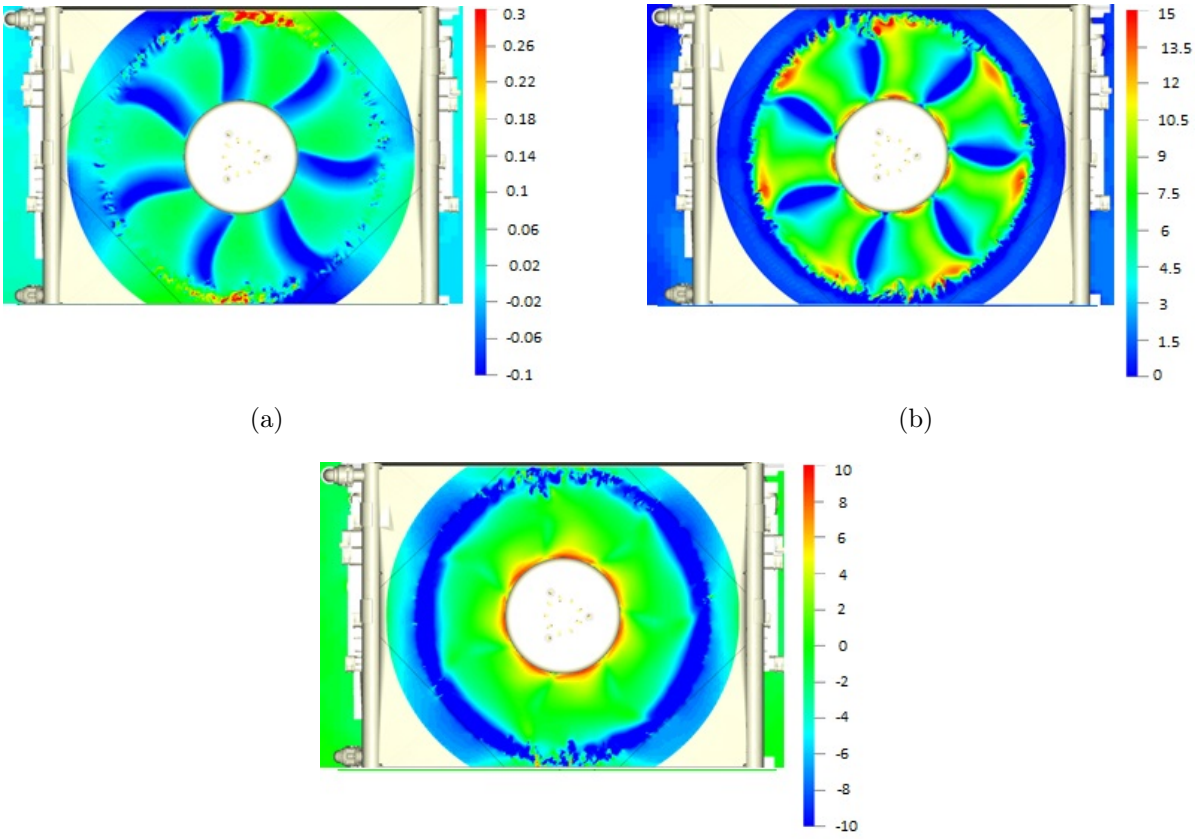

Figure 6.8 Instantaneous velocity field directly upstream of the Mahle fan (a) Azimuthal velocity normalized by the relative tip speed (b) Axial velocity (c) Radial velocity. The velocities are in m/s.

were observed to be excited in the Bosch simulation and in the ducted H380 configuration) as well as introducing secondary sources which can interfere strongly with the fan acoustics. Simulating these installation effects is however necessary to the faithful reproduction of the experimental aerodynamics and acoustics.

In this section, a strategy based on the use of the Ffowcs Williams and Hawkings (FWH) analogy, which was briefly described in Sec. 4.4.2, was employed. It allowed for guidance in creating filtered wall-pressure fluctuation maps to try and identify the acoustic impact of tip leakage flow for each of the fans simulated in-house as part of this study (i.e. with the exception of the Mahle-Behr fan configuration due to confidentiality issues).

6.3.1 Installation Effects and Noise - Ffowcs Williams and Hawkings' Analysis and Wall-Pressure Fluctuations Filtering

In order to orientate the investigation of tip leakage flow noise, it was first necessary to employ the FWH analogy to try and separate the acoustic contribution of the fan blades properly and specifically the tip leakage flow mechanics from the overall noise spectra as measured through the LBM simulations for each of the studied configurations.

The FWH analogy allows to take the wall-pressure fluctuations recorded in the simulations on the blade/rotor surfaces and propagate them into the farfield. Note that in the analogy the propagation is carried out using a free-field assumption and thus neglects all influences from the solid boundaries around the source surfaces; the analogy is used to isolate the acoustic contribution of the fan rotor with the specific objective of identifying the influence of the tip leakage flow on the fan.

The most probable sources of noise on the fan can be further pinpointed on the rotor by bandpass filtering the surface wall-pressure fluctuations, with the word *probable* being the operative word here. In fact, while the investigation of wall-pressure fluctuation maps aid in the identification of the locations where high levels of fluctuations are present; it provides no indication as to whether these source areas will be propagated to the farfield (e.g. evanescent sources, constructive or destructive interaction of the various sources). This is why it is used in conjunction with the FWH analogy.

USI7

While the identification of tip leakage flow structures as the cause of the acoustic subharmonic humps present in the spectra at the part-load flowrate for the large tip clearance was carried out in a parallel study of the USI7 configuration [Zhu, 2016], the fan was also tested in a ducted rig where acoustic propagation effects can have a fair impact on the resulting acoustic spectra as measured in the simulation. Thus, in order to provide a complete analysis of the configuration, it was decided to apply the FWH analogy to the configuration and isolate the specific acoustic contribution of the fan further, which is a step that was missing in the LBM investigation carried out by Zhu. The comparison between the direct acoustic spectra issued from the LBM simulation and the acoustic contribution of the fan rotor surfaces is shown in Fig. 6.9 for a single off-axis microphone located at 1.3 m upstream of the fan.

The FWH analysis does indeed confirm that the three tonal peaks at 175, 350 and 515 Hz in the numerical spectra find their source on the fan rotor. The level discrepancies are

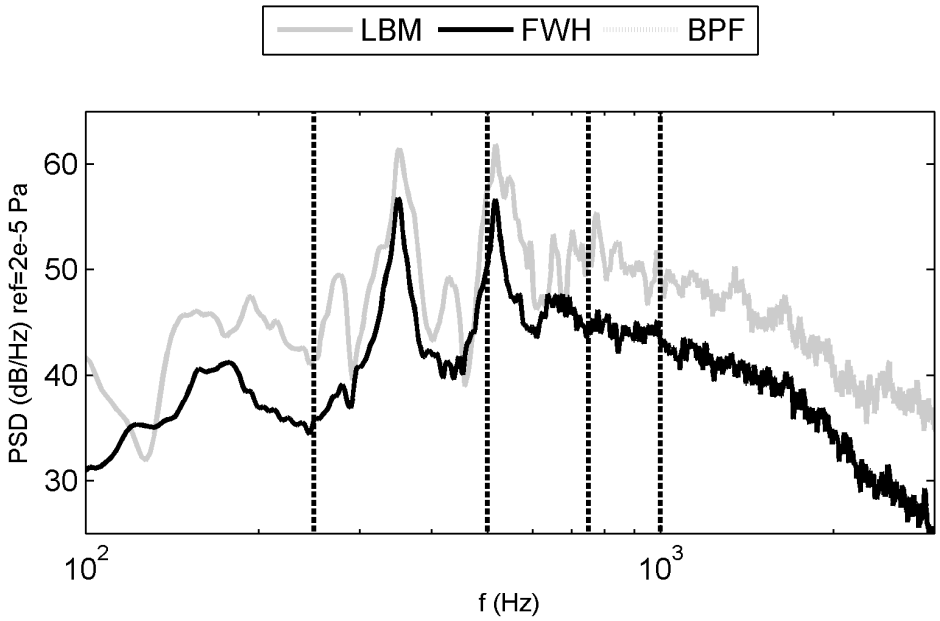

Figure 6.9 FWH analysis of the USI7 configuration for the part-load operating condition and large clearance gap. The BPFs are highlighted by vertical dashed lines.

largely attributable to the free-field propagation employed in the FWH analogy as opposed to the real ducted configuration. Using bandpass filtering on the surface wall-pressure fluctuations according to the identified frequency bands, in all three cases elevated levels of pressure fluctuations are shown to appear in the tip region close to the leading edge of the blades, as shown in Fig. 6.10.

As explained in the introduction to this section, this indicates that the most probable sources of noise on the fan at these frequencies are highly localized in the tip region and correspond fairly well with the points of impact of the vortical structures generated as a result of the secondary flow across the tip of the blades that were shown in Fig. 6.1.

RCDB Fan

The second case covered in this section is the RCDB fan. Whilst it was confirmed that strong spurious acoustic modes created in the simulation as a result of an acoustically reflective massflow outlet boundary condition were eliminated using a velocity outlet condition in Sec. 5.3, it was deemed worthwhile to assess the remaining environmental influence of the setup and further isolate the direct contribution of the fan to the overall acoustic spectra. The predicted acoustic contribution of the fan compared to the direct acoustics obtained from the simulation are presented for the nominal (OC1) as well as the near-stall (OC5) operating conditions in Fig. 6.11. Unfortunately, the FWH analysis for

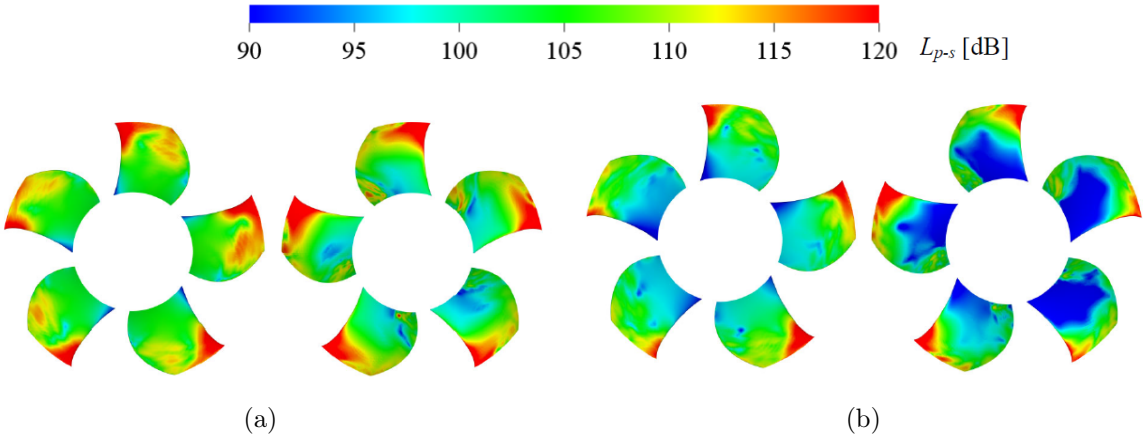

Figure 6.10 Filtered wall-pressure fluctuations on the pressure side (left) and suction side (right) of the USI7 fan at the part-load flowrate for the large clearance for frequency bands associated with tonal tip clearance noise (a) 340-360Hz (b) 505-525Hz

the free-flow operating condition (OC3) could not be generated due to the fact that the wall-pressure fluctuations data were not recorded.

Note here that the contribution of wall-pressure fluctuations from the rotor blades and hub surfaces can be differentiated in the RCDB simulation due to the way the simulation was setup; this is not true however for the remainder of the configurations covered in this section, where the rotor was recorded as a single surface source. However, in this particular case, it serves the analysis of the surprisingly manifold tonal peaks emerging in the spectra from the FWH treatment, allowing for the determination of those peaks originating exclusively from the rotor blades.

For the nominal flow condition, a preliminary comparison of the FWH spectra with the LBM direct acoustics highlights a large deficit between the two, indicating that there are important acoustic sources missing either as a result of installation effects or through the omission of surface sources like, perhaps, the rotor shroud; the impact of omitting critical surface sources on the FWH analogy prediction accuracy, while almost self-evident, was demonstrated on a ring-shrouded fan configuration [Lallier-Daniels *et al.*, 2015]. No clear conclusions can thus be drawn without accounting for these sources, as the fan rotor acoustic contribution is globally 30 dB below the direct acoustic prediction, flirting with absolute sound pressure levels of 10-20 dB, which can be equated to a whisper. However, further analysis to investigate the missing contributors could not be completed on this configuration due to time constraints. Furthermore, from the point of view of a study of tip leakage flow noise, the OC1 and OC3 flow conditions seemed to implicate that tip

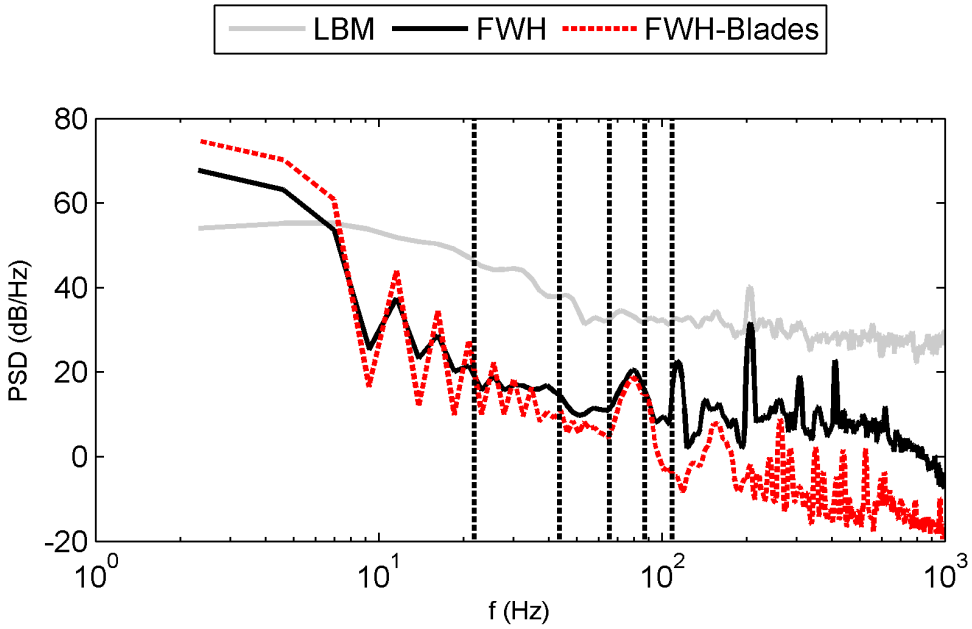

(a)

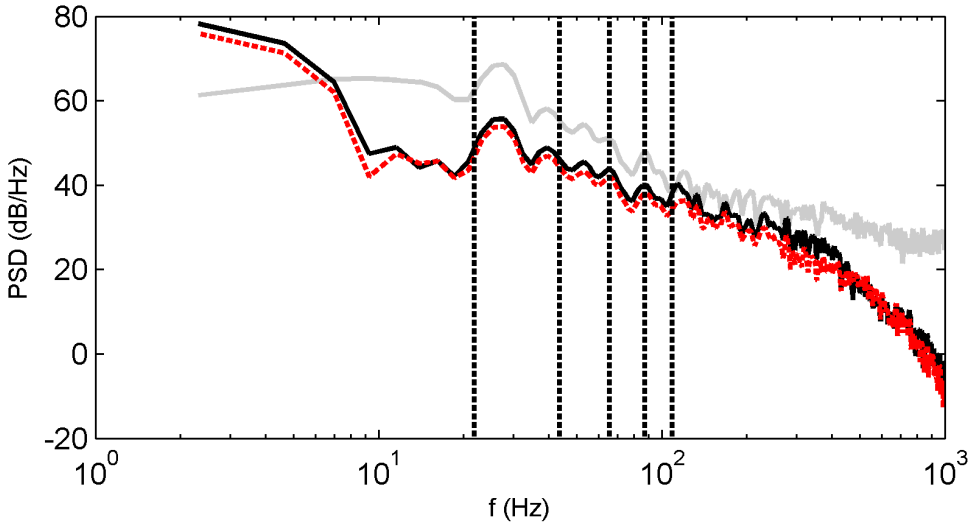

(b)

Figure 6.11 FWH analysis of RCDB configuration at (a) Nominal OC1 (b) Near-stall OC5. The BPFs are highlighted by vertical dashed lines.

noise is not a major contributor to the overall noise from the preliminary analysis of the topology of the vortical flow structures issued from the tip region flow as investigated using the λ_2 criterion in the previous section, as the shed vortical structures did not appear to interfere strongly with the following blades.

This is another matter entirely in the case of the near-stall flow condition, however, as it is observed that the FWH prediction for this case exhibits a strong correlation in both level and shape with the simulated acoustic spectra up to 400 Hz; globally, a shift of up to 10 dB can still be observed between the FWH prediction and the direct acoustics. At higher frequencies, a sharp fall-off is observed in the FWH predicted acoustic levels, indicating that the main sources are likely not linked to the wall-pressure fluctuations on the rotor. However, the rotor blades appear to be the main contributor to the FWH acoustic spectra over the whole frequency range. The series of tonal humps in the 20-100 Hz range were of particular interest given the rotational frequency of 7 Hz (BPF of 21 Hz), working under the assumption that the vortical structures shed from the tip gap generate distortions rotating at a portion of the rotor speed that would impact the blades, resulting in increased broadband and tonal noise. The band-pass filtered wall-pressure fluctuations from the fan rotor for the OC5 flow condition are shown in Fig. 6.12 for the frequency bands associated with the tonal humps in and under 100 Hz.

The first conclusion that can be drawn from the wall-pressure fluctuation maps is that the suction side of the blades is the location where the highest fluctuating levels are observed; in comparison the suction side fluctuations are barely discernable using the displayed scaling. They appear to be concentrated closer to the trailing edge of the blades on the suction side for the first four frequency bands, with the 35-46, 46-60 and 60-76 Hz bands exhibiting consistently higher fluctuations in the upper half of the span whilst the 19-35 Hz band affects the entire span. The last frequency range (75-104 Hz) is a little more complex to interpret, as while there appears to be a preferential area near the tip leading edge where higher fluctuations occur, a very consistent, more chaotic field of high fluctuations is observed in the aft portion of the chord, covering the entire span. In the aerodynamic study for the RCDB case in Sec. 5.3.2, it was shown that the flow was systematically separated from the blade in the trailing edge portion of the blades for all three simulated operating conditions, and is believed to be due to the inability of the LBM simulations to correctly predict the flow transition from laminar to turbulent on the profile; in the case of the near-stall condition (OC5), the flow is actually separated from the blade over a significant portion of the span, which would cause strong pressure fluctuations over a significant portion of the span.

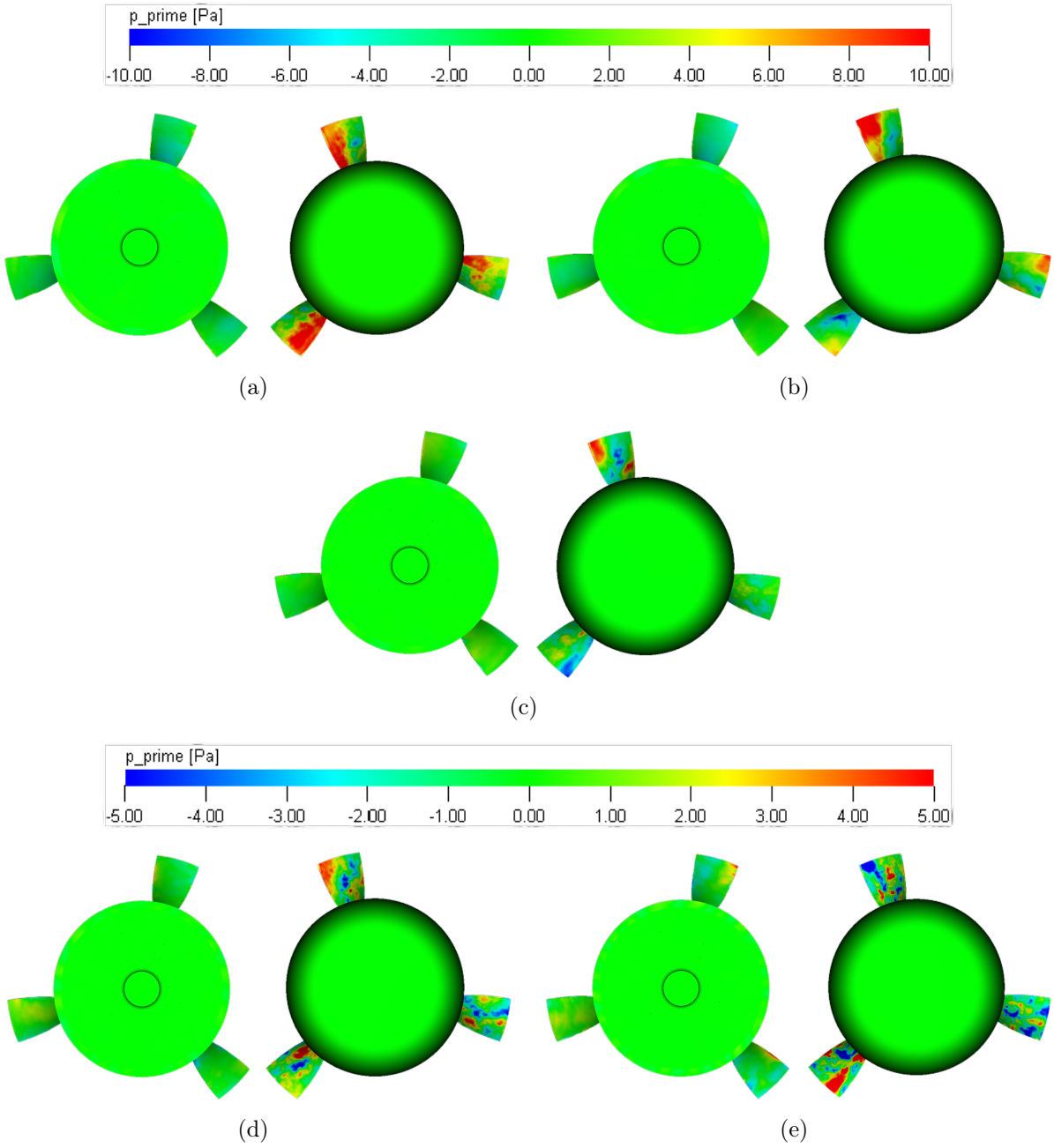

Figure 6.12 Filtered wall-pressure fluctuations on the pressure side (left) and suction side (right) of the RCDB fan at OC5 for frequency bands associated with tonal noise under 100 Hz (a) 19-35Hz (b) 35-46Hz (c) 46-60Hz (d) 60-76Hz (e) 76-104Hz

The reader will note that the scale used for the wall-pressure fluctuations is different between the first three investigated bands and the last two, as it was necessary to properly represent the declining strength of the fluctuations with increased frequency; this is coherent with the decrescendo observed in the acoustic spectra.

Overall, if the wall-pressure fluctuations are representative, the main sources of noise related to the tonal humps observed in the acoustic spectra under 100 Hz for the RCDB fan near the stall margin are located on the suction side of the blades. Furthermore, there appears to be a preferential area for high pressure fluctuations near the trailing edge in the upper half of the span; the trend, however, is much less clear that that observed for the Bosch and H380 fans as will be shown in the following sections.

Bosch Configuration

One of the configurations where installation effects were seen to strongly affect the resultant acoustics was the Bosch free-tipped axial fan for the anechoic chamber setup at nominal flowrate. It was shown in Sec. 5.5.4 through volume pressure filtering maps that the acoustic contribution of the fan was largely overshadowed by the presence of strong propagating duct modes in the rig, preventing the clear identification of fan-specific noise sources. However, looking at the contribution of the fan using the FWH analogy, as shown in Fig. 6.13, clear tonal humps are seen to appear at approximately 85% of the BPF harmonic frequencies.

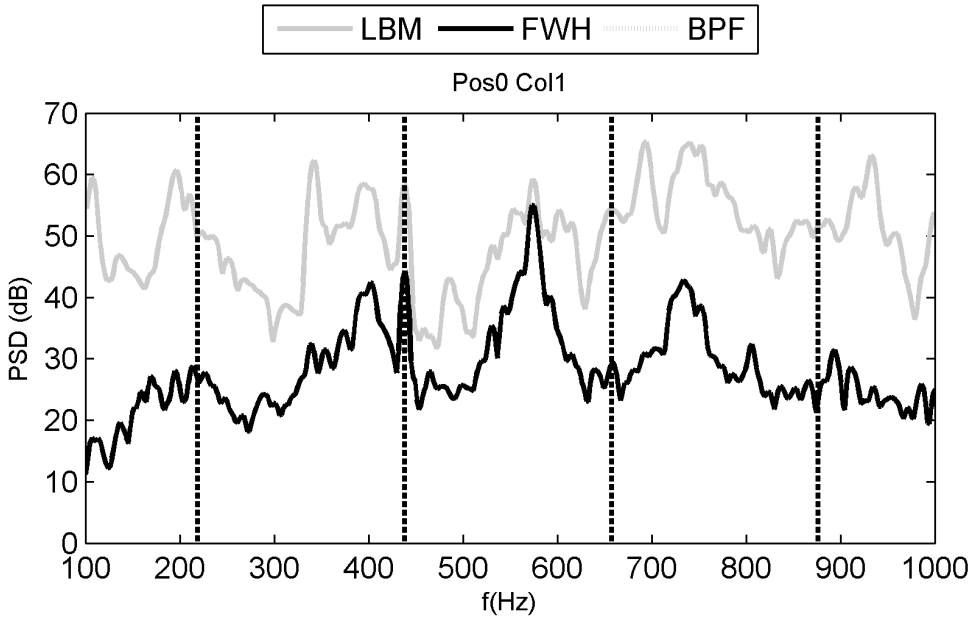

Figure 6.13 FWH analysis of the Bosch configuration. The BPFs are highlighted by vertical dashed lines.

Filtering of the wall-pressure fluctuations on the rotor blades in these identified frequency bands, as shown in Fig. 6.14, yields an interesting observation in that they correspond to the occurrence of high fluctuations in the tip region of the blades and are located especially on the pressure side of the blades.

This is very similar to the behaviour reported for the free-tipped USI7 fan by Zhu et al. [Zhu, 2016; Zhu *et al.*, 2016b] and is likely to be caused by the same phenomena, namely the vortical structures generated from the tip leakage flow of one blade having with a convection speed inferior to the rotor interacting with the following blade, resulting in these tonal humps.

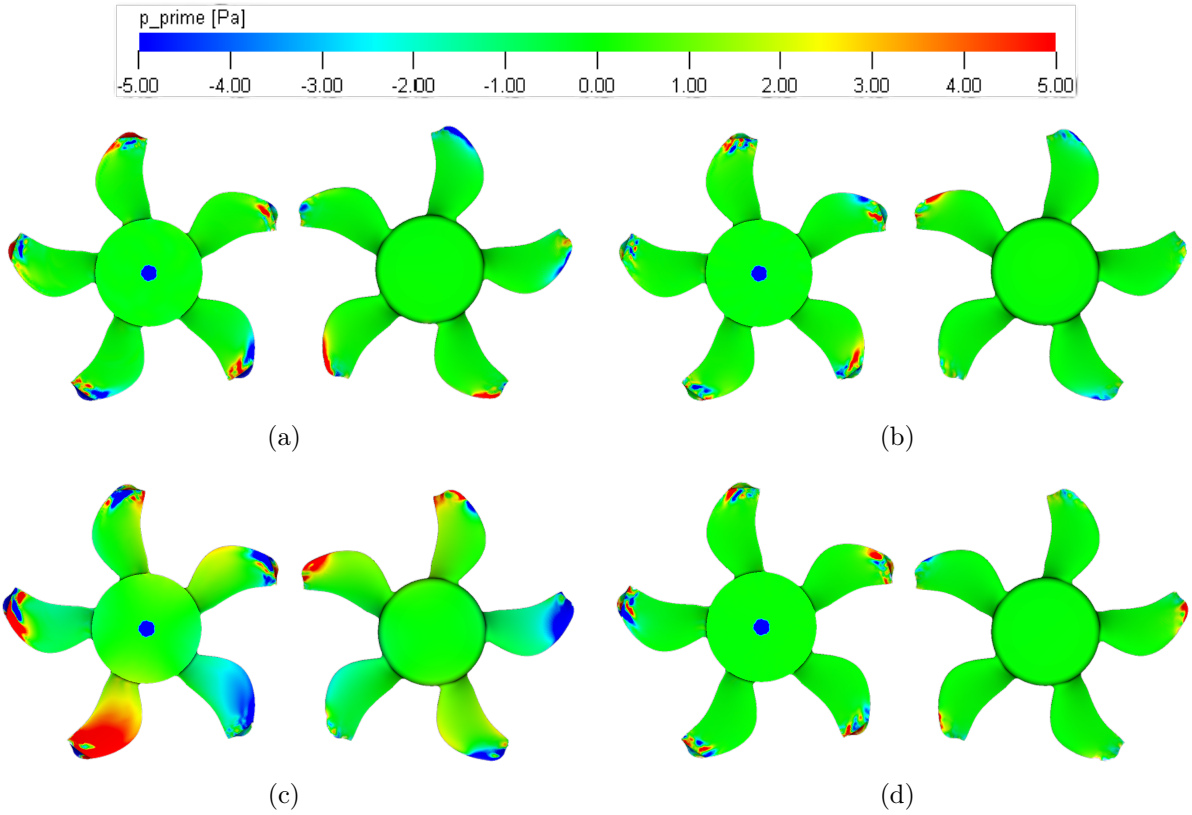

Figure 6.14 Filtered wall-pressure fluctuations on the Bosch fan pressure side (left) and suction side (right) for the frequency bands associated with sub-harmonic humps in the acoustic spectra (a) 143-203 Hz (b) 361-430Hz (c) 537-612Hz (d) 695-768Hz

H380 Configuration

Two ring-shrouded fan geometries were also investigated using the FWH analogy. The first one presented here is the Valeo H380 ring-shrouded fan. The H380 was simulated in both plenum and ducted configurations to accurately represent the test rigs used in separate

experiments (see Sec. 3.4.1). The plenum case allowed for a nearly free-field propagation of sound on the suction side of the fan; however, the duct rig introduced the additional complication of ducted acoustic propagation and was shown to make the trailing-edge noise compete with the tip leakage flow related mechanisms [Christophe *et al.*, 2016]. However, when looking at the SWL emitted on the suction side by the fan rotor only using the acoustic analogy in Fig. 6.15(a), only a series of clear tonal humps which were masked by duct propagation effects remain in the spectra, he occurrence ofwhich in the H380 acoustic spectra was already linked to the interaction of the rotor blades with the coherent flow structures issued from the tip gap flow [Magne, 2015; Magne *et al.*, 2014; Moreau and Sanjose, 2016] highlighted using λ_2 isosurfaces in the previous section.

When the SWL of the ducted configuration is compared to the one from the plenum configuration simulation in Fig. 6.15(b), the resulting acoustic spectra are found to be very similar up to 1000 Hz, with the appearance of clear equally-spaced tonal humps at sub-BPF frequencies up to the third order. The SWL is obtained using the FWH analogy by using the propagated acoustics to the microphone locations from each setup (see Sec. 5.6) and using Eq. 5.5.

The most plausible noise sources can be identified using band-pass filtered maps of the rotor wall-pressure fluctuations in the frequency bands associated with the sub-harmonic humps in the acoustic spectra. The filtered surface pressure maps for the H380 in the ducted configuration corresponding to the four sub-harmonic humps are shown in Fig. 6.16 and indeed seem to indicate that the tip region of the blades and the ringshroud are exposed to high pressure fluctuation levels. The fluctuations are especially strong on the suction side of the blades and seem to impact the entire chord as well as up to a third of the blade span in the case of the first sub-harmonic band.

In the case of the first and second sub-harmonic frequency bands, however, a second area with high wall-pressure fluctuations is observed at the root of the blades on the suction side of the blades. These high fluctuations correspond to the location of disturbances that appeark to be caused by a horseshoe vortex generated near the hub of the rotor at the leading edge (see Fig. 6.5, which grows radially along the blade in the trailing edge portion of backward-curved portion of the blade near the root and breaks off at the cusp.

Investigation of the bandpass-filtered wall-pressure fluctuations for the plenum configuration basically yields the same global global observations as to the locations of elevated levels, as shown in Fig. 6.17. However, fluctuations associated with the first sub-harmonic

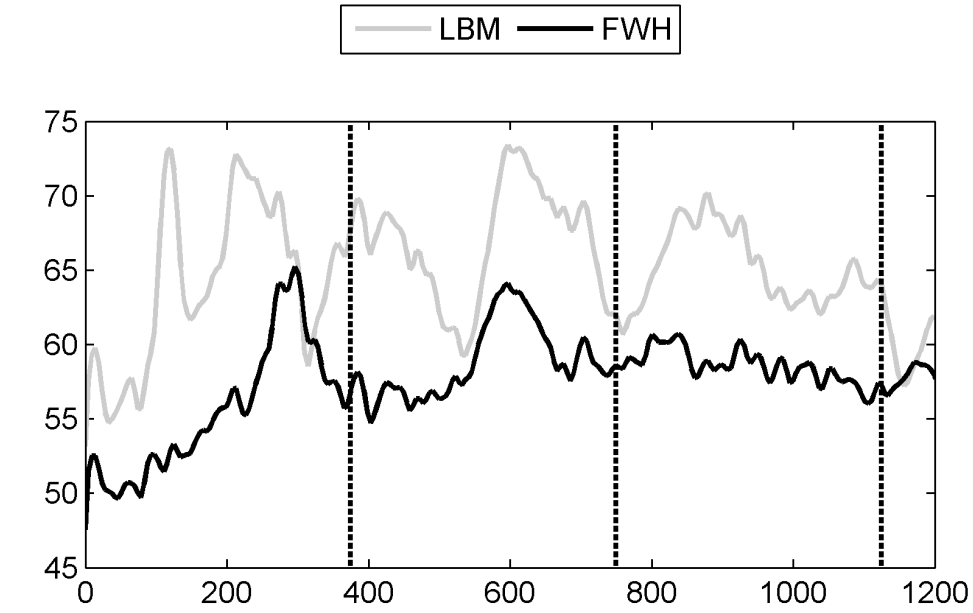

(a)

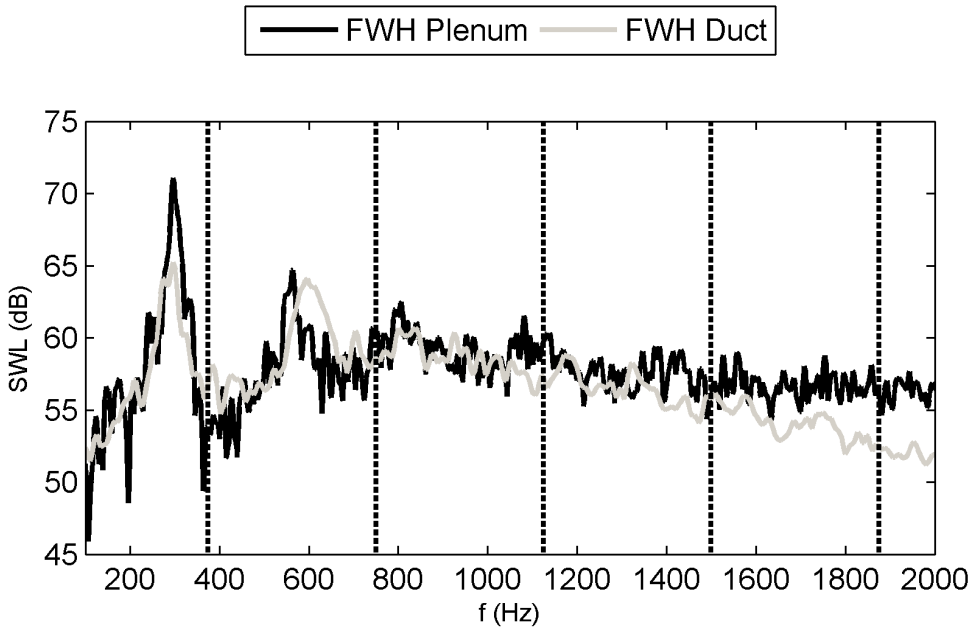

(b)

Figure 6.15 FWH analysis of H380 configuration in the (a) Ducted configuration (b) Comparison of the FWH results between the ducted and plenum configurations. The BPFs are highlighted by vertical dashed lines.

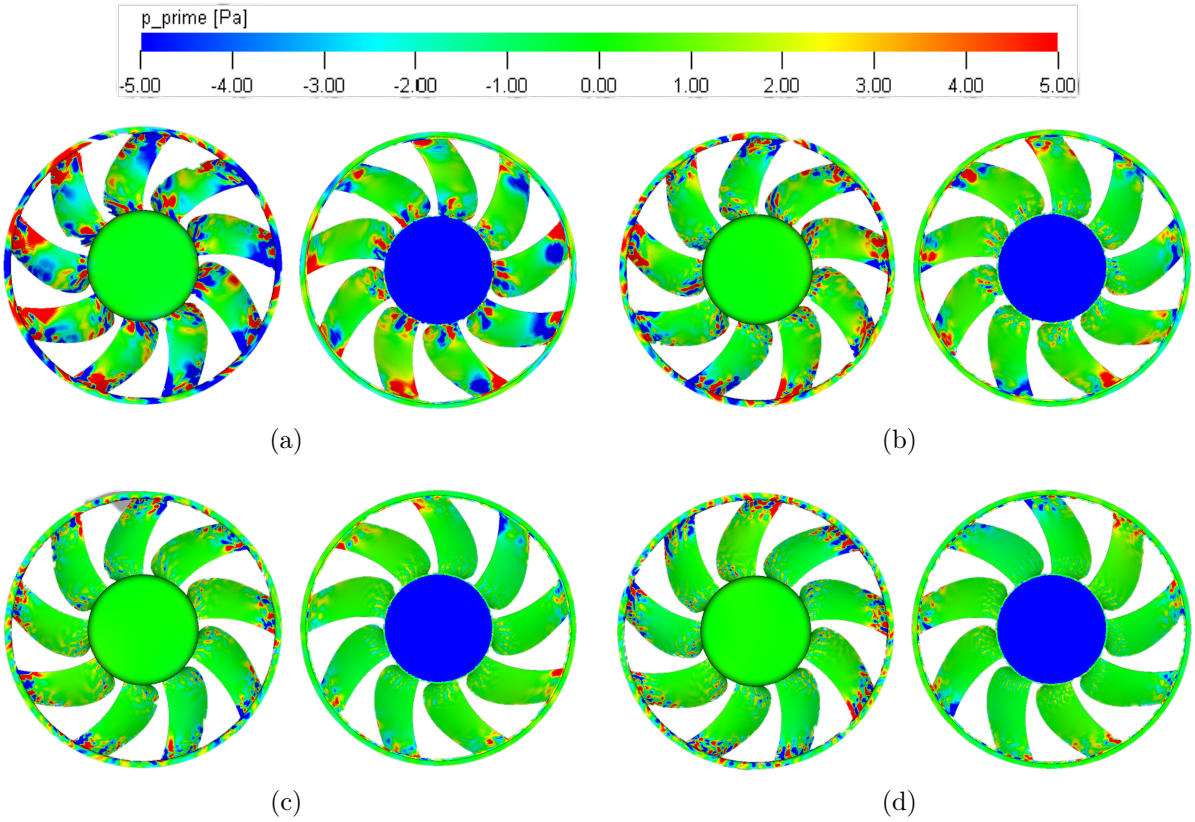

Figure 6.16 Filtered rotor wall-pressure fluctuations on the suction side (left) and pressure side (right) of the blades for the H380 in the ducted configuration in frequency bands corresponding to the observed acoustic sub-harmonic humps (a) 225-365 Hz (b) 530-670 Hz (c) 780-865 Hz (d) 1045-1220 Hz

in the tip region appear to cover a larger portion of the span, indicating stronger sources which is coherent with the FWH analysis for this frequency band.

While a comparison of the topology of the coherent structures generated by tip leakage flow in the plenum and duct configurations for the H380 (Fig. 6.5) showed that the duct wall proximity favored the appearance of larger vortical structures in the ducted setup, from the FWH analogy results, two observations can be made:

— The frequency of occurrence of the spectral humps being very similar, it can be postulated that the flow distortions responsible are similar across the test rigs
— With the exception of the primary hump at 275 Hz, the tonal humps showcase similar levels; this would seem to indicate that the flow distortions cause similar levels of fluctuations in the blade loading overall, as confirmed for all but the first harmonic through the wall-pressure fluctuation maps

Mahle Configuration

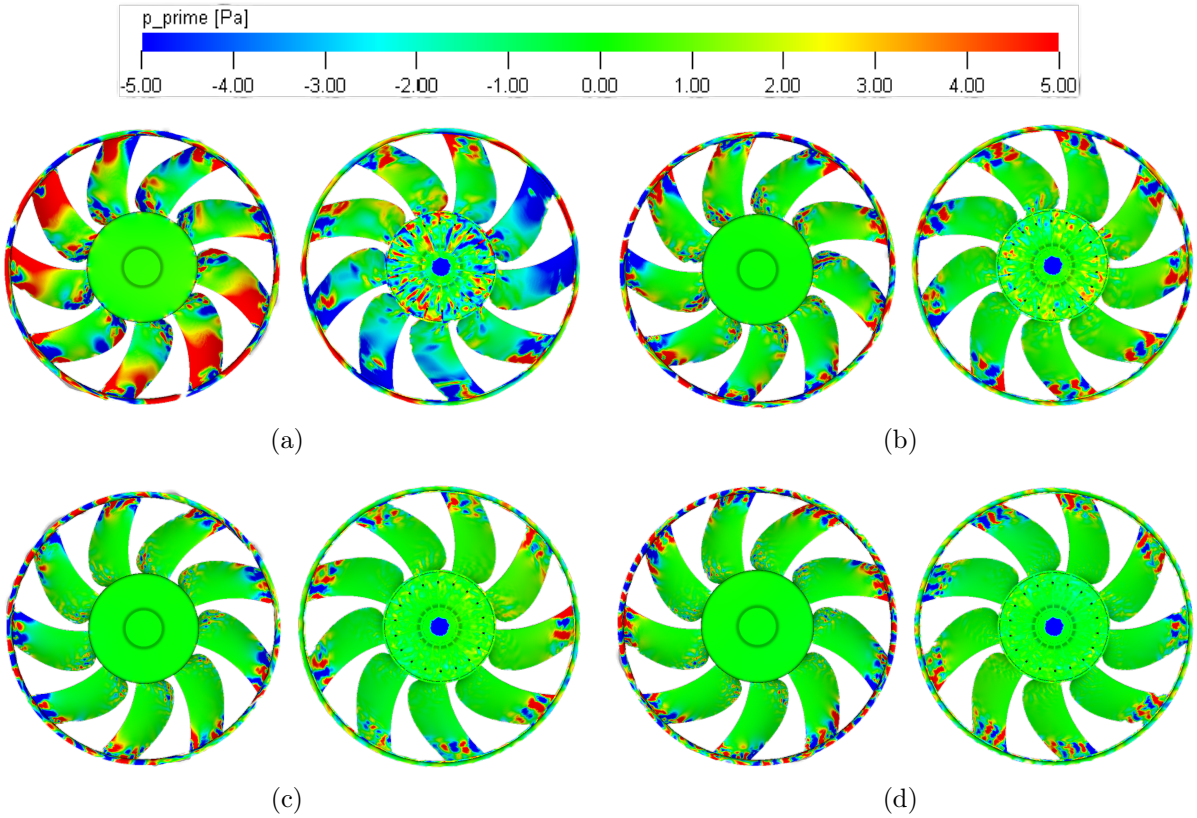

Figure 6.17 Filtered rotor wall-pressure fluctuations on the suction side (left) and pressure side (right) of the blades for the H380 in the plenum configuration in frequency bands corresponding to the observed acoustic sub-harmonic humps (a) 225-365 Hz (b) 530-670 Hz (c) 780-865 Hz (d) 1045-1220 Hz

The final configuration covered in this section is the Mahle ring-shrouded fan, which was presented in Sec. 3.4.2. The fan was tested experimentally and simulated using the LBM as mounted on a real engine cooling module to more accurately evaluate the aerodynamic and aeroacoustic efficiency of the system as installed on a real automobile. A plywood backplate was even included in the setup to reproduce the proximity of the engine block. To properly identify and evaluate the primary sources of noise contributing to the farfield spectra, the FWH analogy was used to propagate the surface pressure fluctuations to the microphone-array positions (a 20 microphone array was used to measure the noise in the experiment, as shown in Fig. 3.23); this was done in order to compare the results of the FWH analogy with both direct acoustic simulation data and experimental measurements. Given the numerous possible surface sources present in the setup, in the simulation the studied geometry is decomposed in a way as to allow for a precise identification and localisation of the dominant noise sources using this method. The solid surfaces for which

pressure data was recorded in both simulation cases studied here are identified in Fig. 6.18.

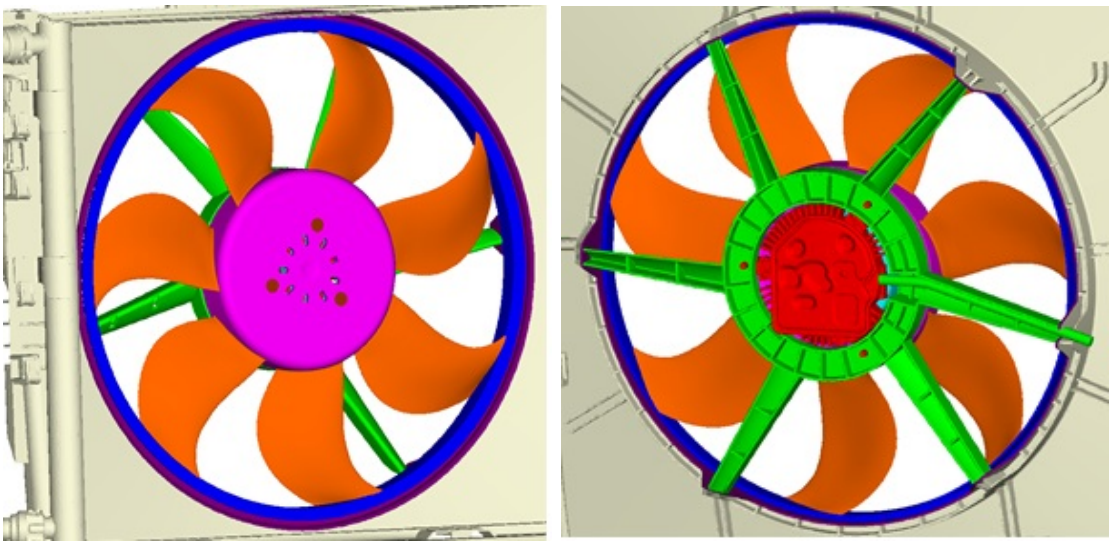

(a) (b)

Figure 6.18 Separation of the surface sources on the fan module (a)View from upstream (b) View from downstream

They consist of several groups: first the fan blades, ring and hub external surface make up the *Rotor* group; secondly the electrical motor and the hub internal surface are included in the *Motor* group; thirdly, the stator vanes or struts, the shroud ring and module frame make up the *Stator* group. A fourth group has also been added with the restriction back-plate located behind the fan module.

Given the fact that the fan rig was only a few centimeters above the ground, the acoustic reflection off the solid floor was included in the FWH modelisation (simple plane reflection); it was shown to provide a net improvement in the prediction by the analogy in this particular cas, as shown in Lallier-Daniels et al. [Lallier-Daniels *et al.*, 2015]. Thus, unlike the previous cases, which employed a fully free-field propagation, this case included what is a fairly important environmental effect.

In addition, a permeable surface encompassing both the fan module and the downstream blockage plate was added in the simulation to investigate whether significant additional noise sources were present in the flow itself or if the majority of the noise was produced as a result of fluid-solid interactions.

The result of the FWH prediction, including ground reflection effects, for the second simulation is shown in Fig. 6.19 for two locations corresponding to microphone-array positions.

The spectra is presented as a function of the normalized frequency (normalization by the fan rotational frequency), hereafter referred to as *Orders* (O), which was deemed necessary to simplify the reference to specific tones in the spectra for the FWH analysis.

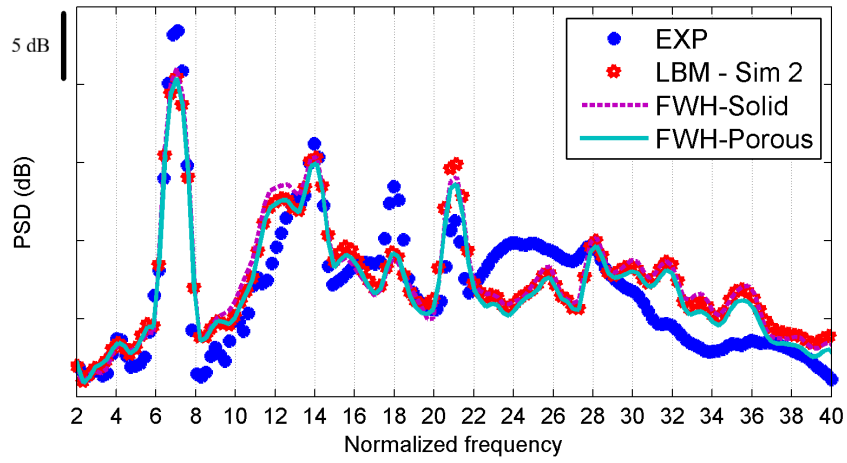

(a)

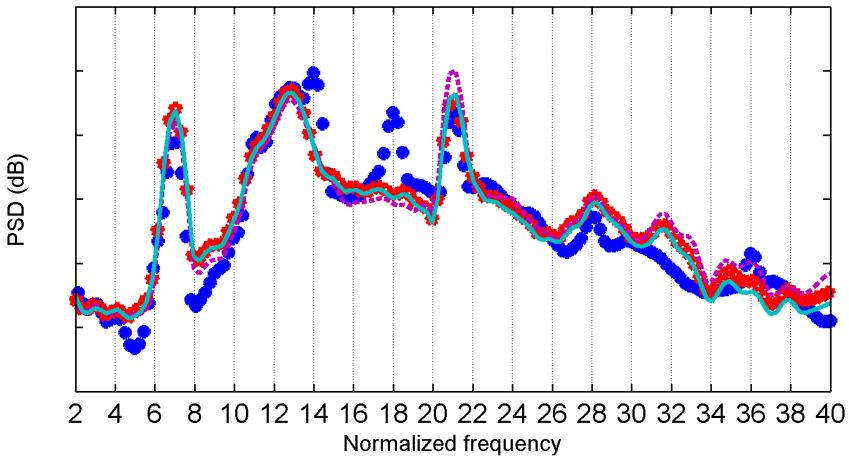

(b)

Figure 6.19 Acoustic pressure PSD for two separate microphone locations, comparing the FWH predictions using the solid formulation (with ground reflection) and porous formulation for the second simulation (a) Microphone 2 (b) Microphone 14

The primary conclusion that can be drawn is that the FWH predicted noise levels follow the direct CAA very accurately, indicating that the majority of the noise sources have been captured. There is also little to no difference between the solid and permeable surface formulations of the analogy for this case, indicating that the main sources of noise are indeed mainly the result of dipolar unsteady pressure loading only.

As mentioned above, the main interest of using the FWH analogy in this case lies in the identification of the dominant noise sources. The wall-pressure fluctuations had been recorded for the four grouped surfaces to allow for tracking of the noise origin on the module. Fig. 6.20 shows the resulting noise spectra at a given microphone-array location, decomposed by source of origin according to the source nomenclature from Fig. 6.18.

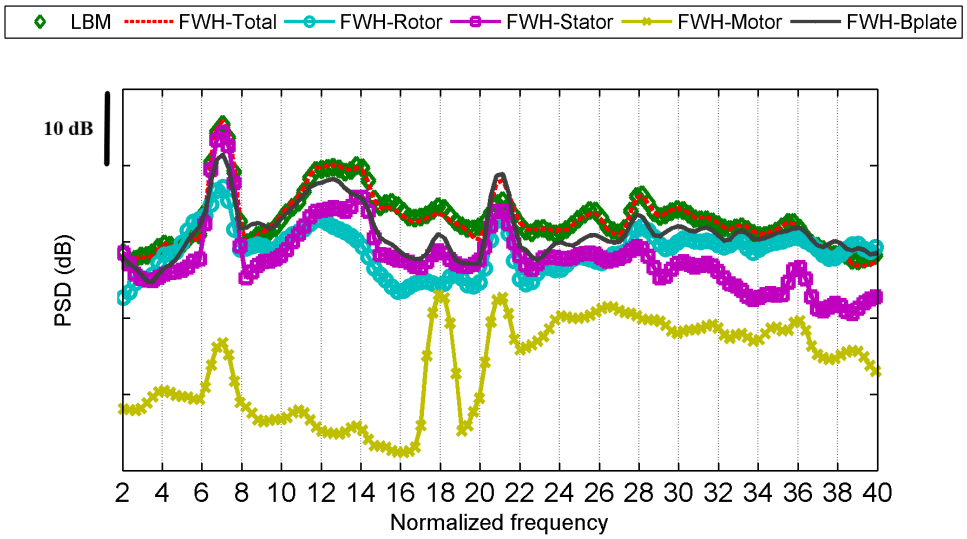

Figure 6.20 Decomposition of the contributions of the different surface sources on the Mahle configuration for microphone 2

The backplate is seen to exhibit a proeminent PSD level across most of the frequency spectrum. This is due to the fact that the plate is exposed to the perturbed exhaust flow from the fan, causing high pressure fluctuations on the surface which are then propagated into the farfield as noise. The backplate contribution is thus correlated with all other sources on the fan. A cross-correlation analysis would be required to investigate it further, but exceeds the scope of the current work.

The PSD levels from the stator elements also follow almost exactly the levels from the module frame, which is included in this category. In the cited study [Lallier-Daniels *et al.*, 2015], the module frame was initially omitted as a noise source in a preliminary simulation, leading to a clear underprediction of the overall spectra.

Taking a closer look at the first three BPF harmonics and the O18 tone highlighted earlier, the source elements can be ranked and some insight can be gained on the possible source mechanisms.

First of all, for the first BPF tone, the rotor and stator elements appear as primary contributors. The flow non-uniformities in the velocity field near the top and bottom

parts of the module frame (seen in Fig. 6.8) would in fact favor periodic fluctuations on the rotor blades near the first BPF and thus the production of the associated tone. The stator elements (stator arms precisely) sometimes surpass the rotor elements as the primary contributor for this tone. This happens on microphone 2, which is the one shown in Fig. 6.20, but also on other microphones in the array. This indicates that rotor-stator interaction noise has a significant influence on the module footprint and can compete with the effects of inlet distortions on the rotor blades.

The second BPF frequency range spanning from O10 to O14 also shows an interesting trend. On the one hand the stator elements are seen to not only contribute to the second BPF where a peak is shown, but also to the large subharmonic hump centered around O12-13. On the other hand the rotor elements show no tonal peak at the second BPF, but rather a subharmonic hump around O12.

This indicates that the second BPF tone originates exclusively from the stator, caused by rotor-stator interaction, and that the rotor does not contribute significantly. The subharmonic hump, however, presents contributions from both the rotor and the stator. The hypothesized cause is the vortical structures primarily issued from the tip gap region seen in Fig. 6.7: vortices formed as a result of the backflow through the L-shaped tip gap interact with the rotor blade tips when re-entrained in the main flow, causing fluctuations in the blade loading, which also impacts the stator arms as a result. Filtered wall-pressure fluctuation maps on the module surfaces in Fig. 6.21 indeed indicate that the tip of the blades and vanes are where the most elevated levels are found for this frequency range, comforting this observation.

For the third harmonic of the BPF, the rotor and stator elements are shown to be the dominant noise sources, although like for the first BPF their relative strength can change depending on the microphone considered. The motor elements also show a significant contribution to this tonal peak, even though the level on microphone 2 from Fig. 6.20 is still approximately 10 dB lower than the rotor and stator contributions. However, once again, depending on the microphone being evaluated, motor elements can produce a tonal peak whose level equals or exceeds that of the rotor and stator.

A significantly high tonal peak is also seen emerging from the motor contribution at O18. Tonal noise at this frequency was also observed consistently in the experimental measurements but the source could not be identified. The FWH analysis however points to the motor assembly as the culprit. Observing the interior of the fan hub in Fig. 6.22, a series of 18 regular ribs can be identified. The motor is also mounted using three

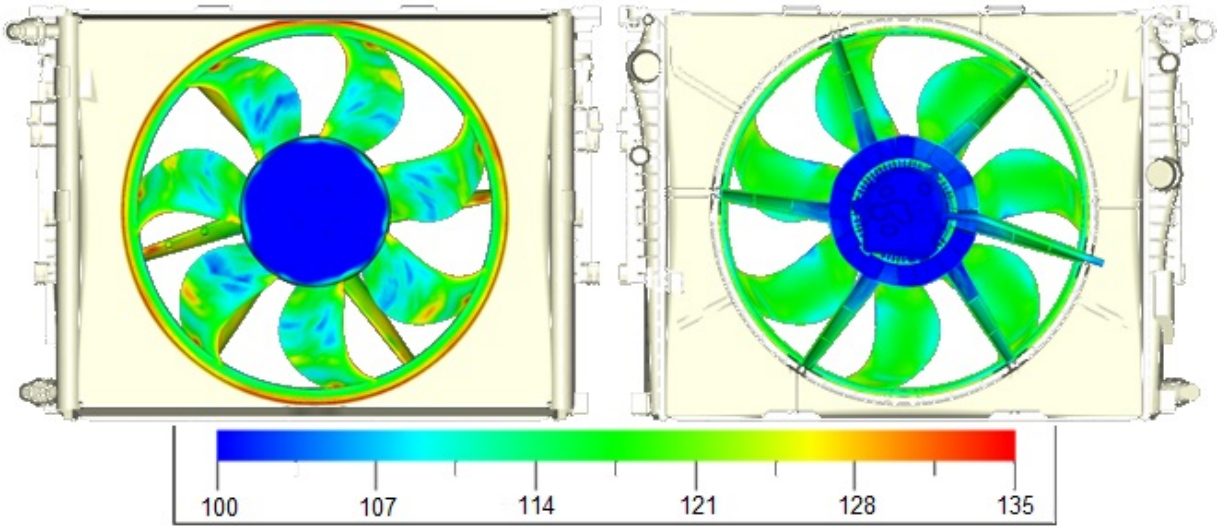

Figure 6.21 PSD of wall-pressure fluctuations on the fan, stator and electrical motor surfaces for the 232-358 Hz frequency range (O12-14) for the Mahle fan.

protruding anchor points sitting a few millimeters from the ribs. The interaction of those two elements during fan rotation yields the O18 tone. This was verified experimentally by modifying the module: when the hub ribs and motor mount were concealed, the O18 tone all but disappeared.

The results of the FWH analysis for the Mahle fan are significantly more detailed that the other configurations given the fact that the complexity of the simulated rig included several competing noise mechanisms. However, a similar sub-BPF quasi-tonal component in the acoustic spectra (O12-13) linked to the influence of the vortical structures [Piellard *et al.*, 2014] generated as a result of the returning flow through the L-shaped gap, as with the H380 configurations, although only one harmonic is visible in the acoustic spectra for the Mahle configuration.

6.4 Conclusion on the Detailed Investigation of the Clearance Flowfield and Fan Noise Sources

In this chapter, the flow features associated with tip clearance flow in axial fans and their impact on the radiated noise of each of the fans presented in the previous chapters have been investigated. A basic overview of the vortical field around each fan was provided using the λ_2 criterion to identify the tip leakage flow. The stark contrast in the tip flow mechanics between free-tipped and ring-shrouded fans was made evident from this analysis.

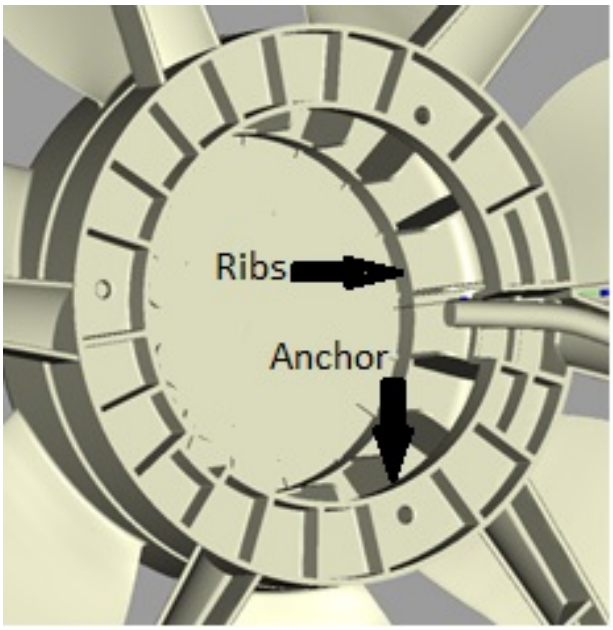

Figure 6.22 Illustration of the interior of the fan hub.

The several free-tipped axial fan configurations studied also allowed to evaluate the impact of several parameters on the formation of tip leakage flow. The increase in strength of the secondary flow with decreasing flowrate was confirmed through the USI7 and RCDB test cases; it also becomes more turbulent in nature as a result. It was also observed that the path of the TLF shifted to a more azimuthal direction as the flowrate is reduced. This further confirms observations from previous studies presented in the literature review in Chap. 2. The modified tip clearance gap on the Bosch configuration also showed that improper shroud contouring can also potentially lead to a forceful interaction of the TLF with the rotor blades.

The inception of a strong TLF for this type of axial fan was also shown to result in increased noise coming from the fan, with the occurrence of non-BPF quasi-tonal noise also observed on the the studied fans as an apparent result of the interaction of the flow distortions created in the tip region with the rotor blades, causing fluctuations in the blade aerodynamic loading which then radiates in the far-field as a dipolar source. However, duct propagation effects can very effectively mask these effects, but they can be filtered out using hybrid methods such as the FWH analogy, which was the tool used in this study.

Two ring-shrouded axial fans with similar characteristics were also studied in three different configurations (i.e. plenum, duct and module). It was shown that the topology of the resulting tip clearance flow, while due to the same basic mechanism (return flow through

the L-shaped tip clearance between the ring and the static shrouds), was largely impacted by the installation. In the presence of a clean inflow, best represented by the H380 plenum configuration, the backflow through the tip leakage flow tends to quickly roll up into a complex field of thin vortical structures along the circumference of the fan rotating shroud. However, the lack of axisymmetry of the module in the Mahle case generates localized disturbances in this field, leading to the formation of larger vortices, while this becomes generalized along the circumference in the ducted H380 configuration.

The H380 fan having been tested using different test rigs provided an opportunity to inspect the impact of this modified vortical field topology on the acoustic radiation. The presence of strong acoustic modes in the duct configuration, however, made a straightforward comparison impossible, which is why the FWH analogy was utilized to identify the direct contribution of the isolated fan. This showed a surprising result, as the same sub-harmonic quasi-tonal components that were easily identified on the plenum configuration were also very clearly produced in the ducted case, only masked by the acoustic modes generated by the propagation conditions. This indicates that while the vortical structures generated upstream of the ring-shroud are strongly impacted by the proximity of the duct, the flow distortions that cause the fluctuating blade loading and the appearance of the strong quasi-tonal harmonics are virtually the same.

A similar sub-harmonic quasi-tone was also identified on the Mahle fan just under the second BPF harmonic frequency, which was linked in previous studies to the influence of the vortical structures [Piellard *et al.*, 2014] generated as a result of the return flow through the L-shaped gap. In the particular case of the Mahle ring-shrouded fan however, the use of the FWH analogy using recorded wall-pressure fluctuations from the module solid surfaces, combined with an extensive decomposition of the surfaces (four representative groups including the rotating fan, the stationary frame and struts, the electrical motor and the back-plate), was necessary for the identification and localization of noise sources on the complex module. It was highlighted that all potential noise-generating surfaces must be included in the analogy to reproduce the directly simulated sound pressure levels accurately. For this particular case the effects of the reflection of acoustic waves on the solid floor of the anechoic room must also be modeled due to the proximity of the rig to the floor in the experiment/simulation [Lallier-Daniels *et al.*, 2015]; this was also previously stressed by Moreau et al. and Roger and Moreau [Moreau *et al.*, 2008; Roger and Moreau, 2008].

From the FWH analysis carried out on the ducted cases (USI7, RCDB, Bosch and H380), it can be observed that the duct amplification effects are systematically captured by the

analogy. The level of the amplification, however, varies from case to case. For example, the USI7 shows an discrepancy of around 5-7 dB while the H380 exhibits differences of around 10-12 dB on average; however, amplifications of up to 30 dB are observed on the Bosch and RCDB cases which showed a notable sensitivity to the occurrence of acoustic modes. It provides a reliable gauge to evaluate the influence the propagation environment has on the resulting acoustics.

The analysis carried out in this chapter, however, cannot provide a characterization of the flow distortions responsible for the occurrence of the observed quasi-tonal noise observed from the various fans and configurations. A quantitative method was devised to try and characterize the vortical structures in the tip region of the blades deemed responsible for these tones and is the subject of the next chapter.

CHAPTER 7

Investigation and Quantification of Narrow-band Tip Leakage Flow Noise Mechanisms

7.1 Context

Tip leakage flow can become an important source of noise in turbomachinery applications under the right conditions, as highlighted in the literature review (Sec. 2.3.2) and through the analysis of the various configurations studied in the previous chapter. Thus, increases in tip clearance flow strength, either as a result of an increasing tip clearance gap or decreasing flowrate, typically generate more elevated broadband noise levels. Moreover, the appearance of strong quasi-tones at sub-BPF frequencies was also quite clearly highlighted on the studied configurations when the interaction of the tip leakage flow with the blades is particularly strong. This was also reported by several authors, with the appearance of tonal noise attributable to tip clearance flow effects in free-tipped [Baumgartner *et al.*, 1996; Kameier and Neise, 1997a,b; Liu *et al.*, 1996; Zhu, 2016] and ring-shrouded [Kameier, 1993; Magne *et al.*, 2015; Moreau and Sanjose, 2016; Pardowitz *et al.*, 2015a,b, 2012; Piellard *et al.*, 2014] fan systems at sub-BPF frequencies having been observed.

For instance, Kameier and Neise proposed the so-called rotating instability (RI) explanation to the appearance of these tones, which was later confirmed to be linked to the appearance of flow distortions linked to tip leakage flow effects rotating at a portion of the rotor speed in the passage flow interacting with the blades. This fact was also confirmed on many of the cases studied in the course of this project in the previous chapter.

However, the phenomenon is still not completely understood to this day and is still the subject of investigation. In this study, a spectral correlation technique was adapted for the detection and characterization of these flow distortions in relation to tip leakage flow is low-speed axial fans was adressed specifically in the current study. The method was previously used in a concurrent study [Zhu, 2016; Zhu *et al.*, 2016b], as it was shared with the author as part of a collaboration between the Université de Sherbrooke and the University of Siegen, to successfully identify the flow structures in the tip region of the blades responsible for the sub-harmonic humps and found a strong link to the aforementioned RI signature.

7.2 Modal Analysis Method

Working under the assumption that coherent structures generated from the tip gap flow and their interaction with the blades, as seen in the previous chapter, are responsible for the narrowband humps observed in the acoustic spectra of the studied configurations, it becomes important to be able to identify and characterize these flow features. In effect, the vortical structures shed from the tip clearance gap into the blade passage are highly turbulent and form intricate vortical systems that can travel from blade to blade, as seen from the illustrations of the tip clearance flow topology in the studied fans in Sec 6.2. However, if one is able to properly identify and characterize these structures and model their interaction with the rotor blades, it becomes possible to try and evaluate the acoustic emissions from this interaction mechanism. The difficulty thus becomes to properly identify these structures.

A correlation technique initially designed for the experimental characterization of flow instabilities in centrifugal [Bent, 1993; Bent *et al.*, 1993; Mongeau *et al.*, 1993; Wolfram and Carolus, 2008] and axial [Sturm and Carolus, 2012] fans using synchronous measurements from circumferentially-spaced probes was repurposed for the characterization of the tip leakage flow instabilities. The method relies on the hypothesis that the rotating flow features issued from the tip leakage flow can be viewed as circumferential wave patterns superimposed on the base flow with a given rotational convection velocity which can be potentially very different from the base rotor speed. The result of these wave patterns, or azimuthal modes, interacting with the rotating turbomachinery blades would then cause fluctuations in blade loading and have repercussions on the tonal noise generated by the fan; adding the contributions of different modes together would generate broadband humps in the spectra.

These circumferential wave patterns can be quantified through two parameters: their mode order m and circumferential convection speed n_{mod}. From these characteristics, their interaction frequency f_{int} with the rotor blades can be calculated. It should be noted that the term *mode* as used in this work refers to the coherent flow structures detected using the current correlation analysis method in the aerodynamic near field around the fan impeller; it should not be mixed up with the acoustic modal nomenclature which is also used to define acoustic modes propagating in a duct.

To calculate the properties of the wave patterns, the correlation method relies on the use of synchronous measurements of flow properties at two or more points along the circumference at a given radial position. Using time signals of two sequential measurement positions (x

the leading signal and y the lagging signal), the cross-spectral density (CPSD) S_{xy} as well as the coherence C_{xy} between the two signals can be computed. In the course of the work presented here, the CPSD is evaluated using Welch's modified periodogram method [Welch, 1967]. The phase lag between the two signals γ_{xy} can also be evaluated by taking the ratio of the real ($\Re$) and imaginary ($\Im$) parts of the CPSD as shown in Eq. 7.1

$$\gamma_{xy}(f) = atan\frac{\Im(S_{xy})}{\Re(S_{xy})} \tag{7.1}$$

The angular spacing between two measurement points ϑ_{xy} being known, using the unwrapped phase lag γ_{xy} the mode order of a given wave pattern as a function of frequency is given by Eq. 7.2

$$m(f) = \frac{\gamma_{xy}}{\vartheta_{xy}} \tag{7.2}$$

Given the interpretation that a modal wave pattern as described previously is a highly coherent structure, at this point it becomes necessary to employ the cross-coherence levels as a high-pass filter to ensure that modes are positively identified only for frequencies for which the coherence is over a given threshold value. This value is application dependent and requires some analysis for the user to determine a suitable value.

Following appropriate coherence filtering, and using the azimuthal order as a function of frequency obtained from Eq. 7.2, quantification of the overlaid modes can be completed by calculating their angular speed in the absolute frame of reference. This can be calculated using stationary measurement points (e.g. stationary pressure taps) as in Eq. 7.3

$$n_{mod} = \frac{2\pi f}{m} \tag{7.3}$$

In the case where measurements performed in a rotating frame of reference (e.g. flying hot-wire measurements or pressure taps imbedded in the blades) are used for the correlation analysis, the modal angular velocity can be calculated as in Eq. 7.4

$$n_{mod} = n_{fan} - \frac{2\pi f}{m} \tag{7.4}$$

where n_{fan} is the angular velocity of the reference frame wherein the measurements are taken.

It is important here to highlight that the unwrapping operation that has to be carried out on the phase lag between the signals to properly identify the order of the modes introduces a critical constraint to the method. In fact, the phase signal needs to be nearly linear for a proper unwrapping to take place. This behavior is very frequently encoutered when looking at strongly correlated signals, and it implies that the structures detected at varying frequencies are associated with an increasing modal order $m(f)$ possess a group rotational velocity n_{mod}. This is where coherence thresholding comes into play, as only those structures associated with high coherence levels will ultimately establish stable modes, whilst the remainder of the structures are expectedly winking in and out of existence.

Thus, the identified coherent flow structures are fully characterized as a function of their mode order m and angular speed n_{mod}. Using these characteristics with knowledge of the number of blades Z and rotational speed of a given impeller design (or stator), one can then calculate the interaction frequency f_{int} between the rotor and the identified modes as Eq. 7.5

$$f_{int} = N_{int}(m, Z) \cdot (n_{fan} - n_{mod}) \tag{7.5}$$

where $N_{int}(m, Z)$ represents the number of independent interactions between a given mode and the blades per relative rotation. This factor takes into account the fact that the interaction of a mode with a number of lobes multiple of the number of fan blades (or inversely) will produce a tone at an order multiple of the modified $(n_{fan} - n_{mod}) \cdot BPF$ fundamental, with several blades contributing at the same time.

The original method, as reprised by Wolfram and Carolus and Sturm et al. [Sturm and Carolus, 2012; Wolfram and Carolus, 2008], does not specifically address the fact that a negative phase would indicate the presence of a mode rotating in a direction opposite to the direction of evaluation. In that case, the mode order will be negative and have an associated negative velocity. These modes should not be discarded as they could potentially have a physical explanation.

Furthermore, while the method allows for the detection and identification of coherent structures as well as their possible interaction frequency from an acoustic standpoint, it only provides an "event counter" approach to the identification; it does not provide any information on the amplitude of the interaction for a given event. This was also noted previously by Wolfram and Carolus, and a qualitative comparison between the actual

acoustics and structure interaction frequency histograms were later presented by Sturm et al.

However, a more in-depth analysis is obviously required in terms of evaluating the amplitude of the events identified using the method presented here and reflecting it in the interaction frequency histogram by weighting the different events. An approach relying on the use of wavelet theory has been tested in the course of this study in order to try and provide a suitable estimate as to the strength of the interactions between the identified coherent structures and the rotor. It is presented in Sec. 7.3.

7.2.1 Specific Application of the Correlation Method to the Identification of Tip Leakage Flow Structures

As evidenced in the previous section, the proposed correlation method aimed at quantifying the interaction of tip leakage flow structures generated in the passage flow of axial fans with the rotor blades was previously used as a means to detect distortions at the inlet or outlet in the main flow in turbomachinery systems.

However, in the present study, this technique has been adapted to allow for the detection of the flow distortions associated with the coherent structures generated from the tip leakage flow in axial turbomachinery applications and predict the noise spawning from their interaction with the rotor blades. The method relies on two hypotheses:

— The correlation technique can be applied to what can be considered as relatively local phenomena when looking at the short-lived coherent structures in the tip region of the studied axial fans
— As a sort of corollary to the first hypothesis, the lifespan of a particular structure identified using the correlation method in the tip region of the blades may be short, but it is probable that similar ones are produced around the circumference, and thus a particular identified mode will interact with all the blades along a relative revolution (i.e. the tip leakage flow produces preferred types of structures for a given fan configuration)

Given these hypotheses, and to insure correct identification of the structures, measurement points with an angular resolution much tighter that the one proposed by both Wolfram, Carolus and Sturm have to be employed on the full circumference of the fan in the passage flow in order to yield a statistically representative identification of the flow structures of interest. This is difficult to achieve in an experimental setting, but is however well within

the realm possibility in the case of unsteady numerical simulations such as those carried out in this study.

The method, developed as part of the current study, was shared as part of a collaboration with the University of Siegen and shown to be able to properly explain the narrowband tip clearance noise on the USI7 test fan [Zhu, 2016; Zhu *et al.*, 2016b].

In Sec. 7.4, the results of correlation analysis on the RCDB, Bosch and Valeo H380 fans are presented, in addition to a short reminder of the results obtained on the USI7 through the collaboration with the University of Siegen which was used as the initial validation case for the method.

7.3 Evaluation of the Strength of the Interactions from Correlated Modes

Before transitioning to Sec. 7.4 and showing the application of the correlation method for the detection and quantification of coherent azimuthal structures in the flow described in Sec. 7.2, the issue regarding the evaluation of the amplitude of the modes that was raised must be adressed.

As explained, the correlation analysis as presented employs a counting approach to evaluate the occurrence of the various modes identified; in effect, as the method relies on cross-spectral analysis, the cross-spectra, coherence and phase lag angles are not continuous in the explored frequency range, but rather defined at discrete frequencies. In the method, each of those points is considered a coherent mode if and only if the coherence is above a certain threshold. By applying this analysis across a whole circumference across several radial and chordwise positions, as explained in Sec. 7.2.1, and summing up the number of occurrences of these modes, a statistically representative distribution of the modes present in the flow can be achieved. However, this counting algorithm cannot account for the fact that the structures associated with these modal patterns most probably produce distortions of different amplitudes, and thus impact the blades at different degrees.

In this study, a novel approach based on the use of the wavelet transform on the circumferentially distributed probes has been devised to provide this missing amplitude information. For those unfamiliar with the concept of wavelets, a brief primer is provided in Appendix A; the presentation of a more complete overview of wavelet theory is outside the scope of

the current study, but the reader is directed to the work of Farge, Torrence and Compo and Iatsenko et al. [Farge, 1992; Iatsenko *et al.*, 2014; Torrence and Compo, 1998].

Globally, the idea proposed here relies on the treatment of the wavelet transforms of each of the data points used in the application of the correlation method demonstrated earlier in the chapter (Sec. 7.2) using a temporal version of the local intermittency measure (LIM) filtering [Farge, 1992; Grilliat, 2009; Grilliat and Camussi, 2010; Grilliat *et al.*, 2010] described in Eq. 7.6 as

$$LIM = \frac{\mid W_s(\omega,t) \mid^2}{\langle \mid W_s(\omega,t) \mid^2 \rangle_t} \tag{7.6}$$

where $W_s(\omega,t)$ is the wavelet transform coefficient matrix of a 1D temporal signal $s(t)$ and $\langle\rangle_t$ represents a time-averaging operation. LIM filtering serves as a denoising measure for the wavelet coefficient matrix, highlighting time-frequency areas where an 'event' whose amplitude is significantly higher than the temporal mean for a given frequency is located. The terminology 'event' here is used, perhaps, in a different context than for the Fourier correlation technique described previously in this section, as there is no way to insure that these wavelet 'events' are correlated with those identified using the Fourier method.

However, the base assumption here is that using the LIM filtered wavelet coefficients as a basis, parts of the wavelet spectra corresponding to LIM values inferior to a certain threshold can be eliminated, retaining in effect the high energy events relative to the mean.

Retaining only those values for the process, a time-averaged value for the amplitude of the wavelet coefficients can be obtained as a function of frequency for the filtered signal. Thus, taking the wavelet transform coefficient matrices $W_x(\omega,t), W_y(\omega,t)$ of the same two synchronous signals x, y used in the correlation analysis, the LIM matrices for each of the signals can be obtained. Keeping only the coefficients of the wavelet matrices $W_x(\omega,t), W_y(\omega,t)$ whose associated LIM values are over a certain threshold (e.g. a LIM threshold of 1 signifies that only coefficients whose power is over the average value for a given frequency are retained) we obtain the filtered coefficient matrices $W_{x,LIM}(\omega,t), W_{y,LIM}(\omega,t)$. Taking the time average of those matrices, the weighting functions $A_x(\omega), A_y(\omega)$ can be obtained, describing the amplitude of the high energy events for each of the signals. In terms of the correlation analysis, a more proper weighting function however, would be to take the average value of the weighting functions such that $A(\omega) = (A_x(\omega) + A_y(\omega))/2$ for that pair of sensors.

The wavelet weighting method is highlighted using a single pressure signal extracted in the tip region of the Bosch acoustic simulation in Fig. 7.1; the wavelet time-frequency coefficient matrix of the signal is graphically represented in Fig. 7.1(a) while the calculated LIM is shown in Fig. 7.1(b), with values exceeding unity highlighted in red.

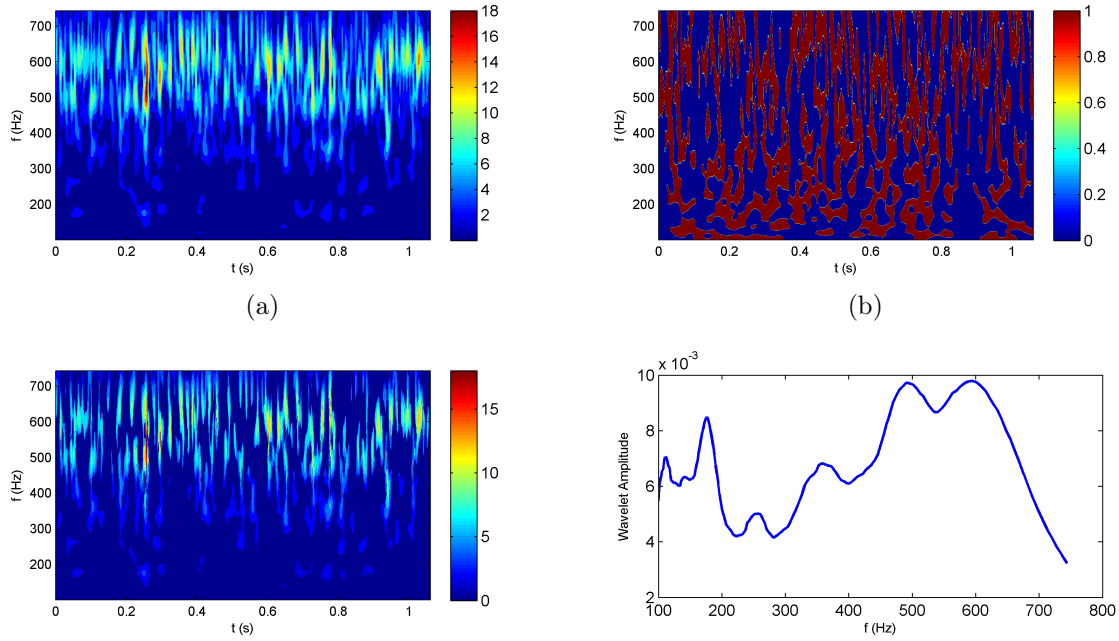

Figure 7.1 Illustration of the wavelet weighting method employed in the proposed modal method (a) Wavelet transform of a pressure signal extracted in the tip region of the Bosch acoustic simulation (b) LIM values of the wavelet transform of the pressure signal (c) LIM-filtered wavelet coefficient matrix of the signal (d) Frequency-amplitude representation obtained through time-averaging of the LIM-filtered wavelet coefficient matrix

Using the unity threshold value to filter out portions of the signal with low energy, the filtered wavelet coefficient matrix shown in Fig. 7.1(c) is obtained. By performing time-averaging on the resulting data matrix, a typical frequency-amplitude plot is obtained, where the ordinate represents the wavelet coefficient amplitude as a function of frequency from the time and frequency filtered signal.

The idea is that this could provide a measure of the amplitude of significant events as a function of the frequency of occurrence for the modes obtained from the correlation analysis method presented earlier in this section, given suitable events are represented by filtering the wavelet transforms this way.

7.4 Correlation Analysis Applied to Tip Leakage Flow of Studied Fans

While the correlation method appears deceptively simple from a mathematical point of view, its practical application is far from straightforward and requires the user to remain attentive to the intermediary results when applying it to a new case. In particular, the frequency range of the analysis and coherence levels (for thresholding of the coherent modes) must be known before any relevant results can be expected.

It is thus required that the used have some idea as to what the proper coherence threshold should be for the positive identification of *coherent* modes, but they are however are highly dependant on the amount of physical time the user has to work with for the cross-spectral analysis (which also dictates the frequency resolution) and the physics of the flow. From a pure signal processing perspective, the window size for the application Welch's periodogram method must be set so that a sufficient number of sample spectra are extracted from the signal (15 to 30 is a minimum recommendation, with a 50% overlap between the segments). A proper resolution for the applications considered here thus requires several seconds of signal to provide some leeway in the analysis.

7.4.1 USI7 Fan

In order to first demonstrate the application of the method, the results obtained on the USI7 configuration studied at the University of Siegen are presented. It was the initial validation case for the correlation analysis [Zhu *et al.*, 2016b] and provided a perfect case study due to the availability of synchronized high quality experimental data from pressure sensors situated on the rotor blades as well as the shroud combined with far-field acoustic measurements for several operating conditions and tip clearance sizes. The configuration was also simulated using the LBM to provide up to 5 seconds of physical converged time, or around 250 fan revolutions; this was one of the motivations for using such a simulation method.

The investigation of narrowband tip noise mechanisms came as a result of a collaboration between the Université de Sherbrooke and the University of Siegen and employed a code using the approach detailed in the previous section. The motivation behind the use of the correlation method was the fact that the USI7 experiments and simulations highlighted the appearance of clear narrowband noise components at non-BPF frequencies with the enlarged tip clearance case at low flow rate, as shown in Fig. 7.2. The appearance of these

harmonic humps at a frequency related to the BPF tones (approximately 74% of the BPF) is observed up to fourth order in the experiment and is fairly well reproduced by the LBM simulation up to third order but with a slight shift in the central frequency to around 70% of the BPF, as previously noted in Sec. 6.3.1.

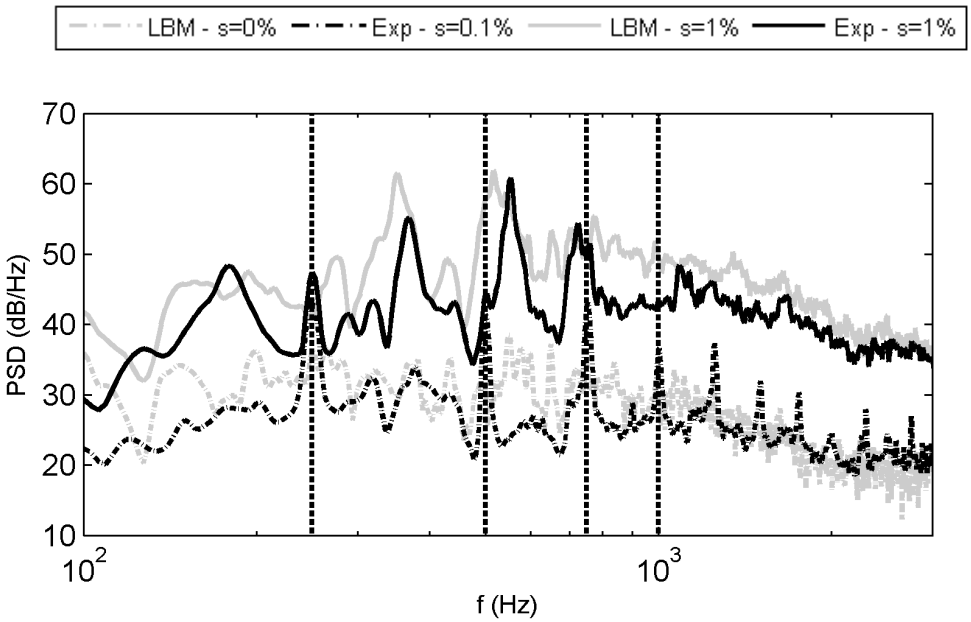

Figure 7.2 Acoustic sound power spectra for one of the off-axis microphone locations for the USI7 fan for the $\phi_{part-load} = 0.131$ operating point.

Furthermore, the appearance of the spectral signature linked to the so-called rotating instability phenomenon was observed from wall-pressure fluctuation measurements in both the simulation and the experiment (see Fig. 5.15) for the case at the lowest flowrate and the larger tip clearance, although the frequency of occurrence of the spectral feature was shifted in the simulation when compared to the experiment. This spectral signature is also clearly visible in the volumetric data extracted from the flowfield, as evidenced in Fig. 7.3.

In his thesis, Zhu showed that by applying the correlation method in the frequency range associated with the RI spectral feature of that particular case, the occurrence of the non-BPF narrowband noise in the acoustic spectra could be predicted by using a fine enough circumferential array of probes for the evaluation of the cross-spectral density; for the USI7 case, a circumferential resolution of 25 degrees (3 points per blade passage) was sufficient for the prediction of all the sub-BPF tones using static shroud wall-pressure measurements in the tip clearance gap.

However, in order to fully investigate the complex system of vortices generated by the tip clearance flow in the blade passage, circumferential measurements taken in the inter-

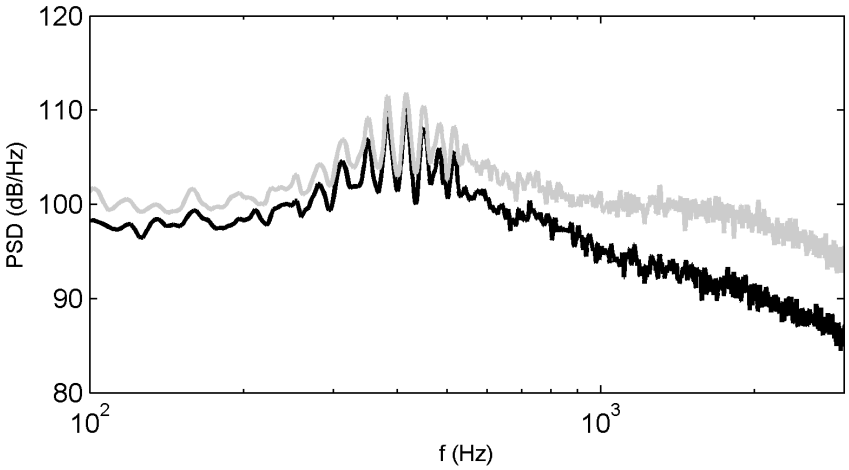

Figure 7.3 Power spectral density of two subsequent signals extracted from the USI7 LBM simulation data. The lead signal is in black and the trailing signal is in grey.

blade flow at various axial and radial positions have to be employed. Furthermore, the circumferential resolution of the measurement points used restricts the order of the mode orders that can be detected with certainty, which is equal to half the number of sensors across the circumference. For these reasons, a full experimental investigation of these coherent structures in turbomachinery applications would necessarily require advanced and often onerous non-intrusive methods such as matched-index PIV [Wu *et al.*, 2011a,b]; even then, a full three-dimensional, 360 degrees analysis is fairly difficult or even impossible to achieve. This is where high-fidelity unsteady CFD simulations such as the LBM provide an interesting alternative to experimental methods, as it becomes possible to fully investigate the flowfield at a fraction of the cost.

In the case of the USI7 simulation, a series of circumferential arrays are setup at various radial positions, starting from a position right under the blade tip (R=146 mm) in decrements of 4 mm down to a radius of R=110 mm; for each radial position, a total of 10 positions along the chord were evaluated. A circumferential resolution of 12 degrees is used (30 sensor positions along the circumference, with 6 points per blade passage). The array probes rotate with the fan. The probe locations are shown in Fig. 7.6.

One of the main pitfalls with the proposed coherence analysis, however, is that it requires some knowledge of the frequency range in which the coherent structures of interest can be found as well as the their expected coherence level. In effect, it requires the user to have some insight into what he's looking for. A blanket approach to cover a wide range of frequencies in the signal could be considered, but it would still require a trial-and-error

approach as to which coherence level is acceptable to use. Furthermore, these parameters are application dependant, making it impossible to determine a *one size fits all* set of values.

In the case of the USI7 configuration, the RI spectral signature identified using pressure measurements in the tip region from sensors imbedded in the rotor blades in the experimental setup as well as the simulation provides a framework with which to work with. Using cross-spectral analysis on the pressure signals from subsequent blade sensors, it was shown that the RI signature is also associated with high coherence levels. By using the proposed correlation analysis in the associated aerodynamic frequency band, the modes identified were shown to interact with the blades at frequencies corresponding to the acoustic sub-BPF humps harmonics of order 2 and above [Zhu, 2016]. This signature is also clearly visible when extracting pressure data in the volume flowfield of the simulation in the tip region in the 300-600 Hz band, as shown in Fig. 7.3. Performing a cross-spectral analysis using the signals from two subsequent circumferentially-spaced locations the RI signature is clearly highlighted by the amplitude of the cross-power spectral density (CPSD), as shown in the median diagram of Fig. 7.4, and is easily linked to equivalent peaks in coherence in the top diagram.

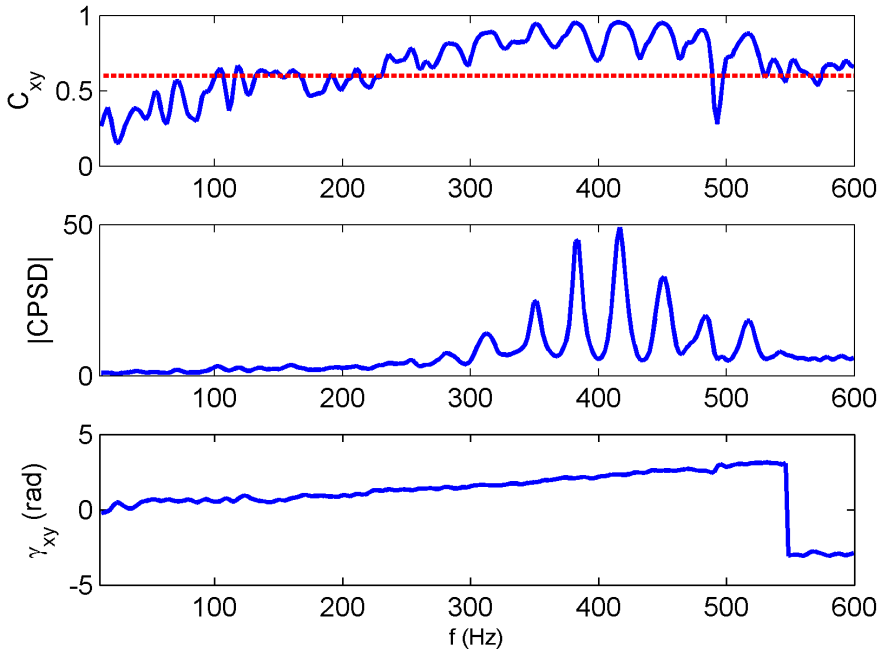

Figure 7.4 Illustration of the intermediary steps of the correlation analysis for a pair of probes in the USI7 LBM volume data. Cross-spectral coherence level C_{xy} (top), cross-spectral density amplitude (middle), phase lag between the signals (bottom)

A strong linearity in the phase is also observed when looking at the bottom diagram; this is actually a requirement for the pair of probes to be considered for the positive identification of modes, as it allows for the unwrapping of the phase to take place for the correct quantification of the modal orders.

Initially, the 300-600 Hz range associated with the RI signature was targeted by the correlation analysis, but it was found that it consistently failed to explain the occurrence of the first harmonic of the observed acoustic sub-BPF humps. In order to capture the first harmonic of the sub-BPF tones, the correlation analysis had to be extended to the low aerodynamic frequency range (10-600 Hz) however. The characteristics of the modes identified through this analysis for the same pair of probes as in Figs. 7.3 and 7.4, using a value 0.6 as the coherence threshold value for positive identification of the modes, are shown in Fig. 7.5. The linear trend of the mode order as a function of frequency and the associated unique modal velocity are highlighted using dashed lines.

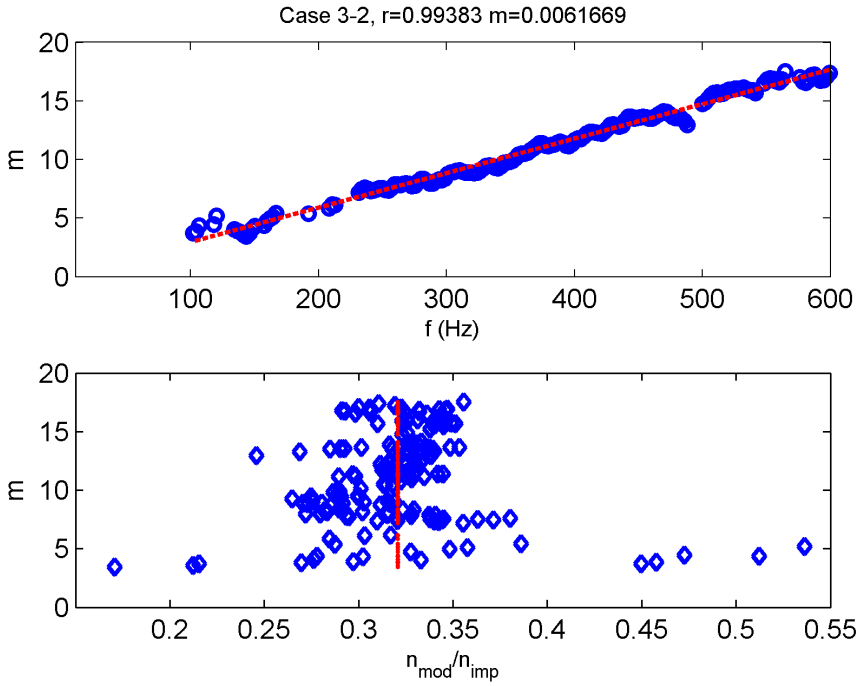

Figure 7.5 Characteristics of the modes identified as a result of the correlation analysis for a pair of probes in the USI7 LBM volume data.

By carrying a similar analysis for all pairs of probes around 360°, a statistical representation of the coherent structures present for a given radial and axial position can be achieved. By extending this process to several radial and axial positions, a spatial analysis of the modes present in the flow can be carried out and a more complete representation of the probable coherent modes in the flow in the tip region is achieved. The order of the modes

detected in the tip region of the blades as well as their rotational velocity is shown for various radii (R146-122) and axial positions (C01-10) in Fig. 7.7. The colormap serves to identify the probe locations in the following bar graphs.

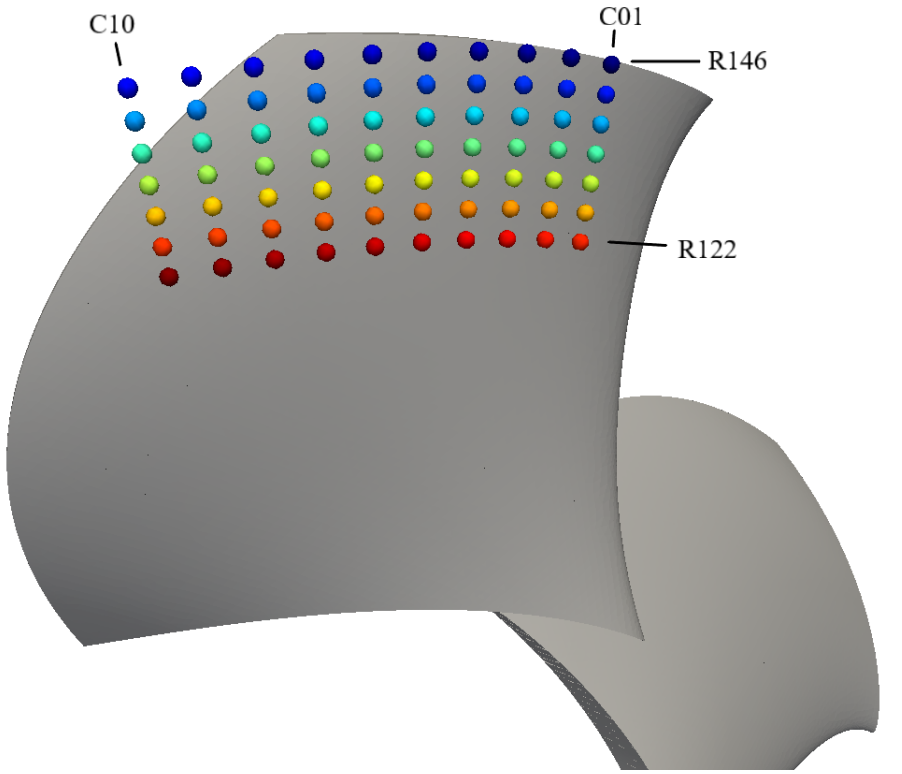

Figure 7.6 Color-coding of the modal analysis positions according to radial (R) and chordwise (C) positions for the USI7 fan.

Overall, it can be seen from Fig. 7.7(a) an almost Gaussian probabilistic distribution of modes (or *events*) with an average order between 12 and 13 is detected in the flow; the most frequently occurring coherent modes thus exhibit between 2 and 3 lobes per blade passage. These modes also appear to rotate at values scattered about a mean of 32-33% of the rotor velocity, as evidenced in Fig. 7.7(b). This observed scattering of the mode orders and velocities yields a consistent explanation to the narrowband spectral shape of the sub-BPF features in the acoustic spectra, as the frequencies of interaction of these modes will also spread across a swath of frequencies.

The identification of these modes in the flowfield is possible using proper filtering techniques using the volume data from the simulation. Fig. 7.8(a) shows the vortical field around the USI7, this time colored by the normalized circumferential speed n_{mod}/n_{fan} in the inertial frame of reference; the limits of the represented velocities were chosen to allow for the identification of flow structures corresponding to the modal velocities from

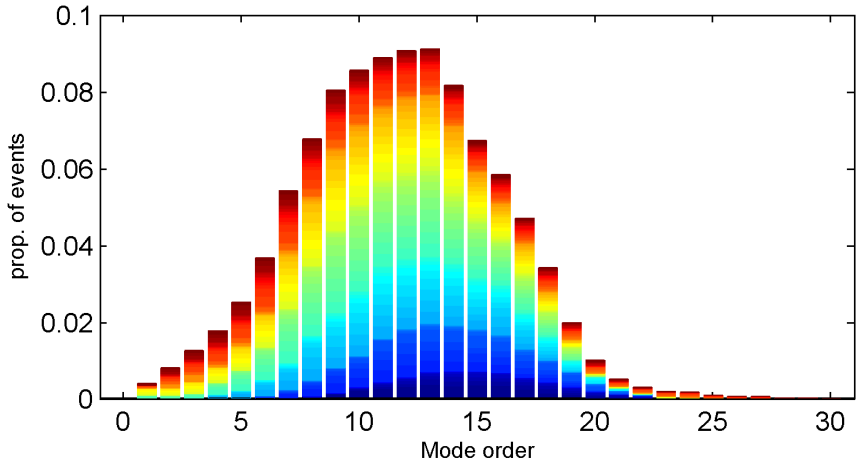

(a)

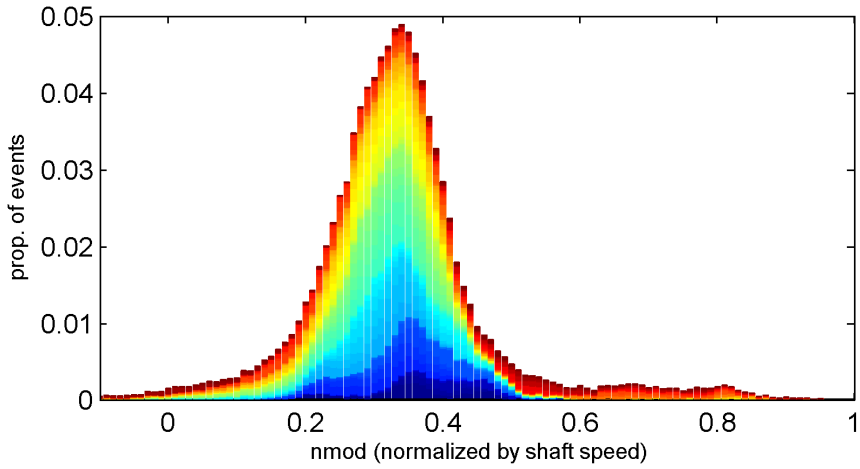

(b)

Figure 7.7 Characteristics of the modes detected through correlations analysis for the USI7 configuration in the tip region (R146-122) of the blades (a) Mode orders (b) Mode rotational velocity.

the correlation analysis. Fig. 7.8(b) shows the filtered vortical field to include only the vortical structures exhibiting rotational velocities between $n_{mod}/n_{fan} = 0.1$ and 0.5.

The pressure modes associated with the coherent structure field from Fig. 7.8(b) can be identified by further filtering the pressure field in certain frequency bands and retaining only the structures associated with a certain mode order. The mode order as a function of frequency is obtained through the correlation analysis, as shown in the top diagram of Fig. 7.5. This additional filtering step is shown for the 340-360 Hz and 505-525 Hz frequency bands, corresponding to mode orders 10 and 15, in Figs. 7.8(c) and 7.8(d) respectively. The λ_2 field is not continuous over the whole circumference, but the modal patterns for each frequency band appear to correspond rather well to the expected mode orders. This firmly confirms the presence of coherent modes in the flow, and comforts the results of the correlation analysis so far by linking the predicted modal characteristics to their actual occurrence in the flowfield.

By making abstraction of the modal characteristics and paying special attention to the spatial origin of the modes, Tab. 7.1 showing the percentage of modes detected for a given radius (R) and chordwise position (C) is obtained and interesting trends appear. First, most of the modes are concentrated between R138 and R130, while the tip radius R146 as well as the lowermost position R122 contain a very small portion of the total number of events. A decreasing proportion of events is also detected closer to the trailing edge from a global perspective.

More specifically, however, two zones with an elevated concentration of modes can be identified from Tab. 7.1 and are highlighted using cell colorations. The first zone (blue) denotes that an elevated number of correlated modes are detected in the leading edge region closer to the tip of the blades. The second zone (red) on the other hand shows a concentration of modes in the trailing edge portion of the blades in the R130-122 range span.

When looking at the vortical structures associated with the identified modes in a single blade passage in the tip region of the blades, as shown in Fig. 7.9, the tip leakage vortex (TLV) is seen to propagate almost azimuthally from one blade to the next, but the turbulent wake created as a result of its breakdown in the blade passage seems to split into two, with a subset of the wake structures impacting the leading edge portion of the following blade whilst the second tuft is redirected towards the trailing edge portion of the blade. The correlation analysis indicated these two subsets of the turbulent wake appear at slightly differing radii.

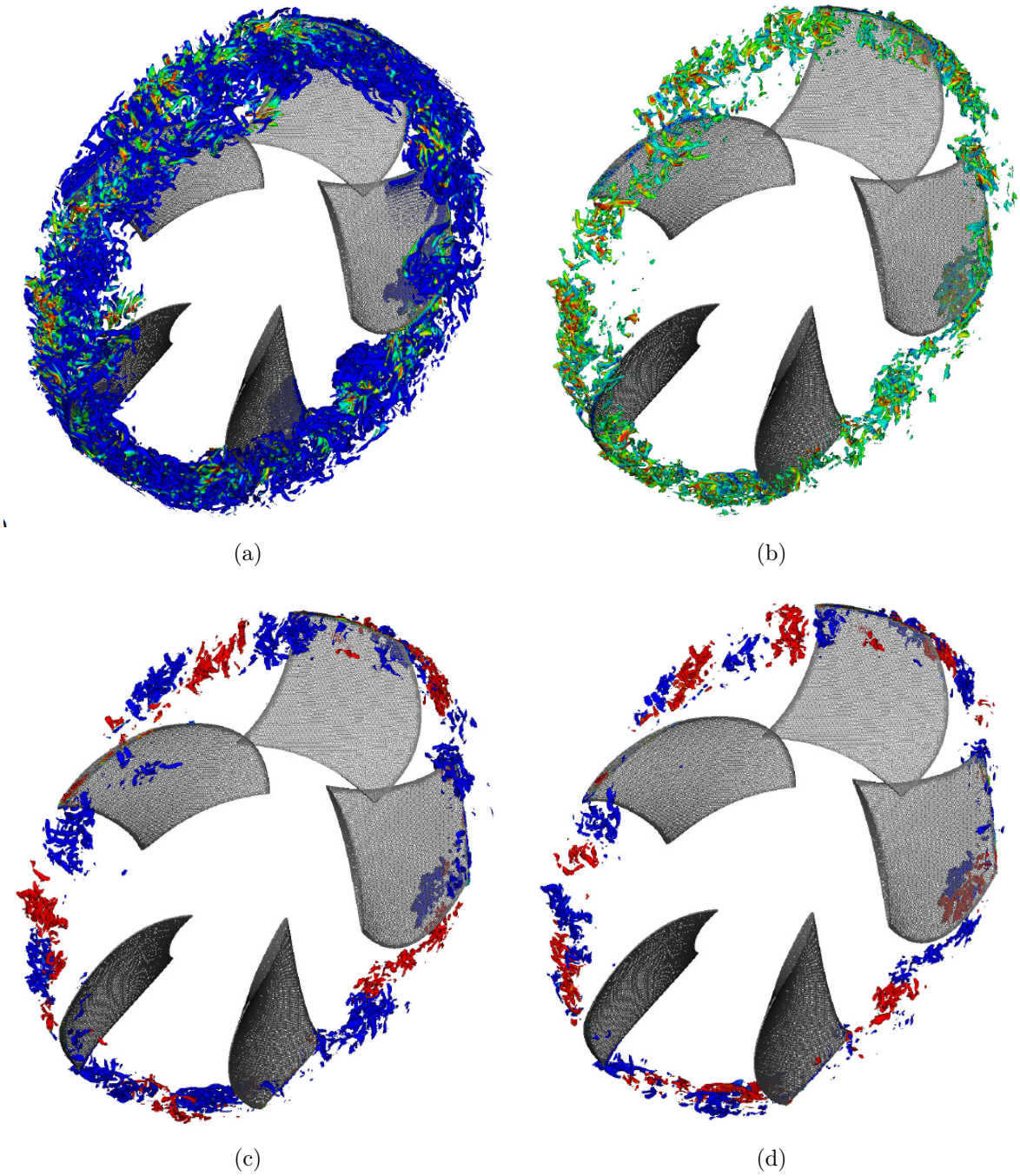

(a) (b)

(c) (d)

Figure 7.8 Instantaneous vortical field around the USI7 highlighted by isosurfaces of $\lambda_2 = -200$ (a) Raw λ_2 field, colored by the the normalized rotational velocity n_{mod}/n_{fan} (b) λ_2 field corresponding to $0.1 \leq n_{mod}/n_{fan} \leq 0.5$ (c) and (d) show the same field as (b) further filtered according to frequency in the 340-360 Hz ($m = 10$) and 505-525 Hz ($m = 15$) bands, colored by pressure amplitude (10 Pa).

Table 7.1 Proportion of events identified at different spatial points according to radius and chordwise position in the tip region of the USI7 fan

% of events		Chordwise ID										
		C01	C02	C03	C04	C05	C06	C07	C08	C09	C10	Total
Radial ID	R146	1.89	1.44	1.00	0.84	0.65	0.34	0.05	0.08	0.10	0.08	6.47
	R142	2.72	2.41	1.94	1.48	1.07	0.75	0.28	0.15	0.12	0.11	11.03
	R138	3.24	3.08	2.81	2.43	2.01	1.60	1.04	0.53	0.36	0.27	17.38
	R134	3.28	3.26	3.16	2.98	2.72	2.41	2.02	1.44	0.91	0.66	22.83
	R130	2.41	1.50	2.03	2.79	3.01	2.09	2.49	2.15	1.55	1.23	21.25
	R126	0.78	0.40	0.75	1.92	0.90	1.37	1.82	2.38	1.27	1.32	12.90
	R122	0.53	0.81	0.14	1.03	1.14	0.50	1.49	1.45	0.57	0.50	8.15
	Total	14.83	12.90	11.82	13.47	11.49	9.06	9.20	8.18	4.88	4.17	

Also, while the array of mode orders represented for each location is equivalent, the modal velocities associated with each are fairly different. In the case of the leading edge zone, the modes appear to rotate with a mean velocity of around 33% of the fan rotational velocity, with a near-normal distribution around the the central value. However, the trailing edge zone modes exhibit a fairly different distribution of velocities, with a bimodal distribution around values 24 of 39% of the fan rotational speed, as shown in Fig. 7.10.

The occurrence of these two modal concentration zones are concordant with observations made from wall-pressure fluctuation maps in Sec. 6.3.1 (Fig.6.10) wherein elevated levels of fluctuations were seen to appear in the tip leading edge region, with a secondary region of occurence closer to the trailing edge on the pressure side of the blades.

Using the aforementioned modal characteristics (mode order and velocity), the correlation analysis can be taken one step further, yielding the predicted interaction frequency of the modes with the rotor blades. The histogram showing the probability density function of the interaction frequency of the detected modes is shown in Fig. 7.11(a).

From a global standpoint, the predicted interaction frequencies of the modes match the first three harmonics of the acoustic sub-BPF humps fairly well ($f_{int} = [3.5, 7, 10.5]$); it was already mentioned that the fourth harmonic was not predicted by the LBM simulation, and a coherent result is here observed in the fact that no structures in the flowfield appear to contribute to this frequency range. However, a fairly strong peak is also observed at $f_{int} = 9.3$ by the correlation method, which does not appear in the acoustic spectra; however, from the comparison of the FWH and LBM spectra, we see that there are some installation effects at work here, and it is possible that this peak is associated with the presence of duct modes, which spread the sharp tonal peak in the FWH prediction in frequency at the third sub-harmonic tone. A secondary tonal peak at $f_{int} = 8.7$ observed in the direct CAA spectra and absent in the FWH analysis can be associated to a corresponding hump in the

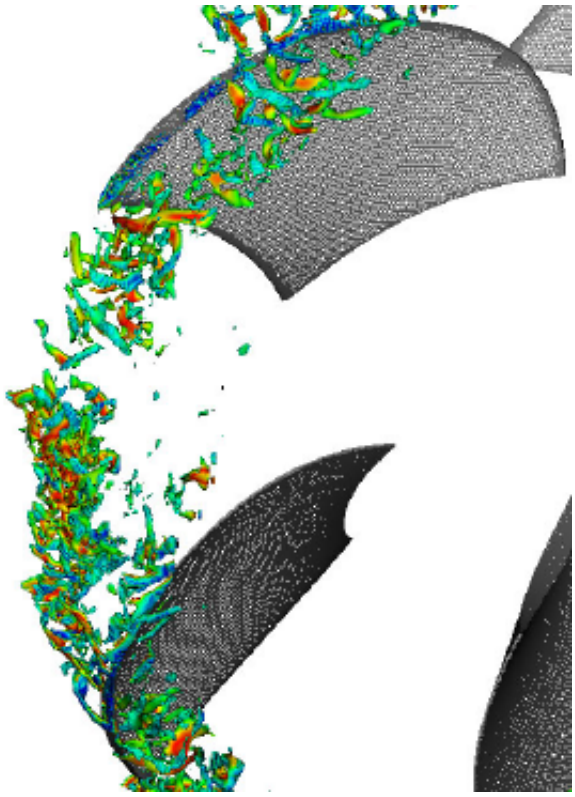

Figure 7.9 Vortical structures corresponding to the correlation analysis modes in a single blade passage.

correlation histogram can also be linked to the presence of duct modes in the installation that is captured by the correlation method.

These results were already presented in Zhu's work, but they are the result of the application of a routine coded as part of the current research effort. Furthermore, Zhu restricted his analysis to applying the correlation method as a simple counting algorithm, whereas it was explained in the previous section that while it was not an unreasonable first approximation a measure to evaluate the amplitude of the distortions caused by the rotating modes is necessary. This was achieved using the wavelet based approach that was also incorporated into the routine, in effect applying a weighting factor to the frequency of each modal occurrence as a function of the aerodynamic frequency where the mode was detected using the cross-spectral analysis, as explained in Sec. 7.3.

The strength-weighted interaction frequency histogram is shown in Fig. 7.11(b), and the spatial distribution of the strength of the modal interactions along the the radial (R) and chordwise (C) positions is reported in Tab. 7.2 with the two previously identified zones still highlighted through cell coloration.

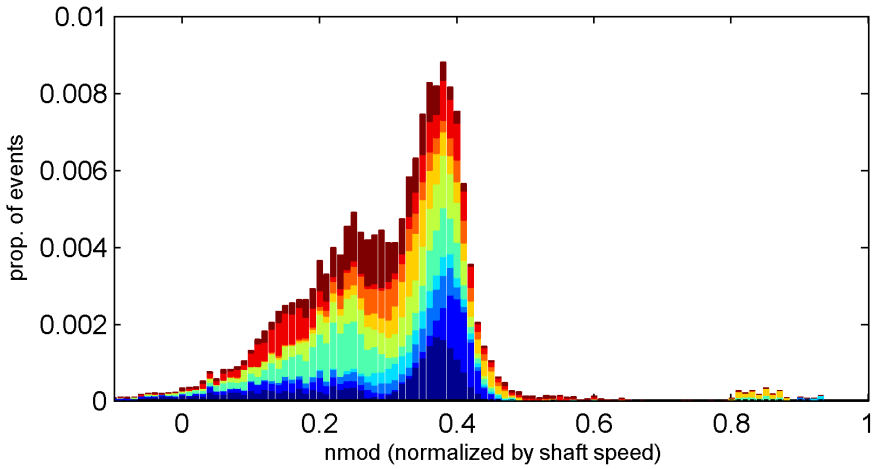

Figure 7.10 Modal velocity of the detected modes in Zone 2 for the USI7 fan.

Table 7.2 Amplitude-weighted proportion of events identified at different spatial points according to radius and chordwise position in the tip region of the USI7 fan

% str. of events		Chordwise ID										
		C01	C02	C03	C04	C05	C06	C07	C08	C09	C10	Total
Radial ID	R146	2.97	1.70	0.62	0.51	0.38	0.14	0.03	0.03	0.04	0.04	6.47
	R142	4.00	3.00	1.65	1.12	0.97	0.45	0.18	0.06	0.06	0.04	11.53
	R138	4.78	4.19	3.74	2.74	2.08	1.40	0.73	0.35	0.14	0.16	20.31
	R134	3.72	3.68	3.96	3.84	3.36	2.49	1.58	1.13	0.58	0.38	24.74
	R130	1.65	1.20	2.01	2.98	3.25	2.46	2.32	1.95	1.21	0.89	19.93
	R126	0.64	0.23	0.56	1.53	0.69	1.49	1.96	2.09	1.23	1.13	11.55
	R122	0.25	0.35	0.06	0.69	0.58	0.28	1.07	1.13	0.56	0.51	5.47
	Total	18.03	14.35	12.59	13.41	11.32	8.70	7.88	6.74	3.83	3.15	

From the observation of Fig. 7.11(b), the strength-weighting operation slightly decreases the proportion of predicted interactions in the first hump at $f_{int} = 3.5$ while providing a notable increase ($\sim 25\%$) to the second hump at $f_{int} = 7$. Overall, the correlation analysis prediction of the mode/blade interactions provides a fairly accurate representation of the overlaid FWH acoustic spectra obtained from the fan rotor wall-pressure fluctuations (copied from Fig. 6.9), but there is no clear improvement as a result of adding the modal amplitude when compared to the pure counting algorithm.

However, going into the details of the spatial distribution of the weighted interactions using Tab. 7.2, it specifically further increases the preponderance of the leading edge modes and of radial positions R142-130, indicating that the average amplitude of the distortions caused by the identified structures is stronger closer to the leading edge in the tip region of the blades. As a result, the interactions strength in the leading edge zone represent nearly 62% of all interactions (up from 54%) and the trailing edge zone importance is

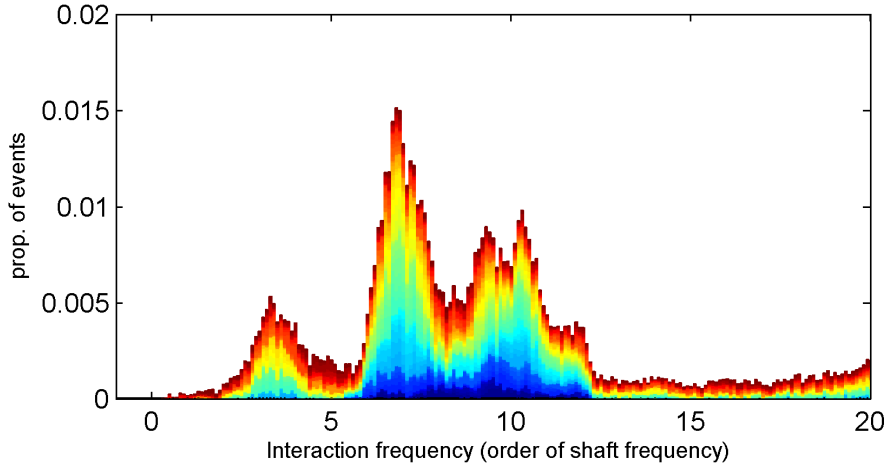

(a)

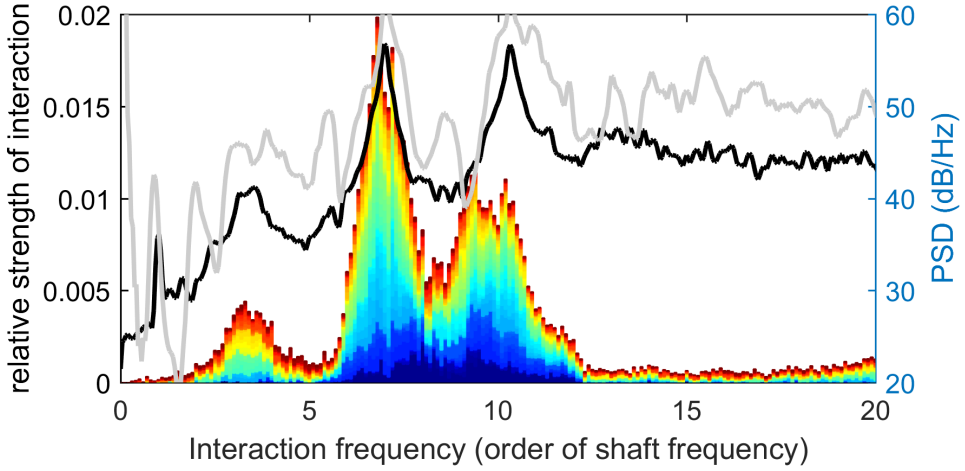

(b)

Figure 7.11 Histogram identifying the interaction frequencies of the detected modes for the USI7 according to (a) Frequency of occurrence (b) Strength of the interactions as weighted by the wavelet thresholding method; the acoustic FWH prediction (black) and direct CAA (grey) spectra are overlaid. Binning is carried out at 10ths of the rotational frequency of the fan.

decreased to 15% (down from 17%). This is coherent with observations carried out in Sec. 6.3.1 where elevated wall-pressure fluctuation levels were identified especially at the leading edge of the blade in the tip region, with a secondary source closer to the trailing edge on the pressure side of the blades.

Conclusion on the USI7 Case

The USI7 configuration was the initial test case for the application of the correlation method on pressure signals measured in the blade passage in the tip region in order to characterize the flow distortions deemed responsible for the appearance of high tonal noise for the low flowrate operating condition at the largest tip gap clearance. The hypothesis behind the method that these flow distortions effectively coalesce into coherent circumferential modes that generate cyclic fluctuations in the blade loading and cause increased tonal and broadband noise as a result was confirmed by the results obtained.

In fact, coherent flow structures traveling azimuthally are consistently identified along the circumference for several radial and chordwise positions, with their circumferential azimuthal order varying between 5 and 20. These coherent modes also rotate at approximately 33% of the fan speed overall. These modes can be identified in the flow using proper filtering techniques using the information provided by the spectral correlation method.

From a spatial perspective, the wide majority of the detected modes seem to occur in the leading edge portion of the blades in the top 20% of the span; a secondary concentration of modes with slightly different velocities was also observed in the last 40% of the blade chord in the 70-80% span region. These local concentrations of modal patterns are concordant with the observed path of vortical structures generated by the breakdown of the TLV in the passage and associated elevated wall-pressure fluctuation levels in frequency bands associated with the acoustic tonal humps on the pressure side of the blades.

Finally, using the modal characteristics of the identified pressure patterns, the occurrence of tonal peaks in the the spectrum is explained and effectively identifies these modes issued from the tip gap flow as the source mechanism behind the observed acoustic tones.

7.4.2 RCDB Fan

The second fan on which the correlation method has been applied is the RCDB fan. It was shown in Chap. 6 that the low flowrate operating condition of the RCDB fan caused the appearance of an intricate vortical system generated as a result of the tip leakage flow. The vortical field occupies the uppermost portion of the span. This flow condition

was also associated to more elevated broadband noise levels at low frequency as well as significant tonal noise when compared to the other simulated flowrates. Using bandpass filtered wall-pressure fluctuation maps at frequencies corresponding to the tonal humps present in the acoustic spectra under 100 Hz, elevated levels of fluctuations were identified on the suction side of the blades in the tip region of the blades at the leading edge.

Working under the assumption that the tip region vortical field is responsible for the occurrence of these tonal humps in the acoustic spectra, the correlation technique for the identification of the coherent structures was applied to investigate the flow in the tip region of the RCDB fan. In effect, numerical circumferential arrays were setup at radial positions varying from just under the tip of the blades (R=365 mm) in decrements of 3 mm down to a radial position of 341 mm; a total of 11 axial positions were evaluated at each radius. The circumferential resolution employed for the RCDB fan numerical correlation sensor arrays was 4 degrees (90 sensors along a circumference). As with the USI7, the pressure signal extracted from the simulation data was collected in a relative frame of reference rotating with the blades.

Unlike the USI7, however, the appearance of the RI spectral signature was not observed on the RCDB configuration and could not be used as a guide to determine the frequency range for which to run the correlation analysis. Rather, the volume data exhibits a broadband spectral characteristic, as shown in Fig. 7.12. In addition, the RCDB operates in a range that is quite different, with a rotational speed of only 437.22 RPM and a very low pressure rise across the fan, coupled with very large dimensions. As such, one would expect a different behaviour in the tip clearance with regard to the involved frequencies. The low rotational speed also entails that a long time period is required to obtain a significant amount of complete fan revolutions; in the present study, the volumetric data available covered around 15 revolutions, or 2 seconds of physical time. In an ideal case, a timeframe of 250 revolutions (35 seconds) as with the USI7 fan would have been preferred, but also required more extensive computational resources (both calculation time and data storage).

For the lowest flowrate (OC5), however, a strong linear trend was found in the cross-spectral phase in the 10-300 Hz frequency range for several probe pairs in the described circumferential arrays, as shown in Fig. 7.13 which is indicative of a series of coherent structures traveling at constant speed according to the theory of the method (Sec. 7.2). The frequency range was also associated to high levels of coherence.

This was not the case for operating conditions OC1 and OC3, where the correlation analysis failed to identify coherent modes in the azimuthal direction, which is coherent

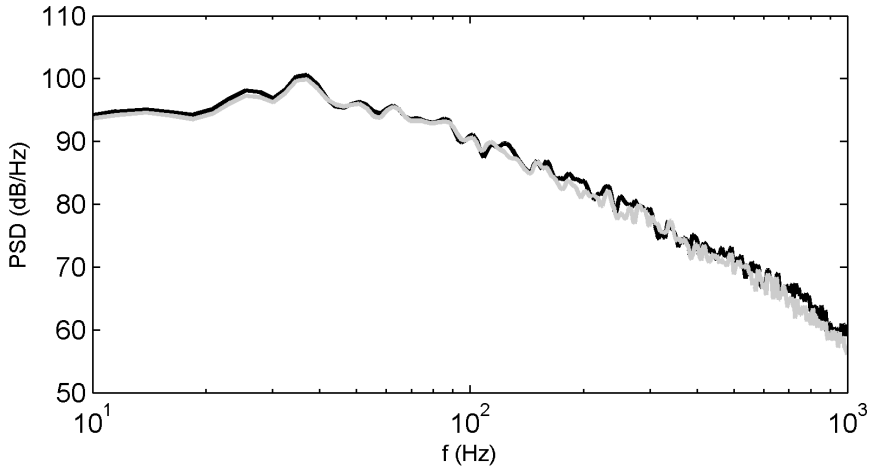

Figure 7.12 Power spectral density of two subsequent signals extracted from the RCDB LBM volume data for OC5. The lead signal is in black and the trailing signal is in grey.

with the observations made regarding the propagation of the tip leakage flow structures using λ_2 criterion vizualisations in Fig. 6.2. The present section thus describes the modal analysis results obtained on the RCDB fan for the OC5 flow condition exclusively.

The physical characteristics of the modes identified through the correlation analysis run in the 10-300 Hz range with a coherence threshold of 0.7. An example of the characteristics of the modes identified for the same pair of probes in Figs. 7.12 and 7.13 is shown in Fig. 7.14.

The maximum order of the modes identified for this single pair of probes is significantly higher than those shown to appear in the USI7 fan. This is confirmed when looking at the results of the global analysis across all radii (R365-341) and chordwise positions in Fig. 7.16, which indicates that the coherent modes have an order of up to 60. The color-coding of the evaluation positions are shown in Fig. 7.15. The vast majority of the detected coherent structures are identified as having a mode order of 4 and above, as seen in Fig. 7.16(a); the most frequently encountered mode orders are between 6 to 8, indicating that there is a predominance of structures that span one half to one third of a blade passage, in a fashion similar to the USI7 case. However, whereas the USI7 configuration exhibits a normal probability density distribution around the most frequently encountered modes (orders 12-13), the RCDB analysis shows a skewed distribution around the most common modes. The distribution of the modal velocities of the detected modes for the RCDB fan is also shown in Fig. 7.16(b) and highlights a slightly skewed normal probability

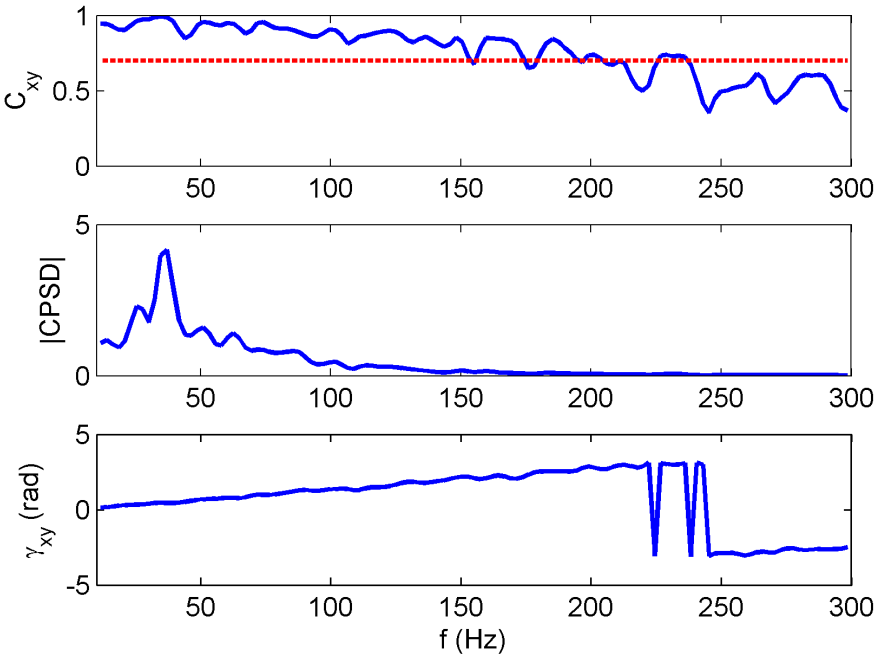

Figure 7.13 Illustration of the intermediary steps of the correlation analysis for a pair of probes in the RCDB LBM volume data for OC5. Cross-spectral coherence level C_{xy} (top), cross-spectral density amplitude (middle), phase lag between the signals (bottom)

distribution around a velocity of around 28-29% of the rotor velocity. This is comparable to the 33% value identified in the USI7 case.

A significant difference, however, lies with the fact that the USI7 showed a high concentration of coherent modes in close vicinity to the leading edge near the tip (R146-R142) whereas the RCDB shows a markedly different trend in that the modes are detected in relatively equal proportion across all radii down to R341 and along the axial dimension when looking at the spatial proportions of detected events in Tab. 7.3.

Table 7.3 Proportion of events identified at different spatial points according to radius and chordwise position in the tip region of the RCDB fan

% of events		Chordwise ID											
		C01	C02	C03	C04	C05	C06	C07	C08	C09	C10	C11	Total
Radial ID	R365	1.51	1.60	1.39	1.38	1.30	1.27	1.29	1.25	1.28	1.41	0.91	14.58
	R362	1.74	1.68	1.48	1.39	1.33	1.30	1.29	1.24	1.24	1.31	1.49	15.50
	R359	1.10	1.69	1.50	1.41	1.34	1.29	1.28	1.22	1.21	1.24	0.70	13.98
	R356	0.30	1.69	1.56	1.43	1.38	1.29	1.27	1.23	1.22	1.25	0.05	12.65
	R353	1.76	1.68	1.60	1.46	1.40	1.29	1.26	1.24	1.20	1.26	0.82	14.97
	R347	1.80	1.67	1.61	1.51	1.42	1.32	1.25	1.24	1.24	1.26	1.31	15.64
	R341	0.29	1.63	1.54	1.45	1.35	1.30	1.25	1.24	1.25	1.19	0.18	12.67
	Total	8.50	11.65	10.68	10.03	9.51	9.07	8.89	8.65	8.65	8.93	5.46	

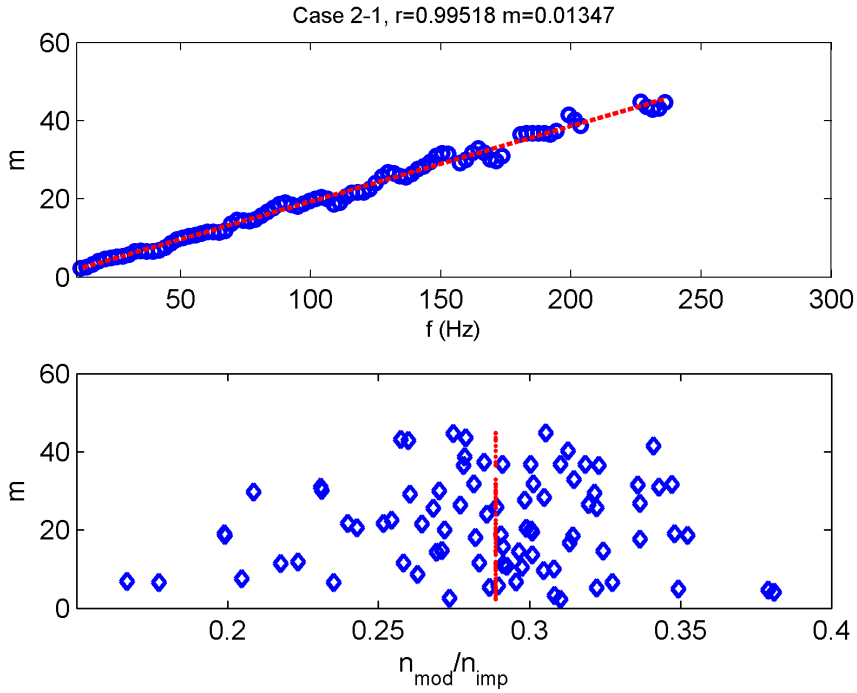

Figure 7.14 Characteristics of the modes identified as a result of the correlation analysis for a pair of probes in the RCDB LBM volume data for OC5.

Structures in the vortical field around the RCDB fan blades (highlighted using the λ_2 criterion once again in Fig. 7.17(a)) whose rotational velocity corresponds to the modal velocities of the identified modes can be seen in the flow by filtering the λ_2 field as shown in Fig. 7.17(b). Using the filtered vortical field vizualisation, the tip region of the RCDB fan is indeed seen to be saturated by a large swath of turbulent structures across the entire blade chord that covers a large portion of the span.

Further filtering the structures from Fig. 7.17(b) according to frequency, it is possible to highlight the appearance of modal patterns with orders corresponding to the predictions from the correlation analysis. This was done for the 90-110 Hz and 160-180 Hz frequency bands for example in Figs. 7.17(c) and 7.17(d), which corresponds to modal patterns of order 20 and 30 respectively according to the top diagram from Fig. 7.14. Only pressure fluctuations surpassing 0.5 Pa are retained. While the λ_2 field is not continuous over the whole circumference and complicates the observation of the patterns compared to the USI7, the estimated number of pressure lobes for each frequency band corresponds rather well to the expected mode orders.

Using their modal characteristics, the interaction frequency of the identified modes with the rotor blades can be calculated using Eq. 7.5 and yields the density distribution shown in Fig. 7.18(a). Using a simple counting algorithm for the occurrence of a given interaction

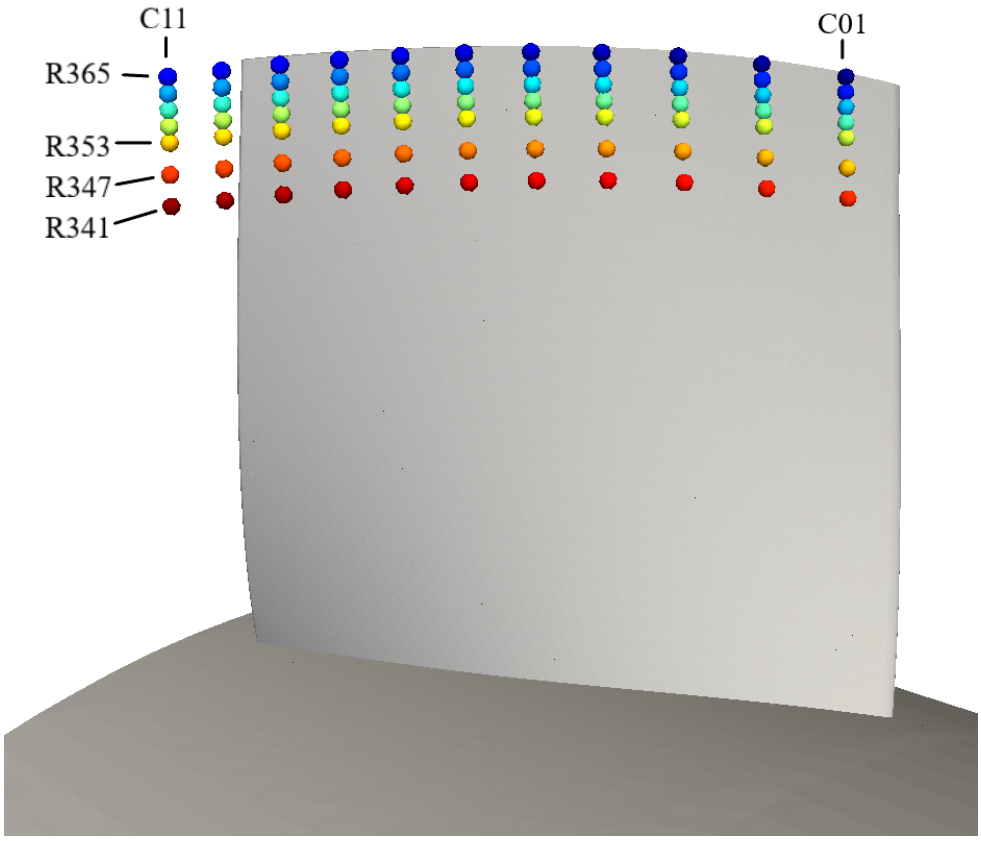

Figure 7.15 Color-coding of the modal analysis positions according to radial (R) and chordwise (C) positions for the RCDB fan.

frequency, elevated broadband levels with some tonal peaks showing through are predicted by the algorithm up to interactions of order 20, with a sharp drop in the number of occurrences thereafter. At first glance, the predicted interactions show little commonality with the acoustic spectra predicted by the LBM simulation.

However, the direct counting approach is a poor evaluator when it comes to evaluating the strength of the interactions, and a properly weighted version of Fig. 7.18(a) using the described wavelet technique is shown in Fig. 7.18(b) with the LBM acoustic spectra superimposed. The amplitude-weighting operation has a marked effect on the relative levels of the predicted interactions; a proeminent dual hump is now present at interaction orders 4 and 5, whilst the predicted levels of interaction at orders superior to 16 are severely decreased. However, only a loose correspondance between tonal components in the acoustic spectra and the predicted peaks is observed using the weighted interaction histogram and it is difficult to interpret the results of the prediction as being accurate.

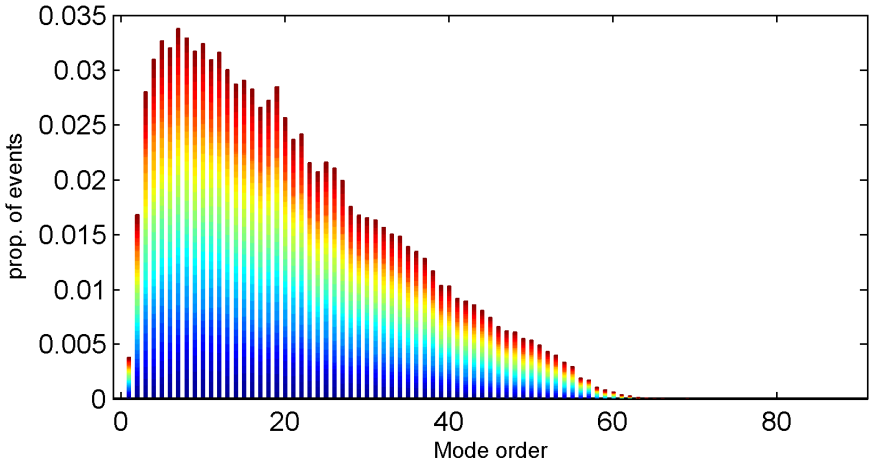

(a)

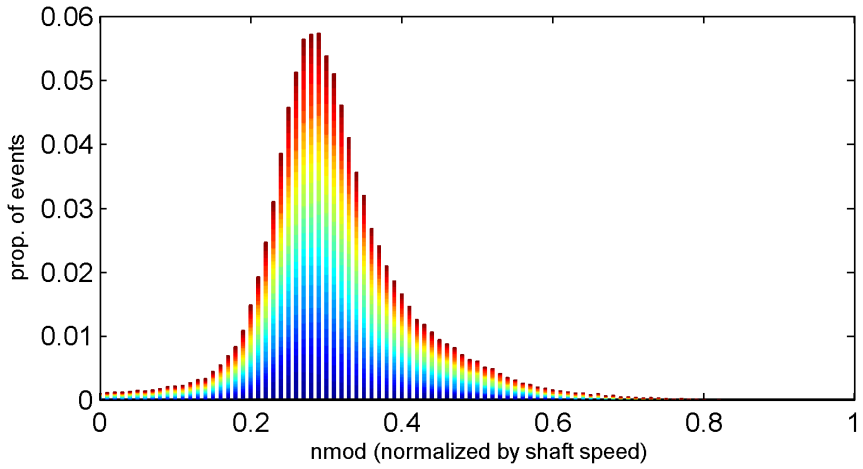

(b)

Figure 7.16 Characteristics of the modes detected through correlations analysis for the RCDB configuration in the tip region (R365-341) of the blades (a) Mode orders (b) Mode rotational velocity.

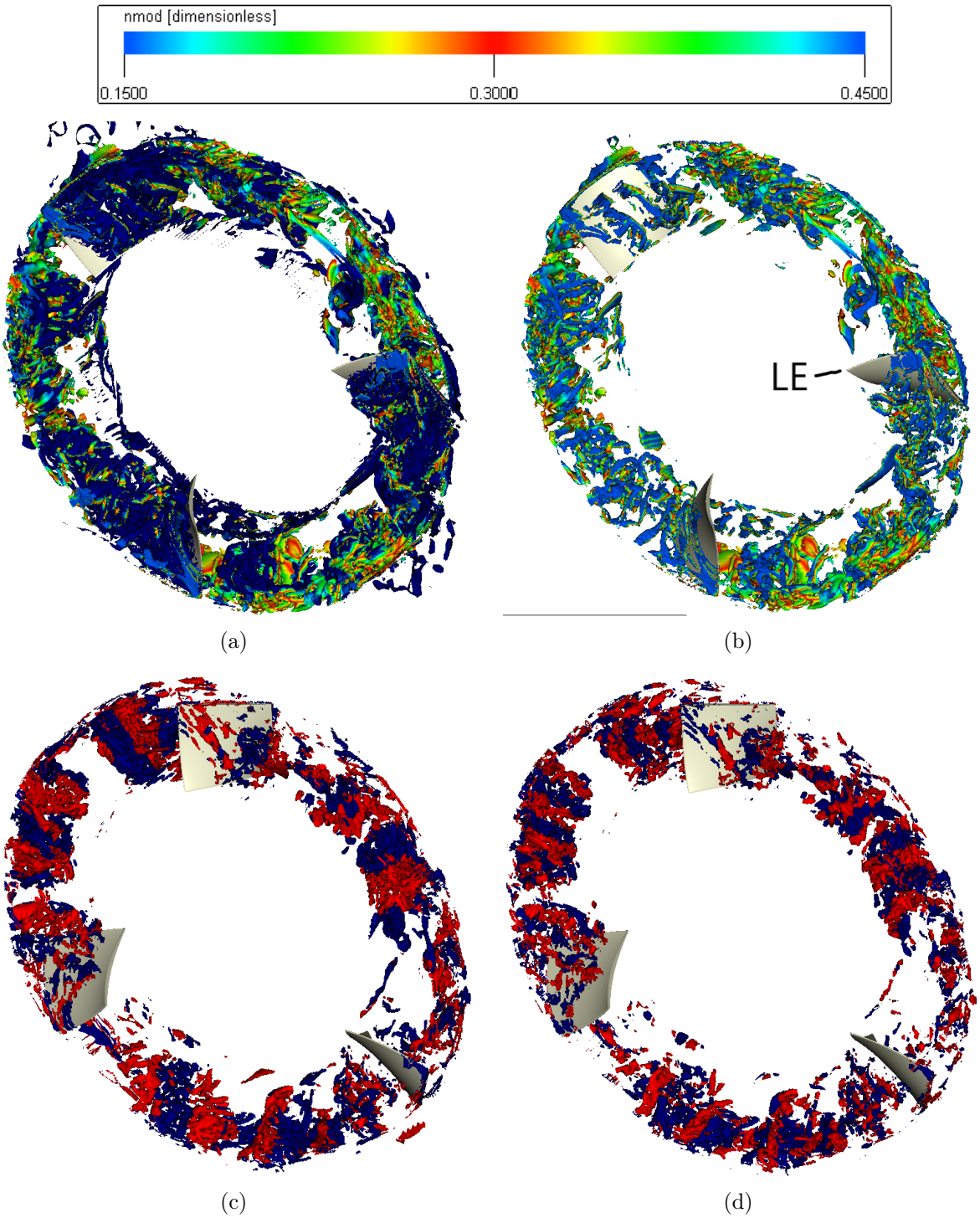

Figure 7.17 Instantaneous vortical field around the RCDB fan at OC5 highlighted by isosurfaces of $\lambda_2 = -10$ (a) Raw λ_2 field, colored by the the normalized rotational velocity n_{mod}/n_{fan} (b) λ_2 field corresponding to $0.15 \leq n_{mod}/n_{fan} \leq 0.45$ (c) (d) show the same field as (b) further filtered according to frequency in the 90-110 Hz ($m = 20$) and 160-180 Hz ($m = 30$) bands, colored by pressure.

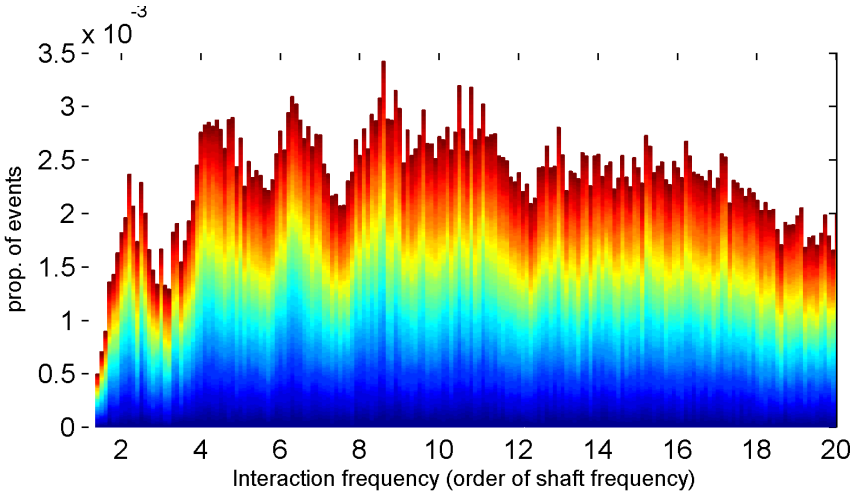

(a)

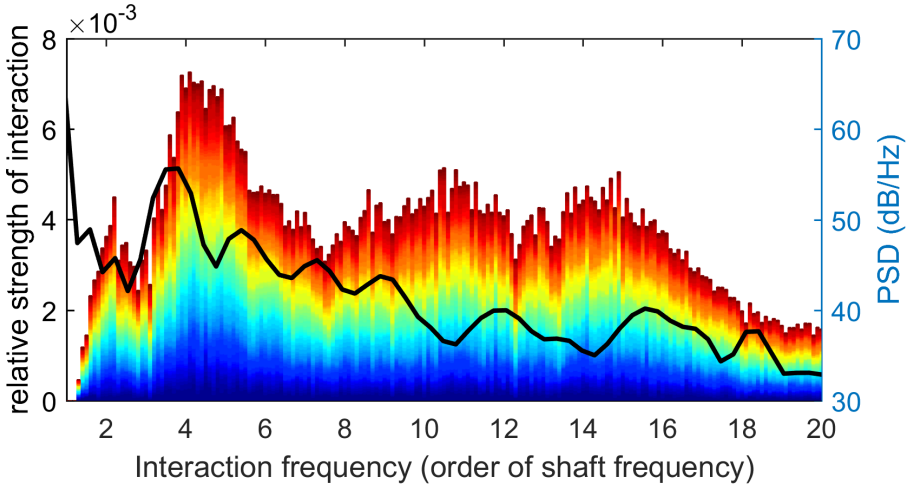

(b)

Figure 7.18 Histogram identifying the interaction frequencies of the detected modes for the RCDB OC5 according to (a) Frequency of occurrence (b) Strength of the interactions as weighted by the wavelet thresholding method. Binning is carried out at 10ths of the rotational frequency of the fan.

More specificly, the acoustic spectral humps at $f_{int} = 4$ and 5 are relatable to the elevated dual peak in the the interaction histogram, but the prediction does not account for their different relative amplitude very well. The acoustic hump at $f_{int} = 7$ is also shown in the prediction. However, between $f_{int} = 8$ and 16, the correlation prediction becomes quite noisy and it becomes difficult to establish a clear concordance between the histogram and the acoustic tonal humps in the spectra. At higher frequencies $f_{int} \geq 17$, the predicted interaction levels are significantly lowered and broadband in nature (no clear tones).

From the perspective of the spatial distribution of the strength-weighted modes across the different radii and chordwise positions of evaluation as shown in Tab. 7.4, all evaluated radii still appear to contribute about equally to the correlation prediction, indicating that the strength of the identified modes is about constant in the top 20% of the span. However, the amplitude of the distortions is seemingly weaker as the trailing edge is approached.

Table 7.4 Amplitude-weighted proportion of events identified at different spatial points according to radius and chordwise position in the tip region of the RCDB fan

% str. of events		Chordwise ID											
		C01	C02	C03	C04	C05	C06	C07	C08	C09	C10	C11	Total
Radial ID	R365	1.89	1.71	1.46	1.32	1.12	0.99	0.88	0.79	0.81	0.83	0.66	12.47
	R362	2.13	1.92	1.62	1.40	1.25	1.07	0.96	0.85	0.83	0.83	0.87	13.74
	R359	1.92	2.02	1.74	1.51	1.34	1.11	1.01	0.89	0.82	0.79	0.59	13.75
	R356	1.14	2.12	1.84	1.61	1.43	1.16	1.01	0.93	0.84	0.79	0.11	12.97
	R353	2.53	2.20	1.95	1.71	1.51	1.20	1.05	0.96	0.84	0.80	0.56	15.29
	R347	2.63	2.36	2.12	1.88	1.60	1.36	1.15	1.01	0.88	0.77	0.71	16.49
	R341	1.17	2.46	2.21	1.99	1.69	1.44	1.27	1.08	0.95	0.82	0.21	15.30
	Total	13.41	14.79	12.95	11.42	9.95	8.33	7.33	6.52	5.97	5.64	3.70	

Conclusion on the RCDB Case

For the RCDB fan, the correlation analysis highlighted a rich field of azimuthal modes in the tip region of the blades for the OC5 flowrate, with a wide array of modal orders being represented, with orders much higher than those encountered in the USI7 configuration. These modes appear to be rotating at a velocity approximately 30% that of the rotor and can again be viewed in the numerical flowfield using appropriate filtering techniques based on the results of the analysis.

According to the spectral correlation analysis, the most impactful modes are located in the first 50% of the blade chord, but appear to be rather equally distributed across the evaluated radial positions; unlike the USI7, the vortical field is too complicated for the clear path of the coherent structures to be confirmed through flow observations. It was however observed through surface wall-pressure maps in Fig. 6.12 that the leading edge

portion of the blades on the suction side was an area where elevated levels of fluctuations were observed. It could indicate that the identified modes primarily impact the suction side of the blades, as it appears to be the main source of noise for the observed tones.

The acoustic interaction histogram of the identified modes, while explaining some of the observed acoustic tones, however provided an underwhelming overall prediction of the farfield sound spectra. Several factors may explain this and warranted further investigation which is already underway.

First and foremost is the fact that the physical time available for the spectral analysis was perhaps insufficient given the low rotational speed of the fan, yielding only 15 rotations worth of temporal data, and the fact that the frequency range for the modal analysis spans low frequencies only; more physical simulation time would provide with the opportunity to refine the cross-spectral frequency resolution and better resolve the coherence in this range. This was not a major problem with the USI7 setup given the higher frequencies involved.

Second is the fact that a rather coarse mesh was utilized for the RCDB simulation due to the several iterations that had to be carried out on the simulation setup to solve several numerical problems; a refined mesh is most assurately needed to perform a convincing analysis of such a fine phenomenon as tip leakage flow, but a refinement study was not properly carried out due to lack of time. This is especially critical on the RCDB fan, where a thin laminar separation bubble at the leading edge on the suction side of the blades was observed experimentally.

The OC1 and OC3 operating points were also investigated using the modal analysis method, but it failed to yield coherent results, as the tip leakage vortices generated are quickly convected downstream of the fan, as shown in Fig. 6.2, and do not lead to the appearance of strong coherency in the passage flow or the necessary linear trend for the phase angle.

7.4.3 Bosch Configuration

The final free-tip fan investigated in the course of this study was the Bosch engine cooling fan. The fan possesses a fairly different tip clearance gap geometry compared to the tube-axial USI7 and RCDB configurations. In effect, while the tip clearance gap is constant (3 mm or 0.9% of the rotor diameter) normal to the tip surface of the blade, the blade tip radius varies along the flowpath in a convergent manner from inlet to outlet. Thus, the vortical structures generated as a result of the tip leakage flow are forcefully kept from

convecting downstream and seem to interact strongly with the following blades, as shown through λ_2 isosurfaces vizualizations in Sec. 6.2.1 (Fig. 6.4). These structures are hypothesized to be reponsible for the sub-BPF harmonic humps identified in the fan acoustic spectra using the FWH analogy, which was used to properly identify the contribution of the fan rotor from among the strong propagation effects observed on the configuration, and that were linked to elevated wall-pressure fluctuations in the tip region of the blades, as explained in Sec. 6.3.1.

This observation is reinforced by the fact that the RI spectral feature, also visible in the USI7 case, is also observed in flowfield measurements from the simulation in the tip region, as shown in Fig. 7.19. The frequency range where it occurs, however, is shifted to the 450-750 Hz band; whereas it was in the 300-600 Hz range for the Siegen configuration.

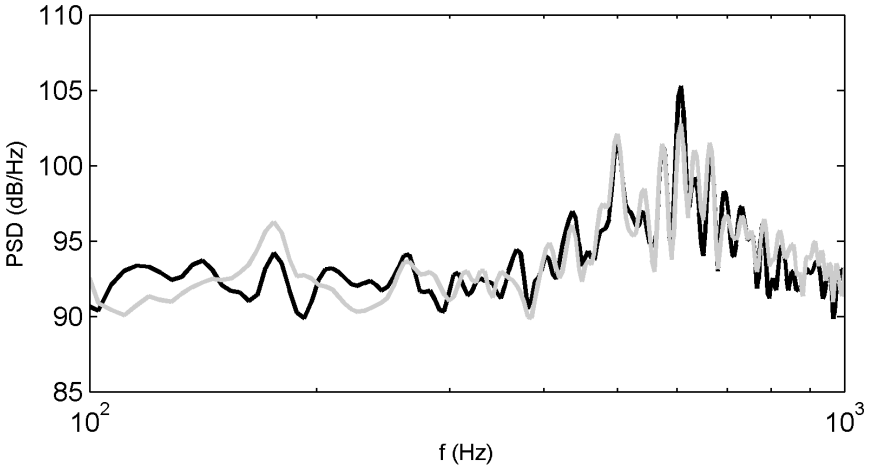

Figure 7.19 Power spectral density of two subsequent signals extracted from the Bosch LBM volume data. The lead signal is in black and the trailing signal is in grey.

It therefore provided some guidance as to the frequency range of interest for the application of the correlation method for the identification of the coherent modes in the tip region based on the observations made on the USI7 [Zhu, 2016]. In order to investigate the tip flowfield properly, a series of circumferential arrays were setup in the flow passage between the blades. Just like in the previous cases, a series of radii ranging from 94% (R154) down to 70% of the blade span (R130) in decrements of 4% (4 mm) were evaluated; 11 chordwise positions were considered for each radius of evaluation. Due to the peculiar shape of the blade in the tip region, however, the uppermost radius covered only about 60% of the axial width of the fan, as shown in Fig. 7.20(a), whilst the R150 station and below covered a complete chord, also shown in Fig. 7.20(b).

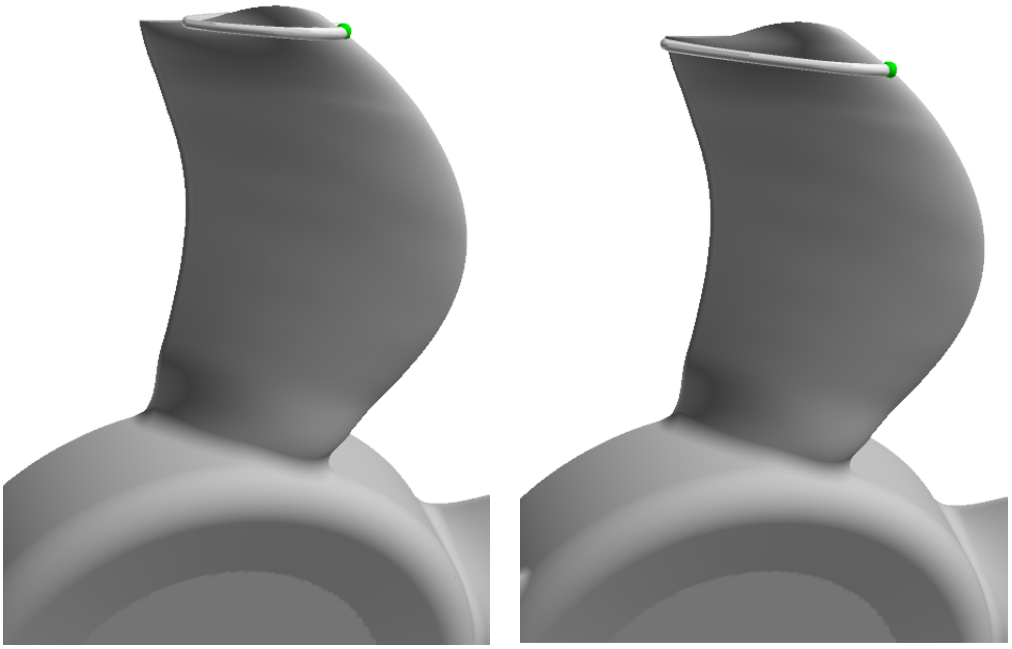

(a) (b)

Figure 7.20 Illustration of the radii evaluated in the uppermost region of the span (a) R154-94% span only evaluates the leading edge bulge of the blade ((b) R150- 70% span and below cover the entire axial width of the fan.

A maximum of 45 probes across a circumference (9 per blade passage) could be used to obtain a continuous array due to the thickness of the blades in the leading edge region, yielding a resolution of 8° between adjacent sensors. As with the previous geometries, the sensors points were set to rotate with the fan and pressure measurements are thus collected in the rotating frame of reference and are shown in Fig. 7.23.

The correlation analysis was carried out using the uppermost frequency of the RI spectral signature range as the maximum value. The minimum value (10 Hz) was set through trial-and-error to try and identify modes corresponding to all of the observed acoustic sub-BPF humps; an initial analysis using the RI spectral range (450-750 Hz) identified modes with an interaction frequency solely around the third BPF harmonic, not unlike the USI7 case. A coherence threshold level of 0.6 was used to filter the coherent modes. An example of the intermediary steps in the correlation analysis for the probe pair used in Fig. 7.19 is shown in Fig. 7.21, and the mode characteristics are shown in Fig. 7.22.

For the probes shown, a high coherence is observed only in the RI frequency range, leading to an identification of modes at the higher frequencies only. The order of the modes identified at the maximum frequency of evaluation (30) is very similar to the USI7 case.

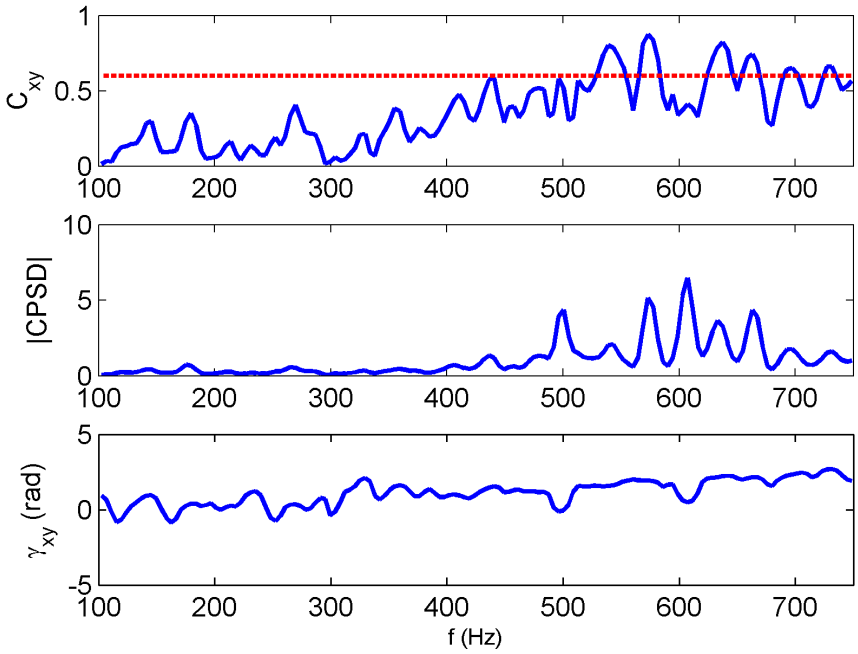

Figure 7.21 Illustration of the intermediary steps of the correlation analysis for a pair of probes in the Bosch LBM volume data.

Running the analysis for all radii and chordwise positions confirms this trend, as shown in Fig. 7.24 where the global results for the characteristics of the modes identified (order and velocity) are shown. The color-coding of the evaluation positions is shown in Fig. 7.23.

The probability distribution showing the mode order in Fig. 7.24(a) of the identified coherent structures shows a near-normal shape around the predominant modes of order 15-17; this indicates that the preferential modes appear to have slightly over 3 lobes per blade passage, which is slightly different from the USI7 case (2.6 lobes per blade passage). Their velocity is also scattered around a value of ∼17% of the fan rotational velocity, which is significantly lower than both of the previous geometries. A second notable difference is that there is a large variance in the observed velocities, with a consistent portion of the modes exhibiting negative modal velocities.

According to the spatial distribution of the modes shown in Tab. 7.5, the large majority (73%) is detected in the upper region of the blades (R154-142) with speeds varying from -0.1 to 0.4 times the rotational speed of the rotor.

The visualization of the coherent vortical features in the flow corresponding to those from the R154-R142 range of radii can be done through filtering of the λ_2 isosurfaces from the

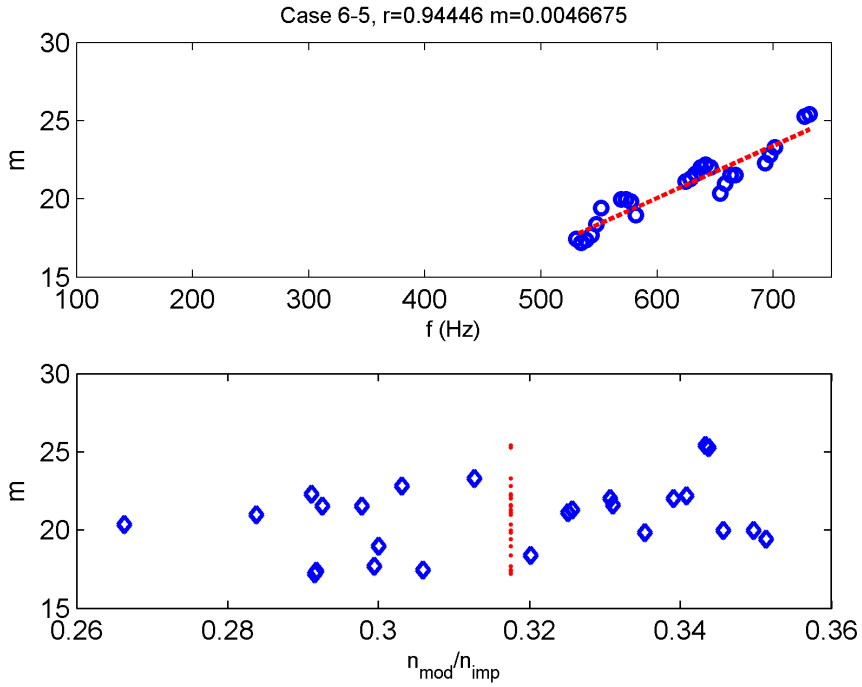

Figure 7.22 Characteristics of the modes identified as a result of the correlation analysis for a pair of probes in the Bosch LBM volume data. Cross-spectral coherence level C_{xy} (top), cross-spectral density amplitude (middle), phase lag between the signals (bottom)

flowfield around the fan (Fig. 7.25(a)) to retain only those with convection velocities that correspond to the rotational velocity of the identified modes (Fig. 7.25(b)).

The appearance of the tip leakage vortex (TLV), originating from the leading edge tip of the blade and scraping against the shroud, is made evident. The TLV travels almost azimuthally from blade to blade and gradually expands into a wider turbulent wake which impacts a large portion of the following blade, and is seen traveling at speeds ranging from 0.1 to 0.2 times the blade speed. Secondary vortical structures (SVS), which are much slower that the TLV, are also seen wrapping around the main vortex and appear proeminently at the leading edge. In the trailing edge portion of the tip (∼R150) a turbulent wake (TW) is also seen shedding from the suction side and traveling towards the following blade along the shroud surface at velocities slightly inferior to the TLV. These three categories of vortical features appear to account for the modal velocities encountered in the upper radii fairly well. The reader will note the turbulence shed from the trailing wake of the blades is still included in the filtered field; this turbulence is however convected downstream and does not interact with the following blades.

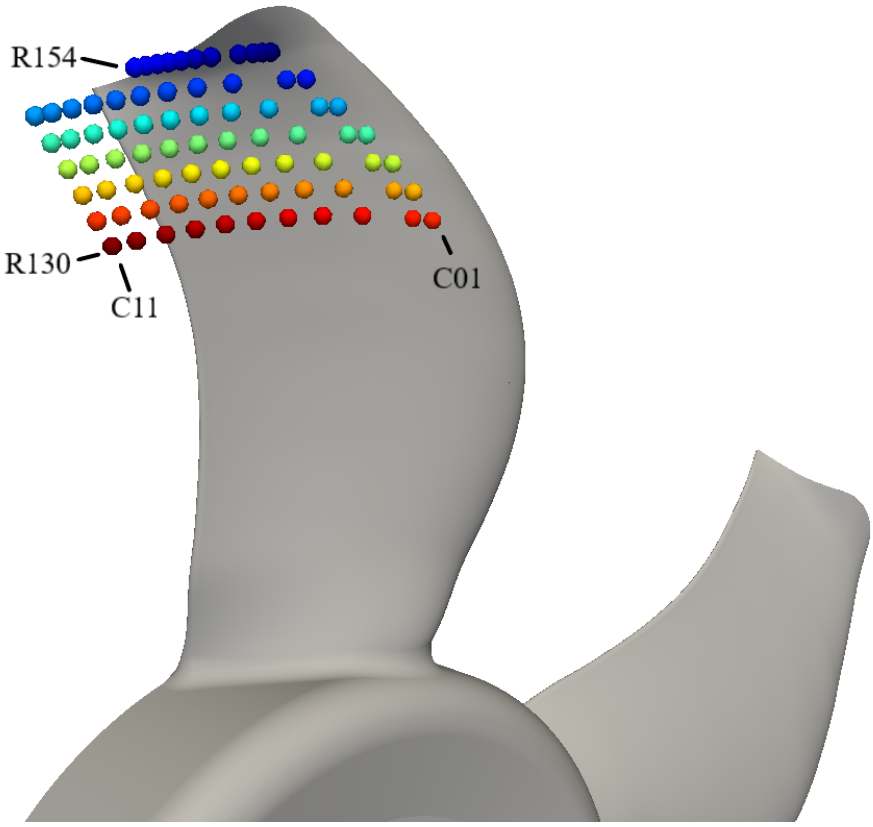

Figure 7.23 Color-coding of the modal analysis positions according to radial (R) and chordwise (C) positions for the Bosch fan.

Just like the previous configurations, the velocity filtered λ_2 field from Fig. 7.25(b) was frequency filtered in the 530-550 Hz band, which corresponds to modes of order 18 according to the top diagram of Fig. 7.22. The result is shown in Fig. 7.25(c), where pressure modes with an amplitude of over 1 Pa are shown. The retained structures appear only in the tip region of the blades along the shroud surface, indicating that the dominant modes in the flow are indeed generated as a result of the tip leakage flow. Moreover, the appearance of between 17 and 18 azimuthal lobes across the circumference is also observed, further reinforcing the results obtained from the correlation analysis.

A significant number of modes also exhibit velocities corresponding to 50-90% of the rotor rotational speed; these modes are preponderantly observed in the lower radii (R138-130) (indicated by the dominantly red colormap of Fig. 7.24(b)). These lower radii only contain 27% of the detected modes, as observed Tab. 7.5, and they are shown to be mostly concentrated in the first 30% of the chord. However, when looking at their relative strength

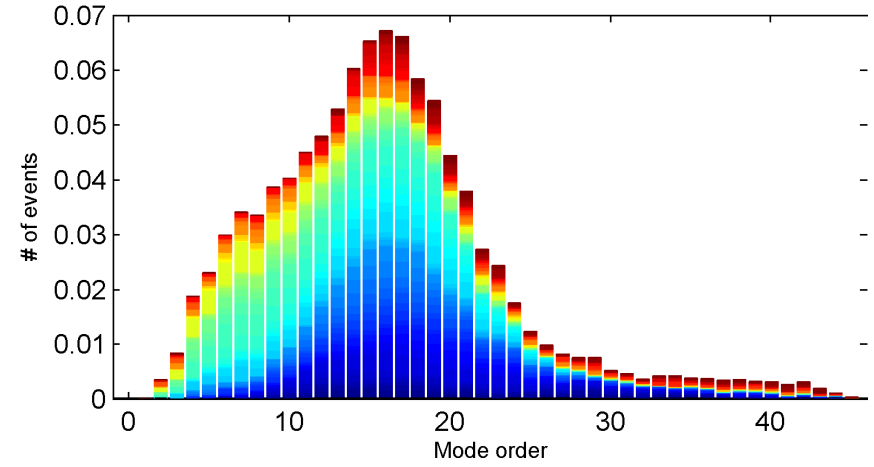

(a)

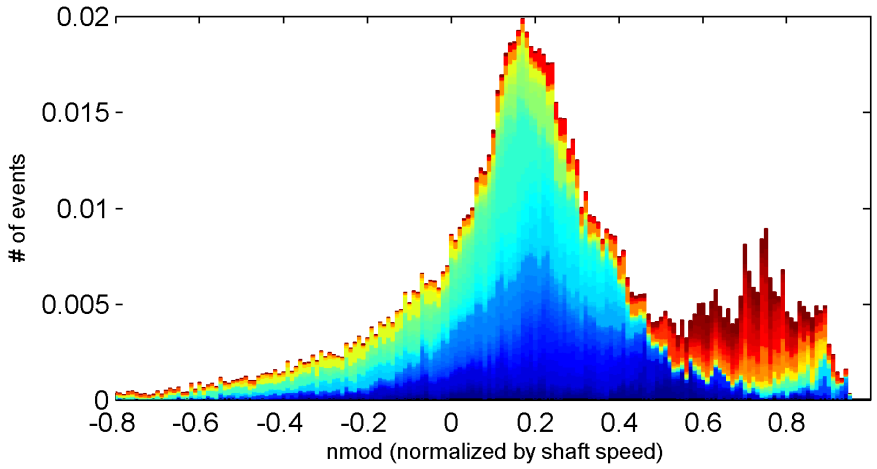

(b)

Figure 7.24 Characteristics of the modes detected through correlations analysis for the Bosch configuration in the tip region (R154-130) of the blades (a) Mode orders (b) Mode rotational velocity.

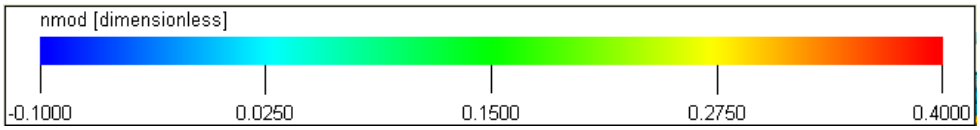

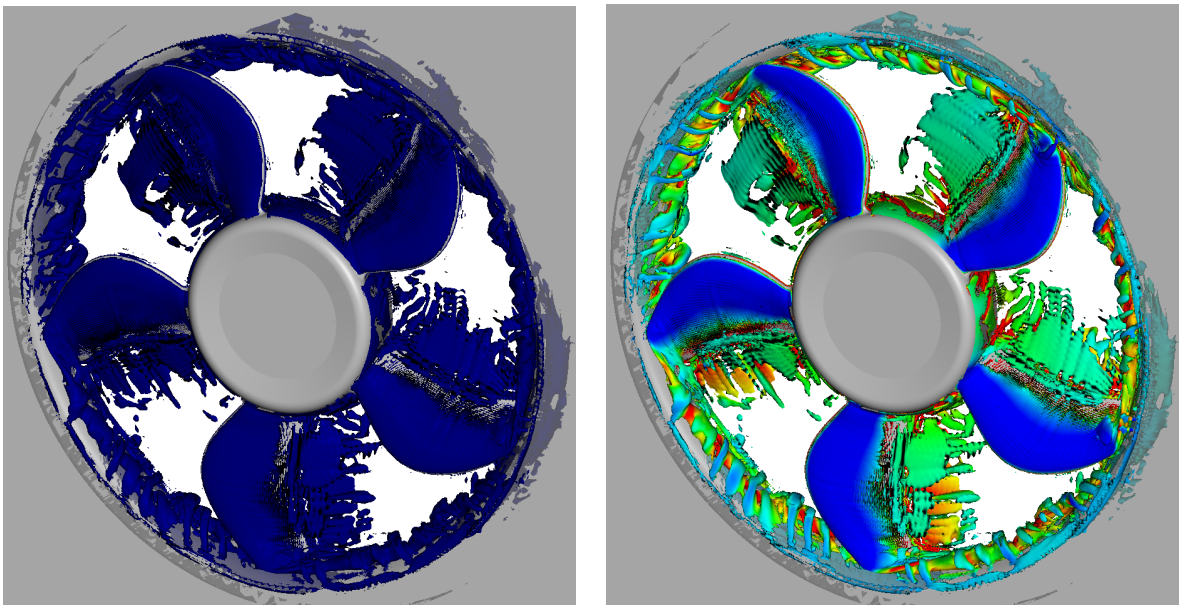

(a) (b)

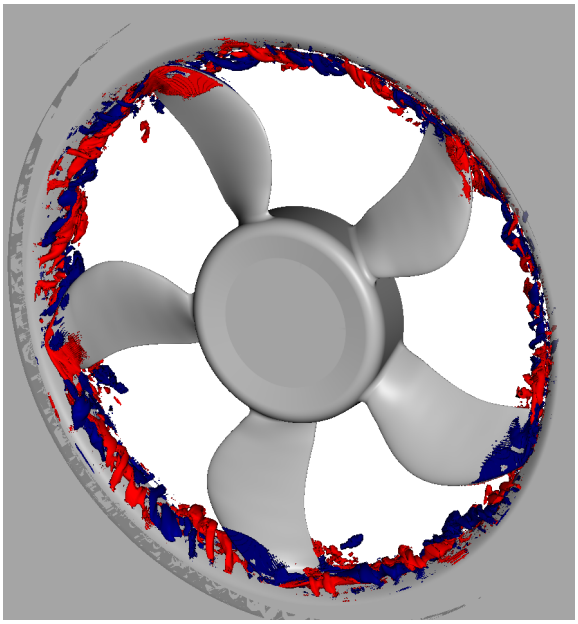

(c)

Figure 7.25 Instantaneous vortical field around the RCDB fan at OC5 highlighted by isosurfaces of $\lambda_2 = -50$ (a) Raw λ_2 field (b) λ_2 field corresponding to $-0.1 \leq n_{mod}/n_{fan} \leq 0.4$, colored by the normalized rotational velocity n_{mod}/n_{fan} (c) same field as (b) further filtered according to frequency in the 530-550 Hz ($m = 20$) band, colored by pressure.

when weighted by the wavelet approach in Tab. 7.6, these modes appear to be very weak when compared to the upper radii and could not be identified using λ_2 visualizations.

Table 7.5 Proportion of events identified at different spatial points according to radius and chordwise position in the tip region of the Bosch fan

% of events		Chordwise ID											
		C01	C02	C03	C04	C05	C06	C07	C08	C09	C10	C11	Total
Radial ID	R154	1.53	1.44	1.56	1.17	1.58	1.76	1.99	1.93	1.82	1.82	1.74	18.35
	R150	1.16	0.82	1.69	1.77	1.93	1.81	2.06	2.32	1.72	0.93	0.26	16.48
	R146	1.39	0.54	2.07	2.15	2.16	2.48	2.50	2.45	2.91	2.48	2.32	23.44
	R142	3.65	2.92	1.21	1.71	1.08	0.99	1.32	0.95	0.22	0.49	0.23	14.77
	R138	2.48	2.33	0.00	0.29	0.58	0.45	0.68	0.26	0.08	0.30	0.15	7.60
	R134	2.37	1.55	0.52	0.77	0.17	0.94	0.12	0.66	0.72	0.22	0.12	8.16
	R130	2.20	1.40	1.06	0.83	0.60	0.21	0.92	1.08	1.13	0.77	0.99	11.21
	Total	14.78	11.01	8.11	8.68	8.10	8.64	9.59	9.65	8.61	7.01	5.82	

Table 7.6 Amplitude-weighted proportion of events identified at different spatial points according to radius and chordwise position in the tip region of the Bosch fan

% of events		Chordwise ID											
		C01	C02	C03	C04	C05	C06	C07	C08	C09	C10	C11	Total
Radial ID	R154	1.48	1.62	1.81	2.03	1.81	2.17	2.81	2.65	2.78	2.36	2.37	23.89
	R150	0.81	0.64	2.19	2.24	2.91	2.57	3.70	3.85	2.80	1.57	0.34	23.62
	R146	0.56	0.25	3.26	2.57	2.16	2.78	3.08	3.25	4.07	4.14	3.62	29.73
	R142	1.45	1.50	1.66	2.43	1.38	0.92	1.12	0.77	0.19	0.58	0.29	12.29
	R138	1.03	1.09	0.00	0.34	0.27	0.36	0.43	0.18	0.04	0.21	0.14	4.09
	R134	0.70	0.75	0.12	0.28	0.03	0.48	0.07	0.22	0.23	0.05	0.02	2.96
	R130	0.59	0.47	0.40	0.16	0.25	0.07	0.28	0.35	0.38	0.17	0.32	3.42
	Total	6.61	6.33	9.43	10.04	8.81	9.36	11.48	11.26	10.49	9.08	7.10	

When looking now at the interaction frequency of the identified modes, shown according to the frequency of occurrence in Fig. 7.26(a) and according to the wavelet-weighted strength of the interactions in Fig. 7.26(b), it can be observed that the weighting operation has a rather noticeable impact on the predicted interaction levels. In effect, it smooths the distribution over the entire frequency range. In particular, much of the noise in the $f_{int} = 5 - 12$ and 16-25 ranges is removed, leaving clearer humps to appear; the modes detected in the lower radii (R138-R130) have little to no impact on the prediction.

Comparing the strength-weighted correlation histogram from Fig. 7.26(b) to the overlaid FWH spectra for the Bosch fan (from Fig. 6.13), the correlation method does succeed in clearly predicting the acoustic tones at $f_{int} = 4$ and 12 and does a fair job at representing the relative levels. One can also see a weak correspondance of the correlation prediction with humps in the acoustic spectra at $f_{int} = 16 - 17$, although the levels are mismatched.

A weak interaction is also predicted around the fourth BPF harmonic $f_{int} = 20$ that loosely corresponds to a tuft of weak peaks in the spectra.

However, neither the second BPF harmonic $f_{int} = 10$ and its sub-harmonic hump at $f_{int} = 8$ are clearly predicted by the method. Furthermore, the correlation analysis predicts a strong tonal interaction at $f_{int} = 14.5$ that corresponds only to a weak peak in the FWH spectra; this frequency is however largely amplified when looking at the direct CAA spectra, which is attributable to the effect of the installation, which further indicates that the method appears to have a difficult time sorting through the installation-related modes and those who are induced by tip leakage flow in certain situations.

Conclusion on the Bosch Case

The Bosch fan configuration provided an interesting variation to the other two free-tipped tube-axial fans with regard to its tip clearance configuration. The converging gap in effect favors the formation of rather peculiar tip clearance flow features that interfere strongly with the blades and produce strong tonal content in the FWH generated acoustic spectra, as confirmed in Sec. 6.3.1. Like the USI7, strong tip region distortions were hinted at due to the presence of the telling RI spectral signature in the flow pressure field, interestingly enough in a different frequency range than its counterpart.

The modes identified through the correlation algorithm showed that the most coherent modes in the flow exhibited a modal order comparable to the USI7 case, but that they globally possessed a fairly different rotational speed at around 17% of the fan speed. The analysis also predicted the appearance of very slow modes, with some possessing a negative rotational speed (i.e. counter-rotating with respect to the fan). The flow structures associated with these varied velocity ranges were however clearly identified using filtered λ_2 visualizations, as were the predicted mode orders.

The final step of the correlation analysis also clearly positively accounted for the presence of the first and third harmonics of the sub-BPF tones associated with tip region blade pressure fluctuations in Fig. 6.14 but however failed to clearly identify the second and fourth harmonics which are barely discernable in the interaction frequency histogram. The method also clearly identified a quasi-tone which weakly emerges in the FWH spectra, but is largely amplified when looking at the direct CAA, indicating that care must be taken when using the approach on configurations where there is acoustic amplification as a result of the propagation environment as it cannot properly distinguish the resulting modes from those who are flow-induced.

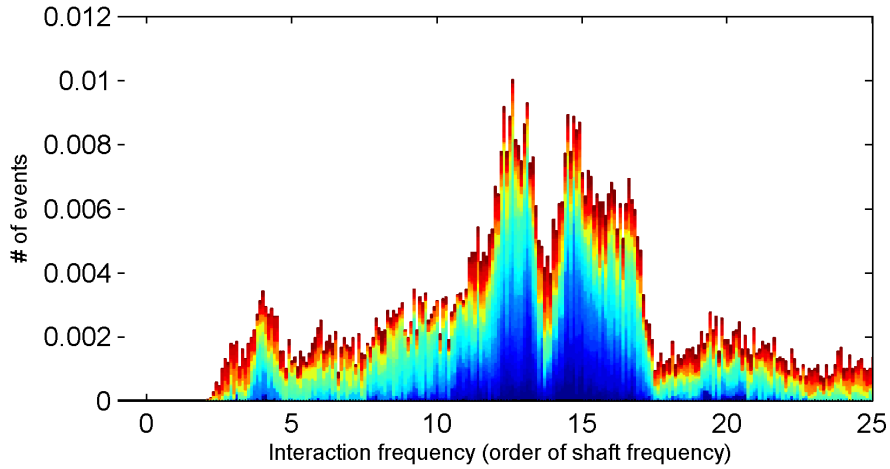

(a)

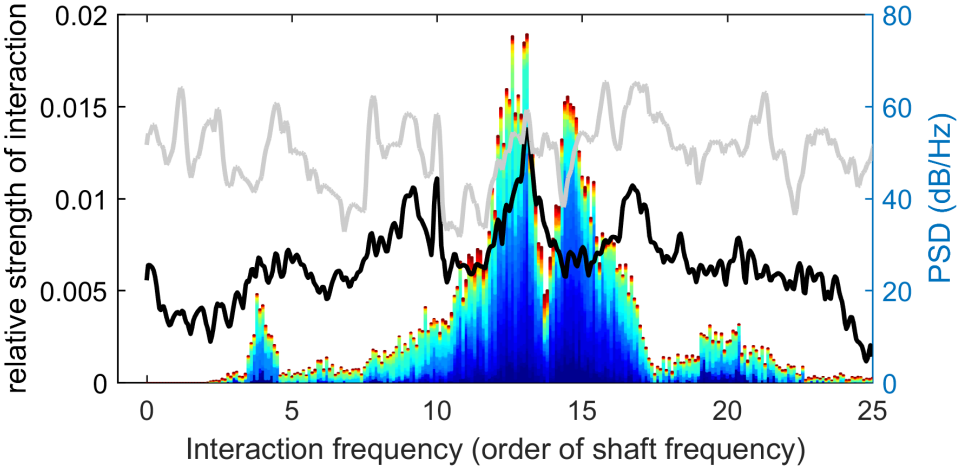

(b)

Figure 7.26 Histogram identifying the interaction frequencies of the detected modes for the Bosch fan according to (a) Frequency of occurrence (b) Strength of the interactions as weighted by the wavelet thresholding method; the acoustic FWH prediction (black) and direct CAA (grey) spectra are overlaid. Binning is carried out at 10ths of the rotational frequency of the fan.

7.4.4 H380EC1

The final fan configuration investigated in the course of the current study is the Valeo ring-shrouded H380 fan. The fan was studied numerically on two fairly different test rigs, as explained in Sec. 5.6. The first simulation was run to reproduce the MSU AFRD facility test configuration, wherein the fan is flush-mounted on the wall of the test plenum with relatively free-field inlet and outlet conditions. The second numerical setup was made to correspond to an in-house experimentation rig at the Université de Sherbrooke, where the fan was inserted in a test duct assembly with an inlet bellmouth and a flowrate control plug aperture. This last configuration was seen to have a large impact on the propagation of acoustic waves generated from the fan with the specific noise of the fan being drowned out as seen in Sec. 6.3.1.

However, in Sec. 6.3.1, the use of the FWH analogy using the wall-pressure fluctuations recorded on the fan rotor for both simulations in conjunction with free-field propagation showed that the acoustic power spectra radiated by both fans was eerily similar, with strong sub-harmonic acoustic humps appearing at 75-80% of the BPF frequency up to the third harmonic. The most probable surface sources on the fan rotors were linked to the tip region of the blades using bandpass filtering of the rotor wall-pressure fluctuations, where the occurrence of a rich vortical field interacting with the blades and generated as a result of tip leakage flow through the ring gap is observed. This further reinforced conclusions from previous investigations of the H380 [Magne, 2015; Magne *et al.*, 2014; Moreau and Sanjose, 2016] wherein the interaction of these vortical structures with the blades was surmised to be the source of the observed sub-harmonic humps.

This leads to the very important observation that the difference in the installation rigs does not appear to fundamentally impact the mechanism responsible for the generation of these sub-harmonic tones, despite the differences observed in the vortical field topology in Sec. 6.2.2 in the tip region of the fan.

An in-depth characterization of the distortion field caused by these vortical structures in the blade passage is made possible using the correlation analysis method described in Sec. 7.2 by using circumferential sensor arrays like with the previously covered free-tipped fan configurations. This section is however structured a little differently than those covering the other fan configurations, and proposes a comparative study of the results from the modal analysis carried out on both setups of the H380 fan.

In both simulations, a series of sensor rings were thus used to extract the pressure signal from LBM volume simulation data in the blade passage to investigate the flow in the tip

region; radial locations from just under the ring-shroud (R182) in decrements of 3 mm down to R161 (80% span) were investigated, with 11 chordwise rings from leading to trailing edge at each radius. A resolution of 90 probes along the circumference (4°, or 10 probes per blade passage) was used for each of the rings, with the probe positions defined as stationary relative to the blades.

Inspection of the volume probe signals yielded the observation that there was no appearance of a consistent RI spectra signature in the flowfield, for both the ducted and plenum configurations; representative examples for both cases are shown in Fig. 7.27.

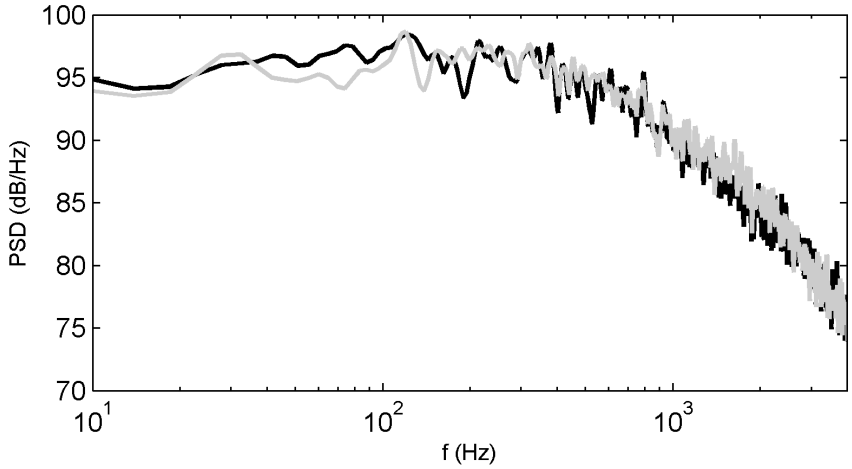

(a)

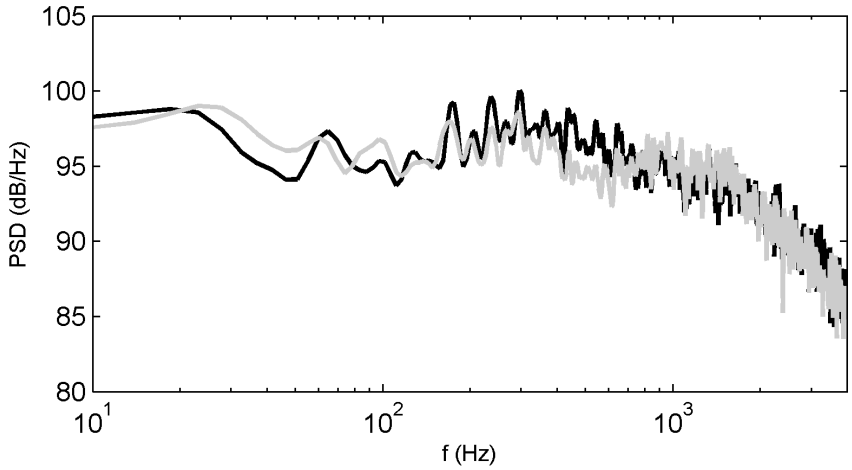

(b)

Figure 7.27 Power spectral density of two subsequent signals extracted from the H380 LBM volume data for the (a) ducted configuration (b) plenum configuration. The lead signal is in black and the trailing signal is in grey.

The first item that was noticed when it came to carrying out the cross-spectral analysis for pairs of probes in the sensor arrays was that the correlation levels associated with the H380 case were much lower than those encountered on any of the free-tip fans in general. Examples of cross-spectral analysis plots are shown in Fig. 7.28 for both configurations for the 40-1000 Hz range, where a strong phase lag linearity was typically observed over the whole spectrum on most probe pairs; the 40 Hz lower bound was found to be where discontinuities in the phase angle occured, probably as the result of a lack of resolution due to having only 1.2 s of physical time to work with for the H380 configurations (generating 10 TB of data for each case).

The correlation analysis was run by setting the coherence threshold to 0.4 for the detection of *coherent* modes, which is significantly lower than the value used for any of the free-tipped configurations. The modal characteristics associated with the probe pairs from Figs. 7.27 and 7.28 for both the ducted and plenum cases are shown in Fig. 7.29.

Since the RI spectral signature could not guide the frequency range in which to perform the analysis, it was the subject of a parametric investigation. Since the H380 in both the plenum and duct configurations correspond to two sides of the same coin, so to speak, but are fairly distinct at the same time, the results of the correlation analysis for both are presented separately in the following sections.

Ducted H380EC1 Configuration (H380D)

Since a strong phase linearity was observed over the 40-1000 Hz range, the correlation analysis could theoretically be run over the entire spectrum and yield results. However, this approach runs the risk of identifying too many modes and drown out those responsible for the occurrence of the observed quasi-tonal noise. A parametric investigation was thus performed in order to investigate the effect the upper bound had on the results from the analysis.

As a first foray, the 40-300 Hz range was investigated; the characteristics of the coherent modes detected in the full circumferential analysis for all sensor arrays in the tip region of the blades for the H380 ducted case (hereafter referred to as H380D) are shown in Fig. 7.31. The colormap of the evaluation positions is shown in Fig. 7.30. The dominant modes orders encountered are between 4 and 8 (0.45 to 0.89 lobes per blade passage), as highlighted by the probability distribution in Fig. 7.31(a); this contrasts with the previously investigated cases wherein the dominant modes were seen to have an order higher than the number of blades on the rotor, on the order of 2 to 3 lobes per blade passage.

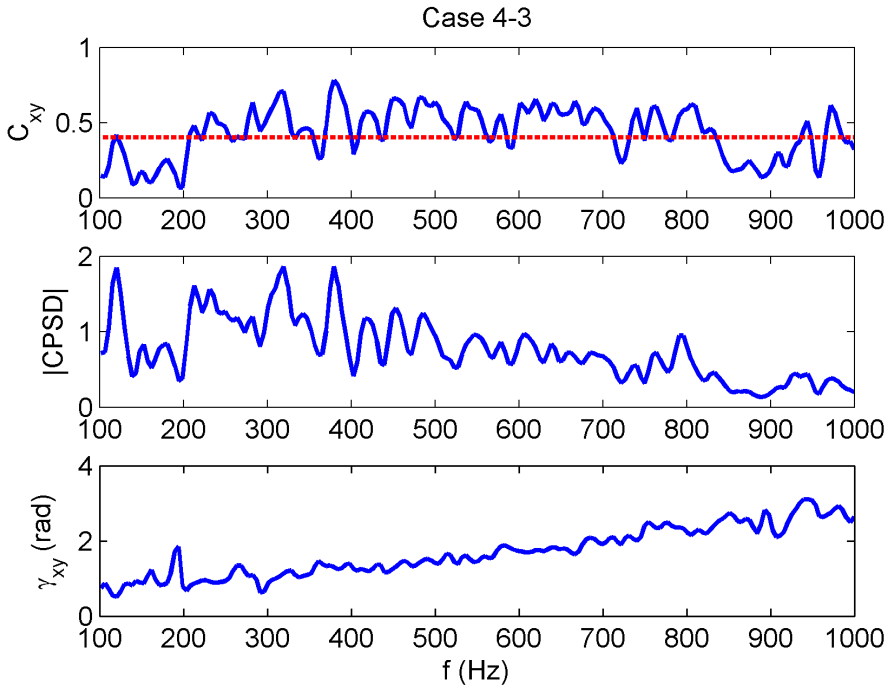

(a)

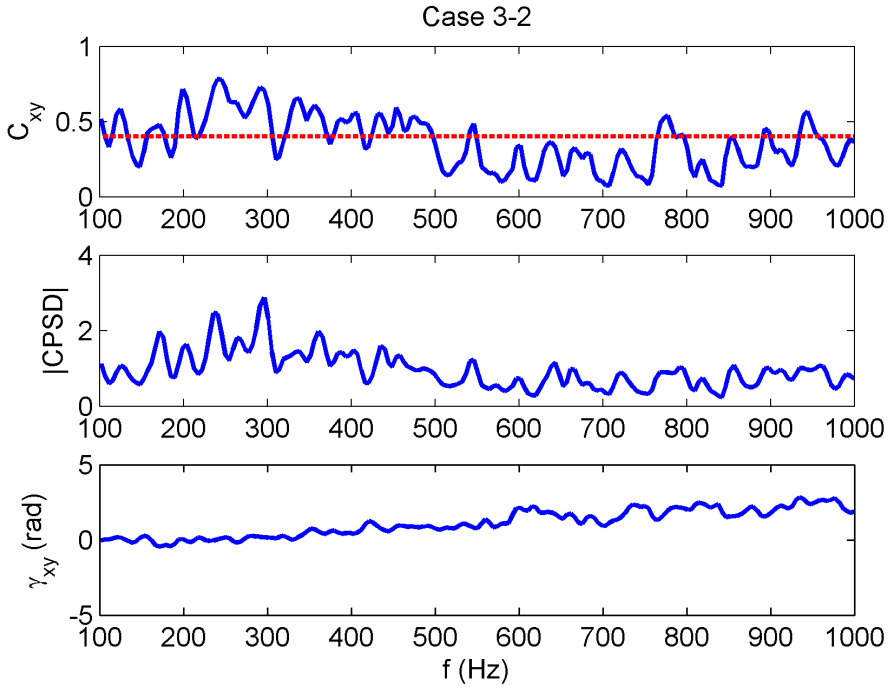

(b)

Figure 7.28 Illustration of the intermediary steps of the correlation analysis for a pair of probes in the H380 LBM volume data in the (a) ducted and (b) plenum configurations

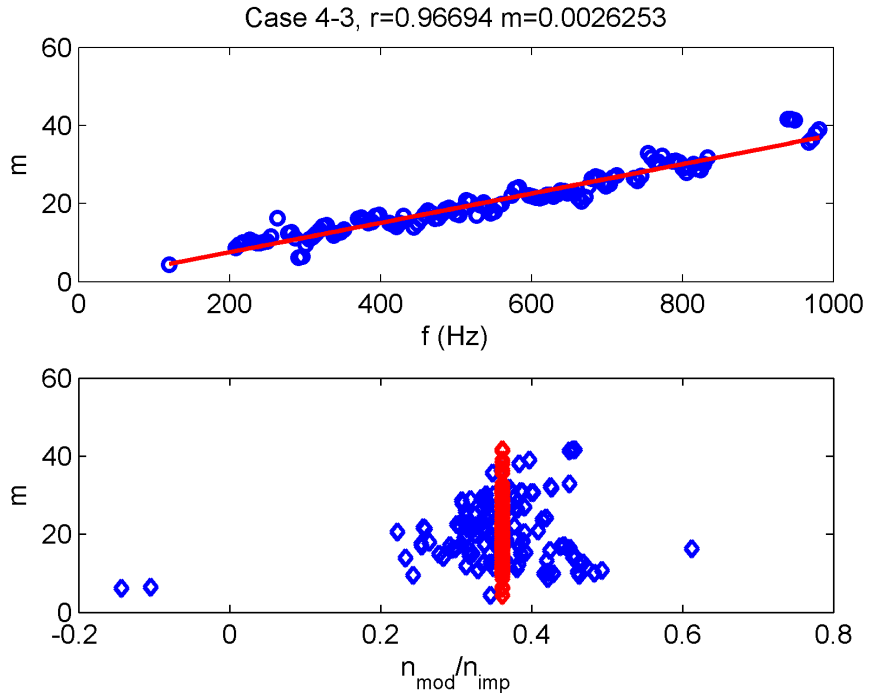

(a)

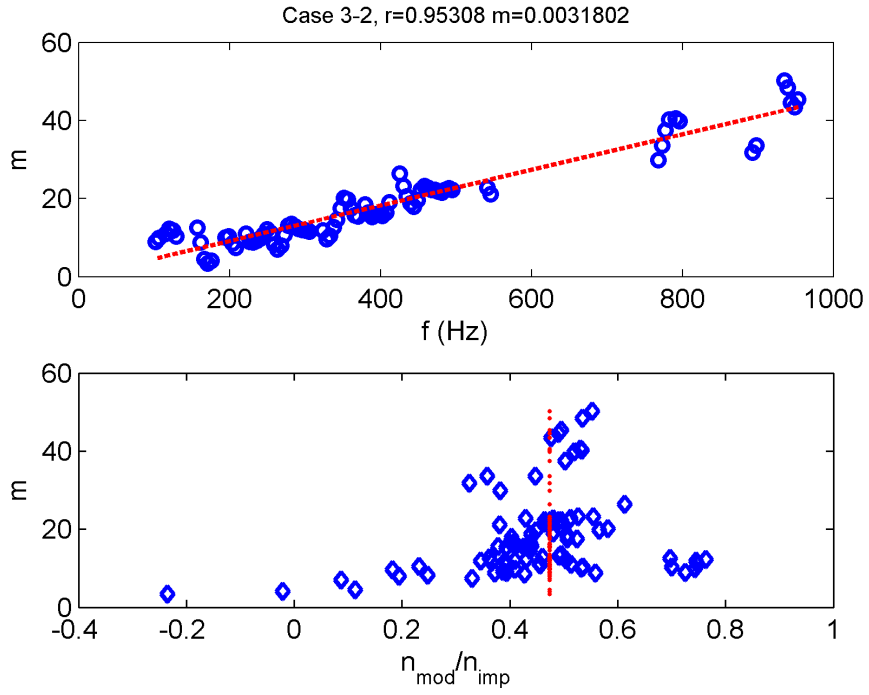

(b)

Figure 7.29 Characteristics of the modes identified as a result of the correlation analysis for a pair of probes in the H380 LBM volume data in the (a) ducted and (b) plenum configurations.

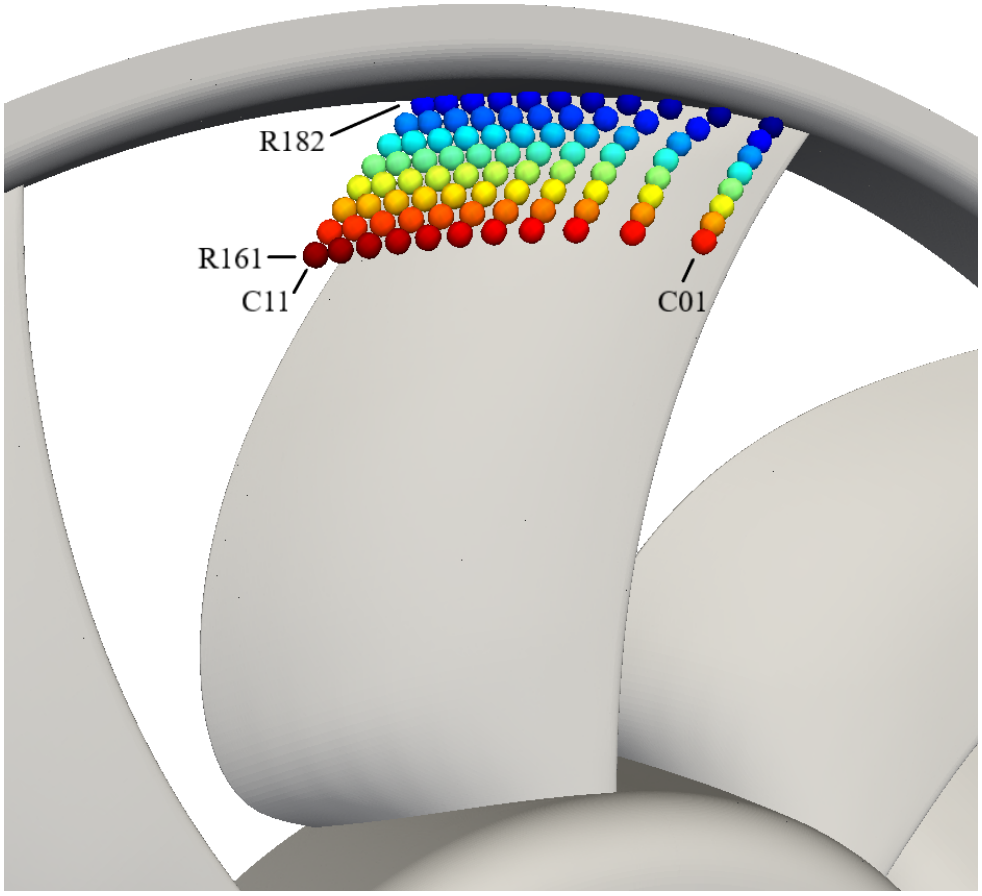

Figure 7.30 Color-coding of the modal analysis positions according to radial (R) and chordwise (C) positions for the H380 fan.

Looking at the modal velocities in Fig. 7.31(b), it also becomes apparent that the velocities associated with these modes are also elevated compared to the previous cases, as they hover around a central value of ∼50% of the fan rotational speed. It is also fairly different from the previous estimate of 23% by Magne et al. [Magne *et al.*, 2015].

The spatial distribution of the modes in the tip region, shown in Tab. 7.7, indicates that they are more sparsely detected in the first 30% of the chord, whilst the remaining number is evenly distributed along the rest of the chord. Moreover, the radial sensor position just under the ringshroud (R182) indicates that fewer modes are seen to appear compared to the R179-R161 positions.

Using the identified modal characteristics, the interaction frequency of the modes can be accounted for according to their frequency of occurrence as with the previous cases, which is presented in Fig. 7.32(a). However, as explained throughout this section, a more representative interaction histogram can be obtained through wavelet-weighting the modal

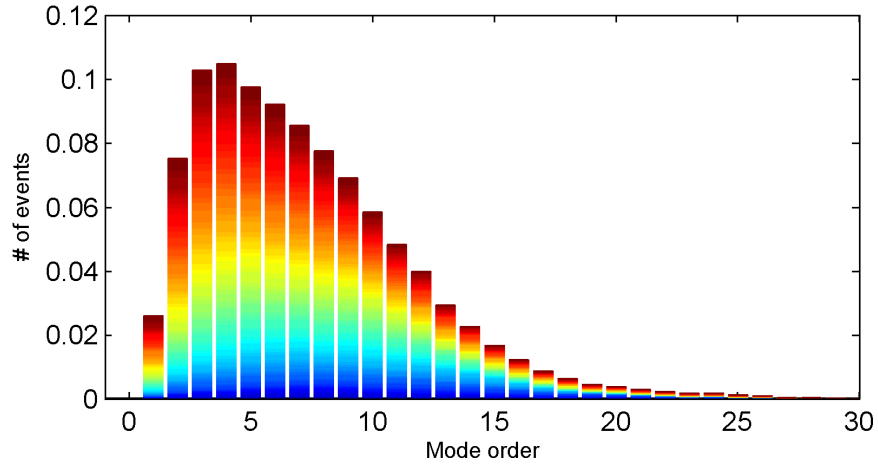

(a)

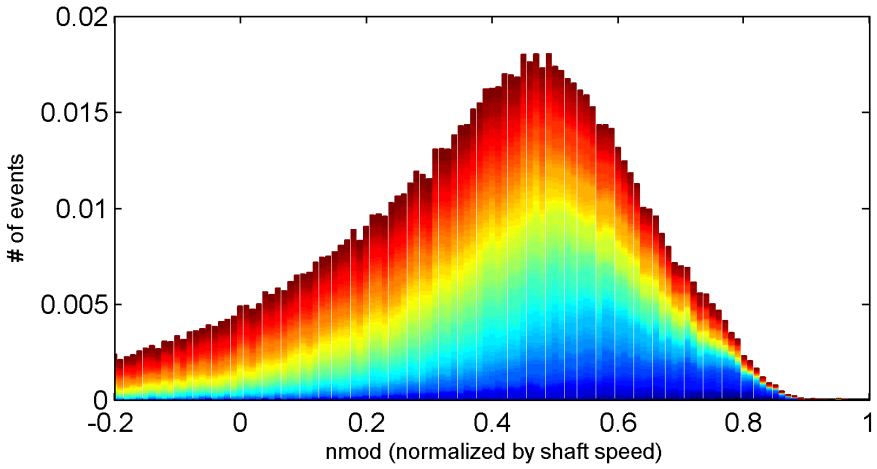

(b)

Figure 7.31 Characteristics of the modes detected through correlations analysis for the H380D configuration in the tip region (R182-173) of the blades for the 40-300 Hz range (a) Mode orders (b) Mode rotational velocity.

interactions to take into account the relative amplitude of the coherent modes. Once the events are strength weighted, the observed chordwise trend in the spatial distribution of the modes is slightly modified in Tab. 7.8 however, indicating that those directly at the leading edge appear to have a strong amplitude. The impact of the modes in the last 20% of the chord is also lessened slightly. However, the radial distribution of the modes isn't significantly modified and modes detected appear to have an even impact down to the lowermost radius (R161) investigated.

Table 7.7 Proportion of events identified at different spatial points according to radius and chordwise position in the tip region of the H380D fan for the 40-300 Hz range

% of events		Chordwise ID											
		C01	C02	C03	C04	C05	C06	C07	C08	C09	C10	C11	Total
Radial ID	R182	0.30	0.22	0.21	0.35	0.31	0.24	0.36	0.53	0.53	0.72	0.64	4.40
	R179	0.53	0.52	0.61	0.74	0.76	0.72	0.75	0.91	0.91	0.88	0.71	8.05
	R176	0.87	0.78	0.99	1.03	1.09	1.13	1.10	1.05	1.05	0.93	0.94	10.96
	R173	1.02	0.87	0.96	1.17	1.22	1.30	1.33	1.20	1.20	1.07	0.95	12.28
	R170	1.30	0.97	1.02	1.31	1.33	1.52	1.59	1.45	1.45	1.35	1.02	14.30
	R167	1.39	1.12	1.08	1.36	1.39	1.59	1.64	1.72	1.72	1.61	1.60	16.22
	R164	1.65	1.12	1.05	1.34	1.42	1.64	1.65	1.79	1.79	1.81	1.72	17.00
	R161	1.85	1.23	0.95	1.26	1.37	1.55	1.63	1.75	1.75	1.73	1.72	16.80
	Total	8.89	6.82	6.87	8.55	8.88	9.71	10.05	10.41	10.41	10.10	9.30	

Table 7.8 Amplitude-weighted proportion of events identified at different spatial points according to radius and chordwise position in the tip region of the H380D fan for the 40-300 Hz range

% str. of events		Chordwise ID											
		C01	C02	C03	C04	C05	C06	C07	C08	C09	C10	C11	Total
Radial ID	R182	0.72	0.50	0.50	0.75	0.62	0.42	0.50	0.58	0.58	0.74	0.54	6.43
	R179	1.23	0.93	1.16	1.38	1.31	1.18	1.25	1.22	1.22	1.06	0.72	12.66
	R176	1.38	0.93	1.26	1.30	1.40	1.44	1.49	1.29	1.29	1.05	0.93	13.76
	R173	1.35	0.82	0.97	1.17	1.26	1.34	1.35	1.25	1.25	1.09	0.90	12.73
	R170	1.49	0.80	0.87	1.16	1.21	1.39	1.46	1.36	1.36	1.29	0.98	13.37
	R167	1.37	0.81	0.81	1.09	1.16	1.36	1.43	1.54	1.54	1.50	1.51	14.13
	R164	1.47	0.73	0.70	1.25	1.06	1.29	1.34	1.55	1.55	1.66	1.62	14.24
	R161	1.45	0.76	0.57	0.80	0.91	1.09	1.20	1.41	1.41	1.49	1.60	12.68
	Total	10.46	6.27	6.85	8.90	8.93	9.50	10.01	10.20	10.20	9.87	8.79	

The relative amplitude of the interaction frequencies in the histogram is also modified slightly as a result, as shown in Fig. 7.32(b); a smoother decrescendo is created as the frequency of interaction increases, whereas a sharp drop was observed in the *event count* histogram at $f_{int} \sim 7$ and 22. However, as we compare the observed peaks obtained from the histogram with the overlaid FWH acoustic spectra, none of the sub-harmonics quasi-tones are predicted by the identified modes. However, the humps from the interaction

histogram at $f_{int} = 5$ and 10 correspond very well to the locations of the large spectral clusters that were associated with installation effects on this configuration [Christophe *et al.*, 2016]. Anything over $f_{int} \sim 12$ is too noisy and involves too much guesswork for any clear conclusions to be drawn for higher frequencies.

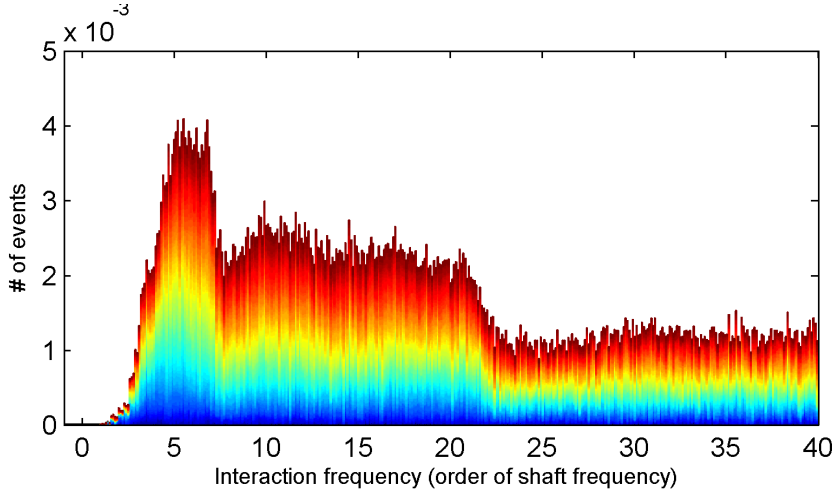

(a)

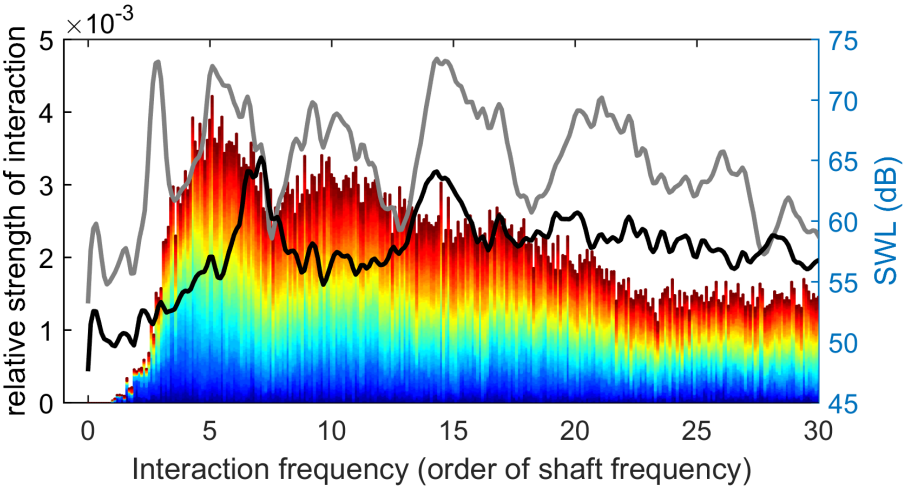

(b)

Figure 7.32 Histogram identifying the interaction frequencies of the detected modes for the H380D fan for the 40-300 Hz range according to (a) Frequency of occurrence (b) Strength of the interactions as weighted by the wavelet thresholding method; the acoustic FWH prediction is overlaid. Binning is carried out at 10ths of the rotational frequency of the fan.

Some experimentation was carried out as to the frequency range utilized for the cross-correlation analysis. For example, by extending the range to 600 Hz, a hint of the first sub-BPF tone is shown at $f_{int} = 7$, as shown in Fig. 7.33.

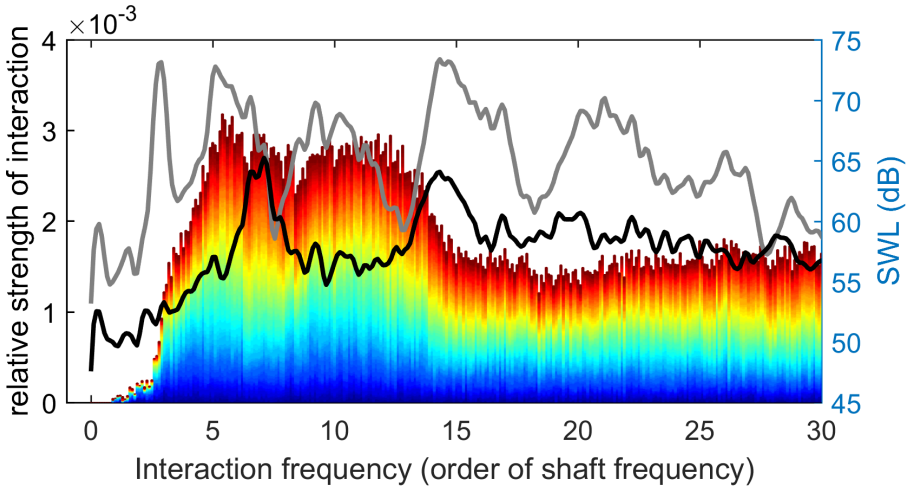

Figure 7.33 Histogram identifying the interaction frequencies of the detected modes in the 40-600 Hz range for the H380D fan according to the strength of the interactions as weighted by the wavelet thresholding method; the acoustic FWH prediction is overlaid. Binning is carried out at 10ths of the rotational frequency of the fan.

Further extending the analysis range to 1000 Hz for the cross-correlation, a large hump at $f_{int} \sim 21-24$ appears in the interaction histogram and is shown to be shifted in frequency compared to the spectral hump in the direct CAA acoustic spectra. At the same time, the $f_{int} = 7$ peak becomes drowned in the $f_{int} = 10$ hump and a hint of the second sub-BPF harmonic appears at $f_{int} = 14$, as shown in Fig. 7.34.

This last range for the analysis also presents a particular distribution as far as the mode orders are concerned, with the appearance of a significant number of modes of order 18 and at subsequent multiples of 3 thereafter, as shown in Fig. 7.35(a). Due to their modal order, some of these distortions would impact all of the blades at the same time (i.e. orders 18, 27, 36 and 45) and potentially generates increased noise levels if all of the contributions are additive.

The modal velocities are also slightly shifted and now scatter around a value of 44% of the fan rotational speed overall, as shown in Fig. 7.35(b), due to these additional modes having lower velocities (around 20 to 30% of the fan rotational speed). Thus their interaction frequency should occur at around 70 to 80% of the BPFs, which is coherent with the tones appearing at $f_{int} = 7, 14$ of the acoustic spectra. Spatially, these modes appear to occur evenly among all radii and chordwise positions and do not have a preferential localization in the blade passage.

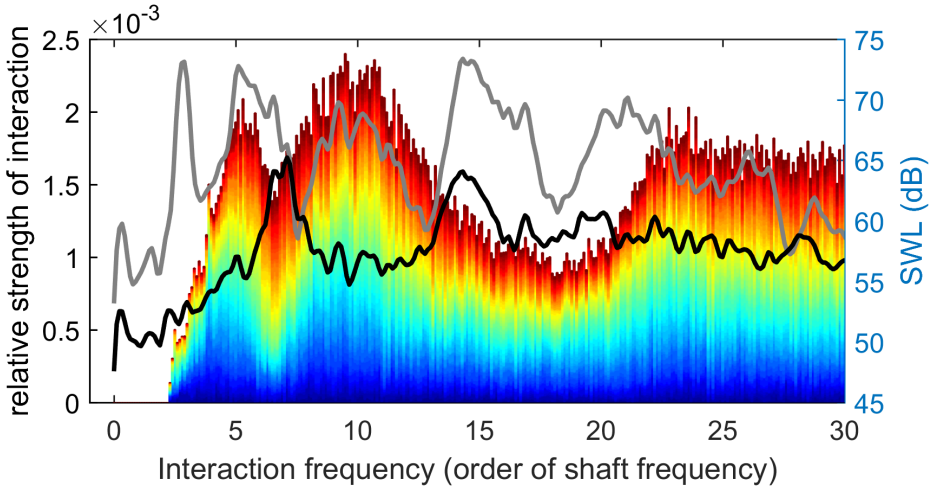

Figure 7.34 Histogram identifying the interaction frequencies of the detected modes in the 40-1000 Hz range for the H380D fan according to the strength of the interactions as weighted by the wavelet thresholding method; the acoustic FWH prediction is overlaid. Binning is carried out at 10ths of the rotational frequency of the fan.

Using visualizations of the speed-filtered λ_2 field to retain only the coherent structures whose rotational speed corresponds to $0.1 \leq n_{mod}/n_{fan} \leq 0.6$, Fig. 7.36(a) is obtained. A fairly dense vortical field is still present around the ring-shroud, with the majority of the structures possessing a rotational speed of around 29 to 41%; however the presence of slower structures ($\sim 20-25\%$) is also observed. Filtering the vortical field eliminated some of the larger structures that were observed with the same $\lambda_2 = -100$ value in Sec. 6.2.2.

Like with the previous configurations, an additional filtering step according to frequency was implemented to identify the pressure modes in the flow. Fig. 7.36(b) shows the same λ_2 field as Fig. 7.36(a), showing only the coherent structures associated with pressure fluctuations in the 340-360 Hz band, which according to Fig. 7.29(a) correspond to a mode order $m \sim 14-16$. The exact number of the modal pattern is difficult to properly identify, unlike the previous configurations. The pressure levels observed were also much lower than in previous cases (on the order of 1 Pa), and where a threshold value of 10^{-4} Pa value had to be used to obtain a visualization, with the maximum amplitude of the pressure fluctuations being around 10^{-3} Pa. This low amplitude of the pressure modes seems to be generalized across the entire spectrum and indicates pressure fluctuations more likely to be related to either acoustic waves or numerical noise.

Several intermediary observations can be drawn from these results on the H380D fan. The first one concerns the fact that the correlation analysis seems unable to clearly discern the effects of the tip leakage flow features properly from among the strong scattering effect the

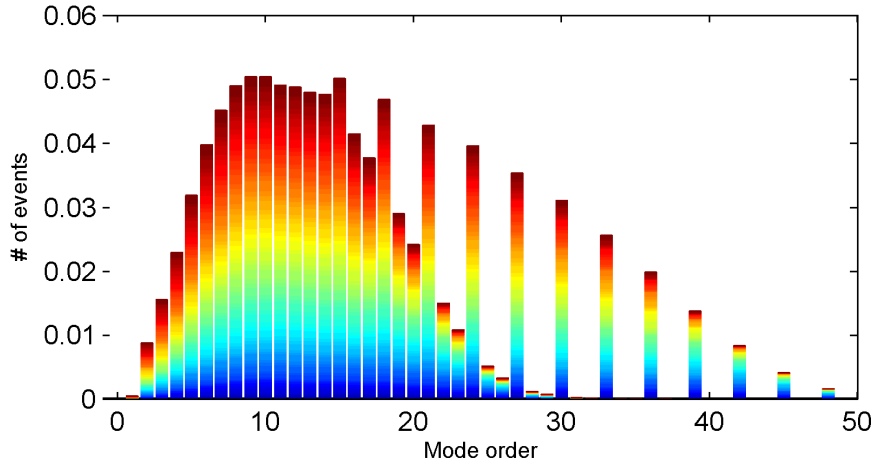

(a)

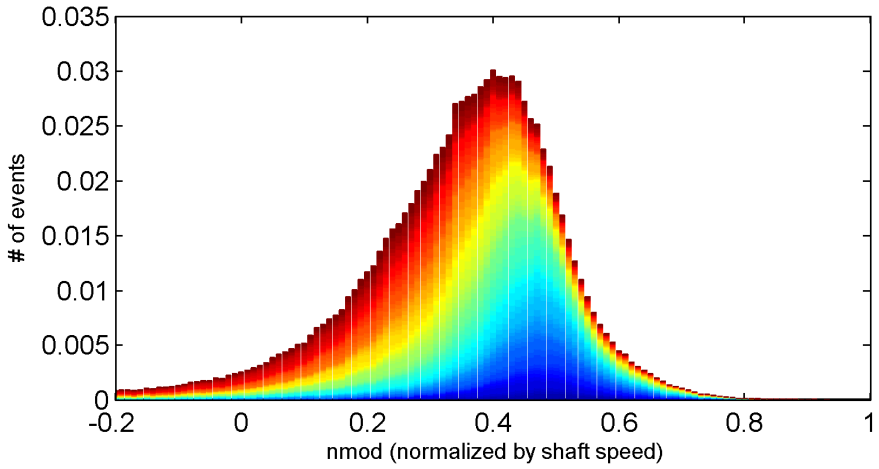

(b)

Figure 7.35 Characteristics of the modes detected through correlations analysis for the H380D configuration in the tip region (R182-173) of the blades for the 40-1000 Hz range (a) Mode orders (b) Mode rotational velocity.

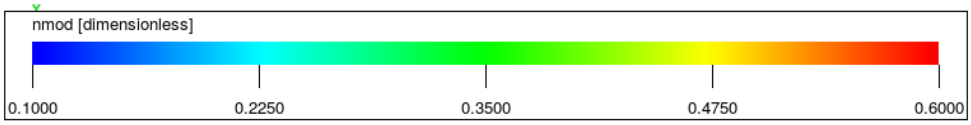

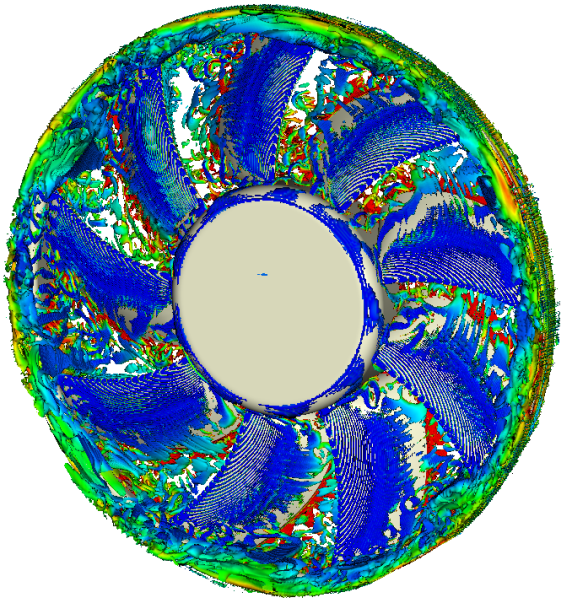

(a)

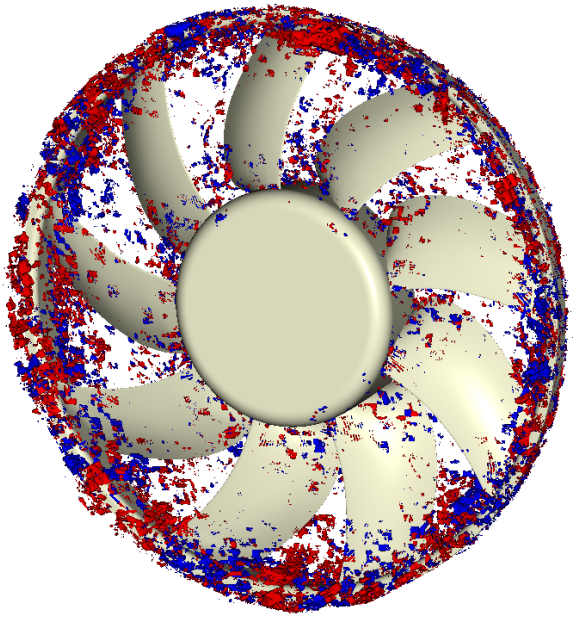

(b)

Figure 7.36 Instantaneous vortical field around the H380D fan highlighted by isosurfaces of $\lambda_2 = -100$ (a)field corresponding to $0.1 \leq n_{mod}/n_{fan} \leq 0.6$ for the H380D fan, colored by the the normalized rotational velocity n_{mod}/n_{fan}; (b) shows the same field as (a) further filtered according to frequency in the 340-360 Hz ($m \sim 14 - 16$) bands, colored by pressure.

duct has on both the trailing edge and tip leakage noise; this reinforces a similar observation on the Bosch fan (see Sec. 7.4.3). In fact, in order to obtain a reasonable identification of the first two sub-harmonic quasi-tonal humps identified by the FWH analysis, the frequency range used as a basis for the correlation analysis must be expanded from the one initially set and that the tip leakage noise mechanism is spread across a much wider range. This is probably what accounts for the substantially more elevated modal velocities identified in Fig. 7.31(b), as this most likely represents the velocity of the acoustic modes rather than those of the aerodynamically-caused distortions.

However, while these acoustic modes are to be attributed to the duct scattering effect, it is impossible at this stage to conclude if they are due to the scattering of the tip noise or trailing edge noise or a mix of the two. The absence of the $f_{int} \sim 14-17$ spectral cluster in the correlation analysis when it is run for frequencies up to 1000 Hz, however, could be an indication that the tip noise scattering does not contribute at these frequencies, which is somewhat odd considering that the second harmonic of the sub-BPF quasi-tones identified using the FWH analogy corresponds exactly with this frequency range and should excite the acoustic modes.

Plenum H380EC1 Configuration (H380P)

The final configuration studied in this chapter is the H380 in the plenum configuration (H380P). In an effort to mirror the analysis carried out on the H380D, the correlation analysis was also run in the 40-300 Hz range using the sensor arrays setup in the tip region of the blades of the H380P. The modal characteristics of the coherent modes detected using the 0.4 value for the coherence threshold are shown in Fig. 7.37. The color-coding regarding the position of evaluation is identical to the H380D case (Fig. 7.30).

Fig. 7.37(a) shows that the orders of the modes detected in the flow still hover around a modal value of 5, but the standard deviation of the mode orders is inferior to that of the H380D in Fig. 7.31(a). These modes also exhibit rotational velocities hovering around a value approximately that 40% of the fan, as shown in Fig. 7.37(b). This presents a significant shift compared to the 50% value identified for the H380D, and lends more credence to the hypothesis that it represents the velocity of the powerful acoustic modes propagating through the duct, which should be absent here.

The spatial distribution of the detected modes is also a bit different for the H380P when looking at Tab. 7.9, with a significant number showing up at the outermost radial station R182 compared to the H380D (see Tab. 7.7). This is coherent with the differences in the topology of the tip clearance flow observed in Sec. 6.2.2 between the two configurations,

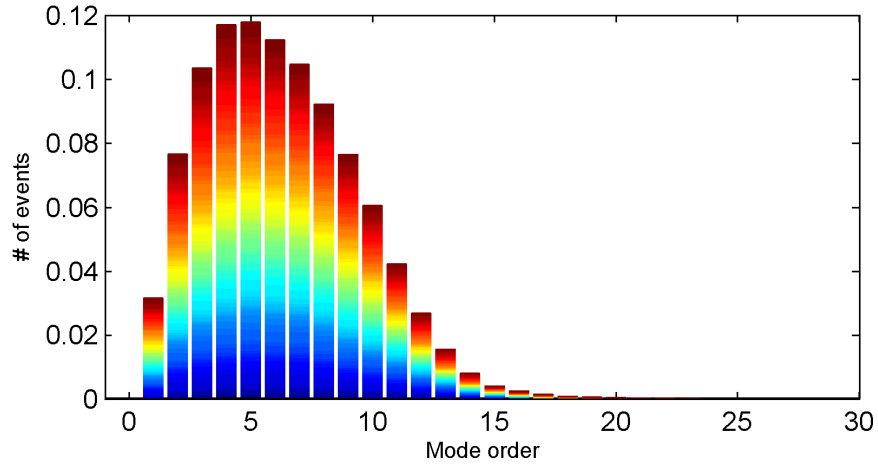

(a)

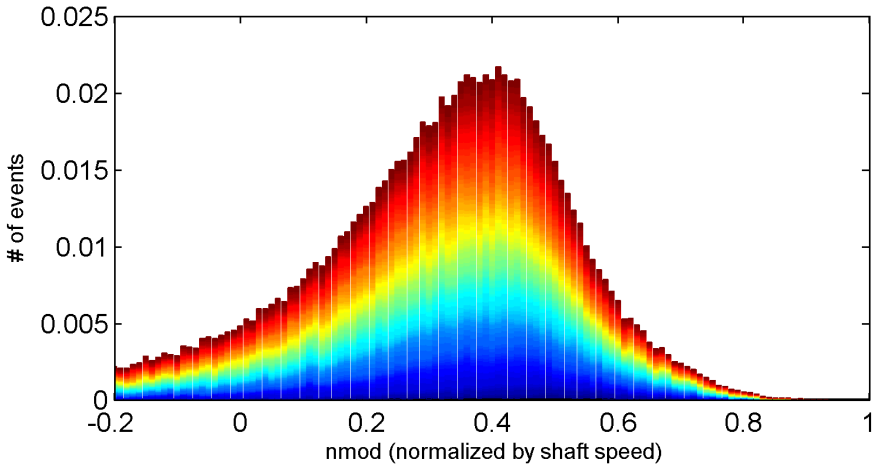

(b)

Figure 7.37 Characteristics of the modes detected through correlations analysis for the H380P configuration in the tip region (R182-161) of the blades for the 40-300 Hz range (a) Mode orders (b) Mode rotational velocity.

wherein the vortical structures generated in the ducted case ahead of the ring-shroud extended much further radially when compared to the plenum case. A significant number of modes are also detected in the last 50% of the chord, which is similar to the H380D. The spatial distribution changes when taking into account the relative amplitude of the modes as weighted by the wavelet method, as shown in Tab. 7.10, and the outermost radii are largely favoritized, indicating that the distortions closer to the ring-shroud are much stronger according to the wavelet LIM analysis.

Table 7.9 Proportion of events identified at different spatial points according to radius and chordwise position in the tip region of the H380P fan for the 40-300 Hz range

% of events		Chordwise ID											
		C01	C02	C03	C04	C05	C06	C07	C08	C09	C10	C11	Total
Radial ID	R182	0.81	0.68	0.58	0.68	0.56	0.59	0.87	1.40	1.40	1.51	1.85	10.92
	R179	0.65	0.68	0.77	0.76	0.78	0.99	1.07	1.43	1.43	1.70	1.69	11.96
	R176	0.74	0.70	0.60	0.72	0.68	0.75	0.94	1.31	1.31	1.51	1.65	10.91
	R173	0.88	0.80	0.87	0.69	0.74	0.76	0.81	0.99	0.99	1.33	1.40	10.25
	R170	1.20	0.92	0.90	0.74	0.62	0.70	0.83	1.06	1.06	1.24	1.54	10.83
	R167	1.12	1.00	0.99	0.89	1.01	1.05	1.16	1.44	1.44	1.50	1.51	13.09
	R164	1.24	1.12	1.12	1.25	1.21	1.44	1.72	1.70	1.70	1.71	1.63	15.83
	R161	1.32	1.13	1.09	1.23	1.35	1.52	1.69	1.77	1.77	1.71	1.60	16.20
	Total	7.96	7.02	6.92	6.97	6.95	7.80	9.10	11.11	11.11	12.20	12.88	

Table 7.10 Amplitude-weighted proportion of events identified at different spatial points according to radius and chordwise position in the tip region of the H380P fan for the 40-300 Hz range

% str. of events		Chordwise ID											
		C01	C02	C03	C04	C05	C06	C07	C08	C09	C10	C11	Total
Radial ID	R182	1.23	0.95	0.77	0.86	0.69	0.68	0.97	1.50	1.50	1.63	2.13	12.90
	R179	1.22	1.17	1.23	1.12	1.10	1.33	1.39	1.78	1.78	2.06	2.00	16.16
	R176	1.16	1.08	0.94	1.07	0.96	1.07	1.25	1.69	1.69	1.92	2.05	14.88
	R173	1.00	0.95	1.06	0.85	0.93	0.98	1.02	1.20	1.20	1.61	1.69	12.50
	R170	1.05	0.78	0.83	0.68	0.60	0.74	0.91	1.17	1.17	1.34	1.69	10.94
	R167	0.67	0.62	0.72	0.68	0.82	0.94	1.05	1.32	1.32	1.42	1.45	11.01
	R164	0.57	0.55	0.65	0.82	0.91	1.12	1.40	1.39	1.39	1.41	1.35	11.55
	R161	0.49	0.47	0.49	0.69	0.83	1.01	1.17	1.28	1.28	1.23	1.14	10.06
	Total	7.39	6.56	6.68	6.77	6.84	7.86	9.14	11.33	11.33	12.61	13.50	

The λ_2 field is filtered according to the rotational speed of the structures to retain only the vortical structures with rotational speed matching the range $0.1 \leq n_{mod}/n_{fan} \leq 0.6$ in Fig. 7.38(a), just like it was done for the H380D case (Fig. 7.36(a)). The thin lower vorticity structures wrapping around the ring-shroud observed in Fig. 6.5(b) are seen to possess a significantly lower velocity ($\sim$ 10% of the fan rotational speed), whereas the ring-shroud is sheathed by structures with velocities ranging from 20 to 40%.

The λ_2 of Fig. 7.38(a) was further bandpass-filtered in the 340-360 Hz band (mode order $m \sim 14 - 16$) as with the H380D configuration, and is shown in Fig. 7.38(b). Like the H380D, the exact modal pattern order is not easy to quantify visually, as it is rather sparse, but it appears there is at least one modal lobe per blade passage. The amplitude of the pressure modes is also fairly weak (10^{-6} Pa), which is even weaker than those observed on the ducted configuration, and it is once again rather generalized across the entire spectrum of frequencies for fine band filters. There is a strong possibility that numerical noise is captured here.

Looking now at the predicted interaction frequency histogram of the identified modes, shown according to the frequency of occurence in Fig. 7.39(a) and to the wavelet-weighting characterizing the amplitude of the modal distortions in Fig. 7.39(b).

The first thing that becomes apparent when comparing the strength-weighted interaction histogram in Fig. 7.39(b) to the corresponding H380D result in Fig. 7.32(b) is that there is no longer any trace of the dominant acoustic modes found in the ducted case. There is however a peak that is predicted by the interaction histogram at $f_{int} \sim 4 - 7$ which is slightly shifted when compared to the quasi-tone observed in the acoustic spectra, which is located at $f_{int} \sim 6.5 - 7.8$, but no clear emergence of the higher order harmonics is observed in the histogram from among the broadband noise.

Expanding the frequency range for the correlation analysis to 600 Hz does not provide an improvement like it did with the H380D fan, however, and in fact worsens the comparison, as shown in Fig. 7.40. So while the first peak in the histogram encompasses the direct CAA peak at $f_{int} \sim 7$, it still overpredicts the levels observed in the acoustic spectra at $f_{int} \sim 4.5 - 6.5$.

The correlation method also predicts elevated levels in the $f_{int} \sim 9 - 14$ range, whereas the second sub-BPF harmonic at $f_{int} \sim 13 - 14$ is rather tonal in shape.

Further expanding the analysis to 1000 Hz further compounds the problems identified, as shown in Fig. 7.41.

The characteristics of the modes detected by the correlation analysis for the 40-1000 Hz range are shown in Fig. 7.42. The modal orders, illustrated in Fig. 7.42(a), are very similar to the corresponding analysis for the H380D fan (Fig. 7.35), down to the appearance of a significant number of modes of order 18 and at subsequent multiples of 3 thereafter.

The modal velocities are however shifted to around 30% of the fan rotational velocity, which is a departure from the H380D. Through an inspection of the modal velocities

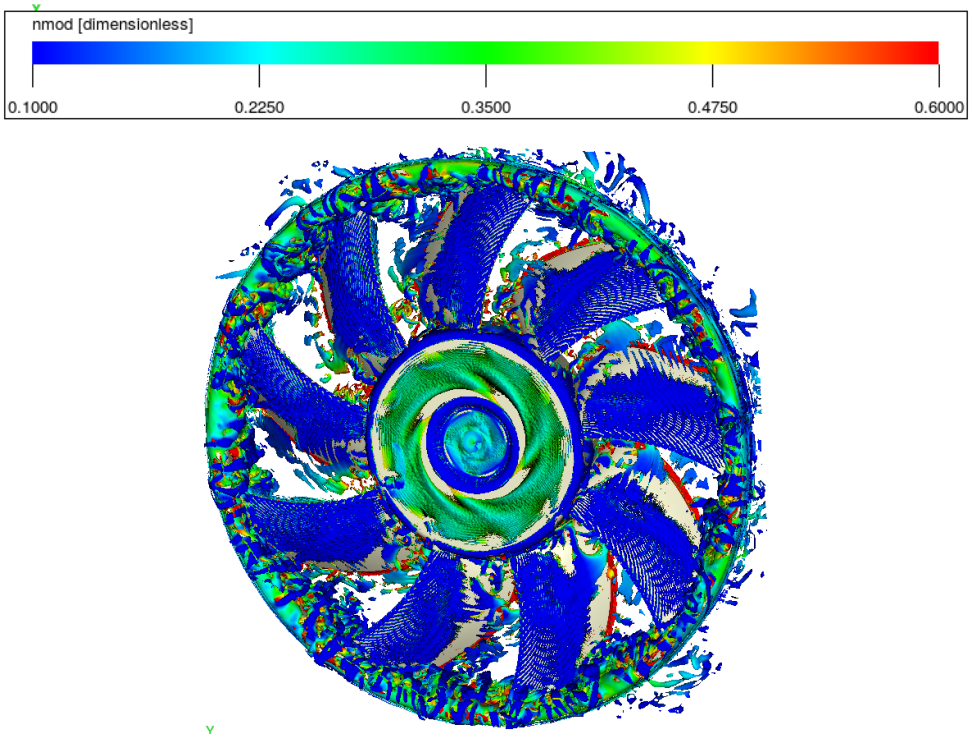

(a)

(b)

Figure 7.38 Instantaneous vortical field around the H380P fan highlighted by isosurfaces of $\lambda_2 = -100$ (a) field corresponding to $0.1 \leq n_{mod}/n_{fan} \leq 0.6$ for the H380P, colored by the the normalized rotational velocity n_{mod}/n_{fan}; (b) show the same field as (a) further filtered according to frequency in the 340-360 Hz ($m \sim 14 - 16$) bands, colored by pressure.

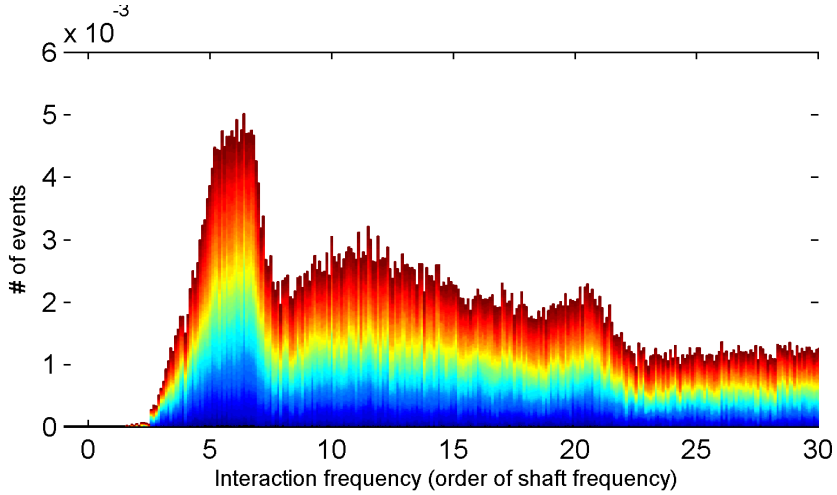

(a)

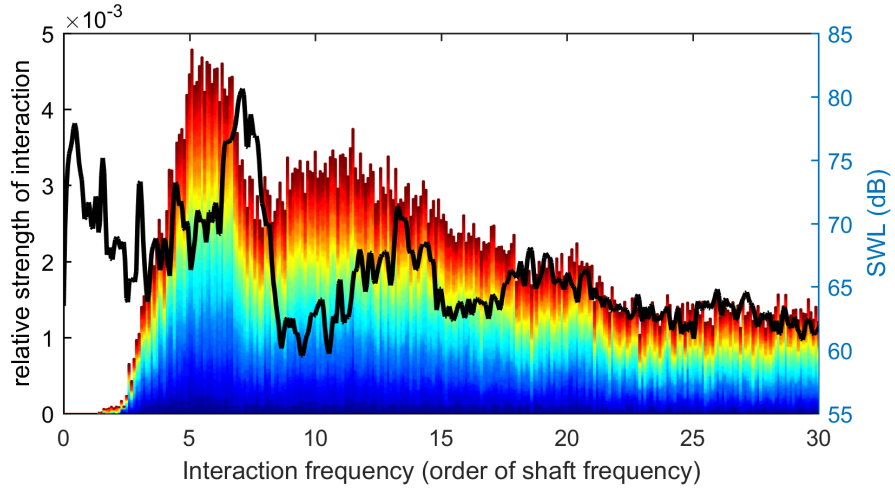

(b)

Figure 7.39 Histogram identifying the interaction frequencies of the detected modes for the H380P fan for the 40-300 Hz range according to (a) Frequency of occurrence (b) Strength of the interactions as weighted by the wavelet thresholding method; the direct CAA acoustic prediction is overlaid. Binning is carried out at 10ths of the rotational frequency of the fan.

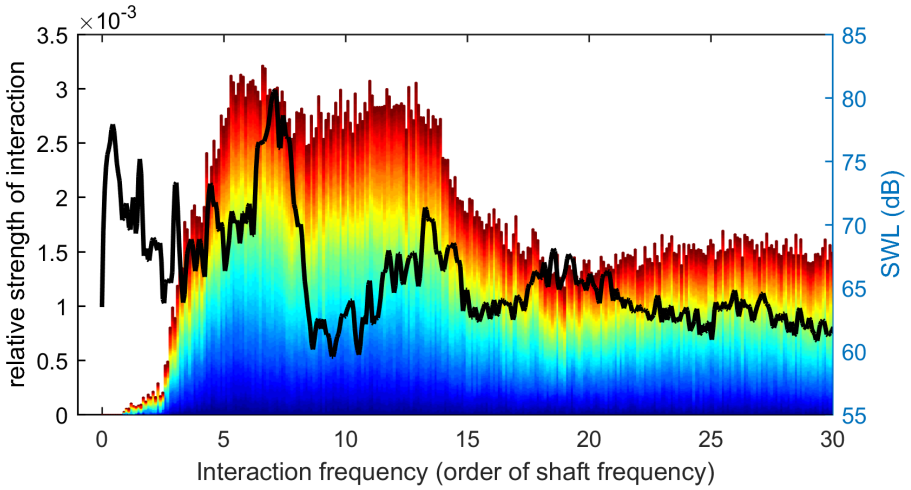

Figure 7.40 Histogram identifying the interaction frequencies of the detected modes in the 40-600 Hz range for the H380P fan according to the strength of the interactions as weighted by the wavelet thresholding method; the direct CAA acoustic prediction is overlaid. Binning is carried out at 10ths of the rotational frequency of the fan.

detected at the various radial and chordwise positions investigated, it was determined that the lower radii (R170-R161), and especially for the leading edge positions (C01-C05) were shown to revolve around a 20% value, as shown in Fig. 7.43(b). The distribution of the modal orders, however, remains very close to the initial analysis from all sensors in the tip region, as seen in Fig. 7.43(a).

This leads to a very different observation when looking at the weighted interaction histogram in Fig. 7.44 for these lower radial positions, as the first two harmonics sub-BPF humps from the LBM spectra are now clearly predicted by the method. This highlights the ability of the method to identify localized phenomena, but also illustrates a pitfall in that the investigator needs to have some idea at to where to direct his analysis in order to obtain significant results.

A similar spatial investigation of the H380D case, however, showed no such improvement as the prediction histogram was always dominated by the presence of strong scattering due to the influence of the installation.

Conclusion on the H380 Case

The success of the application of the correlation analysis method to the Valeo H380 configurations (H380D and H380P) is somewhat mitigated. On the one hand, it highlights the presence of the strong acoustic scattering of the duct configuration (H380D), which it has difficulties discerning from the impact of the actual TLF distortions that occur at

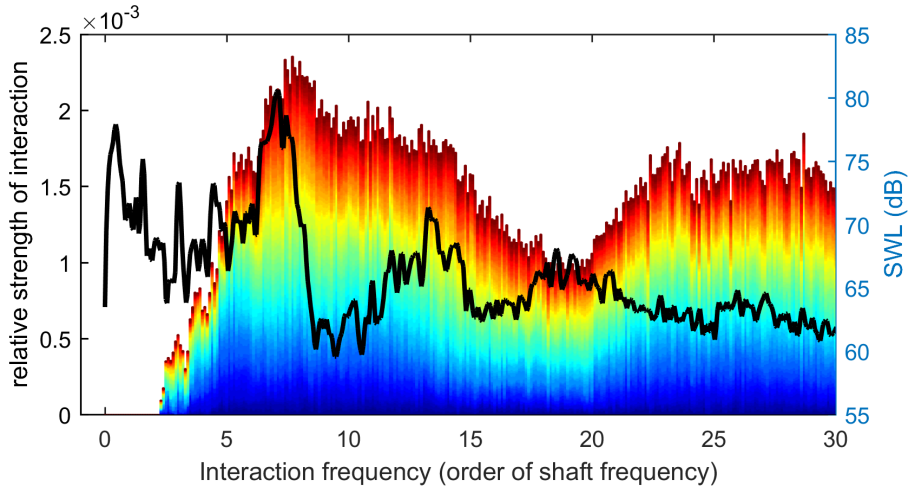

Figure 7.41 Histogram identifying the interaction frequencies of the detected modes in the 40-1000 Hz range for the H380P fan according to the strength of the interactions as weighted by the wavelet thresholding method; the direct CAA acoustic prediction is overlaid. Binning is carried out at 10ths of the rotational frequency of the fan.

similar frequencies, as seen in Sec. 6.3.1. In fact, the scattering of the duct clearly overtakes the source mechanisms (trailing edge and tip leakage flow noise) in this particular configuration, amplifying them to a large degree and leading to the appearance of strong acoustic modes. Using a broad frequency range for the correlation analysis, however, the appearance of the first two sub-BPF harmonics linked to TLF and observed through the FWH analogy in Sec. 6.3.1 is successfully predicted by the method, although weakly so.

It was expected that the application of the correlation analysis to the H380P configuration would allow for the clear identification of the coherent modes responsible for the strong sub-harmonic quasi-tones seen in the acoustic spectra, as the strong acoustic scattering effects from the duct configuration would be absent. However, as it was illustrated, a blanket approach from a spatial point of view (Fig. 7.39) did not allow for the clear prediction of the sub-harmonic humps associated with tip leakage flow effects. However, as a result of spatial filtering of the contributions, the location of the pressure modes responsible for the appearance of these acoustic quasi-tones was shown to be in the 80-90% span (Fig. 7.44) where slower modes rotating at 20% of the fan speed were identified, in close correlation to the results obtained by Magne [Magne, 2015].

The bandpass filtering operation on the flowfield (illustrated in Figs. 7.36(b) and 7.38(b)) for the identification of the coherent modal patterns in the flow also highlighted the fact that their amplitude was much weaker in the H380 configuration when compared to the free-tipped fans from previous sections and that the resulting visualizations are rather

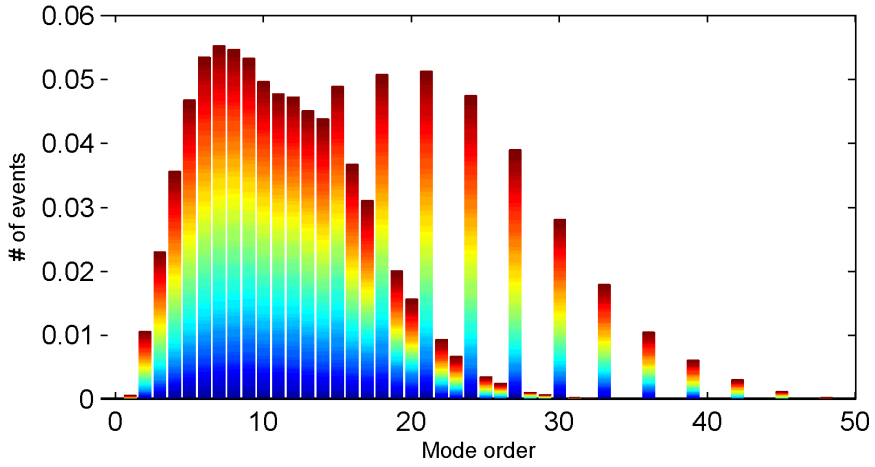

(a)

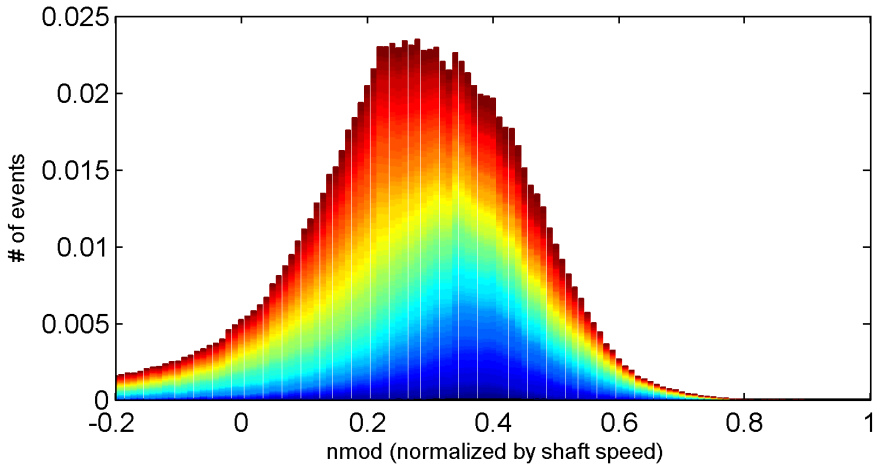

(b)

Figure 7.42 Characteristics of the modes detected through correlations analysis for the H380P configuration in the tip region (R182-161) of the blades for the 40-1000 Hz range (a) Mode orders (b) Mode rotational velocity.

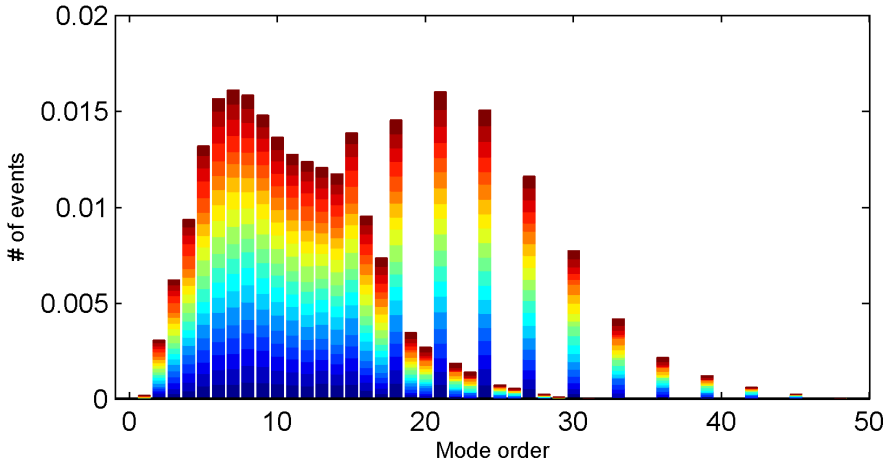

(a)

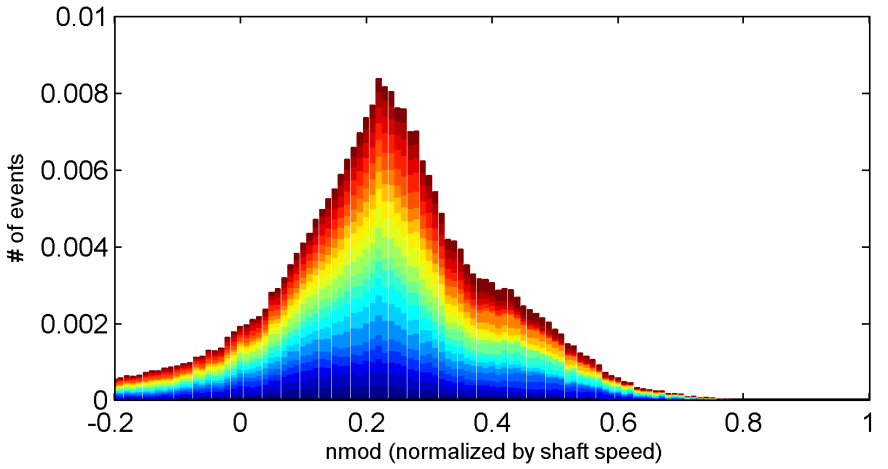

(b)

Figure 7.43 Characteristics of the modes detected through correlations analysis for the H380P configuration in the tip region (R170-161) of the blades for the 40-1000 Hz range at the leading edge (C01-C05) (a) Mode orders (b) Mode rotational velocity.

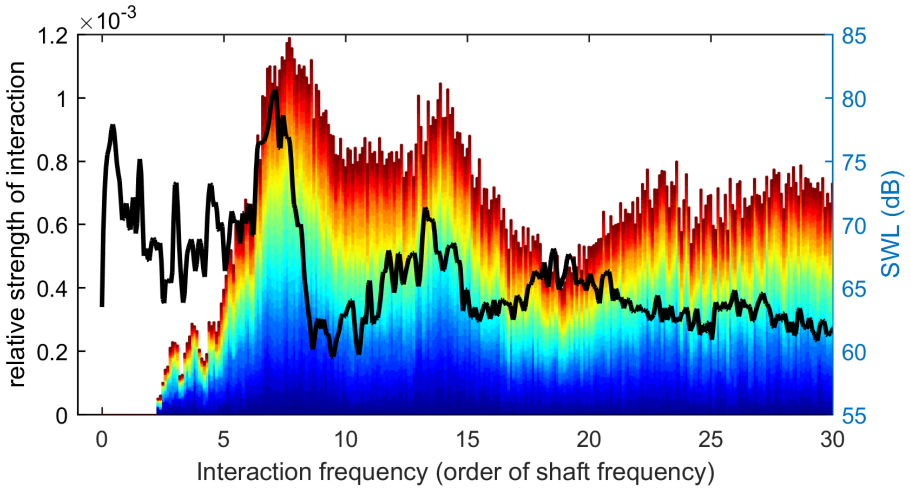

Figure 7.44 Histogram identifying the interaction frequencies of the detected modes for the H380P fan for the 40-1000 Hz range for the R170-161 positions at the leading edge (C01-C05) according to the strength of the interactions as weighted by the wavelet thresholding method; the direct CAA acoustic prediction is overlaid. Binning is carried out at 10ths of the rotational frequency of the fan.

sparse, making the identification of the exact mode orders from the filtered λ_2 vortical field more difficult.

7.5 Conclusion on the Analysis of Narrowband Mechanisms

The current chapter proposed the application of a modal analysis method based on spectral cross-correlation of the near-field aerodynamic pressure present in the passage flow of the studied fan geometries to develop a diagnostic tool able to predict the occurrence of narrowband noise linked to tip clearance flow, which was observed in Chap. 6 for the studied configurations.

The idea behind the method is to try to identify coherent circumferential wave patterns superimposed on the flow, generated as a result of the appearance of periodic flow distortions issued from the TLF. By quantifying these modes in terms of their circumferential order as well as their rotational velocity, the frequency of their interaction with the rotor blades can be calculated and their contribution to the acoustic spectra as a result of the fluctuations in blade loading that they cause can be inferred. An additional step was introduced to the already existing method to try and characterize the strength of the interactions by using a wavelet-based approach based on LIM filtering for the quantification

of the amplitude of the circumferential wave patterns, and provided a way to weigh and compare the fluctuations they can potentially cause on the blades.

The analysis was run in the tip region of the blade passages of each studied configuration for several radii and chordwise positions to provide a wide spatial investigation of the flowfield. In total, four fan geometries were investigated, with three from the free-tipped archetype and one ring-shrouded configuration. From the perspective of the performance of the correlation method towards the prediction of the observed quasi-tonal noise related to tip leakage flow effects on the studied fan configurations in the previous chapter, the method was fairly successful. However, it was highlighted by the H380EC1 ducted configuration as well as the Bosch case that in the presence of strong acoustic scattering effects due to installation, the method will have difficulties discerning the modes generated as a result of aerodynamic distortions and acoustic modes. The specific case of the H380 fan in the plenum configuration also showed that the region of the investigation must either be precisely specified or a large spatial domain must be covered for fear of missing a set of specific pressure modes. The modes are also more blurred in the passage flow in the ring fans due to the fact that the vortical structures issued from the tip gap which are responsible for these modes form ahead of the fan, forming seemingly weaker coherent distortions in the passage flow, whereas in free-tipped fans the strong TLV and other associated features form a strongly coherent vortical field that is responsible for the distortions directly.

From a methodological point of view, a conclusion that can be drawn of the study is that the range of frequencies at which the circumferential modes can be detected can vary from case to case, which was confirmed by the various configurations studied. While it is difficult at this point to enunciate clear guidelines, the appearance of the so-called Rotating Instability spectral signature in the flow can be used to determine an approximate maximum frequency for the analysis; good examples of this are the USI7 and Bosch configurations. However, in the absence of this signature, the investigator has to rely on an analysis of the coherence and phase of the cross-spectra between circumferentially spaced measurement points to identify ranges with higher coherence levels and linear trends in the phase lag. The RCDB fan at OC5 for example, had a rather restricted range of frequencies wherein the phase exhibited a linear trend and in which the method could be applied. A counterexample is represented by both H380 configurations, wherein the phase linear trend criteria was not an issue over a large range of frequencies and required some exploration to try and determine the range required to try and identify the near-field structures responsible for the quasi-tones in the acoustic spectra.

An additional concern, however, is the coherence threshold used for the determination of what constitutes a *coherent* mode; it is also a matter of importance in the analysis and requires a preliminary analysis of the flowfield measurement points to set a suitable value. Elevated coherence levels were observed for the free-tipped fans configurations (≥ 0.6), but the ring-shrouded H380 fan exhibited significantly lowered values($\geq 0.4-0.5$), requiring a lower threshold be used in this particular case; this is related to the previous observation that the modes are blurred into the overall turbulent passage flow for the ring fans.

CHAPTER 8

Summary, Conclusion and Perspectives

The aim of the current study was to provide insight into the flow mechanisms associated with tip clearance flow in turbomachine systems and especially their effect on fan acoustic performance. The relative importance of this secondary flow was made obvious as a result of the literature review of Chap. 2, as it was shown that it can be a source of significant aerodynamic losses (loss of efficiency) as well as a large contributor to the acoustic radiation from a given machine. Its investigation is however made difficult given the complex flowfields encountered in turbomachine applications coupled with the small geometric features and moving parts of a rotor system, and characterization of tip clearance flow is still incomplete and very much an active research field.

This complex phenomenon is also a function of several parameters, both geometric and operational, and thus a comprehensive investigation required that several of these factors be evaluated concurrently, not the least of which is the type of tip clearance configuration. The approach proposed in this study was to evaluate several fan geometries conjointly; a selection of five low-speed axial fans were considered for the investigation of tip leakage flow noise mechanisms, as detailed in Chap. 3. Three of the configurations were from the free-tipped archetype of fans, while the remaining two are ring-shrouded rotors typically used in automotive engine cooling applications.

Given the breadth of the study as well as the complexities and costs involved with an experimental study of tip leakage flow in realistic turbomachine environments, the leveraging of CFD methods was deemed a suitable alternative in order to provide the opportunity to fully investigate the flowfield in the selected fans and the resulting acoustics. A review of CFD methods for Computational Aeroacoustics (CAA) is presented in Chap. 4. For the purpose of obtaining the direct acoustic radiation emanating from the fan in a realistic test environment in a reasonable amount of time, the LBM class of simulation was selected as the investigative tool. This would allow for the identification of direct links between the flowfield and the observed acoustic spectra generated by the fan operation.

The studied configurations were specifically chosen in part due to the availability of an experimental database for validation purposes. The numerical models employed in this thesis as well as the comparison of the numerical results with the available experimental

data are described in Chap. 5. The aerodynamic as well as the aeroacoustic characteristics of the investigated fan systems were evaluated concurrently, but the baseline aerodynamic performance metric for the simulations was the comparison of the numerical and experimental characteristic curves. Overall the simulations performed well on that front, with two notable exceptions:

— The Bosch axial fan simulation was shown to consistently underpredict the experimentally measured pressure rise characteristic for any given flowrate (around 20%), with successive refinements of the simulation resolution showing no improvement; comparison of the time-averaged tangential velocity behind the fan showed that a high velocity near the root of the blades coherent with an open hollow hub was observed in the experiment was not captured in the simulations, where the hub was closed off, and might in part explain the characteristic curve differences observed.
— The H380EC1 fan simulation in the ducted configuration was shown to overpredict the pressure rise for the nominal flowrate case (only operational condition simulated in this work); a sharp drop in fan performance in the experiment was however linked to the failure of one of the stator arms holding up the fan motor in the test rig, resulting in a loss of structural stiffness that adversely affected the performance of the fan.

The radiated acoustics from the fan systems, which are computed directly by the LBM simulations and include the propagative effects of the modeled test environments of each fan, were also compared with corresponding experimental data. Most of the simulations showed good agreement with the experimental acoustics. In the case of the RCDB fan simulation, however, it was found that the massflow outlet boundary condition initially used to set the flowrate through the fan produced artificial acoustic reflections inside the plenum that dominated the spectra and skewed the results; this was resolved through the modification of the outlet flow condition to impose velocity. The sole exception to the norm was the Bosch configuration, as the LBM showed significant differences with the experimental acoustic spectra as a result of the presence of strong acoustic modes in the test duct that were not observed in the experiment. Some of the discrepancy can be explained by the fact that whilst in the simulation solid boundaries are infinitely rigid and provide a perfectly reflective environment, the actual real-life rig is composed of materials with a certain impedance, in effect dampening the modes. It also came in sharp contrast with the H380EC1 ducted configuration simulation, wherein the strong acoustic scattering effects observed in the experiment were accurately reproduced.

Overall, the validation effort carried out in this work provides a rather large numerical database covering several fan configurations in complex environments and it is hoped that it would provide a source of reference for future research.

Following the validation efforts of Chap. 5, Chap. 6 focused on the identification of the noise sources associated with tip clearance flow effects. The first step was to investigate the vortical field surrounding the studied fan rotors using the λ_2 criterion to identify the coherent flow features associated with tip leakage flow for each configuration. The fundamental difference in the formation of tip clearance flow in the free-tipped (cross-flow over the blade tip) and ring-shrouded (return flow through the L-shaped tip clearance) configurations is clearly highlighted. The occurrence of quasi-tonal noise as a result of the interaction of a strong tip leakage flow spanning the flow passage with the fan blades was also highlighted on the studied configurations using an approach based on the Ffowcs Williams and Hawkings (FWH) acoustic analogy and bandpass filtering of the wall-pressure fluctuations on the rotor blades. The use of the FWH analogy was necessary to properly differentiate the contribution of the fan to the overall noise from the installation effects while the wall-pressure fluctuation bandpass filtering operation allowed to identify the noise contribution of the tip clearance flow.

The occurrence of narrowband noise generally occurs as the flowrate is reduced and the TLF trajectory becomes more azimuthal in tube-axial free-tipped fan configurations, as highlighted by the study of the USI7 and RCDB fans where various flowrates were evaluated numerically; the threshold is however wholly dependant on the characteristics of the fan. As the Bosch fan showed, contouring of the shroud can also lead to the forceful interaction of the TLF with the fan blades and adversely affect the efficiency of the machine as well as lead to the appearance of narrowband noise linked to TLF during nominal operation.

Two ring-shrouded axial fans with similar characteristics (Valeo H380EC1 and Mahle-Behr geometry) were studied in three different configurations (i.e. plenum, duct and module), which highlighted that the topology of the resulting tip clearance flow, while due to the same basic mechanism (return flow through the L-shaped tip clearance between the ring and the static shrouds), was largely impacted by installation effects; the proximity of the duct wall and module edges favoritize the appearance of larger, radially-penetrating vortical structures compared to the quick roll-up of the tip leakage backflow into thin vortices around the ring-shroud in the case of a plenum configuration. The occurrence of sub-BPF narrowband noise linked to TLF was however observed in all three configurations during nominal operation. The study of the H380EC1 fan in the plenum and ducted

configurations especially provided a unique opportunity to investigate the impact of the differing tip leakage flow topology between the two cases on the acoustic radiation of the fan. Surprisingly, once the strong acoustic modes present in the duct rig were filtered out by applying the FWH analogy, it was found that the acoustic contribution of the fan was nearly identical between the two configurations, with slight differences in the acoustic power level observed. In essence, this means that the mechanism responsible for the appearance of the narrowband sub-harmonic humps linked to tip clearance flow in the acoustic spectra remains unchanged, although the overall acoustic radiation is strongly influenced by the acoustic modes present in the duct rig.

The parallel investigation of the several studied axial fans exhibiting varied scales, tip configurations as well as varied operating conditions allowed for the identification of quasi-tonal noise components in both free-tipped and ring-shrouded low-speed fan configurations at sub-BPF frequencies linked to the interaction of coherent turbulent structures with the rotating fan blades. It highlights a potential concern for turbomachinery designers as the aim for quieter operation of these systems requires that this mechanism be addressed. However, mitigating the noise from tip clearance flow effects requires a better understanding and quantification of the mechanisms in play. To this effect, the development of a diagnostic tool for the quantification of the distorsion fields responsible for the observed tip clearance associated noise in the studied fans was attempted in this work.

The method, detailed in Chap. 7, is based on cross-correlation analysis and was devised to characterize the coherent distortion field caused by the TLF in the studied fans which is responsible for the appearance of narrowband noise in the acoustic spectra. The method relies on cross-spectral analysis using synchronous measurements from circumferential arrays of probes disseminated in the tip region of the blade passage of each case.

The distortion field is characterized by likening it to a series of azimuthal periodic wave patterns superimposed on the the main flow, possessing a certain modal order and associated rotational velocity which is potentially different from the main rotor speed; they can be characterized using the unwrapped phase lag angle between the correlated azimuthally-spaced signals. In order to properly unwrap the phase angle, however, it is required that it be nearly linear and represents a restriction as to the use of the method. It is however a trend frequently encountered when analyzing strongly correlated signals, and its absence might be indicative of the lack of coherence. The required phase lag linearity also implies that the structures characterized using this method using a given pair of signals will possess a nearly unique group rotational velocity, around which a certain scattering is observed.

The analysis was run in the tip region of the blade passages of the free-tipped RCDB, USI7 and Bosch fan configurations as well as the ring-shrouded H380EC01 (plenum and ducted) configurations. In order to provide a detailed spatial investigation of the flowfield, circumferential arrays of probes were setup in the simulations at several radii and chordwise positions. This allows for a complete statistical description of the frequency of occurrence of modes in the blade passage and identify zones where a larger number of coherent modes are found.

The current study showed that the algorithm allowed for the identification of coherent modes generated by the TLF when the turbulent structures are convected more azimuthally in the blade passage for free-tipped fans, which corresponds to fans usually operating at off-design lower flowrate conditions and to configurations with larger tip clearance gaps (as investigated on the USI7 fan) or with particular clearance configurations (Bosch design). A coherency threshold of 0.6 applied to the the cross-spectral analysis was sufficient for the detection of these modes. These coherent modes can be observed in the flowfield by properly filtering the numerical simulation data λ_2 isosurfaces contours highlighting coherent turbulent structures according to the frequency ranges associated with a given mode order as well as their associated evaluated modal velocities, as shown in Sec. 7.4.

The same analysis for the H380EC01 ring-shrouded configuration highlighted that the rather rich turbulent flowfield present in the blade passage as a result of the different tip clearance flow mechanics also allowed the algorithm to positively identify coherent modes in the blade passages, but a lower coherency thresholding of 0.4 had to be applied. The visualization of the associated modes in the flowfield using λ_2 criteria thresholding suitingly highlighted that very weak pressure modes were identified as a result, with pressure amplitudes more likely to be related to acoustic pressure waves or numerical noise. Further investigation which could not be completed due to time constraints in the course of this study is warranted for this configuration as it is possibly an issue with this fine mechanic of the flow not being properly captured in the simulation. The modes are more than likely blurred in the passage flow in the ring fans due to the fact that the vortical structures issued from the tip gap which are responsible for them form ahead of the fan, forming seemingly weaker coherent distortions in the passage flow, whereas in the free-tipped fan configurations the strong TLV and other associated features form a strongly coherent vortical field that is responsible for the distortions directly.

The interactional frequency of the coherent modes with the rotor blades, causing blade pressure loading and potentially contributing to the farfield acoustic spectra, is also eval-

uated using the designed algorithm. The cross-spectral analysis as utilized, however, does not allow for the evaluation of the strength of the interactions, and the method was coupled with a wavelet-based approach to try and quantify the strength of the distortions caused by the identified modes and evaluate the relative blade loading fluctuations that would be caused on the blades by the different modes.

The performance of the algorithm with regards to the prediction of the quasi-tonal noise observed in the far-field spectra and linked to tip clearance flow effects in Chap. 6 resulting from this interaction is fairly good for the USI7 and Bosch configurations where the cross-spectral analysis frequency range of investigation was closely bounded using the appearance of the RI spectral feature in the near-field aerodynamic spectra in the tip region of the blades.

The algorithm showed more of a mixed result for the RCDB case, with the algorithm loosely predicting the occurrence of some of the far-field acoustic tones but yielding a poor comparison as far as relative level prediction. First, in this case the occurrence of the RI signature was not identified in the near-field spectra in the tip region of the blade passages. However, a strong linearity of the phase angle between adjacent probe pairs associated with elevated coherence levels was found in a restricted frequency band, indicative of a series of coherent structures present in the flow for the lowest investigated flowrate. Several issues with the simulation of this particular configuration may also explain this, namely the small number of fan revolutions covered by the simulation which poses a problem when carrying out the cross-spectral analysis as well as the coarser mesh used in comparison to the other cases due to the numerous difficulties encountered on the setup limiting the accuracy of the physics that are captured. A complementary study is already underway as part of ongoing research.

The appearance of the RI signature could not be observed in the near-field aerodynamic data in the passage flow of the H380EC01 ring-shrouded configurations either. Furthermore, the presence of a linear phase lag angle over a large swath of the frequency range as well as lower overall coherence between adjacent probes in the cross-spectral analysis lead to a blanket investigation with regards to the frequency range analyzed with the algorithm. It highlighted the difficulty in choosing a suitable frequency range of analysis for the application of the cross-spectral method. Furthermore, it was shown in the plenum configuration analysis that the modes responsible for the appearance of the sub-harmonic tones were mostly concentrated near the leading edge of the blades in the 80-90% portion of the span and that the modes had a very specific velocity of around 20% of the blade speed, which was comparable to a prior study by Magne [Magne, 2015].

The analysis of the Bosch fan and H380EC01 ducted setup also highlighted that the presence of strong acoustic scattering effects due to installation can also lead the method to have difficulties discerning modes generated as a result of the aerodynamic distortion field and acoustic modes.

The application of the cross-spectral diagnostic method developed in the course of this work for the characterization of the coherent structures issued from the tip leakage flow in axial fans has shown that it can provide a detailed description of the distortion field generated in the tip region and can provide insight into the source mechanisms responsible for the appearance of quasi-tonal noise as a result of the interaction with the rotor blades. The order as well as the velocity of the modes detected will vary according to the geometry and operating conditions of the fan being analyzed. It is interesting to note that in the course of this study, however, it was found that the predominant modes identified in the free-tipped fan configurations usually amounted to orders corresponding to the presence of 2-3 lobes per blade passage. It was also observed that the tube-axial fan geometries (USI7 and RCDB configurations) had a preferential velocity of 30% of the rotor velocity associated with the detected modes; however, the Bosch design, which has a converging shroud, showed a significantly lowered velocity associated with the detected modes of around 17% of the rotor speed. While the number of cases evaluated in this study is not sufficient to propose a definite model, it is however an interesting trend to note and keep in mind in future work. Given that only one ring-shrouded geometry was analyzed no such proposition can be made at this point for this kind of geometry.

Prediction and control of tip clearance associated noise in turbomachinery applications requires that designers be able to rely on a physical model able to represent the complex interactions of the turbulent tip clearance flowfield with the rotor blades. However, such a model does not exist at present, but the diagnostic tool presented in this work and the modelization of the tip clearance distorsion fields into a series of modal patterns superimposed on the main flow represents a preliminary step towards quantification of these complex processes. In time, it could provide a means to deriving trends and predictive models that could be used to aid in designing quieter air moving systems.

From a methodological standpoint, however, this initial foray has also dredged up some issues which will need to be adressed in the future should this type of analysis become routine. First of all, it was seen that the range of frequencies at which the circumferential modes can be detected can vary from case to case, which was confirmed by the various configurations studied. While it is difficult at this point to enunciate clear guidelines, the appearance of the so-called Rotating Instability (RI) spectral signature in the flow

can be used to determine an approximate maximum frequency for the analysis; good examples of this are the USI7 and Bosch configurations. However, in the absence of this signature, the investigator has to rely on an analysis of the coherence and phase of the cross-spectra between circumferentially spaced measurement points to identify ranges with higher coherence levels and linear trends in the phase lag between the signals, which is a pre-requisite for the analysis to be carried out as it requires a phase unwrapping operation to be carried out.

The algorithm also requires the user to have some foreknowledge of the approximate coherence threshold to be used in the cross-spectral analysis for the identification of the frequencies related to the appearance of coherent structures in the flow. In this study, a detailed preliminary analysis of the time signals extracted from the simulation data of the studied geometries was required to obtain a suitable value for each one. In order to obtain suitable coherence levels from the spectral analysis from a signal processing perspective, which is performed using Welch's periodogram method in this study, it is necessary to have a sufficient amount of physical signal time to be able to employ a minimum of 15 to 30 samples segments with a maximum 50% overlap between them and achieve a frequency resolution of 1-5 Hz in cases where low frequency analysis is required, but it should also allow for the evaluation of tens and possibly hundreds of fan rotations. This requires several seconds of physical time be made available; in the case of the slower RCDB fan for example, the simulation would have needed to reach 30 seconds to have 200 fan rotations like the other configurations.

The methodology will nevertheless have to be refined so that a more rigid framework can be developped. Further investigation of ring-shrouded fan configurations, where the analysis exhibits difficulties sorting through the relevant distorsion modes and the overall turbulence of the passage flow around the ring would be especially mandated, as it was shown that visualization of the detected modes using filtered λ_2 criteria isosurfaces was not sucessfully carried out as with the free-tipped configurations that were studied. The handling of acoustic modes and evanescent pressure fields in particular will have to be improved if the relevant modal distorsions are to be identified. Application to additional types of turbomachines (compressors, turbines) could also be helpful to this end.

The capability of the described method to analyze the spatial distribution of the distorsion modes was also not fully exploited. At a high level, it was for example shown with the USI7 case that relevant modes could be traced to specific radial and chordwise locations and that these modes could be linked to flow occurrences associated with tip leakage vortex breakdown across the blade passage. Another example is the spatial filtering effort that

showed that the modes relevant to the appearance of narrowband sub-harmonic tones in the H380EC01 configuration could be traced to a specific location near the leading edge of the blades at 80-90% of the blade span. However, the method should also able to identify azimuthal locations where preferential distorsion modes are created as a result of a geometrical irregularity along the azimuth for example.

CHAPTER 9

Sommaire, conclusion et perspectives

Le but de l'étude réalisée ici était de tenter d'avancer la connaissance en ce qui a trait aux phénomènes liés à l'écoulement de jeu dans les turbomachines et d'étudier leur impact sur l'acoustique des rotors. L'importance relative de ce type d'écoulement secondaire a été mise en évidence par la revue de littérature du Chapitre 2. Il a en effet été démontré que celui-ci pouvait être une source importante de pertes aérodynamiques (pertes d'efficacité) mais pouvait aussi avoir une large influence sur l'acoustique d'une machine donnée. Le phénomène est cependant difficile à étudier étant donné les écoulements complexes générés dans une turbomachine et le mouvement relatif du rotor; la caractérisation du phénomène de l'écoulement de jeu dans les turbomachines en général est donc encore incomplète et représente un domaine de recherche actif.

L'écoulement de jeu est aussi fonction de plusieurs paramètres à la fois géométriques et opérationnels; une investigation complète doit donc obligatoirement permettre une analyse concurrente de plusieurs de ceux-ci et en particulier la forme du jeu doit être évaluée. L'approche proposé dans la présente étude consistait à évaluer de front plusieurs géométries differentes de ventilateur, avec une sélection finale de cinq machines axiales basse vitesse; ces configurations sont détaillées au Chapitre 3. Trois de ces configurations ont des pales dont l'extrémité est libre, tandis que les deux machines restantes possèdent une virole en bout de pale qui vise fondamentalement modifier la formation de l'écoulement de jeu.

Étant donné l'étendue de la présente étude ainsi que pour éviter les complexités et les coûts associés avec une campagne expérimentale de l'écoulement de jeu dans des configurations réelles de turbomachines, il a été décidé de s'orienter vers une étude numérique de l'écoulement de jeu dans les configurations choisies et permettre une analyse complète de chacune. Une revue de littérature des méthodes de simulation d'écoulements fluides dans le cadre d'une étude acoustique est présentée au Chapitre 4. Dans le but de pouvoir obtenir la propagation directe de l'acoustique des machines sélectionnées dans un environnement réaliste en un temps raisonnable de calcul, un code d'analyse basé sur la méthode Lattice-Boltzmann a été choisi comme outil d'investigation. Cela a permis de tisser des liens entre les observations tirées du champ aérodynamique de l'écoulement et celles obtenues par des analyses de spectre acoustique.

Les configurations axiales considérées dans l'étude ont en partie été choisies à cause de l'existence d'une base de données expérimentale pour la validation des simulations. Les caractéristiques aérodynamiques et aéroacoustiques des système des différentes configurations obtenues des simulations sont donc comparées aux données expérimentales au Chapitre 5. La caractéristique de base pour la comparaison des résultats de simulation est la courbe de performance; dans le cadre de l'étude, les simulations ont fait bonne figure avec deux exceptions notables:

— La simulation du fan Bosch sous-prédit presque systématiquement la hausse de pressione expérimentale d'environ 20%, et l'étude de convergence du maillage n'indique aucune amélioration notable de la prédiction; une comparaison des moyennes temporelles de vitesse tangentielles en aval du rotor montre que le cas expérimental possède une forte composante tangentielle au niveau du moyeu non-captée dans la simulation qui pourrait indiquer que le moyeu moulé aurait pu être laissé ouvert, ce qui n'est pas le cas dans la simulation où celui-ci est complètement bouché
— Dans le cas du H380EC01 dans la configuration en tuyau, la simulation sur-prédit la hausse de pression obtenue lors des tests expérimentaux au débit nominal (le seul simulé); une chute brusque de la performance observée dans l'éxpérience a été expliquée par le bris d'un des bras de stator qui maintiennent le moteur au centre du tuyau, résultant en une perte de résistance structurelle qui a affecté la performance du ventilateur à la baisse

Les signatures acoustiques des systèmes de ventilateurs étudiés, qui sont calculées directement par la méthode Lattice-Boltzmann et incluent les effets de propagation dûs aux environnements de test modélisés dans les simulations, ont aussi été comparées avec les résultats disponibles dans la banque de données expérimentale. Encore une fois, la plupart des simulations performent bien lorsque comparé aux résultats acoustiques expérimentaux. Dans le cas de la configuration RCDB cependant, l'imposition d'une condition limite de débit massique en sortie du domaine de simulation pour réguler le débit à travers la machine produisait des réflexions acoustiques artificielles dans le plénum de sortie qui dominaient le spectre acoustique et faussaient les résultats; en modifiant la condition de sortie et en imposant cette fois une vitesse d'écoulement, cette condition disparaît. Une seconde exception est la configuration Bosch, où la simulation Lattice-Boltzmann montre des différences importantes avec le spectre acoustique à cause de la présence de modes acoustiques dominants générés dans le conduit de test alors qu'ils semblent absent dans l'expérience. Une partie des différences peut être expliquée par le fait que dans la simulation, les parois du conduits sont infiniment solides et reflète les ondes acoustiques parfaitement alors que

la construction réelle est constituée de matériaux ayant une certaine impédance et amortit les ondes réfléchies. Cependant, dans le cas du H380EC01 en conduit, l'amplification acoustique du milieu de test est correctement reproduite par la simulation et contraste fortement avec le cas Bosch.

Sur les traces des efforts de validation du Chapitre 5, le Chapitre 6 visait à détailler le travail d'identification des sources de bruits associées à l'écoulement de jeu sur les configurations étudiées. La première étape se basait l'utilisation du critère λ_2 pour la visualisation du champ vorticiel entourant les ventilateurs pour tenter d'identifier les structures cohérentes associées à l'écoulement de jeu proprement dit. La différence fondamentale dans le mécanisme de formation de l'écoulement de jeu dans les rotors à pales libres et ceux possédant une virole a été mise en évidence. De même, la présence de composantes quasi-tonales dans le spectre acoustique en lien avec la présence d'un écoulement de jeu entrant en interaction avec les pales des différents rotors a pu être démontrée en employant une approche croisée basée sur l'analogie de Ffowcs Williams et Hawkings (FWH) et la visualisation des fluctuations de pression filtrées sur la surface des pales. L'emploi de l'analogie de FWH a été nécessaire pour différencier les effets d'installation du bruit propre des ventilateurs étudiés alors que la visualisation des cartes de fluctuations de pression filtrées a permis d'identifier les fréquences du spectre acoustique liées à l'influence de mécanismes dûs à l'écoulement de jeu.

L'augmentation du bruit large-bande alors que le débit d'opération est diminué et que la trajectoire de l'écoulement de jeu devient plus azimuthale et permet la propagation des structures cohérentes de pale à pale dans les configurations axiales annulaires a pu être observé sur les ventilateurs USI7 et RCDB sur lesquels différents points d'opération ont été simulés; le point critique est cependant variable dépendant des caractéristiques de chaque ventilateur. La configuration particulière du ventilateur Bosch a aussi permis de démontrer qu'une conception incorrecte du carter du ventilateur peut mener à une interaction forcé des structures générées par l'écoulement de jeu avec les pales au point d'opération nominal et mener à l'apparition de bruit tonal.

Le cas des deux ventilateurs axiaux avec virole ayant des caractéristiques similaires (H380EC01 de Valeo et la configuration Mahle-Behr) a permis d'étudier ce type de machine dans trois configurations différentes (i.e. en plenum, tuyau et en installation sur module) et de mettre en évidence que la topologie de l'écoulement de jeu, bien que due au même mécanisme de base (un retour d'écoulement à travers le canal en L entre la virole et le carter) est largement influencée par les effets d'installation. La proximité de conduit sur la configuration H380EC01 en tuyau et la non-uniformité de la surface d'entrée du module pour le ven-

tilateur Mahle-Behr par exemple favorise la formation de structures cohérentes occupant un plus grand volume et affectant un intervalle de rayon plus important comparativement au cas en plenum où elles s'enroulent rapidement en structures minces autour de la virole avant d'être avalés par le rotor. La présence de bruit quasi-tonal à des fréquences sous celle de passage de pale et lié à l'occurrence de ces structures cohérentes issues du jeu a aussi été observée sur les trois géométries.

L'étude du ventilateur H380EC01 en parallèle dans sa configuration plenum et en tuyau a en outre permis d'évaluer l'impact de ces installations très différentes sur la formation de l'écoulement de jeu et la contribution acoustique résultante; surprenamment cependant, une fois les modes acoustiques de la configuration en conduit éliminés par l'analogie de FWH, il a été démontré que le bruit propre du ventilateur était quasi-identique. Cela indique que le mécanisme responsable de l'apparition des tons sous-harmoniques lié à l'écoulement de jeu est largement inchangé, bien que masqué par les effets d'amplification de conduit pour la configuration en tuyau.

L'analyse en parallèle de plusieurs configurations différentes de ventilateurs axiaux possédans des tailles, configuration de jeu et plages d'opération variées a permis l'identification de composantes sonores quasi-tonales dont les fréquences d'occurrence sont sous les fréquences de passage de pale dans les spectres acoustiques à la fois dans les ventilateurs avec et sans virole. Le mécanisme à l'origine de cette signature sonore est l'interaction des pales des ventilateurs avec des structures turbulentes cohérentes générées par l'écoulement de jeu des ventilateurs étudiés. Cette source de bruit pose un défi pour les concepteurs de machines tournantes, requérant que ce phénomène soit adressé si une opération plus silencieuse doit être atteinte. Cependant, la réduction du bruit de jeu passe par une meilleure compréhension et une capacité de quantification des mécanismes. Dans le cadre de cette étude, un outil de diagnostic permettant la quantification du champ de distorsion généré par l'écoulement de jeu et responsable du bruit quasi-tonal associé a été développé.

La méthode, décrite au Chapitre 7, est basée sur l'emploi de la corrélation croisée et vise à caractériser le champ de distorsion causé par l'écoulement de jeu dans les passages de pale des différents ventilateurs étudiés. Ce champ de distorsion est responsable de l'apparition de bruit tonal dans les spectres acoustiques lorsque les structures cohérentes issues du jeu sont convectées de façon à entrer en interaction avec le rotor. La technique se base sur l'emploi de l'analyse spectrale croisée sur des signaux temporels de pression synchronisés mesurés sur des anneaux circonférentiels disséminés autour du jeu dans les passages de pale.

Le champ de distorsion est modélisé comme étant composé d'une succession de fronts d'ondes périodiques superposés sur l'écoulement principal; ces front d'ondes, ou modes, on un certain ordre azimuthal et une vitesse de rotation associée qui peut être potentiellement très différente de la vitesse de rotation du rotor. Les modes peuvent être caractérisés en évaluant l'angle de phase angulaire déroulé entre deux signaux corrélés espacés selon un azimuth donné sur une circonférence. L'obtention de ce signal de phase angulaire déroulé repose cependant sur la présence d'une distibution linéaire de cette phase selon la fréquence et représente une restriction importante de la méthode. Cette tendance linéaire est cependant fréquemment observée sur des signaux fortement corrélés, et son absence est une indication d'un manque de cohérence dans le champ étudié et de l'absence de distorsions organisées dues à l'écoulement de jeu. La présence d'une phase angulaire ayant une tendance linéaire selon la fréquence implique aussi que les structures cohérentes analysées ont une vitesse de phase unique, avec une certaine dispersion aléatoire autour de celle-ci.

L'analyse a été appliquée dans une zone étendue autour des extrémités des pales dans le canal inter-aube des configurations USI7, RCDB, Bosch (pales libres) ainsi que le H380EC01 (ventilateur à virole, en configuration tuyau et plenum). Dans le but de permettre une évaluation méthodique du volume, des peignes circonférentiels de mesures ont été distribués selon la corde et le rayon pour permettre une description statistique complète de l'occurence des modes de distorsions dans le jeu de ces ventilateurs.

L'analyse a permis de démontrer que l'algorithme réussit à identifier des modes de distorsion cohérents générés par l'écoulement de jeu quand les structures turbulentes sont convectées de façon azimuthale dans les configurations à pales libres correspondant à un point d'opération en-dessous du débit nominal, en présence d'un interstice de jeu plus important entre la pale et le carter (tel que confirmé sur le ventilateur USI7) ou lorsque la configuration du jeu favorise l'interaction de structures turbulentes du jeu avec le rotor (configuration Bosch). Un filtre de cohérence de 0.6 employé dans l'analyse de spectre croisé est suffisant pour la détection de ces modes sur les configurations à pales libres. Ils peuvent en outre aussi être identifiés dans l'écoulement en filtrant le champ vorticiel des simulations défini par les isosurfaces du critère λ_2 en se basant sur les fréquences associés à un ordre donné de mode et leur vitesse angulaire, comme démontré à la Section 7.4.

La même analyse pour le ventilateur à virole H380EC01 a aussi permis l'identification de modes cohérents du riche champ turbulent présent sous la virole en tête du passage de pale. Cependant, une valeur seuil de cohérence de 0.4 a du être employée dans ce cas-ci. L'amplitude des fluctuations de pression associées aux modes découverts et visualisées

à l'aide de la technique de filtrage basée sur le critère λ_2 étaient cependant très faibles et plus probablement associées à des ondes acoustiques ou plus probablement du bruit numérique. Une investigation plus poussée de ces résultats n'a pu être complétée dans le cadre de cette étude, mais il est possible que cela indique un problème dans la simulation quant à la capture des détails fins de l'écoulement; un raffinement du maillage pourrait être nécessaire. Quoi qu'il en soit, dans le cadre des simulations réalisées dans cette étude, il apparait que les mode cohérents dûs aux effets de l'écoulement de jeu sont fortement noyés dans le champ turbulent présent dans le passage de pale sous la virole et semblent former des distorsions cohérentes plus faibles, ce qui est probablement redevable au fait que le mécanisme responsable de ces distorsions se situe en amont du ventilateur (structures cohérentes générées par le retour d'écoulement à travers le jeu en L). Dans le cas des machines sans virole, le vortex de jeu et autres structures turbulentes formées dans la zone du jeu forment des modes fortement cohérents en comparaison et des distorsions plus importantes.

L'analyse et la caractérisation des modes de distorsions causés par l'écoulement de jeu avait pour but ultime de pouvoir évaluer leur fréquence d'interaction avec les pales des rotors évalués. Cette interaction amenant des fluctuations de la charge sur les pales, cela peut contribuer une signature acoustique plus élevée, et notamment mener à l'apparition de bruit tonal. La méthode d'analyse spectrale employée ne permet cependant pas l'évaluation de l'amplitude de ces fluctuations de charges, et elle a donc été couplée à une approche basée sur l'emploi d'une analyse par ondelette pour tenter de caractériser l'amplitude des distorsions cohérentes détectées et ainsi permettre l'évaluation de la variation de la charge aérodynamique causée sur les pales des rotors.

Les tons observés dans les spectres acoustique des ventilateurs USI7 et Bosch et liées à l'écoulement de jeu dans le Chapitre 6 sont prédits de manière satisfaisante par l'algorithme ou il a été possible de calquer le domaine fréquentiel de l'analyse sur l'apparition de la signature spectrale associée au phénomène d'instabilité rotative dans les ventilateurs dans le champ aérodynamique.

Une résultat plus mitigé est obtenu dans le cas du ventilateur RCDB, où l'algorithme prédit l'occurence de certains des tons observés dans le spectre acoustique au plus bas débit évalué mais sans réussir à prédire leurs niveaux relatifs de façon satisfaisante. Tout d'abord, il est important de noter que dans le cas de cette configuration, la signature spectrale liée au phénomène d'instabilité rotative n'a pas pu être détectée dans le champ aérodynamique. Cependant, le domaine fréquentiel d'analyse a été déterminé suite à l'observation d'un angle de phase linéaire dans les résultats de spectre croisé associé à

des niveaux de cohérence hauts dans une bande de fréquence restreinte. Plusieurs particularités par rapport à la simulation peuvent aussi explique la contre-performance de l'algorithme, notamment le faible nombre de révolutions physique de rotor couvertes par le temps de simulation, ce qui cause problème lors de l'évaluation du spectre croisé. Un second facteur est le maillage relativement grossier employé pour cette configuration, limitant la précision de la physique pouvant être capturée; un raffinement de maillage n'a pu être réalisé dans le cadre de cette étude à cause des nombreuses difficultés rencontrées lors de l'évaluation de cette configuration. Une étude complémentaire est cependant en cours et poursuit le travail commencé.

L'apparition de la signature spectrale de l'instabilité rotative n'a pas non plus été observée dans le champ aérodynamique du H380EC01 et a compliqué la procédure de sélection du domaine fréquentiel pour l'analyse à cause de la présence d'une tendance linéaire de l'angle de phase sur l'entièreté de la plage fréquentielle analysée et les niveaux de cohérences notamment moins élevés en présence suite à l'analyse spectrale croisée. Ceci illustre une difficulté importante lors de l'application de la méthode d'analyse développée . De plus, l'analyse du can H380EC01 en configuration plenum a illustré que les modes responsable de l'apparition des bosses tonales sous-harmoniques dans le spectre acoustique étaient concentrés dans la première moitiée de la corde à 80-90% de l'envergure de la pale, et que la vitesse de convection associée à ceux-ci tournait autour de 20% de la vitesse de rotation du ventilateur; ceci concorde avec une étude précédente réalisée sur cette configuration par Magne [Magne, 2015]. L'analyse réalisée sur les cas Bosch et H380EC01 en conduit a aussi mis en évidence la présence de puissants modes acoustiques; ceux-ci sont diffiles à départager des modes de distorsions dûs aux effets aérodynamiques à l'aide la méthode.

En somme, l'application de la méthode de spectre croisée proposée dans le cadre de l'étude actuelle pour la caractérisation des structures cohérentes générés par l'écoulement de jeu dans les ventilateurs axiaux a démontré qu'il est possible d'obtenir une description quantitative du champ de distorsion résultant et de prédire l'apparition de bruit quasi-tonal dans le spectre acoustique des ventilateurs étudiés. L'ordre de modes et leur vitesse de convection peut varier selon la géométrie et le point d'opération de la machine considérée. Cependant, il est possible de noter que l'ordre des modes prédominants dans les configurations sans virole correspondait normalement à la présence de 2 à 3 lobes par passage de pale. De plus, dans le cas des configurations annulaires (USI7 et RCDB), les modes détectés avaient une vitesse de convection correspondant à 30% de la vitesse du rotor. La configuration particulière de jeu du cas Bosch semble favoriser l'apparition de modes ayant une vitesse de convection nettement plus lente d'environ 17% celle du rotor. Le nombre de

cas étudiés ici ne permet cependant pas une généralisation mais représente néanmoins une tendance à surveiller. Étant donné qu'une seule configuration avec virole a été analysée ici, aucune tendance claire ne peut être énoncée pour ce type de configuration.

La prédiction et l'éventuel contrôle du bruit de jeu dans les machines tournantes requiert que les concepteurs soient capables de se baser sur un modèle physique capable de représenter les interactions complexes de l'écoulement turbulent issu du jeu avec le rotor. Cependant, aucun modèle satisfaisant n'existe à ce jour, mais l'outil de diagnostique développé dans le projet de recherche actuel représente cependant un premier pas vers une modélisation et une quantification eventuelle de ce processus complexe. aidant à la conception de systèmes plus silencieux.

Du point de vue de la méthodologie d'application de la méthode, cependant, le travail exploratoire réalisé ici a permis d'identifier certains problèmes qui devront être adressés si ce type d'analyse devait devenir routinier. Tout d'abord, le domaine de fréquence sur lequel l'analyse se base pour la détection des modes cohérents peut varier de cas en cas, comme observé sur les configurations étudiées ici. Cependant, il est difficile d'établir des règles claires pour l'établissement de ce domaine, hormis le fait que l'apparition de la signature spectrale liée à l'instabilité rotative dans les turbomachines peut servir de guide pour l'établissement de la fréquence maximale d'analyse comme l'ont démontré les cas USI7 et Bosch. Cependant, en l'absence de celle-ci, l'analyste doit se baser sur une analyse des tendances de la cohérence et de la phase angulaire des signaux étudiés pour tenter d'identifier un domaine probable d'analyse.

L'algorithme requiert aussi une certaine connaissance préalable du niveau seuil de cohérence à utiliser pour obtenir un bon résultat lors de l'analyse spectrale. Dans le cadre l'étude présentée ici, une analyse détaillées des signaux était effectuée au préalable sur chacune des géométries. L'obtention de niveaux de cohérence viable dépend aussi de la longueur des signaux temporels utilisés; d'un point de vue purement technique, si la méthode du périodogramme de Welch est employée pour l'évaluation de la cohérence, un minimum de 15 à 30 fenêtrages avec un chevauchement mitoyen sont nécessaires et une résolution fréquentielle de 1 à 5 Hz est souhaitable lorsqu'une analyse à basse fréquence est nécessaire. De plus, il aussi fortement souhaitable d'avoir des dizaines ou centaines de rotation complètes de rotor et requiert l'obtention de plusieurs secondes de temps physique pour l'analyse; dans le cas du ventilateur RCDB par exemple, l'obtention d'un échantillon temporel correspondant à 200 tours de rotors correspond à 30 secondes de temps physique, ce qui est difficilement réalisable sans ressources importantes en terme de puissance de calcul et de stockage de données.

La méthodologie d'analyse a encore besoin d'être raffinée avant de pouvoir être considérée utilisable dans un environnement industriel. Une analyse plus poussée dans le cas des ventilateurs avec virole, où l'outil a démontré des ratés en ce qui a trait à la différentiation des modes de distorsion et la turbulence dans le passage de pale, est spécialement recommandée. La capacité de la méthode à filtrer les modes acoustiques et les champs évanescents devra aussi être améliorée pour que les modes de distorsion soient correctement identifiés dans les cas où des effets d'installations sont présents. Une application de la méthode à d'autres classes de machines tournantes telles que des systèmes de compresseur et de turbine pourrait aussi s'avérer utile en ce sens.

ANNEX A

Wavelet Transform Theory

The wavelet transform (WT) theory is a relatively new field of research pertaining to the frequency domain analysis of signals. Wavelet transform is, in essence, a generalization of Fourier theory and surmounts some of the shortcomings associated with classical Fourier transforms using sinusoidal functions.

In fact, one of the main 'hurdles' of Fourier theory (FT) is that it extracts the frequency domain representation of a given signal using the entire length of said signal and is thus best suited for stationary processes. In cases where the signal processed in transient in nature, any non-stationary features of the signal are spread into the frequency domain representation and may induce a certain error in the representation of the signal; typically, strong singular features will not be well reproduced when computing the inverse Fourier transform to recover the original signal from its frequency domain components. The recognition of this limitation of Fourier theory has led to the development of the windowed Fourier transform, where the signal to be analyzed is multiplied by a window function which is non-zero over a certain range of the physical space which is slid iteratively over the complete range, and the Fourier transform (WFT) is computed for each increment, allowing for the definition of a time-varying representation in the frequency domain of the signal.

Wavelet theory is a generalization of the Fourier theory in that it uses time-contiguous functions as a basis for the analysis of signals; a parallel can easily be drawn with the windowed Fourier transform , which can be seen as using a sin wave modulated by a window function, which yields a time-contiguous function, as a basis for the frequency decomposition for a given position in the physical domain. However, in the case of the WT, the functional basis of the decomposition is not restricted to the use of modulated sin waves but rather extends to a large (possibly infinite) number of suitable decomposition functions known as 'wavelets'. The convolution of the signal with the selected wavelet function thus leads to a what is best described as a time-frequency representation of the signal, with the frequency components of the signal being represented as a function of time.

The current section aims at presenting the reader with a global overview and working understanding of wavelet theory. Thus, the basic mathematics of the method are first presented. The description of some of the wavelet functions used in literature and their properties along with the basic principles required to construct a suitable wavelet function is also presented. Basic signal processing techniques using wavelets are also covered. Finally, some examples of signal processing applied to the CRFM geometry data are shown.

A.1 Wavelet Theory

The wavelet transform (WT) is, akin to the classical and well-known Fourier transform (FT), a type of frequency analysis aimed at identifying and quantifying the time-variant components present in the signal. However, while the FT uses functions which are localized in frequency but not in time (*sin* and *cos*), making it suitable for the analysis of periodic signals, the idea of the WT is to use time-contiguous functions as a basis to identify the basic components of a signal in both time and frequency, making it more suited to the analysis of transient signals, where the oscillatory components have varying amplitudes and frequencies in the time domain.

The WT of a signal s(t) can be defined mathematically as the convolution of the signal $s(t)$ with a given function $\varphi(\tau)$ known as the mother wavelet function [Iatsenko *et al.*, 2014], as shown in Eq. A.1

$$W_s(a,t) = \int s(\tau)\varphi^* \left(\frac{\tau - t}{a}\right) \frac{d\tau}{a} \tag{A.1}$$

Where $(*)$ denotes complex conjugation and a is the scale of the wavelet. This yields a matrix of coefficients $W_s(a,t)$ describing the transformation applied to the basic wavelet function at time t and scaling a. Note here that here a temporal formulation is referenced, but it could be construed that the wavelet transform could be carried out on a spatial signal [Farge, 1992]. Whatever the case may be, the wavelet transform can be viewed as a series of bandpass filters being applied to the source signal at different 'locations' (time) and with differing 'widths' (scale). In the remainder of this document, emphasis is put on the 1-D temporal formulation for the wavelet transform, as the work presented here is concerned with the analysis of 1D temporal signals.

In the time domain, the scaling parameter a can be linked to an equivalent frequency ω using the central frequency of the wavelet ω_φ used in the decomposition as shown in Eq. A.2

$$a(\omega) = \frac{\omega_\varphi}{\omega} \tag{A.2}$$

With ω_φ the central frequency of the chosen wavelet for the analysis. Reconstruction of a decomposed signal is possible using a proper wavelet function basis, as shown in the Eqs A.3 to A.5

$$s(t) = \langle s(t) \rangle_t + Re(s_a(t)) \tag{A.3}$$

$$s_a(t) = C_\varphi^{-1} \int_0^{\inf} W_s(\omega, t) \frac{d\omega}{\omega} \tag{A.4}$$

$$C_\varphi \equiv \frac{1}{2}\int_0^{\inf} \hat{\varphi}^*(\xi)\frac{d\xi}{\xi} \equiv (\varphi(t)e^{-i\omega_\varphi t}dt)^* \tag{A.5}$$

Where $s(t)$ is the signal, $\langle\rangle_t$ a time-averaged quantity, $s_a(t)$ is the reconstruction of the fluctuating portion of the signal using the inverse WT, $\hat{\varphi}$ denotes the FT of the wavelet function and ξ is the dimensionless frequency. There are several families of proper wavelet functions, but not just any function will provide with a meaningful transformation, as evidenced by the reconstruction equations. By observing Eq. A.4, it becomes apparent that to allow for reconstruction, the coefficient C_φ must be finite. Thus, a wavelet function must meet what is known as the admissibility condition that requires that the FT of the wavelet must vanish at nil frequency (no mean component in the physical space).

A.2 Selection of a Mother Wavelet

As it was mentioned in the previous section, there are numerous families of wavelet functions that could be used to perform a wavelet transform of a given signal. The only condition for a function to be suitable as a mother wavelet, as evidenced by Eq. A.5, is known as the admissibility condition cited in the previous section. The choice of the wavelet for a given analysis, however, is paramount, as the wavelet coefficients are dependent on both the nature of the signal and the nature of the wavelet used in the analysis, as evident from Eq. A.1.

In this section, the aim is to provide the reader with a basic understanding of the large variety of available and potentially undiscovered wavelet functions that could be used in the course of a wavelet transform analysis.

A listing of the wavelet functions treated in literature could not begin with any other wavelet than the well-known Morlet wavelet function [Morlet *et al.*, 1982], whose authors could be construed to be responsible for the base of the modern wavelet theory [Farge, 1992; Liu, 1993]. The Morlet wavelet represents a plane wave with a Gaussian modulation. It is to be added that it is considered marginally admissible, as it does not possess a null average in the time domain; this is remedied by the addition of a correction term to the wavelet function. The equation for the Morlet wavelet is presented in Eqs. A.6 and A.7 in the time and Fourier space [Iatsenko *et al.*, 2014].

$$\varphi(t) = \frac{B_{f_0}}{\sqrt{2\pi}}(e^{i2\pi f_0\eta} - e^{-\frac{(2\pi f_0)^2}{2}})e^{-\frac{\eta^2}{2}} \tag{A.6}$$

$$\hat{\varphi(\xi)} = B_{f_0}e^{-\frac{(\xi-2\pi f_0)^2}{2}}(1 - e^{-2\pi f_0\xi}), \xi > 0 \tag{A.7}$$

Where f_0 is the resolution parameter of the Morlet wavelet and η is the normalized time or location. The second term in Eq. A.6 represents the correction term for the Morlet wavelet in order to make the function admissible. With increasing f_0, the correction term

becomes negligible (a value of 5 or 6 is cited as suitably high [Farge, 1992; Grinsted *et al.*, 2004; Torrence and Compo, 1998].

The Morlet wavelet is very commonly used in literature and thus very well documented; according to [Iatsenko *et al.*, 2014] its popularity is based on the incorrect belief that it maximizes time-frequency resolution, which it does in the linear scale. However, since the WT has a logarithmic frequency resolution [Farge, 1992; Iatsenko *et al.*, 2014], Iatsenko et al. propose instead what is called the Lognormal wavelet as an optimal basis function, which scales with a logarithm of frequency; they show that it generally possesses better resolution properties than the Morlet. The Fourier space equation for the Lognormal wavelet is presented in Eq. A.8.

$$\hat{\varphi(\xi)} = e^{-\frac{(2\pi f_0 log(\xi))^2}{2}}, \xi > 0 \tag{A.8}$$

The Lognormal wavelet is infinitely admissible, in contrast to the Morlet wavelet, and can thus reproduce any time-derivative from the wavelet transform. Several other families of wavelet functions exist, and the reader is directed to [Farge, 1992] for further reference.

A.3 Wavelet Transform – Signal Processing

While the time/frequency representation of a signal through its WT coefficients can sometimes allow for the identification of general trends, the WT is not complete in and of itself, as the amount of information generated is rather important and the 2D image representations it is usually turned into are often biased due to the amplitude differences in the different wavelet scales.

Thus, akin to the FT, additional signal processing must usually be performed to extract useful information from a WT. There are some clear parallels with the Fourier theory, with some particularities in the case of the wavelet theory that must not be overlooked [Liu, 1993].

In real-life applications, the avowed aim of performing frequency decomposition of a signal is often to compare two or more signals and try to extract the differences and resemblance between them. In Fourier theory, one of the basic tools that can be used is cross-spectral density analysis, and it has a parallel in wavelet theory, which is called the cross-wavelet transform, which, aside from being performed in the time-frequency plane instead of just across frequency space, brings us to the same equation form as the one used for FT cross-spectrum calculations. Thus, for two signals $x(t)$ and $y(t)$ with respective WT coefficient matrices W_x and W_y, the cross-wavelet transform (XWT) [Ge, 2008; Grinsted *et al.*, 2004; Liu, 1993; Torrence and Compo, 1998] is defined by Eq. A.10

$$W_{xy} = W_x W_y^* \tag{A.9}$$

It is to be noted that the special case W_{xx} is the wavelet equivalent of the auto-power spectra in the Fourier transform. Furthermore, the phase difference between the two signals can be calculated as usual, as shown in Eq. A.10

$$\gamma_{xy} = \frac{Im(W_{xy})}{Re(W_{xy})} \tag{A.10}$$

Where Re and Im refer to the real and imaginary parts of the XWT. Additionally, the coherence of the XWT can be calculated in a fashion similar to the Fourier equivalent. Just like in the Fourier theory, some measure of smoothing must be applied to the cross spectrum and auto-spectra, lest the coherence obtained be identical to unity for all values. Whilst in FT the only dimension along which smoothing can be applied is the frequency domain, in the case of the wavelet transform there are two dimensions across which smoothing can be performed. Wavelet coherence calculation can be defined as in Eq. A.11 below [Grinsted *et al.*, 2004]

$$WC_{xy}(\omega, t) = \frac{\mid S(a^{-1}W_{xy}) \mid}{\mid S(a^{-1}W_{xx}) \mid\mid S(a^{-1}W_{yy}) \mid} \tag{A.11}$$

Where $S()$ indicates a smoothing operator. The smoothing operation should optimally be done in both scale S_a and time S_t in the time-frequency domain of the wavelet coefficients as in Eq.A.12

$$S(W) = S_a S_t(W) \tag{A.12}$$

This subject has been covered by several authors [Cohen and Walden, 2010; Mehrkanoon *et al.*, 2013; Torrence and Compo, 1998; Torrence and Webster, 1998], with a large emphasis on the use of the Morlet wavelet, which is largely used in the literature due to the amount of research into this particular family of wavelets.

A.4 Special Considerations

What could be considered as basic signal processing techniques using wavelet transforms have been presented in the preceding section. However, while it is probable that any meaningful analysis of a time-varying signal using wavelets will include some form or another of the previously discussed methods, presented here are some special considerations with regards to signal processing using wavelets.

A.4.1 Wavelet Filtering

As a first topic in this special considerations section, the idea of filtering signals through the use of wavelets is presented. Looking at Eqs. A.4 for the reconstruction of a signal from a set of wavelet coefficients, it would be possible to consider only a subset the Fourier

space for the integral in the reconstruction equation ($\int_(\omega_1)^(\omega_2)$), thus eliminating contributions from unwanted frequencies. In practice, given a proper wavelet decomposition was performed, the reconstruction should provide a wavelet-filtered signal, with the response function of the filter given by the sum of the wavelet functions in the selected scales [Farge, 1992; Torrence and Compo, 1998].

One could also consider filtering a signal through the concurrent use of a wavelet transform and some sort of thresholding according to a given criteria; in effect, depending on the thresholding criteria, the filtering could occur simultaneously in locale and scale. The design of a proper thresholding criteria is however a delicate matter. Torrence and Compo [Torrence and Compo, 1998] exemplified 'denoising' of data using wavelet coefficient power as a criterion.

Another criteria could be created from the normalization of the wavelet coefficients $W_s(\omega, t)$ at every frequency by the time-averaged value of the wavelet coefficients for that given frequency, as shown in Eq. A.13.

$$LIM = \frac{\mid W_s(\omega, t) \mid^2}{\langle \mid W_s(\omega, t) \mid^2 \rangle_t} \tag{A.13}$$

This measure, which is based on the local intermittency measure (LIM) proposed by Farge [Farge, 1992] for space scale wavelet decomposition applied to turbulence filtering, was reprised by Grilliat [Grilliat, 2009] for application to time signals, yields values in Re_+; high values in a given time-frequency range indicate an event with a high variance from the time-averaged value of the wavelet coefficients for those frequencies. This criterion can be used to highlight singularities in a given signal.

Farge et al. [Azzalini *et al.*, 2005; Farge *et al.*, 1999; Ruppert-Felsot *et al.*, 2009] also presented a method to try and separate, using space-scale wavelet transforms, the coherent structures in a flowfield, separating it from the turbulent noise, using the wavelet transform of the vorticity field.

A.4.2 Smoothing for Wavelet Coherence Estimation

As was mentioned before, the correct estimation of the wavelet cross-spectrum coherence relies on the use of a smoothing operator, as described in Eq. A.11. In the literature on the subject, there is a heavy reliance on the use of the Morlet wavelet and the associated smoothing operators in both time and scale proposed by Torrence et al. [Torrence and Compo, 1998; Torrence and Webster, 1998]. More recent work on the subject also investigates the use of a time-smoothing only procedure for the Morlet wavelet [Cohen and Walden, 2010]. A more *general* procedure is also shown in [Mehrkanoon *et al.*, 2013], where smoothing operators are chosen differently for both the numerator and denominator of Eq. A.14. Some authors also proposed multi-wavelet methods to provide an implicit estimator of the coherence function [Brittain *et al.*, 2007; Cohen and Walden, 2010; Daubechies, 1988].

However, the choice of the smoothing operator is largely dependant on the wavelet used in the transform procedure, and has a great influence on the precision of the estimator. While in Fourier theory, the use of Welch's periodogram method [Welch, 1967] with varied windows is widely used to provide the coherence estimator, in wavelet theory there isn't a single accepted 'cure-all' method as of yet.

One particular case of the smoothing operator which represents a simplified case consists in taking time-averaged values over a certain period of time T to obtain what is known as the wavelet linear coherence (WLC) as a function of frequency [Ge, 2008]

$$WLC_{xy} = \frac{|\int_T W_{xy})|}{|\int_T W_{xx}||\int_T W_{yy}|} \tag{A.14}$$

The WLC yields, as is expected of typical coherence estimators, a value between 0 and 1, with 0 indicating the lack of a linear relation between the evaluated signals, and high values indicating consistently large values of wavelet power for both signals with an almost perfect phase difference along the time axis. Realistically, this indicator should not be very efficient when analyzing real signals, save for a few very synchronized applications, as the presence of noise in the signals should significantly lower the WLC values at all scales of the WT. High values might however provide indications as to the presence of synchronization between the two signals at a given frequency, possibly reinforcing the validity of observations done through other methods.

LIST OF REFERENCES

Azzalini, A., Farge, M. and Schneider, K. (2005). Nonlinear wavelet thresholding: a recursive method to determine the optimal denoising threshold. *Applied and Computational Harmonic. Analysis*, volume 18, pp. 177–185.

Bailly, C. and Bogey, C. (2004). Contributions of computational aeroacoustics to jet noise research and prediction. *International Journal of Computational Fluid Dynamics*, volume 18, number 6, pp. 481–491.

Barrent, D. (2015). *Controlled Diffusion Blade Axial Fan : Fluid Mechanical Mechanistic Effects on Fan Performance*. Master's thesis, Michigan State University, East Lansing, Michigan, USA, 230 pp.

Baumgartner, M., Kameier, F. and Hourmouziadis, J. (1996). Non-engine order blade vibration in a high pressure compressor. In *2nd AIAA Aeracoustics Conference*. AIAA, State College, Pennsylvania, USA.

Bent, P. H. (1993). *Experiments on the Aerodynamic Generation of Noise in Centrifugal Turbomachinery*. Ph.D. thesis, The Pennsylvania State University, University Park, Pennsylvania, USA.

Bent, P. H., McLaughlin, D. K. and Thompson, D. E. (1993). Identification of Non-Tonal Noise Sources in Centrifugal Turbomachinery. *ASME -PUBLICATIONS- FED*, volume 168, pp. 207–216.

Bhatnagar, P. L., Gross, E. P. and M., K. (1954). A model for collision processes in gases. i. small amplitude processes in charged and neutral one-component systems. *Physical Review E*, volume 94, number 3, pp. 511–525.

Bianchi, S., Corsini, A., Rispoli, F. and Sheard, A. G. (2009). Detection of aerodynamic noise sources in low-speed axial fans with tip end-plates. *Proceedings of the Institution of Mechanical Engineers, Part C: Journal of Mechanical Engineering Science*, volume 223, number 1, pp. 1379–1392.

Bindon, J. P. (1989). Measurement and formation of tip clearance loss. *Journal of Turbomachinery*, volume 111, number 3, pp. 257–263.

Bogey, C., Bailly, C. and Juvé, D. (2002). Computation of flow noise using source terms in linearized euler's equations. *AIAA Journal*, volume 40, number 2, pp. 235–243.

Brentner, K. S. (1986). *Prediction of Helicopter Discrete Frequency noise - A Computer Program Incorporating realistic Blade Motions and Advanced Formulation* (Technical report). NASA, Langley Research Center, Hampton, Virginia.

Brittain, J., Halliday, D. M., Conway, B. A. and Nielsen, J. B. (2007). Single trial multiwavelet coherence in application to neurophysiological time. *IEEE Transactions on Signal Processing*, volume 54, pp. 854–862.

Broadwell, J. (1964). Study of rarefied shear flow by the discrete velocity method. *Journal of Fluid Mechanics*, volume 19, pp. 401–414.

Brès, G., Pérot, F. and Freed, D. (2009). Properties of the lattice Boltzmann method for acoustics. In *15th AIAA Aeracoustics Conference*.

Brès, G., Wessels, M. and Noelthing, S. (2010). Tandem cylinder noise predictions using lattice Boltzmann and Ffowcs Williams-Hawkings methods. In *16th AIAA Aeracoustics Conference*. AIAA, Stockholm, Sweden.

Caro, S. and Moreau, S. (2000). Aeroacoustic modelling of low pressure axial flow fans design. In *6th AIAA/CEAS Aeracoustics Conference*. AIAA, Lahaina, Hawaii, USA.

Carolus, T., Schneider, M. and Reese, H. (2007). Axial flow fan broadband noise and prediction. *Journal of Sound and Vibration*, volume 300, pp. 50–70.

Carolus, T., Zhu, T. and Sturm, M. (2015). A low pressure axial fan for benchmarking prediction methods for aerodynamic performance and sound. *Noise Control Engineering Journal*, volume 63, pp. 537–545.

Casalino, D., Jacob, M. C. and Roger, M. (2003). An advanced time approach for acoustic analogy predictions. *Proceedings of the Royal Society of London, Series A, Mathematical and Physical Sciences*, volume 261, pp. 583–612.

Cawood, A. F. (2012). *Surface Pressure Measurements on a Rotating Controlled-Diffusion Blade*. Master's thesis, Michigan State University, East Lansing, Michigan, United States of America, 167 pp.

Chapman, D. R. (1979). Computational Aerodynamics Development and Outlook. *AIAA Journal*, volume 17, pp. 1293–1313.

Chapman, S. and Cowling, T. G. (1990). *The Mathematical Theory of Non-uniform Gases: An Account of the Kinetic Theory of Viscosity, Thermal Conduction and Diffusion in Gases*, 3rd edition. Cambridge University Press, Cambridge, United Kingdom, 423 pp.

Chen, H., Chen, S. and Matthaeus, W. (1992). Recovery of the navier-stokes equations using a lattice-gas boltzmann method. *Physical Review A*, volume 45, pp. 5339–5342.

Chen, H., Kandasamy, S., Orszag, S., Shock, R., Succi, S. and Yakhot, V. (2003). Extended Boltzmann kinetic equation for turbulent flows. *Science*, volume 301, number 5, pp. 633–636.

Chen, H., Orszag, S., Staroselsky, I. and Succi, S. (2004). Expanded analogy between Boltzmann kinetic theory of fluids and turbulence. *Journal of Fluid Mechanics*, volume 519, pp. 301–314.

Chen, S. and Doolen, G. D. (1998). Lattice Boltzmann method for fluid flows. *Annual Review of Fluid Mechanics*, volume 30, pp. 1815–1820.

Choi, H. and Moin, P. (2012). Grid-Point Requirements for Large-Eddy Simulation: Chapman's Estimates Revisited. *Physics of Fluids*, volume 24.

Christophe, J., Kucukcoskun, K., Lallier-Daniels, D., Sanjosé, M. and Moreau, S. (2016). Experimental Validation of Ducted Low-Speed Cooling Fan Noise Prediction Methods Including Broadband Scattering. In *22nd AIAA/CEAS Conference*.

Chumakov, S., Bose, S. and Ham, F. (2015a). EFFICIENT LARGE EDDY SIMULATION OF A LOW-MACH NUMBER AXIAL FAN. In *Fan 2015 Conference*.

Chumakov, S., Shin, Y. S., Brès, G., Ham, F. and Nichols, J. (2015b). NOISE PREDICTION FROM A LOW-MACH NUMBER AXIAL FAN WITH LES AND BEM. In *Fan 2015 Conference*.

Cohen, E. A. K. and Walden, A. T. (2010). A statistical analysis of Morse wavelet coherence. *IEEE Transactions on Signal Processing*, volume 58, pp. 980–989.

Coleman, G. N. and Sandberg, R. D. (2010). *A Primer on Direct Numerical Simulation of Turbulence - Methods, Procedures and Guidelines* (Technical report). Aerodynamics and Flight mechanics Research Group, School of Engineering Sciences, University of Southhampton, 21 pp.

Colonius, T. and Lele, S. (2004). Computational aeroacoustics : Progress on nonlinear problems of sound generation. *Progress in Aerospace Sciences*, volume 40, pp. 345–416.

Corsini, A. and Rispoli, F. (2004). Using sweep to extend stall-free operational range in axial fan rotors. *Proceedings of the Institution of Mechanical Engineers, Part A: Journal of Power and Energy*, volume 218, number 3, pp. 129–139.

Corsini, A., Rispoli, F. and Sheard, A. G. (2007). Development of improved blade tip endplate concepts for low-noise operation in industrial fans. *Proceedings of the Institution of Mechanical Engineers, Part A: Journal of Power and Energy*, volume 221, number 5, pp. 669–681.

Curle, N. (1955). The influence of solid boundaries upon aerodynamic sound. *Proceedings of the Royal Society A: Mathematical, Physical and Engineering Sciences*, volume 231, number 1187, pp. 505–510.

Daubechies, I. (1988). Orthonormal Bases of Compactly Supported Wavelets. *Communications on Pure and Applied Mathematics*, volume 41, pp. 909–996.

Davoudi, B. (2014). *Aeroacoustic and Wake Measurements on a Rotating Controlled Diffusion Blade*. Master's thesis, Michigan State University, East Lansing, Michigan, USA, 120 pp.

Davoudi, B., Morris, S. and Foss, J. (2016a). Aeroacoustic measurements for an axial fan in a non-anechoic environment. *Journal of Measurement Science and Technology*, volume 27, number 4, pp. 3918–3927.

Davoudi, B., Morris, S. and Foss, J. (2016b). Self-noise and wake velocity of an axial fan for different operating conditions. *AIAA Journal*, volume 54, number 12, pp. 3918–3927.

de la Riva, D. H. (2001). *Turbulence Interaction in a Highly Staggered Cascade-Propulsor Configuration.* Master's thesis, Virginia Polytechnic Institute and State University, Blacksburg, Virginia, United States of America, 99 pp.

Ewert, R. and Schroeder, W. (2003). Acoustic perturbation equations based on flow decomposition via source filtering. *Journal of Computational Physics*, volume 188, pp. 365–398.

Farassat, F. (2007). *Derivation of Formulations 1 and 1A of Farassat* (Technical report). NASA, Langley Research Center, Hampton, Virginia.

Farassat, F. and Succi, G. P. (1980). A review of propeller discrete frequency noise prediction technology with emphasis on two current methods for time domain calculations. *Journal of Sound and Vibrations*, volume 71, pp. 399–419.

Farge, M. (1992). Wavelet Transforms and their Applications to Turbulence. *Annual Review of Fluid Mechanics*, volume 24, pp. 3395–457.

Farge, M., Kevlahan, N. K. R., Perrier, V. and Schneider, K. (1999). Turbulence analysis, modelling and computing using wavelets. *Wavelets in Physics*, volume 24, pp. 117–200.

Ffowcs Williams, J. E. and Hawkings, D. L. (1968). Sound generation by turbulence and surfaces in arbitrary motion. *Philosophical Transactions of the Royal Society of London. Series A, Mathematical and Physical Sciences*, volume 264, pp. 321–342.

Foss, J., Neal, D., Henner, M. and Moreau, S. (2001). Evaluating cfd models of axial fans by comparisons with phase-averaged experimental data. In *Vehicle Thermal Management System 5.*

Frisch, U., Hasslacher, B. and Pomeau, Y. (1986). Lattice-gas automata for the navier-stokes equation. *Physical Review Letters*, volume 56, number 14, pp. 1505–1508.

Fukano, T. and Jang, C.-M. (2004). Tip clearance noise of axial flow fans operating at design and off-design condition. *Journal of Sound and Vibration*, volume 275, number 3, pp. 1027–1050.

Fukano, T., Takamatsu, Y. and Kodama, Y. (1986). The effects of tip clearance on the noise of low pressure axial and mixed flow fans. *Journal of Sound and Vibration*, volume 105, number 2, pp. 291–308.

Ge, Z. (2008). Significance Tests for the Wavelet Cross Spectrum and Wavelet Linear Coherence. Annual Geophysics. *Annals of Geophysics*, volume 26, pp. 3819–3829.

Gourdain, N. (2013). Validation of large-eddy simulation for the prediction of compressible flow in an axial compressor stage. In *Turbo Expo 2013.* ASME, San Antonio, Texas, United States of America.

Grilliat, J. (2009). *Contribution à l'étude acoustique des écoulements de jeu.* Ph.D. thesis, École Centrale de Lyon, Lyon, France, 199 pp.

Grilliat, J. and Camussi, R. (2010). Back-ground noise decontamination of experimental turbulent time signals using wavelet transforms. In *16th AIAA Aeracoustics Conference.* AIAA, Stockholm, Sweden.

Grilliat, J., jacob, M. C., Camussi, R. and Caputi Gennaro, G. (2010). Aeroacoustic investigation of a single airfoil tip leakage flow. *International Journal of Aeroacoustics*, volume 9, number 3, pp. 253–272.

Grinsted, A., Moore, J. C. and Jevrejeva, S. (2004). Application of the Cross Wavelet Transform and Wavelet Coherence to Geophysical Time Series. *Nonlinear Processes in Geophysics*, volume 11, pp. 561–566.

Groth, C. P. T. (2010). Aer1310 turbulence modelling. University of Toronto, Institute of Aerospace Studies (UTIAS).

Guo, Z., Zhen, C. and Shi, B. (2002). Theory of the lattice Boltzmann equation: From the Boltzmann equation to the lattice Boltzmann equation. *Physical Review E*, volume 65, number 4, pp. 6308–6313.

Hamakawa, H., Shiotsuki, M., Adachi, T. and Kurihara, E. (2012). Correlation between aerodynamic noise and velocity fluctuation of tip leakage flow of axial flow fan. *Open Journal of Fluid Dynamics*, volume 2, number 4, pp. 228–234.

He, X. and Luo, L.-S. (1997). Theory of the lattice Boltzmann equation: From the Boltzmann equation to the lattice Boltzmann equation. *Physical Review E*, volume 56, number 6, pp. 6811–6817.

Hunter, I. H. and Cumpsty, N. A. (1982). Casing wall boundary layer development through an isolated compressor rotor. *Journal of Turbomachinery*, volume 104, number 3, pp. 805–818.

Iatsenko, D., McClintock, P. V. E. and Stefanovska, A. (2014). Linear and synchrosqueezed time–frequency representations revisited: Overview, standards of use, resolution, reconstruction, concentration, and algorithms. *Digital Processing*, volume 42, pp. 1–26.

Inoue, M. and Kuroumaru, M. (1989). Structure of tip clearance flow in an isolated axial compressor rotor. *Journal of Turbomachinery*, volume 111, number 3, pp. 250–256.

Inoue, M., Kuroumaru, M. and Fukuhara, M. (1986). Behavior of tip leakage flow behind axial compressor rotor. *Journal of Engineering for Gas Turbine and Power*, volume 108, number 1, pp. 7–14.

Jang, C.-M., Fukano, T. and Furukawa, M. (2003). Effects of the tip clearance on vortical flow and its relation to noise in an axial flow fan. *Japan Society of Mechanical Engineering International Journal*, volume 46, number 3, pp. 356–365.

Jeong, J. and Hussain, F. (1995). On the Identification of a Vortex. *Journal of Fluid Mechanics*, volume 285, pp. 69–94.

Kameier, F. (1993). *Experimentelle Untersuchung zur Entstehung und Minderung des Blattspitzen-Wirbellarms axialer Stromungsmaschinen*. Ph.D. thesis, Technical University Berlin, Berlin, Germany.

Kameier, F. and Neise, W. (1997a). Experimental study of tip clearance losses and noise in axial turbomachines and their reduction. *Journal of Turbomachinery*, volume 119, number 3, pp. 460–471.

Kameier, F. and Neise, W. (1997b). Rotating blade flow instability as a source of noise in axial turbomachines. *Journal of Sound and Vibration*, volume 203, number 5, pp. 833–853.

Kang, S. and Hirsch, C. (1993). Experimental study on the three-dimensional flow within a compressor cascade with tip clearance: Part i-velocity and pressure fields and part ii—the tip leakage vortex. *Journal of Turbomachinery*, volume 115, number 3, pp. 435–450.

Kang, S. and Hirsch, C. (1994). Tip leakage flow in linear compressor cascade. *Journal of Turbomachinery*, volume 116, number 4, pp. 657–664.

Kirkup, S. (2007). The boundary element method in acoustics. *Journal of Computational Acoustics*.

Lakshminaraya, B., Zaccaria, M. and Marathe, B. (1995). The structure of tip clearance flow in compressors. *Journal of Turbomachinery*, volume 117, number 3, pp. 336–347.

Lallier-Daniels, D., Piellard, M., Coutty, B. and Moreau, S. (2015). Aeroacoustic study of an axial engine cooling module using lattice-Boltzmann simulations and the Ffowcs Williams and Hawkings' analogy. *European Journal of Mechanics B*, volume 61, pp. 244–254.

Lee, G. H., Baek, J. H. and Myung, H. J. (2003). Structure of tip leakage flow in a forward-swept axial-flow fan. *Journal of Flow, Turbulence and Combustion*, volume 70, number 1, pp. 241–265.

Li, Y., Shock, R., Zhang, R. and Chen, H. (2004). Numerical study of flow past an impulsively started cylinder by the lattice-Boltzmann method. *Journal of Fluid Mechanics*, volume 519, pp. 273–300.

Lighthill, M. J. (1952). On sound generated aerodynamically. i. general theory. *Proceedings of the Royal Society A: Mathematical, Physical and Engineering Sciences*, volume 211, number 1107, pp. 564–587.

Lighthill, M. J. (1954). On sound generated aerodynamically. i. general theory. *Proceedings of the Royal Society A: Mathematical, Physical and Engineering Sciences*, volume 222, number 1148.

Liu, J. M., Holste, F. and Neise, W. (1996). On the azimuthal mode structure of rotating blade flow instabilities in axial turbomachines. In *2nd AIAA Aeracoustics Conference*. AIAA, State College, Pennsylvania, USA.

Liu, P. C. (1993). Wavelet Spectrum Analysis and Ocean Wind Waves. *Wavelet Analysis and Its Applications*, volume 4.

Longhouse, R. E. (1976). Noise mechanism separation and design considerations for low tip-speed, axial-flow fans. *Journal of Sound and Vibration*, volume 45, number 4, pp. 461–474.

Longhouse, R. E. (1977). Vortex shedding noise of low-speed, axial-flow fans. *Journal of Sound and Vibration*, volume 53, number 1, pp. 25–46.

Longhouse, R. E. (1978). Control of tip-vortex noise of axial flow fans by rotating shrouds. *Journal of Sound and Vibration*, volume 58, number 2, pp. 201–214.

Lyrintzis, A. (1994). Review: The use of kirchhoff's method in computational aeroacoustics. *ASME Journal of Fluids Engineering*, volume 116, number 4, pp. 665–676.

Lyrintzis, A. (2002). Surface integral methods in computational aeroacoustics - from the (cfd) near-field to the (acoustic) far-field. CEAS Workshop From CFD to CAA, Athens, Greece.

Ma, R. (2003). *Unsteady Turbulence Interaction in a Tip Leakage Flow Downstream of a Simulated Axial Compressor Rotor*. Ph.D. thesis, Virginia Polytechnic Institute and State University, Blacksburg, Virginia, United States of America, 257 pp.

Maaloum, A., Kouidri, S., Bakir, F. and Rey, R. (2003). Effect of inlet duct contour and lack thereof on the noise generated of an axial flow fan. *Applied Acoustics*, volume 64, pp. 999–1010.

Magne, S. (2015). *Numerical Investigation of Tonal Noise Control of Low-Speed Fans with Flow Obstruction*. Ph.D. thesis, Université de Sherbrooke, Sherbrooke, Quebec, Canada, 158 pp.

Magne, S., Moreau, S. and Berry, A. (2015). Subharmonic tonal noise from backflow vortices radiated by a low-speed ring fan in uniform inlet flow. *Journal of the Acoustical Society of America*, volume 137, pp. 228–237.

Magne, S., Sanjosé, M., Moreau, S. and Berry, A. (2014). Numerical Optimization of Fan Tonal Noise Control using Acoustic Modulation of Slowly-Rotating Obstructions. In *20th AIAA Aeracoustics Conference*. AIAA, Atlanta, Georgia, USA.

Mailach, R., Lehmann, I. and Vogeler, K. (2001). Rotating Instabilities in an Axial Compressor Originating From the Fluctuating Blade Tip Vortex. *Journal of Turbomachinery*, volume 123, pp. 453–463.

Mann, A., Kim, M.-S., Wu, J., Pérot, F., Grilliat, J., Jacob, M. C. and Colman, M. (2016). Airfoil tip leakage aeroacoustics predictions using a lattice Boltzmann method. In *22nd AIAA/CEAS Conference*.

Marburg, S. and Nolte, B. (2008). *Computational Acoustics of Noise Propagation in Fluids – Finite and Boundary Element Methods*. Springer, Berlin, Germany, 584 pp.

Marcinowski, H. (1953). Einfluss des laufradspalts und der luftfuehrung bei einem kuehlgeblaese axialer bauart. *Motortech Z.*, volume 14, number 9, pp. 259–262.

Marié, S. (2008). *Étude de la méthode Boltzmann sur Réseau pour les simulations en aéroacoustique*. Ph.D. thesis, Université Pierre et Marie Curie, Paris, France, 132 pp.

Marié, S., Ricot, D. and Sagaut, P. (2009). Comparison between lattice Boltzmann method and Navier-Stokes high order schemes for computational aeroacoustics. *Journal of Computational Physics*, volume 228, pp. 1056–1070.

Marsan, A., Lallier-Daniels, D., Sanjosé, M., Mann, A. and Moreau, S. (2018). Tip Leakage Flow and its Implication on the Acoustic Signature of a Low-Speed Fan. In *Fan 2018 Conference*.

Marz, J., Hah, C. and Neise, W. (2002). An Experimental and Numerical Investigation Into the Mechanisms of Rotating Instability. *Journal of Turbomachinery*, volume 124, pp. 367–375.

Mehrkanoon, S., Breakspear, M., Daffertshofer, A. and Boonstra, T. W. (2013). Non-identical smoothing operators for estimating time-frequency interdependence in electrophysiological recordings. *EURASIP Journal on Advances in Signal Processing*, volume 73.

Mei, R., Shyy, W., Yu, D. and Luo, L.-S. (2000). Lattice Boltzmann method for 3-d flows with curved boundary. *Journal of Computational Physics*, volume 161, number 2, pp. 690–699.

Mongeau, L., Thompson, D. E. and McLaughlin, D. K. (1993). Sound Generation by Rotating Stall in Centrifugal Turbomachines. *Journal of Sound and Vibration*, volume 163, pp. 1–30.

Moreau, S. (2011). Gmc 729 - cours aéroacoustique. Université de Sherbrooke.

Moreau, S. and Bakir, F. (2003). Detailed Study of an Efficient Small Diameter Automotive Engine Cooling Fan System. In *4th ASME-JSME Joint Fluids Engineering Conference*. ASME, Honolulu, Hawaii, USA.

Moreau, S. and Bakir, F. (2004). Aeroacoustic Characteristics of Efficient Automotive Engine Cooling Fan Systems. In *2004 ASME Heat Transfer/Fluids Engineering Summer Conference*. ASME, Charlotte, North Carolina, USA.

Moreau, S., Foss, J. and Morris, S. (2016). A numerical and experimental test-bed for low-speed fans. *Proceedings of the Institution of Mechanical Engineers, Part A: Journal of Power and Energy*, volume 230, number 5, pp. 456–466.

Moreau, S., Magne, S., Sanjosé, M. and Henner, M. (2011a). Unsteady turbulent simulations of low-speed axial fans. In *46th Symposium of Applied Aerodynamics*. 3AF, Orléans, France.

Moreau, S., Marck, O. and Roger, M. (2008). Aeroacoustic Installation Effects in Cooling Fan Systems Part 2: Near-Field and Ground Effects. In *ISROMAC 12*.

Moreau, S. and Roger, M. (2005). Effect of airfoil aerodynamic loading on trailing-edge noise sources. *AIAA Journal*, volume 43, number 1, pp. 41–52.

Moreau, S. and Roger, M. (2007). Competing broadband noise mechanisms in low-speed axial fans. *AIAA Journal*, volume 45, number 1, pp. 48–57.

Moreau, S., Sanjosé, M., Magne, S. and Henner, M. (2011b). Unsteady turbulent simulations of low-speed axial fans. In *46th Symposium of Applied Aerodynamics (3AF)*. 3AF, Orléans, France.

Moreau, S. and Sanjose, M. (2016). Sub-Harmonic Broadband Humps and Tip Noise in Low-Speed Ring Fans. *The Journal of Acoustical Society of America*, volume 139, pp. 118–127.

Morlet, J., Arens, G., I., F. and Giard, D. (1982). Wave Propagation and Sampling Theory. *Geophysics*, volume 47, pp. 203–236.

Munz, C.-D., Dumbser, M. and Roller, S. (2007). Linearized acoustic perturbation equations for low mach number flow with variable density and temperature. *Journal of Computational Physics*, volume 224, pp. 352–364.

Muthanna, C. (1998). *Flowfield Downstream of a Compressor Cascade with Tip Leakage*. Master's thesis, Virginia Polytechnic Institute and State University, Blacksburg, Virginia, United States of America, 115 pp.

Muthanna, C. (2002). *The Effects of Free Stream Turbulence on the Flow Field through a Compressor Cascade*. Ph.D. thesis, Virginia Polytechnic Institute and State University, Blacksburg, Virginia, United States of America, 218 pp.

Najafi-Yazdi, A., Mongeau, L. and Brès, G. (2010). An acoustic analogy formulation for arbitrary source motions in uniformly moving media. *Proceedings of the Royal Society of London, Series A, Mathematical and Physical Sciences*, volume 467, pp. 144–165.

Neal, D. (2010). *The Effects of Rotation of the Flow Field over a Controlled-Diffusion Airfoil*. Ph.D. thesis, Michigan State University, East Lansing, Michigan, United States of America, 183 pp.

Pardowitz, B., Moreau, A., Tapken, U. and Enghardt, L. (2015a). Experimental identification of rotating instability of an axial fan with shrouded rotor. *Proceedings of the Institution of Mechanical Engineers, Part A: Journal of Power and Energy*, volume 229, pp. 520–528.

Pardowitz, B., Peter, J., Tapken, U., Thamsen, P. U. and Enghardt, L. (2015b). Visualization of secondary flow structures caused by rotating instability: Synchronized stereo high-speed piv and unsteady pressure measurements. In *45th AIAA Fluid Dynamics Conference*. AIAA, Dallas, Texas, USA.

Pardowitz, B., Tapken, U. and Enghardt, L. (2012). Time-resolved rotating instability waves in an annular cascade. In *18th AIAA Aeracoustics Conference*. AIAA, Colorado Springs, Colorado, USA.

Piellard, M., Coutty, B., Le Goff, V., Pérot, F. and Vidal, V. (2013). Direct aeroacoustics simulation of automotive engine cooling fan system: an application study. In *Fan 2015 Conference*.

Piellard, M., Coutty, B., LeGoff, V., Vidal, V. and Pérot, F. (2014). Direct aeroacoustics simulation of automotive engine cooling fan system: effect of upstream geometry on broadband noise. In *20th AIAA Aeracoustics Conference*. AIAA, Atlanta, Georgia, USA.

Pogorelov, A., Meinke, M. and Schroder, W. (2015). Cut-Cell Method Based Large-Eddy Simulation of Tip-Leakage Flow. *Physics of Fluid*, volume 27.

Pogorelov, A., Meinke, M. and Schroder, W. (2016). Cut-Cell Method Based Large-Eddy Simulation of Tip-Leakage Flow. *International Journal of Heat and Fluid Flow*, volume 61, pp. 466–481.

Pope, S. B. (2000). *Turbulent Flows*. Cambridge University Press, Cambridge, United Kingdom, 802 pp.

Pérot, F., Kim, M.-S., Moreau, S., Henner, M. and Neal, D. (2010a). Direct aeroacoustics prediction of a low speed axial fan. In *16th AIAA Aeracoustics Conference*. AIAA, Stockholm, Sweden.

Pérot, F., Moreau, S., Kim, M.-S. and Neal, D. (2010b). Investigation of the flow generated by an axial 3-blade fan. In *13th ISROMAC Conference*.

Qian, Y.-H., D'Humières, D. and Lallemand, P. (1992). Lattice bgk models for Navier-Stokes equation. *Physical Review E*, volume 61, number 3, pp. 401–414.

Quinlan, D. A. and Bent, P. H. (1998). High frequency noise generation in small axial flow fans. *Journal of Sound and Vibration*, volume 218, number 2, pp. 177–204.

Rains, D. A. (1954). *Tip Clearance Flows in Axial Compressors and Pumps*. Ph.D. thesis, California Institute of Technology, Pasadena, California, United States of America, 98 pp.

Rogallo, R. S. and Moin, P. (1984). Numerical simulation of fluid flows. *Annual Review of Fluid Mechanics*, volume 16, pp. 99–137.

Roger, M. (2009). Cours d'aéroacoustique. École Centrale de Lyon.

Roger, M. and Moreau, S. (2008). Aeroacoustic Installation Effects in Cooling Fan Systems Part 1: Scattering by Surrounding Surfaces. In *ISROMAC 12*.

Rozenberg, Y. (2007). *Modélisation analytique du bruit aérodynamique à large bande des machines tournantes : utilisation de calculs moyennés de mécanique des fluides*. Ph.D. thesis, École Centrale de Lyon, Lyon, France, 174 pp.

Ruden, P. (1944). *Investigation of Single Stage Axial Fans* (Technical report). National Advisory Committee for Aeronautics, 117 pp.

Ruppert-Felsot, J., Farge, M. and Petitjeans, P. (2009). Wavelet tools to study intermittency: application to vortex bursting. *Journal of Fluid Mechanics*, volume 636, pp. 427–453.

Ryan, F. J. and Ohashi, H. (1955). *Effect of Tip Clearance on the Performance of an Axial Fan* (Technical report). Gas Turbine laboratory, Massachussets Institute of Technology, 33 pp.

Sampath, K., Uppaluri, S. K., Katz, J., Shin, Y. S. and Sortor, M. (2015). PHASE LOCKED PIV MEASUREMENTS IN WAKE OF AN AUTOMOTIVE FAN MODEL. In *Fan 2015 Conference*.

Seo, J. and Moon, Y. J. (2006). Linearized perturbed compressible equations for low mach number aeroacoustics. *Journal of Computational Physics*, volume 218, pp. 702–719.

Shimada, K., Kimura, K. and Watanabe, H. (2003). Computational aerodynamic study of automotive cooling fan in blocked condition. *JSAE Review*, volume 24, pp. 431–439.

Soulat, L. (2010). *Définition, analyse et optimisation aérodynamique d'un nouveau concept de traitement de carter au moyen d'outils numériques. application aux turbomachines basse vitesse*. Ph.D. thesis, École Centrale de Lyon, Lyon, France, 356 pp.

Sturm, M. and Carolus, T. (2012). Tonal Fan Noise of An Isolated Axial Fan Rotor Due to Inhomogeneous Coherent Structures at The Intake. *Noise Control Engineering Journal*, volume 60, pp. 699–706.

Sturm, M., Sanjosé, M., Moreau, S. and Carolus, T. (2013). Aeroacoustic Simulation of an Axial Fan Including the Full Test Rig by Using the Lattice-Boltzmann Method. In *Aachen Acoustic Colloquium 2013*.

Taghavi-Zenouz, R. and Eslami, S. (2011). Numerical simulation of unsteady tip clearance flow in an isolated axial compressor rotor blades row. *Proceedings of the Institution of Mechanical Engineers, Part C: Journal of Mechanical Engineering Science*, volume 226, number 1, pp. 82–93.

Tang, G. (2004). *Measurements of the Tip-gap Turbulent Flow Structure in a Low-speed Compressor Cascade*. Ph.D. thesis, Virginia Polytechnic Institute and State University, Blacksburg, Virginia, United States of America, 360 pp.

Tennekes, H. and Lumley, J. L. (1972). *A First Course in Turbulence*. MIT Press, Cambridge, Massachusets, United States of America, 300 pp.

Tetu, L. G. (1993). *Experiments on the Aeroacoustics of Centrifugal Turbomachinery*. Master's thesis, The Pennsylvania State University, University Park, Pennsylvania, USA.

Torrence, C. and Compo, G. P. (1998). A Practical Guide to Wavelet Analysis. *Bulletin of the American Meterological Society*, volume 79.

Torrence, C. and Webster, P. J. (1998). A Practical Guide to Wavelet Analysis. *Quarterly Journal of the Royal Meteorological Society*, volume 125, pp. 1985–2004.

Volpe, G. (1993). Performance of Compressible Flow Codes at Low Mach Numbers. *AIAA Journal*, volume 31, pp. 49–56.

Wadia, A. R., Szucs, P. N. and Crall, D. W. (1998). Inner workings of aerodynamic sweep. *Journal of Turbomachinery*, volume 120, number 4, pp. 671–682.

Wang, M., Freund, J. and Lele, S. (2006). Computational prediction of flow-generated sound. *Annual Review of Fluid Mechanics*, volume 38, pp. 483–512.

Wang, Y. (2000). *Tip Leakage Flow Downstream of a Compressor Cascade with Moving End Wall*. Master's thesis, Virginia Polytechnic Institute and State University, Blacksburg, Virginia, United States of America, 90 pp.

Weichert, S. A. (2011). *Tip Clearance Flows in Axial Compressors: Stall Inception and Stability Enhancement*. Ph.D. thesis, University of Cambridge, Cambridge, United Kingdom, 221 pp.

Welch, P. D. (1967). The Use of Fast Fourier Transform for the Estimation of Power Spectra: A Method Based on Time Averaging Over Short, Modified Periodograms. *IEEE Transactions on Audio Electroacoustics*, volume 15, pp. 70–73.

Wells, V. L. and Han, A. Y. (1995). Acoustics of a moving source in a moving medium with application to propeller noise. *Journal of Sound and Vibrations*, volume 184, pp. 651–663.

Wolfram, D. and Carolus, T. (2008). Detection and Analysis of Azimuthal Modes in a Centrifugal Impeller. In *The 12th International Symposium on Transport Phenomena and Dynamics of Rotating Machinery*.

Wu, H., Miorini, R. L. and Katz, J. (2011a). Measurements of the tip leakage vortex structures and turbulence in the meridional plane of an axial water-jet pump. *Journal of Experimental Fluids*, volume 50, pp. 989–1003.

Wu, H., Tan, D., Miorini, R. L. and Katz, J. (2011b). Three-dimensional flow structures and associated turbulence in the tip region of a water-jet pump rotor blade. *Journal of Experimental Fluids*, volume 51, pp. 1721–1737.

You, D., Wang, M., Moin, P. and Mittal, R. (2007). Large-eddy simulation analysis of mechanisms for viscous losses in a turbomachinery tip-clearance flow. *Journal of Fluid Mechanics*, volume 586, pp. 177–204.

Zhu, T. (2016). *On the Flow Induced Tip Clearance Noise in Axial Fans*. Ph.D. thesis, Universitat Siegen, Siegen, Germany, 170 pp.

Zhu, T., Lallier-Daniels, D., Sanjosé, M., Moreau, S. and Carolus, T. (2016a). Rotating coherent flow structures as a source for narrowband tip clearance noise from axial fan. In *18th AIAA Aeracoustics Conference*. AIAA, Lyon, France.

Zhu, T., Lallier-Daniels, D., Sanjosé, M., Moreau, S. and Carolus, T. (2016b). Rotating coherent flow structures as a source for narrowband tip clearance noise from axial fans. *Journal of Sound and Vibration*, volume 417, pp. 198–215.